INVESTIGATION OF STRENGTH-ENHANCEMENT MECHANISM AND SIZE EFFECT ON ULTIMATE SHEAR STRENGTH OF STEEL FIBER-REINFORCED CONCRETE (SFRC) SLENDER BEAMS

by

MOHAMMAD REZA ZARRINPOUR

Presented to the Faculty of the Graduate School of

The University of Texas at Arlington in Partial Fulfillment

of the Requirements

for the Degree of

DOCTOR OF PHILOSOPHY

THE UNIVERSITY OF TEXAS AT ARLINGTON

May 2016

ACKNOWLEDGMENTS

Firstly, I would like to express my sincere gratitude to my advisor Dr. Shih-Ho (Simon) Chao for the continuous support of my Ph.D study and related research, for his patience, motivation, and immense knowledge. Besides my advisor, I would like to thank the rest of my dissertation committee: Dr. Ali Abolmmaali, Dr. Anand Puppala, and Mr. Joe Lundy, for their insightful comments and encouragement.

Concrete and formwork materials used in this investigation were provided by Mr. Vartan Babakhanian from Forterra Pipe & Precast in Grand Prairie, TX. The SFRC specimens were cast at Forterra Pipe & Precast by their workers. Steel fibers used in this investigation were provided by Maccaferri. Dr. Gustavo Parra-Montesinos at the University of Wisconsin-Madison reviewed the design of the specimens. Dr. Jae-Sung Cho greatly contributed to specimen construction. Each person and company represented here offered an essential help that is gratefully appreciated.

Also, special thanks goes to Dr. Pourya Hajalikhani, Chatchai Jiansinlapadamrong, and Dr. Regina Waweru, the members of our research group at the University of Texas at Arlington, each of whom played an important role in the development of this research project.

Finally, I am deeply indebted to my wife, Hoda Alavi, for her unwavering love, understanding, support, encouragement and patience during my graduate student career. At the same time, I offer my special thanks to my beloved family for their encouragement and love.

May 2016
Mohammad Reza Zarrinpour

ABSTRACT

INVESTIGATION OF STRENGTH-ENHANCEMENT MECHANISM AND SIZE EFFECT ON ULTIMATE SHEAR STRENGTH OF STEEL FIBER-REINFORCED CONCRETE (SFRC) SLENDER BEAMS

Mohammad Reza Zarrinpour, PhD

The University of Texas at Arlington, 2016

Supervising Professor: Shih-Ho Chao

This research study consists of two separate phases. In the first phase, an experimental study was conducted to identify the shear-enhancement and failure mechanisms behind the ultimate shear strength of steel fiber-reinforced concrete (SFRC) slender beams by utilizing the full field deformation measuring capability of digital image correlation (DIC) technology. A total of 12 large-scale simply supported SFRC and RC beams with a range of heights including 12 in. (305 mm), 18 in. (457 mm), 24 in. (610 mm), 36 in. (915 mm), and 48 in. (1220 mm) were tested under monotonic point load. The greater shear strength in SFRC beams stems from the fiber bridging effect which delays the propagation of the cracks into the compression zone. In contrast to the traditional assumption for either plain concrete or SFRC beams, where the shear contribution resulting from dowel action is completely neglected, this research clearly shows that the dowel action has an appreciable effect on the ultimate shear strength. Its contribution varies from 10% to 30% as the beam depth increases from 12 in. (305 mm) to 48 in. (1220 mm). On the other hand, the compression zone's contribution decreases from 69% to 36% with the increase in beam depth. In addition, the shear contribution from the fiber bridging effect along the critical shear crack stays virtually unchanged at 20%, regardless of beam

depth. In this study, the minimum shear strength obtained was in the range of $5\sqrt{f'_c}$ psi ($0.42\sqrt{f'_c}$ MPa) for the beams with the greatest depth. This indicates that the maximum allowed shear stress limit of $1.5\sqrt{f'_c}$ psi ($0.125\sqrt{f'_c}$ MPa) specified in ACI 318-14 is on the very conservative side.

While the size effect on ultimate shear strength of plain concrete beams has been well researched in the past decades, limited tests were carried out to study the extent and mechanism of size effect in steel fiber-reinforced concrete (SFRC) beams. Current American Concrete Institute's ACI 318 Building Code restricts the use of steel fiber as minimum shear reinforcement to beams with a height up to 24 in. (610 mm). In the next phase of the study, in addition to the analyzing of the current testing data, the laboratory test results from the first part of the study and the respective digital image correlation (DIC) images were examined to identify the underlying factors that cause size effect on ultimate shear stress of SFRC slender beams. Moderate size effect was observed in the beams tested in this study. Through the full field strains and a mechanical based analysis, it was found that the size effect is a function of both the beam height and the shear span length. In larger beams, due to the greater horizontal and vertical distance from the compression zone to the supports, the critical diagonal shear crack was able to propagate deeply into the top of the beams. As a consequence, the compression zone exhibits less contribution to shear resistance in larger size beams, and the dowel action becomes more critical. Therefore, a minor flaw in dowel zone such as lacking well-distribution of steel fibers results in early destruction of dowel resistance and shear failure.

TABLE OF CONTENTS

LIST OF ILLUSTRATIONS

LIST OF TABLES

Chapter 1

INTRODUCTION

1.1 General and Motivation

Shear failure in plain concrete is brittle in nature and can result in a catastrophic failure with no warning. For that reason, ductile flexural failure is to be favored over the failure caused by shear when a structure is overloaded. Therefore, in order to prevent a slender beam from prematurely failing in shear before attaining its ultimate flexural strength, the concrete beam is usually heavily reinforced by means of conventional transverse reinforcing (stirrups, Av). This in turn leads to additional labor and higher material costs with the possibility of poor quality due to congested reinforcement.

One measure to protect concrete members from brittle shear failure under excessive loads is to use steel fiber reinforced concrete (SFRC). Considerable research has been conducted on the shear behavior of SFRC over the past decades, and the results have shown that high performance SFRC can considerably improve the post-cracking tensile behavior and toughness of concrete (e.g. Chao et al., 2011; Dinh, 2009; Hannant, 1978). These improvements have resulted in the application of SFRC to an extensive spectrum of structural elements including industrial floors, bridge deck overlays, airport runways, highway pavements, tunnel linings, spillways, dams, slope stabilization, and many precast concrete utility products. However, in building construction, the application of SFRC is currently not very common in spite of the fact that the shear and flexural behavior of concrete members are considered to be improved by the addition of steel fibers (Baston et al., 1972; Hannant, 1978). The lack of design provisions in the governing building codes is the major reason for this deficiency. For instance, the American Concrete Institute (ACI) Committee 544 report associated with the shear design procedure for beams reinforced by steel fibers, did not provide a design procedure despite their discussion of

recent test results and the presentation of an equation estimating SFRC shear stress. Only until recently did the ACI Building Code in its 2008 edition, allow SFRC as an alternative for conventional shear reinforcement (i.e. steel stirrups)"……when $\phi 0.5 v_c \leq v_u \leq \phi v_c$, steel fibers can be used to replace the minimum shear reinforcement for flexural members (prestressed and nonprestressed) constructed of steel fiber-reinforced concrete with compressive strength not exceeding 6 ksi, depth not greater than 24 in., and shear stress v_u not greater than $\phi 2\sqrt{f'_c}$. It also requires that beams constructed with steel fiber reinforced concrete have a minimum volume fraction of steel fibers of 0.75%." The absence of a shear design equation and the existence of the above restrictive ACI criteria, such as imposing a limitation on beam height, implies an uncertainty in extending the recent advances in the understanding of the shear behavior of SFRC for all cases. There are two possible reasons for the uncertainty. First, the majority of SFRC beam tests were carried out on beams with small heights ranging from 4 to 11 in., including some beams reinforced with obsolete types of fibers such as straight fibers. It should be noted that the shear strength of plain concrete decreases as the size (depth) of a beam increases due to so-called “size effect” (Kani, 1964; Kani, 1967; Shioya et al., 1989; Collins and Kuchma, 1999; Lubell et al., 2004 and Sherwood et al., 2007) as clearly depicted in Figure 1.1. Although some researchers have claimed that the size effect for shear is less evident in SFRC beams compared to plain concrete beams (Dinh, 2009), this needs to be verified through tests performed on beams with greater depths. The second reason for the uncertainty is the lack of sufficient knowledge concerning the shear resistance mechanism in SFRC beams. Therefore, this research is geared to experimentally investigate these two factors through the use of large-scale slender beams reinforced by steel fibers.

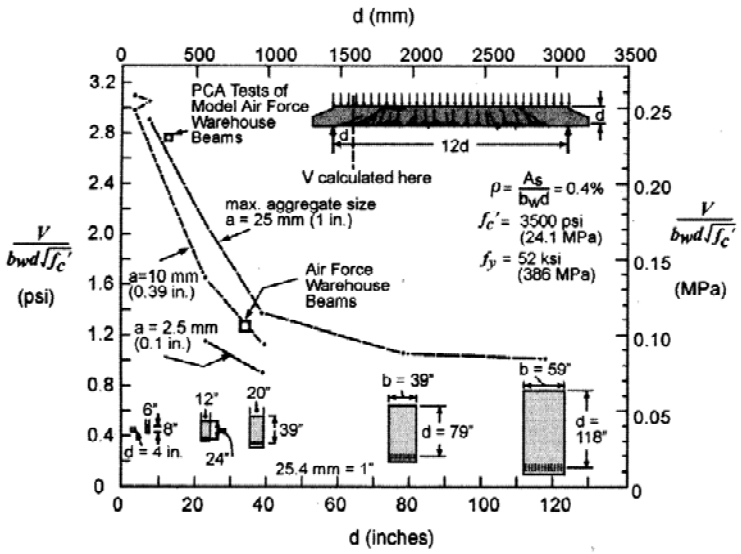

Figure 1.1 Size effect in plain concrete beams

1.2 Objectives

1.2.1 Determination of strength-enhancement and failure mechanisms of SFRC beams by using Digital Image Correlation system (DIC)

While there is rather universal acknowledgement and understanding of diagonal shear failure in plain concrete (PC) beams (without transverse reinforcement) under shear, different models with distinct perspectives have been proposed to explain the shear resistance mechanism of PC beams. One explanation is explored in the Modified Compression Field Theory (Vecchio and Collins, 1986), where aggregate interlock (based on aggregate sizes), crack width/spacing, and straining effect due to longitudinal reinforcement are used to explain the shear behavior. Another popular approach is the Compression Force Path Theory (Kotsovos, 1988) in which the resistance against shear is assumed to be provided by a compression path through which the external force is transmitted to the supports. Finally, the Critical Shear Crack Theory (Muttoni and Ruiz, 2008) introduces arch action as the possible shear-carrying mechanism of a PC beam upon formation of a critical shear crack.

In general, the micro and macro-mechanical behavior of fiber-reinforced concrete (FRC) is significantly different from plain concrete depending on the fiber volume fraction, fiber geometry, fiber orientations, and fiber-to-matrix bond characteristics. Numerous studies have shown that steel fiber-reinforced concrete (SFRC) can considerably improve the post-cracking tensile behavior and toughness of concrete (e.g., Mobasher, 2012). When considering SFRC behavior at the structural element scale, the addition of steel fibers in concrete beams can also result in a substantial increase in the ultimate shear capacity and deflection at failure in comparison with identical plain concrete beams. The enhanced shear strength was usually attributed to the fiber bridging stress across shear cracks (e.g., Choi et al., 2007). For design purposes, ACI 318 (2014) allows the use of steel fibers as minimum shear reinforcement when $\phi 0.5 v_c \le v_u \le \phi v_c$, where the compressive strength of concrete does not exceed 6 ksi (41 MPa), beam depth is no greater than 24 inches (610 mm), and shear stress v_u is no more than $\phi 2\sqrt{f'_c}$ (i.e., $1.5\sqrt{f'_c}$ where f'_c in psi). ACI 318 (2014) also requires a minimum volume fraction of steel fibers of 0.75% (100 lb. steel fibers per cubic yard of concrete). To date, a very limited number of models have been proposed for the shear resistance mechanisms of SFRC beams. Choi et al. (2007) proposed a theoretical strain-based model to account for the effect of flexural deformation on shear capacity of an SFRC beam. The shear resistance from aggregate interlocking and dowel action has been ignored because the intact compression zone was assumed to prevent slip of the crack interface (Choi et al., 2007; Kotsovos and Pavlović, 1998). They assumed that the shear resistance of an SFRC beam is provided by the intact compression zone and the bridging tensile strength of steel fibers crossing the critical shear crack. The location of the critical shear crack was first determined by their strain-based formulations through an iterative process, and then the shear contribution of the

compression zone was determined by Rankin's failure criteria. In contrast to the procedure used by Choi et al. (2007), in our study, the full field strains (thus stresses) were measured by digital image correlation (DIC) directly along the critical crack just prior to failure, thereby eliminating any assumptions or iterative procedures to establish shear strength. Dinh et al. (2011) used a similar approach, where the shear contribution of aggregate interlocking and dowel action were ignored. They reported (Dinh et al., 2010) that 18 of the 23 SFRC specimens failing in shear were caused by tension failure. Nevertheless, in their model, they assumed that crushing in the compression zone was the cause of failure and employed the compression failure criterion established for plain concrete by Bresler and Pister (1958) with the average ultimate compressive stress of $0.85f'_c$ in Whitney's stress block.

In general, the current models used to predict the ultimate shear strength of SFRC beams were developed on the basis of simplified assumptions concerning shear failure mechanism. These assumptions can sometimes either conflict to some extent with reality or be oversimplified by eliminating the shear resisting components. Even though some shear resisting components have proven negligible for RC beams, their contribution to SFRC beams has not yet been assessed. Furthermore, the strength-enhancement mechanism of SFRC beams as a result of fiber inclusion is still not well defined. Establishment of the strength-enhancement mechanism serves as a preliminary step to investigate size effect in ultimate shear strength of SFRC beams and to determine the design shear strengths of SFRC beams which has resulted in a conservative low value in current ACI 318 provisions (2014). This research aims to determine the shear-enhancement and failure mechanisms of SFRC beams by means of an advanced three dimensional deformation-monitoring digital image correlation (DIC) technique. DIC captures the full field deformations and their progression as load increases.

1.2.2 Identification of the potential factors causing size effect and its intensity in SFRC beams by using a Three Dimensional Digital Image Correlation system (DIC)

A large body of research conducted on the shear behavior of reinforced concrete (RC) slender beams with no shear reinforcement (plain concrete beams) has demonstrated the existence of size effect on the ultimate shear stress (e.g., Kani, 1967; Shioya et al., 1990; Collins and Kuchma, 1999; Sherwood, 2008), where the shear strength (in terms of stress) decreases as the beam depth increases. Therefore, the test results from relatively small beams are not applicable to large-scale beams. Size effect on ultimate shear stress for plain concrete beams is explained by an observation by Shioya (1989), where the crack spacing was about a half of the beam depth. This led to the assumption that the crack spacing would increase when a slender beam becomes deeper. If the strain in concrete between two consecutive cracks is neglected, the average width of the inclined cracks can be approximately represented by the product of the average crack spacing and the strain of the reinforcement. Therefore, at a given longitudinal bar strain, an increase in crack spacing causes wider cracks, thereby reducing aggregate interlock capacity in resisting the shear (Shioya et al., 1990; Lubell et al., 2004). Based on the aforementioned assumption, any factor causing an increase of either crack spacing or tensile strain in longitudinal reinforcement can lead to an increase in crack width and subsequent reduction of the aggregate interlock capacity, thus exacerbating the size effect. This can occur either when using reinforcement with a smaller modulus of elasticity or with an insufficient reinforcement ratio (Walraven, 1981; Vecchio and Collins, 1986; Khaja and Sherwood, 2013). On the other hand, any factor which enhances aggregate interlocking such as using larger aggregate size, placing layers of longitudinal reinforcement along the depth of the beam, or using stirrups can minimize the size effect (Sherwood, 2008; Walraven, 1981).

However, the recent experimental tests by Sneed and Ramirez (2010) indicated that the assumed relation between the beam depth and crack spacing may not be always true. They tested plain concrete beams with a beam height between 12 and 36 in. (203 and 610 mm) and reported that the average crack spacing stays nearly constant and does not scale with the beam depth.

It is well established that the addition of discrete steel fibers into concrete can considerably increase the sectional shear strength (Swamy and Bahia, 1985; Mansour et al., (1986); Narayanan and Darwish, 1987; Ashour et al., 1992; Swamy et al. 1993; Kwak et al., 2002). Although the use of steel fiber-reinforced concrete (SFRC) to replace minimum conventional mild steel shear reinforcement has been permitted by the design code (ACI 318, 2014), it is unclear if size effect is also a concern in SRFC slender beams. This concern is reflected in the ACI code, where the maximum beam overall depth, h, is not allowed to be greater than 24 in. (610 mm). Nevertheless, some researchers have suggested that size effect on ultimate shear stress could be less of an issue for SFRC beams (Dinh et al., 2010).

Information collected in Figure 1.2 illustrates the relationship between normalized shear strength and total depth for the SFRC beams with 0.75% fiber volume fraction (Dinh, 2009; Parra-Montesinos, 2006). Note that the steel fiber volume fraction of 0.75% is the minimum amount of steel fiber used to replace the conventional minimum shear reinforcement (stirrups) (ACI 318, 2014). As noticed, all the test beams had an effective depth ranging from 7 in. (178 mm) to 22.5 in. (571.5 mm) and an approximate average shear strength from $5\sqrt{f'_c}$ psi ($0.4\sqrt{f'_c}$) with no obvious size effect.

Minelli et al. (2014) undertook a series of tests on SFRC and companion plain concrete beams with three different heights of 20 in. (500 mm), 39.4 in. (1000 mm), and 59 in. (1500 mm).

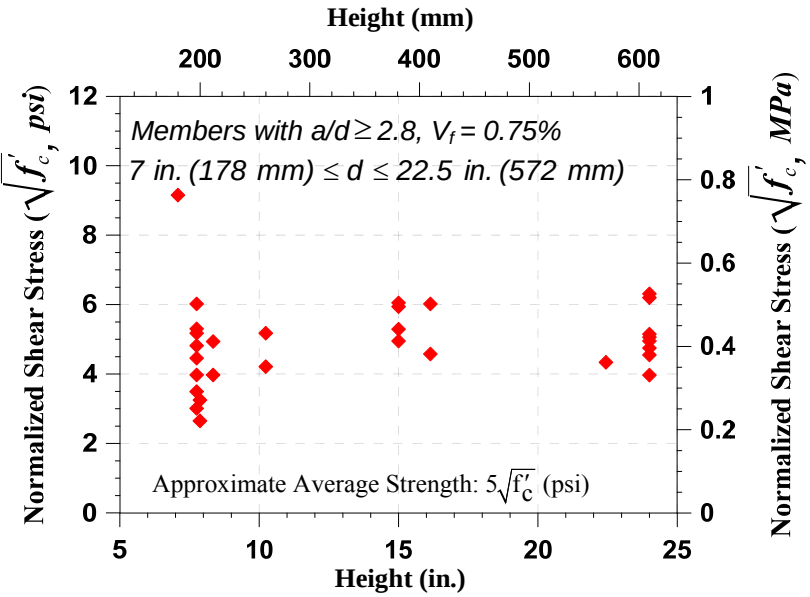

Figure 1.2 Shear stress at failure in terms of $\sqrt{f'_c}$ vs. total depth for the members with a/d greater than 2.8 and containing 0.75% fiber volume fraction (collected by Parra-Montesinos, 2006)

For each series of beams with the same height, the steel fiber volume fraction was varied at 0, 0.64, and 1%. Their test results are replotted in Figure 1.3. As noticed, when the effective depth was increased about twice from 17 in. (440 mm) to 37 in. (940 mm), the shear strength of the plain concrete beams reduced by 24%. On the other hand, the strength of SFRC beams with 0.64% and 1% V_f dropped 47% and 30%, respectively. Their results show that SFRC beams had an even more severe size effect than plain concrete. In addition, when the effective depth was increased further to 57 in. (1440 mm), the previously observed trend was not maintained. Nevertheless, they concluded that size effect could be substantially reduced as a result of the presence of steel fiber.

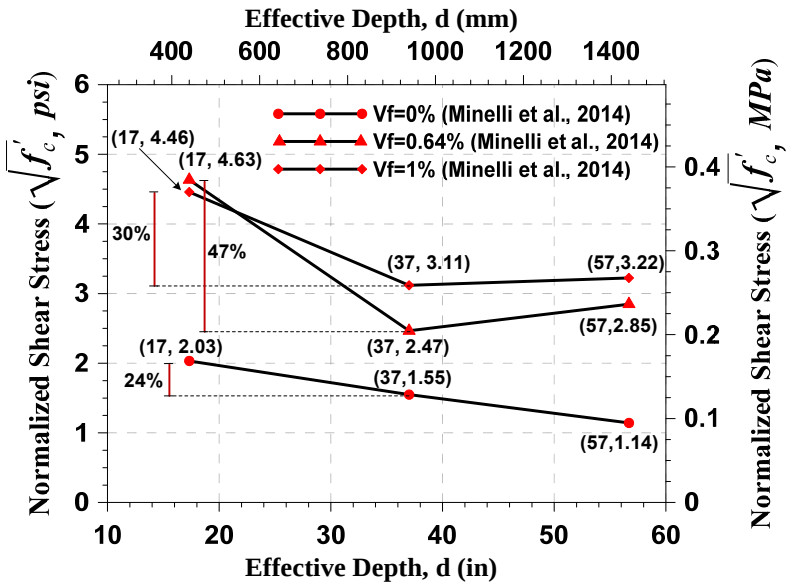

Figure 1.3 Shear stress at failure in terms of $\sqrt{f'_c}$ vs. effective depth (reproduced from Minelli et al., 2014)

Shoaib et al. (2014) tested 12 SFRC specimens with an overall depth from 12.1 to 39.4 in. (308 to 1000 mm) to examine the size effect in SFRC beams with 1% steel fiber volume fraction. Longitudinal reinforcement ratio was varied from 1.88 to 4.03%. Their results, as illustrated in Figure 1.4, also showed the existence of size effect in SFRC beams, where the average of SFRC beam strengths were reduced by 54% for the range of the considered beam depths. They noticed that the crack widths before failure were large irrespective of the depth of the beams, therefore the smaller shear strength of deeper beams could not be related to the reduction of aggregate interlock. Instead, they attributed size effect to a larger amount of steel fiber pull out (thus decreasing the contribution from fiber tensile force) just before the failure as the beam height becomes larger.

Similar finding on the less importance of minor contribution of aggregate interlock, regardless of the beam depth, to shear resistance for SFRC beams prior to failure was observed in this study (discussed later). This study aims to identify the potential factors causing size effect in SFRC beams.

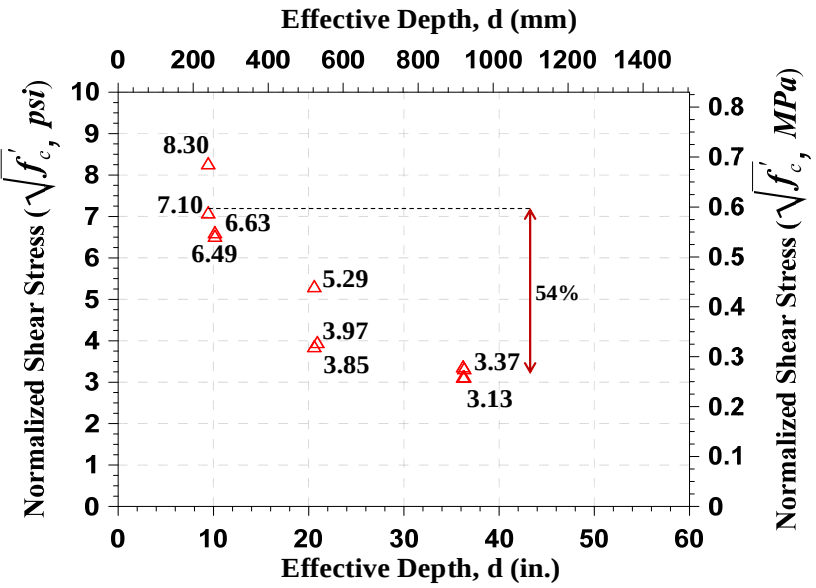

Figure 1.4 Variation of the ultimate shear strengths of the tested beams in the study of Shoaib et al. (2014)

1.3 Organization of the Dissertation

This dissertation consists of six chapters. Each chapter is outlined as follows:

Chapter 1 **– Introduction:** This chapter starts with a general philosophy of the use of conventional transvers reinforcement (stirrups) in RC beams, the potential replacement of stirrups with steel fibers and the possible reasons inhibiting the usage of SFRC in the building industry. Then, the chapter proceeds with pointing out the research objectives.

Chapter 2 **– Literature Review:** This chapter reviews the majority of the past studies conducted toward the identification of shear-influencing factors, development of a model(s) representing load-carrying mechanism, and an assessment of the size effect in RC beams with no conventional stirrup reinforcing (PC beams). Subsequently, this chapter summarizes the preceding research dealing with the recognition of parameters affecting the mechanical properties of SFRC as well as the tests through which the various

mechanical properties of SFRC can be determined. Finally, the chapter ends with a summary of the prior studies concerning shear behavior of SFRC beams.

***Chapter 3*–Experimental Program:** This chapter describes all the arrangements adopted for conducting an experimental study including design and construction of the large-scale specimens, concrete and SFRC mix design, test setup, instrumentations, and the tests oriented toward the determination of the material properties.

***Chapter 4*–Experimental Results:** The chapter discusses the shear behavior of each test beam in terms of cracking pattern, failure mode, ultimate shear strength, and reinforcement strains.

***Chapter 5*–Analysis of Experimental Results:** This chapter explains the shear strength-enhancement and failure mechanisms as well as the causes behind size effect in SFRC beams by analyzing the cracking patterns and three dimensional DIC-measured full-field strain components developed on the surface of each test specimen.

***Chapter 6*–Summary and Conclusions:** The summary of this experimental investigation along with the major findings and conclusions are presented in this chapter.

Chapter 2

LITERATURE REVIEW

2.1 Introduction

In the Reinforced Concrete (RC) beam design, the quantity of the longitudinal bars is determined in accordance with the flexural demand in a manner that if the beam were to fail, it would do so gradually and be accompanied with ample warning. Afterward, the shear capacity of the beam is to be checked for the critical section throughout the member to ensure the failure is dominated by flexure rather than shear. This is because shear failure is well-established to have unpredictable and instantaneous nature to the contrary. Therefore, in case of the insufficient shear capacity provided by concrete, transverse bars are required to provide.

As well-known, RC slender beams without shear reinforcement are vulnerable to substantial shear strength (ultimate shear stress) degradation as the height increases. This phenomenon is called size effect. According to Sherwood (2008), large lightly reinforced slender RC beams with no web reinforcement whose shear capacity is analyzed to be adequate in accordance with the American Concrete Institute's ACI 318 Building Code is likely subjected to the threat of brittle shear failure before the flexural capacity is fully achieved. The reason was attributed to the fact that ACI 318 Building Code does not account for size effect in the equations designated to predict the shear capacity of concrete in RC beams. Nevertheless, the work done by Collins and Kuchma (1999) indicated that the size effect in shear strength of RC beams could be insignificant by applying minimum shear reinforcement.

Steel fibers and concrete constitute a composite material termed Steel Fiber Reinforced Concrete (SFRC). In comparison with plain concrete, SFRC exhibits better mechanical behavior particularly after cracking. As a matter of fact, the presence of steel

fibers crossing the crack allows the induced tensile stresses to keep being transferred by holding the two sides of the crack connected together (bridging effect). In this situation, the performance of steel fiber is dominated by two factors: the fiber-concrete interfacial bonding and the steel fiber fracture strength. Therefore, the failure in the SFRC could be the result of either the steel fiber pull-out or fracture. However, the former is still favored because the fiber pull-out is a stable and gradual process, and the energy could be dissipated before the sudden fracture of fibers. At the early stages of steel fiber development, the application of steel fibers in concrete was mostly limited in controlling the cracks in concrete pavement and flat slabs. However, the results from experiments have recently indicated that it can be effectively replaced with the conventional shear reinforcement in RC beams. This chapter consists of a brief discussion about the development of the ACI 318 shear design provision, size effect and other parameters influencing shear resistance mechanism in RC beams, various models explaining the shear mechanism in concrete beams without shear reinforcement, steel fiber and the mechanical properties of SFRC, and the shear behavior and related factors of SFRC beams.

2.2 Development of the ACI 318 Shear Design Provision

A Swiss and German engineer, Ritter and Mörsch, individually presented a simple shear design method respectively in 1899 and1902 for a concrete beam with shear reinforcement. This method was termed 45° truss model by which the extremely indeterminate system of the internal stresses in a cracked beam could be simply simulated with a determinate truss. In this model, shear in the cracked web was postulated to be transferred by means of the inclined compression struts developing parallel to the diagonal cracks and vertical tensile members (stirrups). In this simple model, the intact compression zone and the longitudinal bars corresponded to the top and bottom chord of this equivalent truss respectively. Therefore, a designer was able to easily determine the entire unknowns

in the truss members employing the current methods being used to analyze a truss. Unfortunately, the necessarily assumed 45° inclined members in the truss model indicated by Mörsch to be in conflict with the reality. Regardless, the ease of this method raised the popularity to such an extent that it became the basis of the expression used to predict the shear resistance provided by stirrups in various building codes. The ACI 318 was not an exception from the fact.

Based on the truss analogy, concrete has no contribution in shear resistance, and the entire shear is solely carried through the stirrups. Therefore, a concrete beam designed by this method would be expected to be overdesigned for shear. In order to quantify the contribution of the concrete in shear resistance, the intensive efforts of the researchers eventually resulted in the development of an empirical equation, $v_c = 0.3f'_c$ (ACI 318-51). Therefore, the web reinforcement for a particular section in a concrete beam was determined such that the discrepancy of the shear demand and the concrete shear contribution was attributed to the shear amount necessary to be provided by the stirrups. Eventually, the quantity of the stirrups was calculated using the expression derived from the 45° truss analogy. Among the abundant structures designed based on the proposed expression for the concrete contribution during 1950's and early 1960's, a large portion of the roof of the Wilkins Air Force Warehouse in Selby, Ohio collapsed on Aug. 17, 1955 due to the abrupt shear failure of the supporting beam. Apparently, there was no stirrup provided in the beam based on the aforementioned empirical equation, and the concrete itself was strong enough to take the total shear demand force (ACI-ASCE Committee 326). Following this incident, further investigations were aimed at finding a better expression estimating the shear strength of concrete.

In 1962, the ACI-ASCE committee 326 attributed the ultimate load carrying capacity of a reinforced concrete member without web shear reinforcement to the load in

which the critical diagonal tension crack forms to develop a design criterion. According to the committee's report, the diagonal cracking was considerably influenced by three primary parameters verified from both test data and mathematical model in basis of the principal stress concept. These three variables were: (a) shear span to effective depth ratio, a/d; (b) longitudinal tensile reinforcement ratio, ρ; and the square root of the compressive strength of concrete after 28 days, $\sqrt{f'_c}$. In fact, the shear span to effective depth ratio represented the influence of horizontal flexural tension on diagonal tension. Since this parameter could not be defined for every cross section and general loading configuration, the effect of a/d on diagonal cracking (shear strength of RC beam) was expressed in terms of M/Vd ratio, where M and V were both the bending moment and shear force of a section. In the case of when a concrete beam is subjected to a point load, the term M/Vd was stated to be equal to a/d. Finally, by means of the above concepts and curve-fitting through 194 test data (Figure 2.1), Equation (2.1) was suggested as shear strength of concrete to be employed in shear design of RC beams.

$$\frac{V_c}{b_w d} = 1.9\lambda\sqrt{f'_c} + 2500\frac{\rho V d}{M} \le 3.5\sqrt{f'_c} \qquad (psi)$$

$$\frac{V_c}{b_w d} = \frac{1}{7}\lambda\sqrt{f'_c} + 17\frac{\rho V d}{M} \le 0.29\sqrt{f'_c} \qquad (MPa) \qquad (2.1)$$

In Equation (2.1), V_c is the shear carried by the concrete; b_w and d are respectively the beam's width and effective depth; λ is the concrete modification factor; f'_c is the 28 days concrete compression strength. Note, in evaluation of the test data to derive Equation (2.1), M/Vd was picked at the section of the critical diagonal crack. The critical diagonal crack was assumed to initiate at the distance of d from the section of the maximum moment for the beams with a/d in excess of 2. However, for the ratio less than 2, the location of diagonal crack was assumed to be at the mid-shear span.

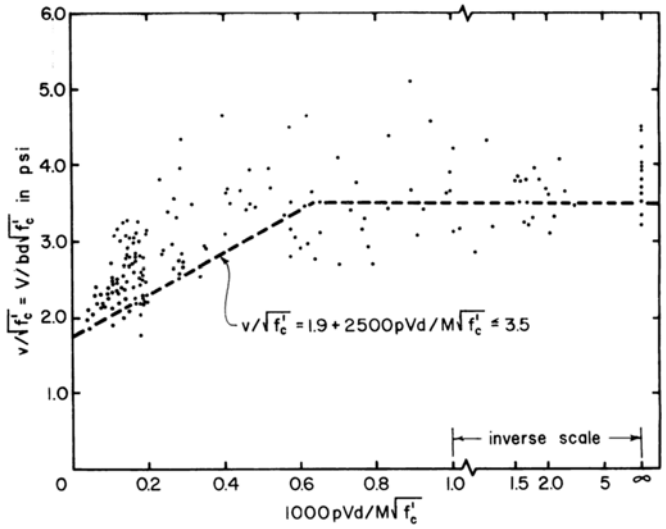

Figure 2.1 Derivation of Shear design Equation (ACI-ASCE committee 326, 1962)

Equation (2.2) represents a simplified version of Equation (2.1) incorporated in current ACI 318-14 which is abundantly used in the practical design due to its simplicity. Equations (2.2) corresponds to Equation (22.5.5.1) in the ACI 318-14.

$$\frac{V_c}{b_w d} = 2\lambda\sqrt{f_c'} \qquad (psi)$$
$$\frac{V_c}{b_w d} = 0.167\lambda\sqrt{f_c'} \qquad (MPa) \tag{2.2}$$

2.3 Shear Resistance Mechanism in Concrete Beams without Stirrup Accepted by ACI

The equilibrium equation established for a portion of a beam with an infinitesimal length and between two vertical sections indicates that the internal shear force develops as the moment varies along the beam axis. In an RC beam, the moment in each section is a function of the tensile force in the steel bars and the moment arm (jd) each of which is, in turn, a function of x, the distance of an arbitrary section relative to an origin. Therefore, shear along a concrete beam can be mathematically expressed as follows:

$$V = \frac{dM}{dx} = \frac{d}{dx}(T.jd) = (jd)\frac{dT}{dx} + T\frac{d(jd)}{dx} \quad (2.3)$$

This equation signifies two primary actions through which the shear is transferred from loading point to support, including beam action and arch action (Fenwick and Paulay, 1968). The first term in Equation (2.3) represents the beam action, while the second one represents the arc action. If the lever arm "jd" remains consistent across the shear span, the second term will vanish and shear is resisted by beam action. $\frac{dT}{dx}$ is called shear flow that exists in any horizontal plane along the beam's effective depth and required in formation of the beam action (Park and Paulay, 1975). Of course, any reason such as unbonded tensile bars or occurrence of a diagonal crack extending from the pointing load to the support can inhibit the shear flow. In this case, the first term equals zero, and the second one, arch action, becomes activated. The external shear is hereby transferred through an inclined compression strut in form of a compressive force directly from the loading point to the support. Therefore, according to ASCE- ACI 426 (1973), the arch action cannot be a shear mechanism, in which the external transverse load is resisted by an internal tangential force from section to section. However, since the arch action could directly transfer a major proportion of the transverse concentrated force to the support and by this means, increase the shear capacity, it is classified as a sort of the shear transfer mechanism (ASCE- ACI 426, 1973). Note, in order for the arch action to develop, the tensile stress in the flexural reinforcing bars needs to stay constant all over the length of the shear span. In the beam action, once the beam cracks, the combination of three major components contributes in carrying the external shear as shown in Figure 2.2: the shear in the compression zone (V_{cy}), the vertical component of the aggregate interlock stresses engaged across the surface of the crack (V_{ay}), and the vertical force induced in the longitudinal bars due to the dowel effects (V_d) (Fenwick and Paulay, 1968).

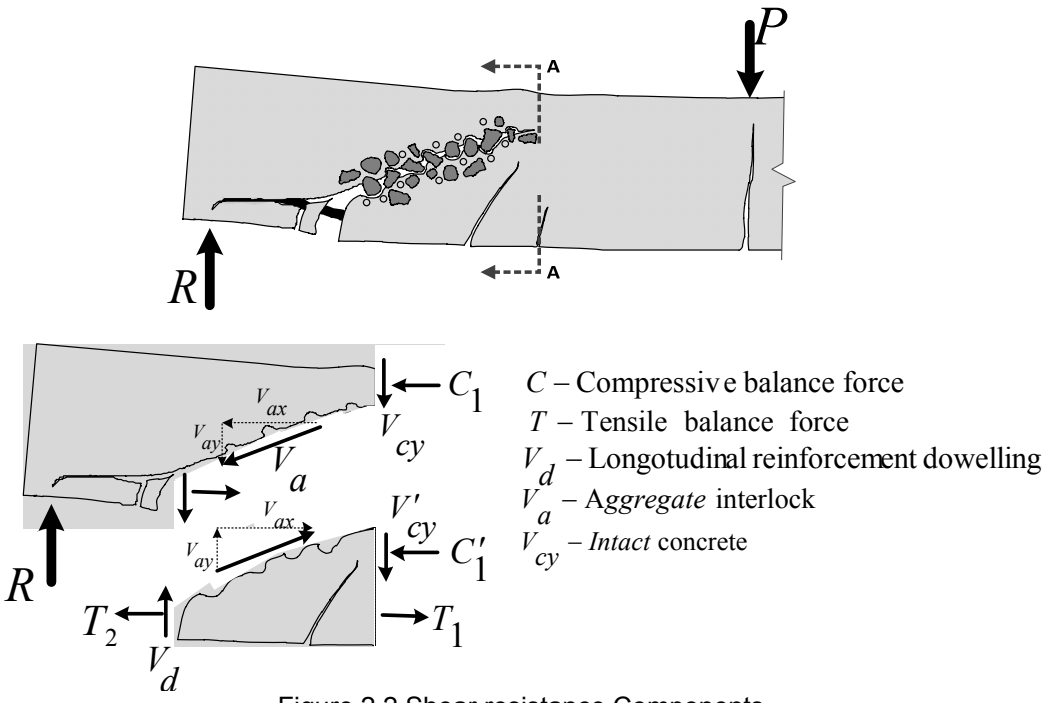

Figure 2.2 Shear resistance Components

In RC beams without web shear steel, the diagonal crack quickly propagates toward the loading point upon the initiation and shortly after having a marginal increment in the external load, significantly reduces the depth of compression. Therefore, the area of the intact compression zone is normally claimed to be insufficient to solely resist the total shear force. However, some early researchers such as Zwoyer and Siess (1954), Moretto (1955), Moody et al. (1954), Hanson (1958), Bresler and Pister (1958), and Walther (1962) had either directly or implicitly assumed that a cracked concrete beam resists the entire shear force by the intact compression zone; hence, they disregarded the shear contribution resulting from aggregate interlocking. Nevertheless, Moe (1962) demonstrated that the variation of tensile stress in longitudinal bars is contingent upon the transfer of the internal shear force across the existing crack though aggregate interlocking. According to Walraven (1981), aggregate interlocking diminishes as the width of crack increases.

As inferred, the relative contribution of each component in taking the total shear force still remains controversial. For the first time in 1968, Fenwick and Paulay concluded that 60% of the vertical shear load is resisted by aggregate interlock, and in some cases, it can even be raised up to 75%. While their investigation was primarily focused on the significance of aggregate interlocking on the shear strength of a concrete beam, the relative contribution of the dowel action was estimated to ascend barely above 20%. Therefore, the remaining portion was attributed to the compression zone. Taylor (1970) found that compression zone and dowelling action of longitudinal bars account for 20-40% and 15-25% of the total shear resistance, respectively. The remaining 33-50% was correlated to aggregate interlock. Sherwood et al. (2007) mounted a series of strain gages along the intact compression zone depth in a pattern shown in Figure 2.3 to quantify the total shear force carried by that. The beam was loaded up to the occurrence of the dominant flexural-shear crack that was equivalent to 93% of the final failure load. Then, the beam was unloaded, and the strain gages were placed at the head of the crack in two columns kept 3.2 in. apart. The beam was then reloaded as the strains were being recorded. Using the Hook's law and Young's modulus, the acquired strain was converted to stress. The difference between the two stresses obtained at the same level was regarded as the shear stress acting at that level. Therefore, by having the shear stress at different levels revealed the shear stress distribution along the compression zone depth. Eventually, the shear force carried by the compression zone was evaluated by integrating the shear stress distribution curve. The results indicated that compression zone resists only 24% of the total shear load.

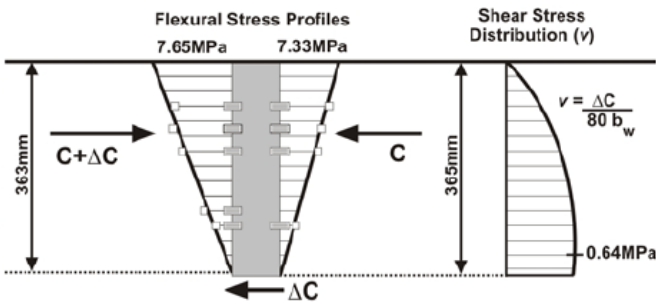

Figure 2.3 Measurement of Shear Carried in Compression Zone
(Sherwood et al., 2007)

In shear critical RC beams with no shear reinforcement, that the arch action or beam action to provide the shear resistance has a major impact on the shear behavior which is recognized to be tightly dependent on the shear span to the effective depth ratio. Therefore, according to Wight and Macgregor (2009), beams are divided into 4 groups based on their shear span to the effective depth ratio: very short, short, slender, and very slender. The term “very short” refers to those beams with a/d between 0 and 1. In this group of beams, the developed inclined crack directly joins the loading point to the support which results in the disturbance of the shear flow, thus changing the shear behavior of the beam in terms of the load-carrying mechanism from beam action to arch action. In these beams, the steel bars act as the tension tie of a tied arch. The anchorage failure at the end of the tension tie would be their common failure. Short beams are characterized by their a/d ranging between 1 and 2.5. When an inclined crack develops in the beams, they are still able to carry additional load partly by the arch action. ASCE- ACI 426 (1973) reported that in this type of beam, one of the two modes of failure may occur from a curved tensile crack developing in the combined shear and moment region. In the first mode termed as shear-tension failure, the dowel action of longitudinal bars develops a secondary crack propagating back toward the support and along the steel bars from the inclined crack that would lead to the destruction of the concrete-steel interfacial bond. As a result, the wedging

action of the longitudinal bars following the bars' slipping accounts for the splitting of the concrete and further propagation of the crack which results in the anchorage failure of the longitudinal reinforcement. Prior to such a failure, the beam acts as a tied arch. On the other hand, in the second mode of failure, crushing of the concrete above the upper tip of the inclined crack triggers the failure, which is called shear-compression failure. These two modes of failure are distinguished in Figure 2.4.

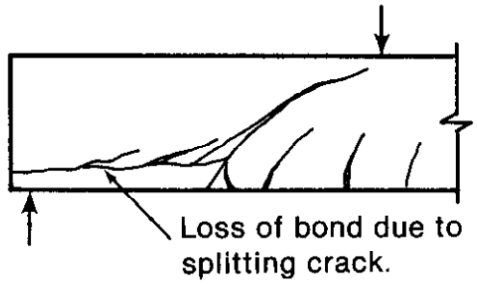

(a) Shear-tension failure.

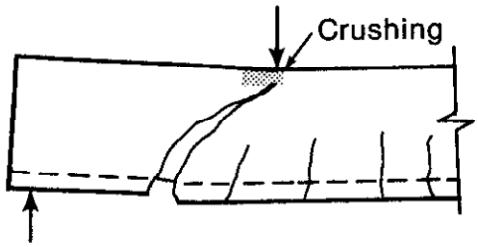

(b) Shear compression failure.

Figure 2.4 Modes of Failure for Short Beams, $1 \leq a/d \leq 2.5$ (ASCE- ACI 426, 1973)

The shear span to effective depth ratio for the slender beams ranges between 2.5 and 6.5. According to ASCE-ACI 426 (1973), for the smaller values of the a/d in the range, one of the inclined cracks developed in the beam may continue to propagate as the load increases such that at some stage of the loading, it becomes unstable and causes the beam to fail as shown in Figure 2.5b, whereas for the larger values of a/d, the beam might fail through

a flexural-shear crack before the fully achievement of the flexural moment capacity as depicted in Figure 2.5a.

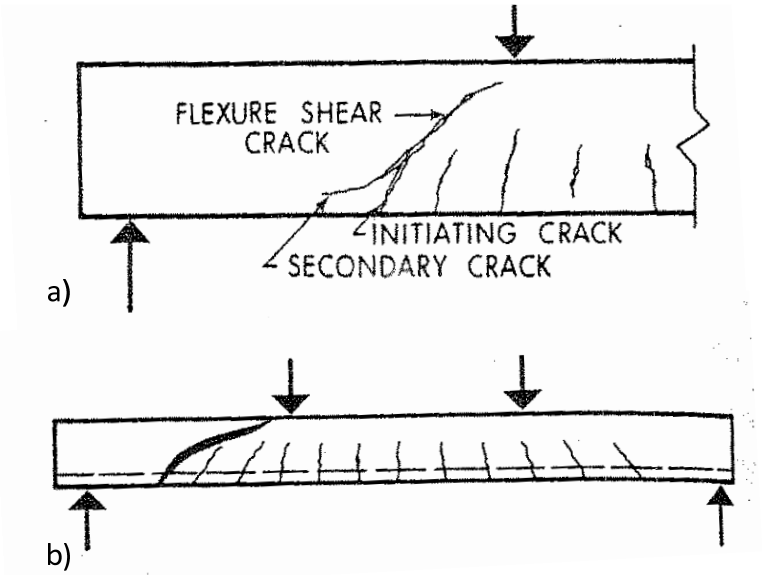

Figure 2.5 Modes of failure in slender beams (ASCE- ACI 426 (1973))

2.4 Different Perspectives in Shear Resistance Mechanism of the Concrete Beams with No Stirrup

Moe (1962) proposed a shear stress distribution which slightly differs from the one suggested by the classic theory of Mörsch (Figure 2.6). In his model, the part of concrete located between two consecutive flexural cracks is regarded as a vertical cantilever beam restrained at the neutral axes of the original beam. Therefore, as expected, it is naturally subjected to a pair of transverse loads at its end. In fact, the transverse loads are the tensile forces developing in the longitudinal bars due to the effective bending moments acting at the corresponding cracked sections. The end forces are indicated by T and $T + \Delta T$ in Figure 2.6. ΔT signifies the difference between the two forces generated from the different bending moments. For this reason, the concrete cantilevers are to be pulled toward the side with the larger tensile force under the force ΔT.

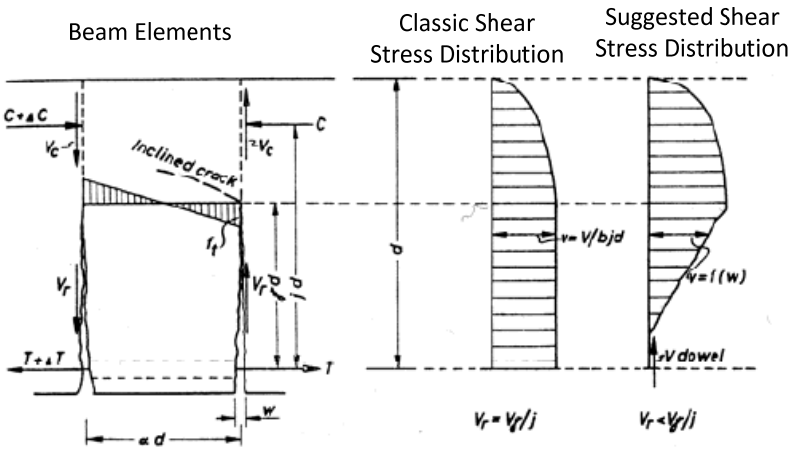

Figure 2.6 Shear Failure Model proposed by Moe, 1962

In this model, the resulting bending moment due to ΔT is assumed to be counteracted by a couple moment arising from the aggregate interlocking forces of V_r activated between the surfaces of the cracks at both sides of the cantilever beam. However, the widening of the cracks gradually lowers the coupled forces and results in the development of the bending reaction in the root of the cantilever beam. Eventually, shear failure in the form of an inclined crack occurs when the bending tensile stresses at the root of the cantilever beam become sufficiently high.

According to Kani (1964), a reinforced concrete beam with no web shear reinforcement transforms into a comb-like structure while the load is increasing. In the tensile zone, the concrete between two adjacent flexural cracks constitutes the teeth of the concrete comb, whereas the compression zone account for its backbone as illustrated in Figure 2.7.

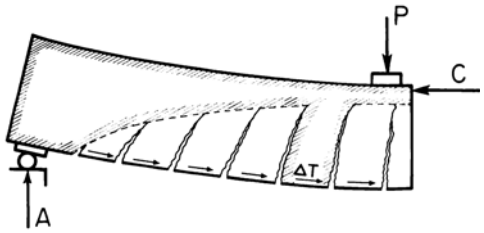

Figure 2.7 A view of concrete teeth and compression zone as the backbone of the concrete comb

In this model, the beam action mechanism is governed until the flexural capacity of the concrete teeth is exceeded. Following the beam action destruction, the potential development of tied arch may enable the beam to carry some additional loads. It is noteworthy that the models considered by Kani (1964) and Moe (1962) were similar. However, Kani did not take into account the contribution of aggregate interlocking along the flexural cracks; hence, the full flexural capacity of a concrete tooth was assumed to be fully provided by its root. Nevertheless, Kani et al. (1979) concluded that only 40% of the flexural resistance of the concrete teeth is provided by their root, and the remaining is required to be gained from the aggregate interlock across the flexural cracks on the both sides of the tooth and dowel action. To develop a general method for shear design, Vecchio and Collins (1986) presented a model termed Modified Compression Field Theory (MCFT). This model has a theoretical base and able to predict the shear behavior of RC elements in the absence of experimental data. Currently, the MCFT lies beneath all the provisions comprised in AASHTO (1994) and CSA Committee A23.3 (1994) to predict the shear strength of a concrete beam. The advantage of all design methods developed in the basis of this theory is their capability to account for the influence of aggregate size and size effect in shear. In the MCFT, cracks were assumed to initiate and open in the direction of minimum and maximum principal stresses, respectively. In addition, the principal stresses and strains are to develop in the same direction. Therefore, the width of the crack can be calculated by the product of the crack spacing in the principal tensile direction, S_θ, and the principal tensile strain, ε_1, ($w = S_\theta \times \varepsilon_1$). In determination of the crack width, the strain in concrete is neglected.

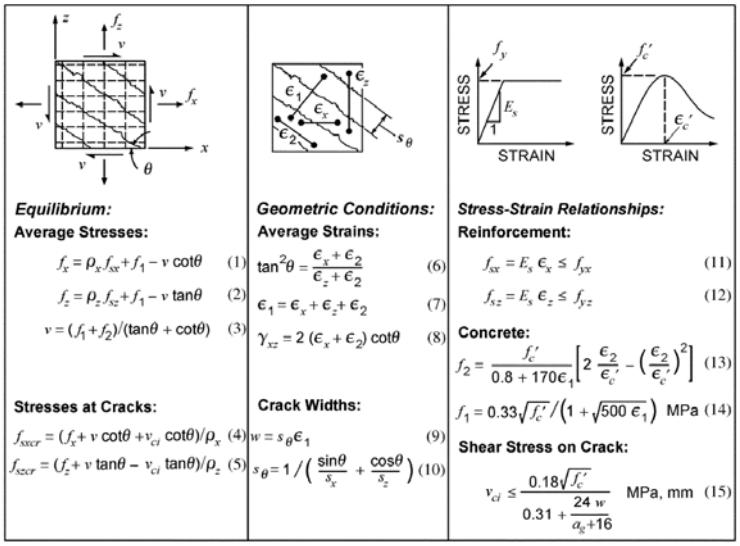

Figure 2.8 Relations of the MCFT (Bentz et al., 2006)

S_θ represents the ability of the reinforcing bars to control the crack spacing in the principal tensile direction and is expressed in terms of S_x and S_z as indicated by Equation 10 in Figure 2.8. The terms S_x and S_z are the crack spacing in x and z directions when the element is subjected to pure longitudinal and pure transversal tension, respectively. The stresses acting on an arbitrary inclined intact and cracked sections of a reinforced concrete panel, which is in equilibrium, are shown in Figure 2.9. Prior to crack development, equilibrium requires that both concrete and reinforcements contribute in transferring the tensile force on the principal plane as shown in terms of the average stresses in section 1. Since this section assumed to be principal plane, concrete is just subjected to the principal tensile stresses. When a crack occurs, the tensile force in the concrete is reduced to zero, and subsequently, the stress locally increases in the reinforcing bars. It may further lead to sliding of the two sides of crack and development of the aggregate interlock resistance, v_{ci} (Figure 2.9c). Eventually, the panel fails if the capacity of the aggregate interlock is exceeded. This would be especially the case if the steel yields in one or two directions.

Therefore, the MCFT limits the shear strength of a reinforced concrete element to the aggregate interlock capacity along a developed crack as expressed by Equation (2.4). Equation (2.4) was derived by Walraven (1981), through which the capacity of aggregate interlock is correlated to concrete compressive strength, f'_c, crack width, w, and maximum aggregate size, a_g.

$$v_{ci} \le \frac{2.16\sqrt{f'_c}}{0.31+\frac{24w}{a_g+0.63}} \qquad (psi)$$

$$v_{ci} \le \frac{0.18\sqrt{f'_c}}{0.31+\frac{24w}{a_g+16}} \qquad (MPa) \qquad (2.4)$$

Equation (2.4) indicates that the shear capacity of aggregate interlock is to be reduced by either increasing the crack width, or decreasing the maximum size of the aggregates used in the mix. On the other hand, since the average width of inclined cracks can be approximately represented by the product of the average crack spacing and the strain of the reinforcement, any factor causing an increase of either factors can lead to an increase in crack width and subsequent reduction of the aggregate interlock capacity.

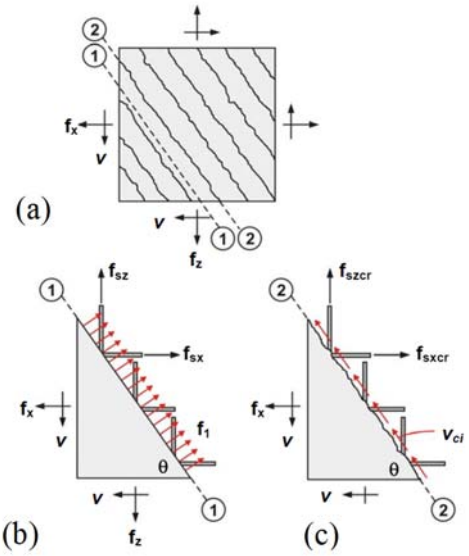

Figure 2.9 Stresses acting on the principal plane before and after the crack formation (Sherwood, 2008)

Tureyen and Frosh (2003) proposed a simplified model to predict the shear strength of a cracked concrete beam with no stirrup. They assumed that the shear strength of the beam was fully provided through the intact concrete above the neutral axis. Equation (2.5) represents their proposed equation, where the shear strength of the beam is expressed in terms of the neutral axis depth, c (i.e. the depth of the compression zone). Therefore, in case of different flexural reinforcement ratio and modulus, the stiffness of the flexural bars is to be reflected in the neutral axis depth.

$$V_c = K\sqrt{f'_c}\,b_w c \qquad (psi) \qquad (2.5)$$

where

$$K = \sqrt{16 + \frac{4\sigma_m}{3\sqrt{f'_c}}}$$

σ_m is the stress corresponding to the outermost compression fiber generated by the cracking bending moment at distance of d (effective depth) from the support. For design purposes, K was evaluated through the experimental results at 6.79. However, this value was reduced to 5 to provide a conservative estimation of shear strength. The behavioral model underlying their idea is shown in Figure 2.10. Note, while the expression could be applied to the slender concrete beams, it does not account for the size effect.

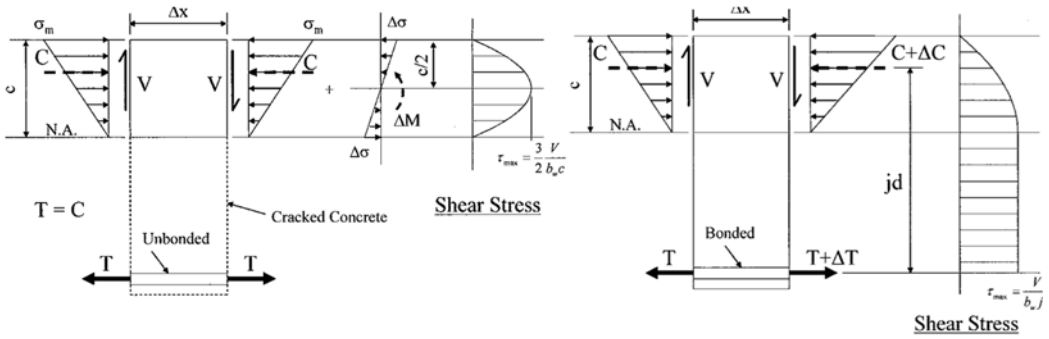

Figure 2.10 Free-body diagrams of a cracked section and average shear stress distribution (Tureyen and Frosh, 2003)

Kotsovos (1988) claimed that the widely admitted aggregate interlock concept is not well-matched with the fundamental concrete properties. It was stated that a crack initiates when the principal tensile stress exceeds the tensile strength of concrete, propagates in direction of the maximum principal compressive stress, and opens perpendicular to its direction. For this reason, the sliding of the two faces of the crack over one another, which is required for the mobilization of aggregate interlock, cannot be achieved; hence, no aggregate interlock can be activated along the crack. He alleged that for an RC beam at its ultimate limit state,the shear is resisted through a region in the path along which the applied compressive force is transferred to the supports. As pointed out, the shear failure proceeds from the tensile stresses developing in the compression path and perpendicular to that (Figure 2.11). These tensile stresses may develop due to several reasons: (a) changes in the compression path direction toward support (resultant force T

at zone 1 in Figure 2.11), (b) substantial tensile stresses concentrated at the tip of the inclined crack perpendicular to the direction of the max principal compression stress (t_1 at zone 2 in Figure 2.11), (c) concrete expansion at the smallest section as a result to the highest compressive stress intensity (t_2 in Figure 2.11), (d) extension of a flexural crack into the compression path due to the bond failure at level of the tension reinforcements between two consecutive flexural cracks that, in turn, intensifies the compressive stresses and subsequently, increases the transverse tensile stresses (t_2 in Figure 2.11).

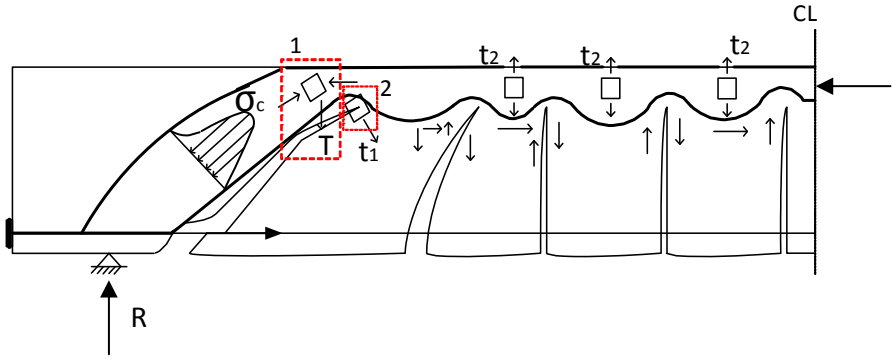

Figure 2.11 Compression force path and the tensile stresses causing failure

Drucker (1961) proposed Direct Load Transfer Mechanism for RC beams without transvers reinforcement, plain concrete (PC) beams, where the applied load is directly transferred to the support through a direct compression strut. This model was based on the theory of plasticity in which the flexural bars plays the role of tension ties for a compression tied strut because the concrete was assumed to be not able to carry tension at all. The Direct load transfer suggested by Dracker is shown in Figure 2.12 for two different load configurations. This theory was criticized by Muttoni and Ruiz (2008) pointing out that this model overestimates the predicted shear strength of a PC beam where critical shear crack interferes with compression strut and consequently lowers its strength.

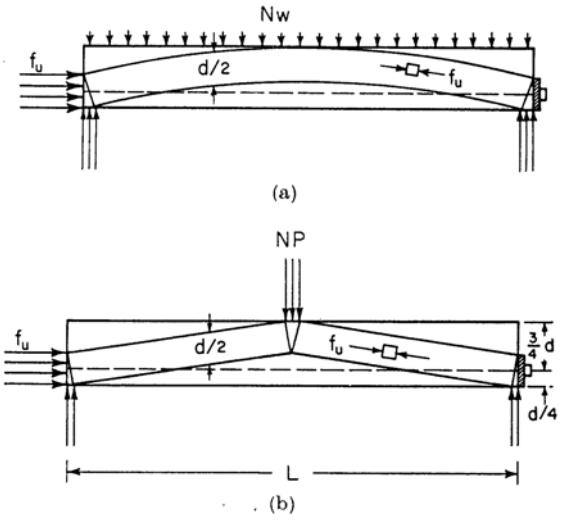

Figure 2.12 Arch and compression strut proposed by Drucker 1961 for a. uniform and b. concentrated loading configuration

Muttoni and Ruiz (2008) proposed Critical Shear Crack Theory, where arch action is introduced as the shear-carrying mechanism of a PC beam upon formation of critical shear crack. To detail, they pointed out that three different types of possible mechanism initially contribute to shear resistance in beam shear span considering flexural cracking pattern, as follows: cantilever action, aggregate interlock action, and dowel action as shown in Figure 2.13b, Figure 2.13c, and Figure 2.13d, respectively. These three mechanisms induce tensile stresses near the tips of the existing cracks and at the level of flexural reinforcement. Once the tensile stress in any points in the concrete shown in Figure 2.13e exceeds the concrete tensile strength, the existing flexural crack in the neighborhood deviates from a vertical to a diagonal direction which results in the development of the critical shear crack. Formation of the critical shear crack disrupts the previous shear-carrying mechanisms. Nevertheless, the concrete beam does not necessarily fail in shear; on the contrary, another shear resistance mechanism, arch action, may become involved.

Two physical mechanisms result in the arch action development as illustrated in Figure 2.14.

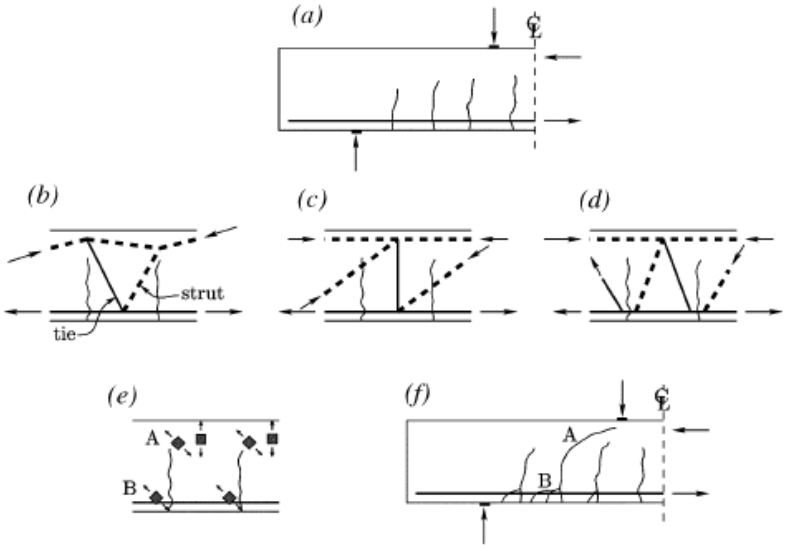

Figure 2.13 Crack pattern in a concrete beam: (a) initial flextural cracks; (b) Cantilever action; (c) Aggregate interlock action; (d) dowel action; (e) tensile stresses resulting from (b-d); Final crack pattern

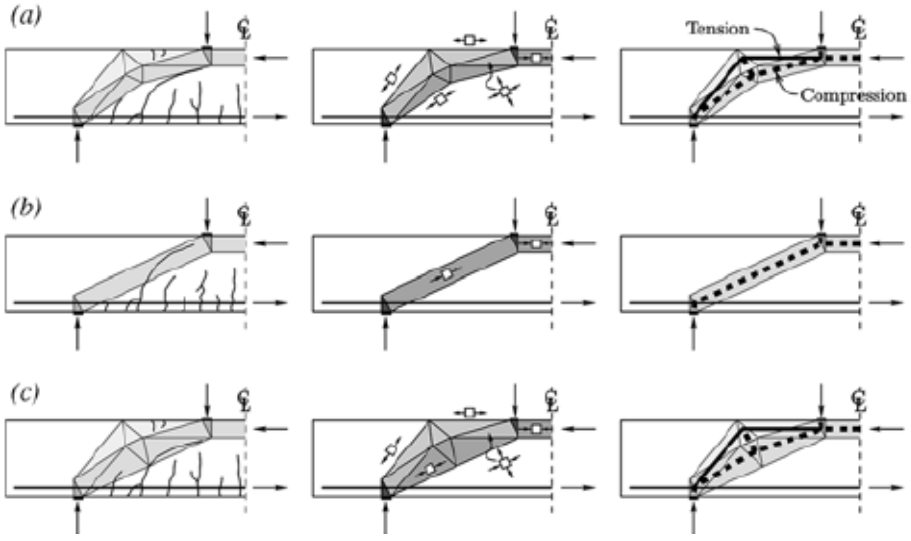

Figure 2.14 Possible arch action mechanisms: a. Elbow-shaped strut b. straight strut c. Combined action

As noticed in Figure 2.14a, the arch action may develop due to the formation of the elbow-shaped strut when the compressive stresses tend to be transmitted from loading point to the support with no crossing of the critical shear crack. According to them, the initiation of the elbow-shaped strut mainly depends on the crack pattern. The arch action would also initiate as a result to the direct compression strut from the loading point to the supports which is contingent upon the mobilization of the aggregate interlock at the interface of the critical shear crack interfering the strut (Figure 2.14b). In reality, both aggregate interlock and elbow-shaped strut are active at the failure as presented in Figure 2.14c. According to this theory, the strength of the arch action, thus the shear strength of the beam, is influenced by the intensity of the critical crack interference with the compression strut. This effect in predicting the shear strength of a PC beam was considered in form of an equation being a function of critical shear crack width and aggregate size.

Gustafsson and Hillerborg (1988) performed a finite element analysis of shear failure to find the shear strength of a concrete beam. To do so, the stress-strain behavior of the materials subjected to tension was defined based on a nonlinear fracture mechanics model called the fictitious crack approach. In this model, the dowel action and aggregate interlock were neglected. Moreover, it was assumed that two sides of the crack are in contact once the crack width is less than the critical crack width. In this numerical study, a variety of the ultimate shear strengths was obtained in basis of the development of the critical shear crack in several locations. Eventually, the minimum shear strength was considered as the shear strength of the beam. As a note, the beam was assumed to fail in shear following crushing of the concrete above the crack.

Park et al. (2013) developed an analytical method to estimate the shear strength of prestressed and ordinary concrete beams, where shear force was assumed to be mainly

carried by the uncracked compression zone. This method was derived in accordance with the strain-based shear strength model established by Park et al. (2006) in which the shear capacity of the compression zone was defined as a function of the flexural deformation of beam. In the suggested method, the interaction of compressive normal stress was considered in the Shear strength assessment of concrete at the inclined failure surface using the Rankin's maximum stress criteria. Their method was verified by the test results.

2.5 Size Effect in Shear for Reinforced Concrete Beams without Shear Reinforcement

2.5.1 General

Current shear design procedures specified by different Building Codes resulted from the intensive research programs conducted during a large period of time. From a design point of view, a proper shear design procedure should be characterized by its simplicity, rationality, generality, and, above all, safety and accuracy. In order to appraise the safety and accuracy of shear design expressions that was required by a particular code for RC beams, it should be revealed how those expressions account for the effects of: (a) member depth, (b) maximum aggregate size, (c) reinforcement ratio, (d) minimum stirrups, (e) web width, and (f) crack control steel. The following section is focused on the influences of member depth and maximum aggregate size on shear behavior of RC beams.

2.5.2 Member depth and aggregate size constituting two major factors of the size effect phenomenon

Shear strength reduction with an increase in the height of slender plain concrete beams with no web reinforcement is a phenomenon called size effect. Although the existence of this phenomenon is well known, there is still no universal consensus achieved on the severity and potential factors underlying this phenomenon. In 1962, Leonhardt and Walther carried out an experimental study to investigate size effect in RC beams without stirrups. Their test consisted of two distinct series of specimens with the same shear span

to effective depth ratio of 3.0. In the first series referred to as “D-series”, the number of the longitudinal bars was kept constant for all the specimens, while their diameters were enlarged with an increase in the beam cross section to maintain the flexural reinforcement ratio. This action resulted in the reduction in steel-concrete interface bond quality as the beam depth rises. It is noteworthy that the effective depth of the beams was varied from 70 mm to 280 mm. On the contrary, in the second series referred to as “C-series”, the longitudinal bar diameter remained constant, though the number of them was adapted to keep the reinforcement ratio invariable with an increase in the beam effective depth, thus leading to similar bond quality. The effective depth in this set ranged from 150 to 600 mm. The size effect turned out significant for the D-series, where the bond quality was predicted to deteriorate as effective depth increases. Beam size nearly had no effect on the C-series shear strength due to the constant quality of bounds as stated. Kani (1967) alleged that the results of the experiments performed on rather small beams with a height of 10 to 15 in. which constitute the majority of the tests on RC beams cannot correctly represent the safety factors of large beams. Therefore, a number of tests were conducted on concrete beams without stirrups to investigate the effect of depth on their shear strength and also prove that in spite of claims from earlier studies (e.g. Rüsch et al., 1962; Forsell, 1954), there is no critical depth value to find above which the size effect does not exist. The test results are summarized in Figure 2.15 through which Kani confirmed the presence of size effect in RC beams without stirrup, where the a/d falls greater than 2 as well as the lake of an evidence supporting the critical depth concept. Collins et al. (2008) by referring to Figure 2.15 argued that the ACI 318 Building Code’s shear expression, Equation (2.1), overestimates the effect of concrete compressive strength (f'_c) and underestimates the influence of ($M/\rho Vd$) Nevertheless, according to Collins et al. (2008), the test results

reported by Kani (1967) cannot clearly reflect the deficiency since in all the beams, the longitudinal reinforcement ratio (ρ) was near to the balanced reinforcement ratio that resulted in high shear failure stress in excess of 2. Figure 2.15 also contains a test result reported by Kani (1969), where the test specimen was a concrete beam with a depth of 42.9 in. and no shear reinforcements. The shear span to effective depth ratio was picked 3.1 along with the longitudinal reinforcement ratio of 0.8%. This beam failed in $\beta = 1.33$ which is much lower than the predicted value of 2 in accordance with ACI318-14, thus supporting the statement of Collins et al. (2008).

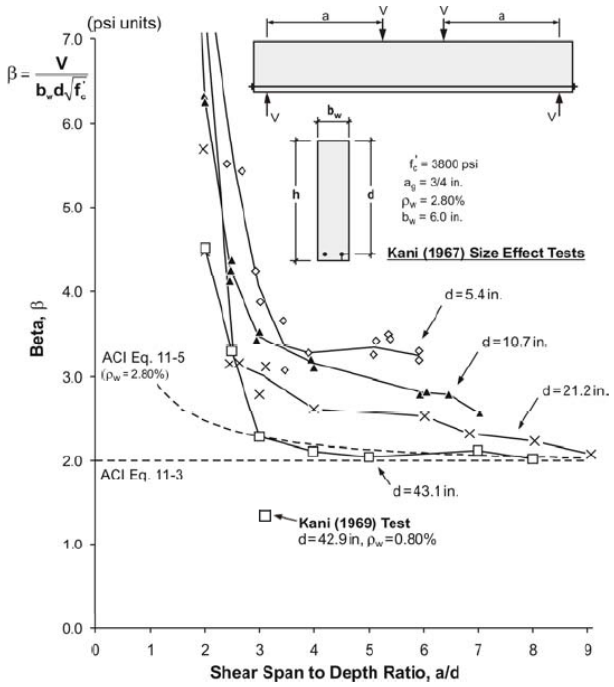

Figure 2.15 Kani's Size Effect Tests (Sherwood, 2008)

To verify the size effect in RC beams with larger effective depths of more than 39 in. (1000 mm) as well as the influence of aggregate size on its severity, Shioya et al. (1989) and Shioya (1989) tested a large number of reinforced concrete beams without stirrups under uniformly distributed loads up to failure. Effective depth for the specimens was selected in

a range of 4 in. (100 mm) to 118 in. (3000 mm). In these experiments, loading span to effective depth ratio, concrete compressive strength, and longitudinal reinforcement ratio were maintained consistent at 12, 3408 psi (23.5 MPa), and 0.4%, respectively. Maximum aggregate size was varied from 0.04 in. (1 mm) to 0.98 in. (25 mm) in proportion to the beam depth. The test results re-affirmed the existence of size effect even for the beam depths greater than 39 in. (1000 mm). In addition, size effect was concluded to arise from both influences of maximum aggregate size and size effect in concrete tensile strength. To elaborate, two distinct shear stresses were defined as τ_{cr} and τ_u. The former was the shear stress at which a flexural crack turns into the critical shear crack developing at 1.5d away from the support, while the latter was associated with the shear stress at which the beam fails (shear failure). The difference between these shear stresses was considered as the shear carried by aggregate interlocking. The variation of each designated shear stress versus beam effective depth is shown for two different maximum aggregate sizes through Figure 2.16. It was observed that as the depth of a beam increases, τ_{cr} decreases, which led to the conclusion that the size effect in shear is influenced by the size effect in flexural tensile strength of the concrete. In addition, for the larger maximum aggregate size (G_{max}=25 mm), the shear resisted by aggregate interlock (τ_u) followed the same descending trend as for the specimens with the smaller maximum aggregate size, whereas for the effective depths greater than 24 in. (600 mm), the reducing rate became smaller. Therefore, the reduction in aggregate interlocking for the larger beams resulting from the wider crack was compensated by the existence of greater maximum aggregate size (Figure 2.16). Shioya (1989) recognized that in a PC beam, the flexural crack spacing at the mid-height equals to roughly half of the effective depth. Hence, based on the MCFT described earlier, at a given strain in longitudinal bars, the increase in crack spacing resulted from larger effective depth causes wider critical crack and the consequent reduction in

aggregate interlock capacity (Lubell et al., 2004). Noghre Khaja and Sherwood (2013) suggested the lowered ability of longitudinal bars to control the crack spacing in higher beams as the primary reason of size effect in shear.

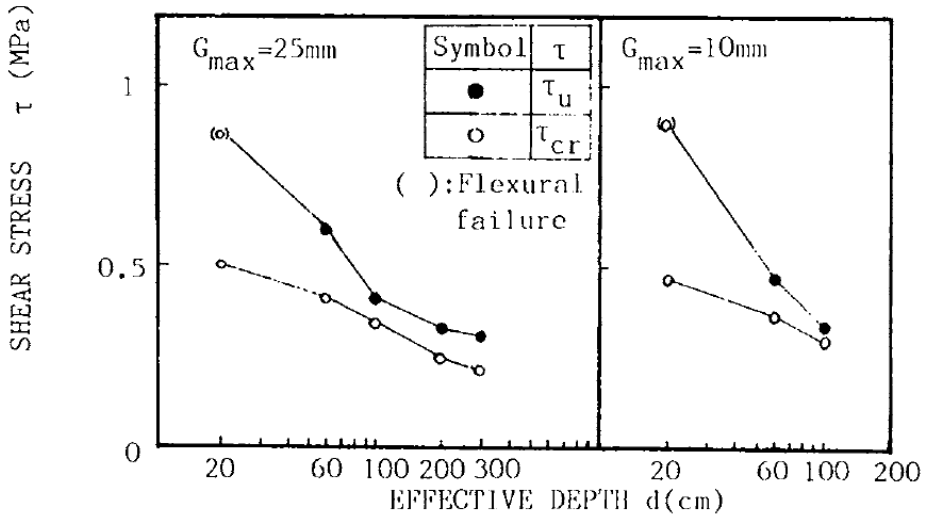

Figure 2.16 Shear stress versus effective depth response for two different maximum aggregate sizes (Shioya et al., 1989)

According to Collins and Kuchma (1999), the database underlying the ACI shear expressions contained experimental results on slender beams with rather short effective depth. Therefore, the ACI deficiency in predicting the safe shear strength of high slender beams is inherent. Size effect and the associated unconservative nature of ACI for large concrete beams was realized to be significantly alleviated if minimum shear reinforcement is provided or the concentrated longitudinal bars are dispersed in different layers along the depth known as skin horizontal reinforcements. Also, they found that the application of high strength concrete in PC beams could exacerbate size effect in shear. This is due to the fact that in high-strength concrete beams, the failure crack prorogates through the aggregates causing the crack surfaces to become smoother. For this reason, the use of larger aggregate size to increase the roughness of crack surfaces would have no improving impact upon beam shear strength.

In order to investigate the ACI's capabilities in providing an accurate and safe shear design procedure when applied to tall beams, Sherwood et al. (2007); Sherwood (2008) undertook an extensive experimental program with a focus on size effect and the influence of max aggregate size. This program consisted of two series of 10 large-scale and 10 equivalent 1/5-scale (small-scale) beams (slab-strip specimens) loaded to shear failure. These specimens were assumed to well represent the shear behavior of a wide slab as well because the width had been found to have no major effect on the failure shear stress of a beam (Lubell et al., 2004; Sherwood et al., 2006).

The large-scale beams were 59 in. (1510 mm) deep, 12 in. (300 mm) wide and 354 in. (9000 mm) long, while as for the small ones, they were designed to be 13 in. (330 mm) deep, 4.8 in. (122 mm) wide, and 71 in. (1800 mm) long. 18 out of the entire specimens were provided no stirrup; on the contrary, the remainders contained minimum amount of stirrups based on SMCFT (Simplified Modified Compression Field Theory (Bentz et al., 2006). In the specimens lacking shear reinforcement, the only variable was the maximum aggregate size changing from 0.39 in. (10 mm) to 1.97 in. (50 mm) in diameter. These specimens were fabricated with the normal strength concrete. In contrast, the large and small specimens reinforced with the minimum shear reinforcements were constructed by high strength concrete and constant maximum aggregate size of (0.39 in.) 10 mm. The lower shear stress and deformation at failure exhibited by their larger beams confirmed the presence of size effect and was justified by the more reduced aggregate interlock capacity in the larger beams due to the development of wider critical crack at failure. In addition, a decrease in maximum aggregate size turned out to develop smooth failure crack surfaces, thus reducing the shear capacity of PC beams. On the other hand, increasing maximum aggregate size was illustrated to not necessarily elevate the shear capacity of PC beams

because using larger aggregate size seems to ascend the chance of aggregate fracturing along crack path during the crack development.

Sneed and Ramirez (2010) carried out an experimental study aimed at the influence of effective depth and width on the concrete contribution to the shear strength of plain concrete beams. For this purpose, they tested two sets of four simply supported PC beams where for each set, the depth was varied between 12 and 36 in. (305 and 915 mm). In the first group of beams, specimen width was held invariable, while in the latter, it was altered at a constant ratio of depth. It is noteworthy that the entire traditional factors influencing the shear behavior remained unchanged. Test results indicated a reduction in shear strength when effective depth increases; the shear strength of the 12 in. beams, however, greatly differed from the rest of the beams. As demonstrated, this huge distinction did not entirely result from size effect; instead, it associated partially with the factors causing the observed difference in the shear behavior and the shear transfer mode. As the beam height changed from 24 to 36 in. (610 to 915 mm), the average shear strength was reduced by 14% in a rather linear trend. However, by including the 12 in. specimens in their assessment, a nonlinear reduction in the shear strength was noticed ranging between 64% and 44% for the first and second series of beams, respectively as the beam depth increased from 12 to 36 in. (305 to 915 mm). In addition, changing in the depth of the specimens from 12 to 36 in. (305 to 915 mm) returned no difference in the average flexural crack spacing at the level of longitudinal bars despite of the high variation in the depth up to 300%. This was in fact in contrast with the widely accepted assumption explaining size effect in deeper beams where the larger spacing between flexural cracks accounted for wider cracks and more reduced aggregate interlocking. In their assessment, average spacing between flexural cracks was correlated to concrete cover rather than effective depth. Note, in all the specimens the concrete covers were nearly the same in spite of the

change in the beam depths (Sneed and Ramirez, 2014). Sneed and Ramirez (2010) suggested that the load corresponding to fully development of inclined crack should be considered as the effective shear capacity of a PC beam because their test results evidenced that shear compression failure mode occurs at a load higher than that required for fully development of inclined crack.

Bentz and Buckley (2005) duplicated a series of PC specimens tested by Bazant and Kazemi (1999) to explore if they can reproduce the original test results. To elaborate, the specimens tested by Bazant and Kazemi (1999) had evidenced the existence of severe size effect (71% reduction in ultimate shear strength) when beam depths varied from 21 to 330 mm (Figure 2.17). Therefore, the validity of the test results was in need to be verified because it simply questioned the safety of ACI code for even smaller beam depths than those indicated by other researchers, as stated by Bentz and Buckley (2005). In the fabrication of the new specimens, beam width was increased from 38 mm, as used in the original beams, to 100 mm by relying on the assumption that beam width has no effect on ultimate shear strength (stress at failure). In addition, coarse aggregates with 4 mm maximum size were replaced with larger size aggregates (10 mm maximum aggregate size). Other variables were held the same as those considered in the original specimens. Since all the shear stresses at failure were to be normalized by $\sqrt{f'_c}$, concrete strength was expected to not signify in the overall results. The results from these two studies were compared in Figure 2.17 by Bentz and Buckley. As noticed, the average shear strength of the specimens was enhanced in a range of 31 to 70% compared to that of the counterparts in the original study. For the range of the tested specimen depths, both ACI and CSA 2004 were indicated to be conservative contrary to the inference taken out of the results from the original study. No sign of concrete crushing was noticed for the largest specimens. Moreover, cracking pattern was observed to be proportional to the size of beams. At the

end, they suggested some potential reasons to unusual reduced shear strength reported by Bazant and Kazemi (1999).

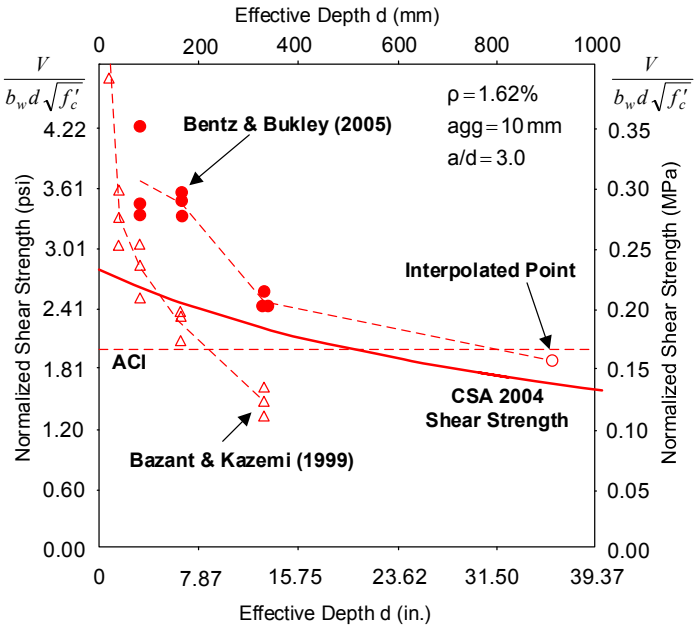

Figure 2.17 Comparison of test results between two studies (Reproduced from Bentz and Bukley, 2005)

2.6 Steel Fiber-Reinforced Concrete (SFRC)

2.6.1 General

Steel fiber-reinforced Concrete (SFRC) is a composite material from discrete steel fibers and concrete. Some of the distinctive characteristics of steel fiber such as its high stiffness, strength, and capability to simply scatter made it as an effective material for being significantly used in concrete. Addition of steel fibers in concrete enhances the mechanical properties of the mix in terms of post-cracking strength, toughness, and ductility compared to plain concrete. However, the extent of the improvement varies as a function of the following parameters including the bond quality between steel fibers and concrete, fiber content, and the distribution of steel fibers in concrete.

Steel fibers in concrete were traditionally applied to control concrete cracking, thus being regarded as a secondary reinforcement in concrete members. However, the extensive research undertaken in recent decades particularly on the shear behavior of SFRC members have proved the effectiveness of steel fiber inclusion on enhancing the shear behavior in terms of the strength, deformation, and ductility, to name a few. For this reason, the shear performance of steel fiber seems to be analogous to some extent to the role of conventional shear reinforcement (stirrups). This has led researchers to conceive the idea of partially or entirely replacement of stirrups with steel fibers.

Once a crack occurs, the steel fiber crossing the crack allows tensile stress to keep being transferred across the crack width. The transfer of tensile stress lasts until the steel fibers are either ruptured, or pulled out of concrete due to the lack of sufficient interfacial bond strength between steel fiber and concrete. Indeed, the failure following the fiber pull-out is more favored since during the pull-out process, a larger extent of energy can be dissipated where SFRC shows additional ductility. As noticed, bond strength constitutes one of the major parameters influencing the SFRC behavior so it requires especial treatment for the improvement. Straight fibers are the fibers which the bond strength is considerably supplied by the friction established between the fiber and concrete. Therefore, an increase in the lateral surface of a straight fiber relative to the volume would raise the interfacial friction force and consequent bond strength. In other words, for the same length and cross-section area of fibers, the one with the square cross section has higher bond strength than the circular one. On the other hand, for the same length of circular fibers, the smaller diameter may result in a better bond quality. For steel fibers with circular section, the proportion of length to diameter (L/D) known as fiber aspect ratio is a factor governing bond quality. In spite of the fact that having higher aspect ratio stands for better bonding resistance, it does not necessarily lead to an improvement in the SFRC mechanical

behavior. This arises from the fact that excessively long fibers may hinder their uniform distribution or random orientation in the specimen. For this reason, the maximum aspect ratio of the steel fibers is required by ACI committee 544 (1996) to be not greater than 100.

Another type of fiber is deformed fiber, whose bond quality is greatly provided through the deformation of their ends or overall geometry. Some common types of deformed fibers are illustrated in Figure 2.18.

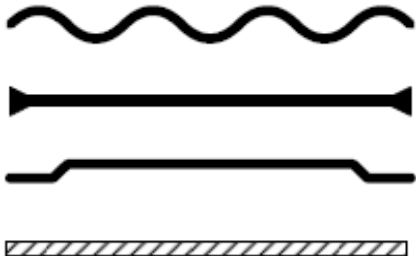

Figure 2.18 Common deformed fibers

Fibers displayed in Figure 2.18 are termed from top to bottom as Crimped, Strand, End-Hooked, and Twisted fibers. For all these different types of fiber, the pull-out process is delayed by means of the mechanical contribution of the deformed shape. As a matter of fact, for a fiber to pull out, the predefined deformation must be destroyed which involves yielding and straightening of the fiber. This process causes the SFRC to absorb a considerable amount of energy before the complete failure that very often results in a higher ductility and toughness, unless the original deformation of the fibers inhibits the workability of the mix and uniform distribution of the fibers (ACI Committee 544, 1988).

2.6.2 Mechanical properties of SFRC

Mechanical properties of SFRC are primarily proportional to fiber types and their amount. Therefore, a thorough understanding of the mechanical properties of SFRC is the main condition for a successful design. These properties are discussed in the following sections.

2.6.2.1 Various factors influencing the bond quality between steel fiber and matrix

Naaman and Najm (1991) carried out a series of pull-out tests using various types of fibers including end-hooked, deformed, and smooth fibers. Fibers were embedded in cement-based matrix. They inferred that for end-hooked fibers, the major pull-out resistance is provided by the hooked ends rather than the frictional bond between fiber and matrix such that as shown in Figure 1.19, a hundred percent increase in the embedded length of fibers did not signify in pull-out load-slip curve. In addition, the work required to pull out a hooked-end steel fiber was four times larger compared to the one needed for a smooth steel fiber. On the other hand, a hooked-end steel fiber indicated higher slip up to two times at peak load than that of a smooth fiber.

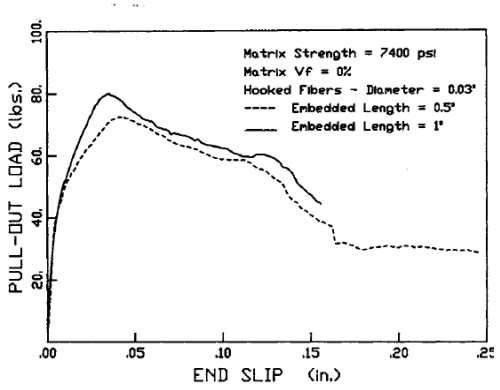

Figure 2.19 Effect of the fiber embedded length on pullout load-Slip behavior (Namman and Najm, 1991)

In addition to the influence the geometrical shapes of fiber have on bond strength, the bond would be also affected by matrix strength. The experiments conducted by Namman and Najm (1991) verified that if the compressive strength of a matrix increases, the bond strength (bond stress at peak load) is accordingly enhanced, though de-bonding occurs more quickly as represented by the smaller extent of slip at peak load for the matrix with higher strength in Figure 2.20. Figure 2.20 indicates the pull-out load-slip responses of a hooked fiber embedded in different matrix in terms of the compressive strength. As noticed, for a change in matrix compressive strength from 4850 to 8650 psi, the peak pull-out load

and the corresponding slip varied from 59 to 103 lb. and 0.031 to 0.029 in., respectively. For the range of the increasing variation in the matrix strength, the average bond stress at peak load was ascending from 640 to 1100 psi

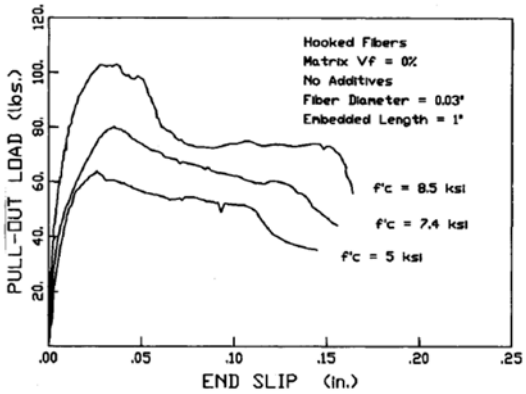

Figure 2.20 Effect of matrix strength on pullout behavior (Namman and Najm, 1991**)**

Banthia and Trottier (1994) undertook an experimental program to examine the bond-slip behavior of three types of deformed steel fibers (Hooked end, crimped, and strand fibers) embedded in the concrete based matrix with different strength. In this program, the effect of fiber inclination relative to loading direction on bond-slip characteristics was also considered. They realized the angle of inclination of deformed fibers, except Hooked-end fibers, with respect to the direction of load accounts for a reduction in the peak pullout load. In the other word, such that the more fiber is inclined, the more peak load decreases. However, concerning smooth fibers, the peak pullout load for the fibers inclined relative to the load direction is at least identical with that of the aligned ones (Naaman et al., 1976). The same behavior was observed for Hooked-end fibers in the tests conduct by Banthia and Trottier (1994). Therefore, based on the above explanation, the optimal case for extremely deformed fibers is where the load is aligned with the fibers. This is in conflict with the 45 degree optimal inclination established by Morton and Groves (1974). In pull-out load-slip behavior, the peak pullout load represents the ultimate condition of a fiber that by considering the mechanical properties of the steel

used, it could signify yielding, rupture, and fully pullout of the fiber. On the other hand, yielding of a material is associated with the dislocation of the material's atoms caused by the shear stresses existing in the critical section. Therefore, the existence of an extra shear force could trigger yielding process faster. Indeed, in case of crimped or strand fibers, since yielding typically occurs where the fiber enters the concrete, the presence of an extra shear force resulting from fiber inclination leads to premature yielding, thus decreasing the maximum pullout load. On the contrary, for hooked-end fibers, the existence of extra shear force does not affect the maximum pullout load because the section being susceptible to yielding is located at the fiber's ends (Banthia and Trottier, 1994). Unlike steel fibers, peak pullout load increases for the synthetic fibers subjected to higher fiber inclination relative to applied load. The enhancement is attributed by Li et al. (1990) to the enhanced frictional force between fiber and matrix as a result of the fiber's bending.

Li et al. (1990) stated that the typical premature yielding for crimped and strand fibers helps the steel fibers exhibit more ductility and larger slip at peak load. In addition, Banthia and Trottier (1994) associated the larger slip at the peak load to the fiber straightening that results from the matrix crushing at the corner where the fiber is inclined and enters the matrix.

2.6.2.2 Tensile behavior of SFRC (Direct Tensile Strength)

Diagonal cracks that may cause shear failure in SFRC beams are initiated once principle tensile stress reaches the tensile strength of SFRC. Therefore, knowing the tensile properties of SFRC such as elastic modulus, tensile strength, strain-hardening or strain-softening, and stress-strain relationships would be very beneficial in predicting the shear behavior of SFRC structural elements. One of the tests being used to evaluate the tensile behavior of SFRC is Uniaxial Direct Tensile Test. According to Dinh (2009), the cross section area of the specimen requires to be adequately large assuring the same steel

fiber dispersion across the cross section as in reality. From this point of view, the problem often arises when there is a need for designing a fixture to grip the ends of the specimen with such a large cross section. The lack of a suitable fixture might result in the specimen cracking at the grip. For this reason, the test results are substantially scattered as stated by Dinh, 2009. In addition, in direct tensile test, after the cracking of the specimen, strain cannot be thought of as the uniform strain distributed along a gage length. On the contrary, the strain is principally due to local crack opening. Therefore, he suggested to report the deformation in terms of crack width rather than the average strain over the gage length. Figure 2.21 displays test setup for direct tensile test along with the dimensions of the dog-bone specimen used by Dinh (2009). Stress versus strain responses for some of the SFRC dog-bone specimens tested by him under direct tensile test are depicted in Figure 2.22. All the specimens were casted from same material and contained steel fibers with 0.75% volume fraction. Figure 2.22 clearly visualizes the typical large scatter in the results obtained from direct tensile test.

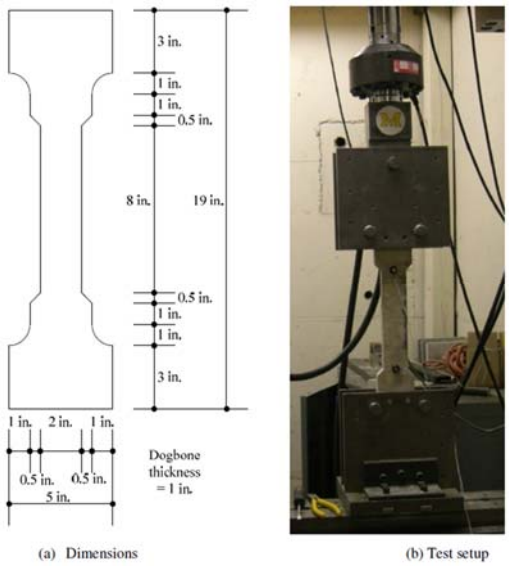

Figure 2.21 Direct tensile test set up and the dog-bone specimen dimensions used by Dinh (2009)

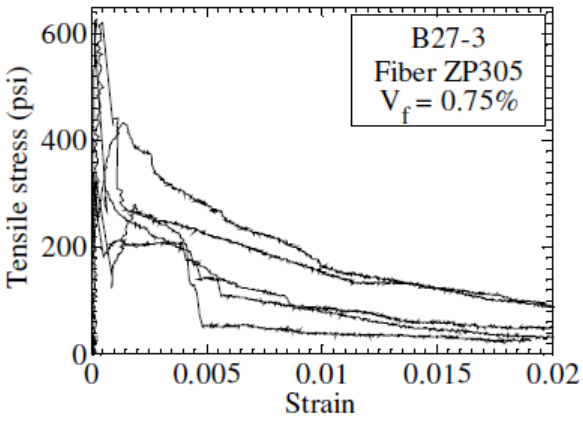

Figure 2.22 Typical Inconsistency of the test results for the same materials of SFRC (Dinh, 2009)

The large inconsistency of test data in post-cracking behavior associates with the lack of control over the location of crack(s) as pointed out by Chao et al. (2011). Therefore, they suggested placing four layers of mesh at both sides of the intended gage length as shown in Figure 2.23 to concentrate all the cracking within the gage length. Also, to prevent steel fibers from being aligned in one or two dimensions, a dog-bone specimen with larger cross section area than that used in Dinh tests was employed in their tests.

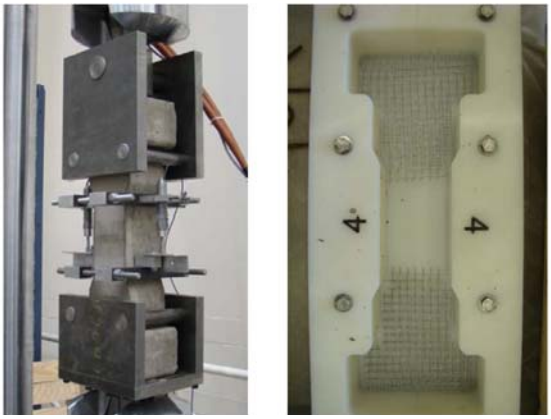

Figure 2.23 Direct tensile test set up and the relevant specimen mold (Chao et al., 2011)

The fibers used in their test were hooked-end steel fiber with the aspect ratio of 40 (length=1.55 in.; diameter=0.038 in.). The test results for two specimens with different fiber contents are displayed in Figure 2.24.

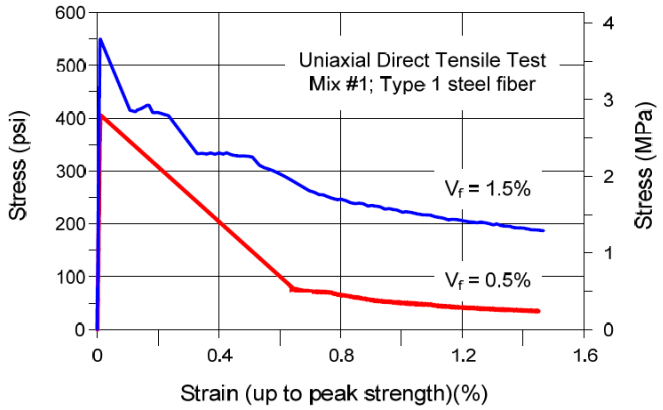

Figure 2.24 Stress versus strain (crack opening) responses of specimens with different fiber fractions under direct tensile test (Chao et al., 2011)

The plots showed in Figure 2.24 brought to attention that inclusion of higher volume content of steel fiber can increase both pick and residual tensile strength of SFRC. However, this enhancement appears to be pronounced for the residual tensile strength than the maximum load-carrying capacity. Furthermore, as illustrated, the variation of fiber content mostly becomes effective after the initiation of crack. Figure 2.25 illustrates the load-extension responses reported by Lim et al. (1987) for the specimens subjected to direct tensile test and reinforced by hooked steel fiber with 0.02 in. diameter. As a matter of fact, this study was intended to assess the performance of SFRC mixtures comprising straight or hooked steel fibers.

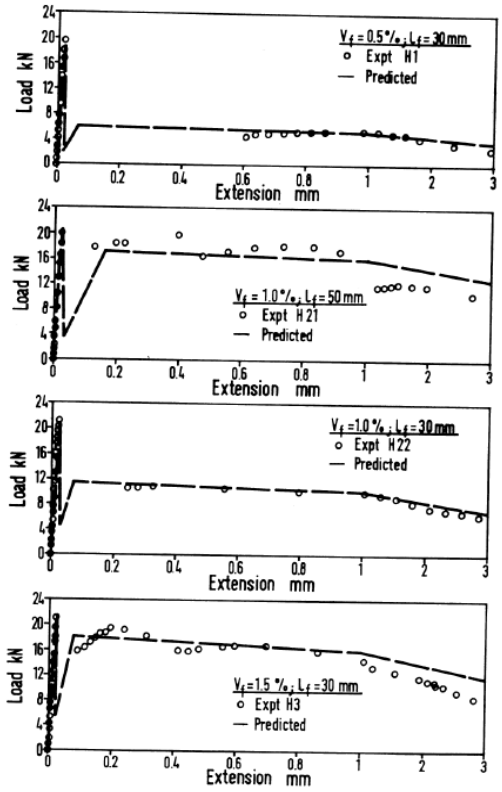

Figure 2.25 Load-extension behaviors of various hooked end SFRC mixtures under direct tensile test (Lim et al., 1987)

As it turned out, increasing the steel fiber volume fraction while the length of fibers are kept constant would result in an increment in both cracking and post-cracking tensile strengths. Nevertheless, the increase in the post-cracking strength seemed more evident. Likewise, inclusion of longer fibers in the mixes with identical fiber content leads the post-cracking tensile strength to grow.

To evaluate the importance of the tensile characteristic of high strength concrete, Noghabai (2000) performed a uniaxial tensile test employing a notched concrete cylinder specimen. All the dimensional properties of the specimen are presented in Figure 2.26. In this test, the variation of tensile stress during loading process was determined with respect to crack opening within a gage length of 1.18 in (30 mm). According to him, when using

longer steel fiber particularly with lower fiber volume fraction, the test is not able to sufficiently reflect the tensile characteristic of material as a consequence of the small cross section of the specimen and the alignment of fibers and the specimen axis. This may result in a higher scatter in the softening curve of the material behavior. The use of high strength concrete was demonstrated to enhance both first cracking and residual tensile strength of FRC as noted in Figure 2.26. High and normal strength concrete are respectively denoted by HSC and NSC in Figure 2.26.

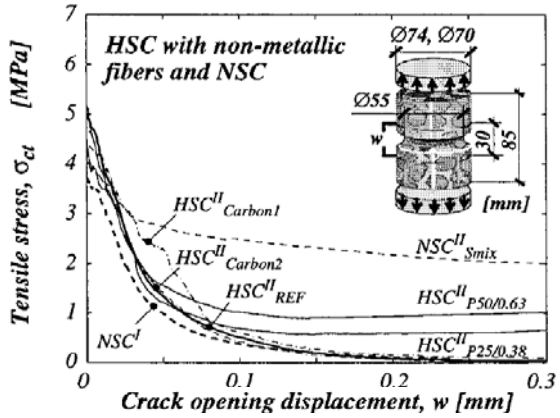

Figure 2.26 Tensile stress-crack opening response for variety of FRC mixtures (Noghabai, 2000)

In order to develop a better understanding of tensile stress-strain behavior associated with SFRC, presenting some theoretical information regarding fiber, matrix, and their interaction in a composite material was deemed necessary. For a composite material reinforced by continuous fibers and subjected to a tensile force, where the fibers and applied load are aligned, the following expressions represent the FRC tensile strength, σ_{cc}, and its elastic modulus, E_c at the first crack (Balaguru and Shah, 1992).

$$\sigma_{cc} = \sigma_f V_f + \sigma_{mu}(1 - V_f) \tag{2.6}$$

$$E_c = E_f V_f + E_m(1-V_f) \tag{2.7}$$

where σ_{mu} is the matrix tensile strength at the first crack, and σ_f is the stress in the fibers at matrix cracking. In addition, V_f, E_f, and E_m signify the fiber volume fraction, fiber modulus of elasticity, and matrix modulus, respectively. For discrete fibers aligned in 2 or 3 dimensions, Equations (2.6) and (2.7) are transformed into the following expressions where η_1 and η_2 are indicative of fiber length factor and fiber orientation factors, respectively.

$$\sigma_{cc} = \eta_1\eta_2\sigma_f V_f + \sigma_{mu}(1-V_f) \tag{2.8}$$

$$E_c = \eta_1\eta_2 E_f V_f + E_m(1-V_f) \tag{2.9}$$

In Equations (2.8) and (2.9), the fiber length factor accounts for the effectiveness of fiber influenced by its length to develop the bond along itself. Fiber length factor can be determined through the equation proposed by Allen (1972) as follows:

$$\eta_1 = \begin{cases} \dfrac{L_f}{2L_c} & if \;\; L_f \le L_c \\ 1-\dfrac{L_c}{2L_f} & if \; L_f > L_c \end{cases} \tag{2.10}$$

In Equation (2.10), L_f is the length of fiber, and L_c is twice of the minimum length of fiber required to induce fiber fracture rather than fiber pullout.

Fiber orientation factor, η_2, implies the effect of fiber orientation on the extent of fiber efficiency to carry the applied load. The fiber orientation factor was estimated by Cox (1952) to be 1/3 and 1/6 for randomly distributed fibers in 2 and 3 dimensions, respectively. Note, to derive all the aforementioned relations, it was assumed that there is a perfect bond between fiber and matrix.

Once matrix cracks, fibers start being debonded and pulled out. Therefore, the residual strength of a composite material would be affected by the resistance of fibers against pull-out. The fiber pullout resistance, in turn, depends on average interfacial bond strength between matrix and fiber, τ; the length of fiber along which bond is acting; and the number of fibers existing in a unit area along the crack. Equation (2.11) was suggested by Naaman and Reinhardt (1995) through which the post-cracking tensile strength of SFRC (fiber pull-out resistance) is to determine:

$$\sigma_{pc} = (\lambda_1 L_f \pi D_f \lambda_2 \tau)(\lambda_3 \frac{V_f}{\pi D_f^2}) = \lambda_1 \lambda_2 \lambda_3 \tau V_f \frac{L_f}{D_f} \quad (2.11)$$

λ_1 and λ_2 are fiber length and fiber orientation factors, whereas λ_3 accounts for the number of fibers lying in a unit area. By substitution of the proposed values for $\lambda_1, \lambda_2,$ and λ_3, Naaman and Reinhardt (1995) predicted the peak post-cracking tensile strength of SFRC as $0.6\tau V_f(L_f/D_f)$. In this equation, $\lambda_1 = 1/4$ based on the assumption made by Aveston et al. (1974), where the embedded length of a fiber is in average equal to a quarter of its original length. In addition, the number of fibers per unit area was considered as $\frac{2V_f}{\pi D_f^2}$ resulting in $\lambda_3 = 2$ (Aveston et al., 1974). λ_2 was set to 1.2 by Naaman and Reinhardt (1995).

In order to ensure that a composite material is still able to carry some additional loads after matrix cracking by solo contribution of the included fibers, the number of fibers, or in other words, the fiber volume fraction, requires to be greater than a minimum value known as fiber critical volume fraction. In this state, the post-cracking stress developed in the fibers, σ_{pc}, is positively in excess of the cracking strength of composite, σ_{cc}, (Figure 2.27).

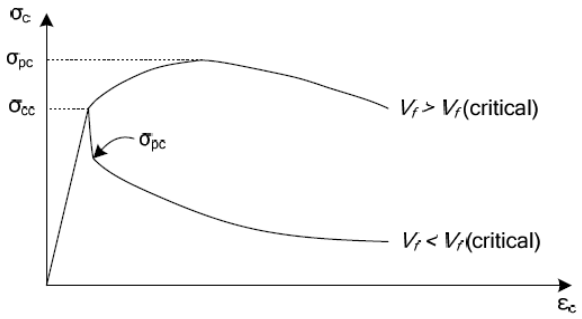

Figure 2.27 Stress-strain curves for brittle matrix composites (Dinh, 2009)

Critical fiber volume fraction is determined through Equation (2.12), where σ_{mu}, ε_{mu}, and σ_{fu} are matrix ultimate tensile strength, matrix ultimate tensile strain, and fiber ultimate tensile strength, respectively. Note, Equation (2.12) is only used for the composite materials in which the fibers are aligned with the applied load, and the composite failure is as a result of fiber fracture rather than fiber pullout.

$$V_{fcritical} = \frac{1}{1 + \frac{\sigma_{fu}}{\sigma_{mu}} - \frac{\varepsilon_{mu} E_f}{\sigma_{mu}}} \tag{2.12}$$

For Conventional SFRC, the steel fibers are randomly distributed in three dimensions, and the failure resulted from fiber pullout rather than fiber fracture. Hence, the critical fiber volume fraction is expected to be noticeably larger for typical SFRC than the one calculated by Equation (2.12). Equation (2.13) was presented by Naaman and Reinhardt (1995) to account for the effect of both randomly distributed fibers and fiber-matrix interfacial bond between.

$$V_{fcritical} = \frac{1}{1 + \frac{\tau}{\sigma_{mu}} \frac{L_f}{D_f} (\lambda_1 \lambda_2 \lambda_3 - \alpha_1 \alpha_2)} \tag{2.13}$$

In Equation (2.13), α_1 and α_2 represent fiber length and fiber orientation factors for intact composite. For concrete reinforced by hooked-end steel fibers with an aspect ratio of 100, the critical fiber volume fraction is 2% as estimated by Naaman and Reinhardt (1995).

2.6.2.3 Flexural behavior of SFRC (Modulus of Rupture)

Flexural performance of SFRC can be evaluated through third-point loading test in compliance with ASTM C1609 (2012). The stress-deflection response for an SFRC specimen is to obtain by evaluating the equivalent tensile stress at the extreme fiber of the cross section for each recorded mid-span deflection. The word “equivalent” refers to the maximum tensile stress calculated at the mid-span by assuming uncracked concrete and elastic constitutive laws. Among all the calculated stresses, two flexural strength values are critical to report including the first flexural crack strength and post-cracking strength based on ACI committee 544 (1988). The flexural strength corresponding to the first flexural crack is referred to as the modulus of rupture and is a function of the square root of concrete compressive strength. ACI 318 (2014) also requires this flexural test method in accordance with ASTM C1609 (2012) to assess the shear performance of SFRC material for being applied in structural members.

Flexural test performed by Shah and Rangan (1971) indicated up to 100% increase in the first-crack flexural strength when a 1% volume fraction of straight fibers were included into concrete. Wafa and Ashour (1992) examined the flexural behavior of high strength SFRC based on ASTM C1018 (1997), which used to be employed to assess toughness index. Nevertheless, it was omitted in the higher edition in 2006 due to the lack of knowledge with respect to the concept of toughness index (ASTM C 1018, 2006). In this study, the SFRC compressive strengths were varied from 13.7 to 14.2 ksi. Moreover, the type of fiber used was hooked-end steel fiber with the aspect ratio of 75 (length = 2.36 in.; diameter = 0.03 in.). They found that addition of 1.5% steel fiber by volume into concrete

could increase the modulus of rupture by 67%. However, the amount of increment was reduced as the size of specimens increased. In their study, the modulus of rupture for larger specimens was measured 91% of that for the smaller ones irrespective of the fiber content.

Ramakrishnan et al. (1980) demonstrated through their test results that the presence of steel fiber also enhances the toughness of concrete in addition to the modulus of rupture (Figure 2.28). As it turned out from SFRC load-deflection curves in Figure 2.28, the formation of the first crack in SFRCs did not end up to immediate failure as opposed to plain concrete, instead either softening or hardening was observed in the post-cracking behavior. Note that the beams tested by Ramakrishnan et al. (1980) had a size of $4 \times 4 \times 14$ in., and they were tested through the third-point loading test method. Moreover, they established that hooked end fibers are more effective in increasing the ultimate flexural strength and toughness of SFRC than straight fibers in spite of the fact that the content of hooked end fibers was even less. They also observed that in the specimens comprising hooked end fiber, the post cracking strength would be almost equal or larger than the first cracking strength once the fiber volume fraction is in excess of 80 lb/yd^3 (V_f = 0.6%).

Gao et al. (1997) performed an experimental study to investigate the influence of fiber aspect ratio on flexural behavior of SFRC. They observed that using steel fiber with higher aspect ratio enhances the flexural performance of SFRC.

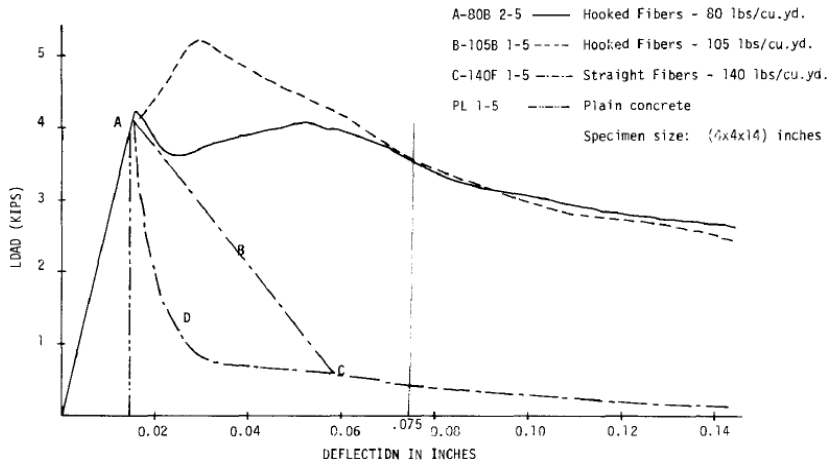

Figure 2.28 Flexural performance of concrete reinforced by different shapes and volume fractions of steel fiber (Ramakrishnan et al., 1979)

2.6.2.4 Compressive behavior of SFRC

Numerous research investigating the behavior of SFRC confirmed that the effect of fiber incorporation does not really signify in peak compressive strength. For instance, Fanella and Naaman (1983) reported that the addition of steel fiber in concrete with volume fraction up 2% would improve the peak compressive strength between 0 to 15%. This range turned out to be less than 10% when the steel fiber volume fraction is reduced to 1.5% (Thomas and Ramaswamy, 2007). Nevertheless, there has been some higher increment in compressive strength reported for example, by Khaloo and Kim (1996), where the compressive strength rises by 30% as a result of 1.5% fiber inclusion by volume. Gao et al. (1997) affirmed the limited extent of improvement in the compressive strength of SFRC as a result of fiber addition. It means that after attaining a certain level of enhancement, even an extra increase in the fiber dosage cannot suggest any further increment in SFRC compressive strength. According to them, this drawback arises from the fact that steel fiber volume fraction in excess of 2.5% hinders the dispersion of the steel fibers, thereby concrete cannot be completely compacted. This issue was also confirmed for high strength concrete by Song and Hwang (2004), where addition of 1.5% fiber content

by volume led to an increase of 15.3% in compressive strength of high strength concrete, while this extent was reduced to 12.9% when the volume fraction of fiber ascended to 2%. Despite the minor effect of steel fiber inclusion on compressive strength enhancement, presence of steel fibers could substantially improve the toughness and ductility of concrete in compression (Fanella and Naaman, 1983). It is noteworthy that the post-peak compressive behavior of SFRC correlates with the type of fiber. Soroushian and Bayasi (1991) reported that hooked and crimped steel fibers are more effective to reduce the rate of strength loss after peak strength than straight fibers. However, the performance of hooked or crimped steel fibers seems quite similar in post-peak behavior of SFRC.

2.6.2.5 Shear behavior of SFRC

2.6.2.5.1 Material shear test methods for SFRC

In order for the new provisions of ACI 318 (2014) to be utilized, a standard laboratory test for the evaluation of SFRC shear performance is essential. A standard test is necessary since it allows for a comparison of experimental results obtained in different laboratories around the world. However, currently neither ASTM nor ACI Committee 544 recommend any standardized test method to measure material properties of fiber reinforced concrete (FRC) in shear. ACI 318 (2014) requires the use of residual strengths at specified deflections obtained from ASTM C1609 as SFRC shear performance evaluation. However, the experimental tests performed by other researchers (e.g. Cho, 2011) indicated not only the inability of ACI performance criteria in assessing the shear performance of SFRC, but also the inconsistency of the test results for the specimens with the same mix proportion. The high variations make the application of ASTM C1609 questionable for use in quality control and in project specifications. It should be noted that this high variability issue in this type of test has been recognized as an inherent problem (Bernard, 2002). Much effort has been devoted to develop a standard laboratory test for

FRC in shear; however, finite element analyses performed by Cho (2011) showed that those shear test methods being used on FRC by other researchers do not cause the test specimens to fail in a state of, or even close to pure shear. These test methods and their drawbacks are briefly reviewed as follows. Several researchers have attempted to measure the shear strength and shear toughness of FRC by using Z-type push-off specimens (Barragan et al., 2006; Hofbeck et al., 1969; Mirsayah and Banthia, 2002; Valle and Buyukozturk, 1993), in which two L-shaped blocks are connected through a ligament, along which shear loading is applied (Figure 2.29). The stress distributions (i.e. two normal stresses in horizontal and vertical directions, shear stress, and maximum principal stress) along the intended failure plane (AB) obtained from FEA (Cho, 2011) are also shown in Figure 2.29. It is seen that at the location of maximum principal stress (points A or B at notched end) there are, in addition to the shear stress (τ_{xy}), relatively large normal stresses (σ_x, σ_y) which will contribute to material failure. Consequently, failure occurs at the notches (Barragan et al., 2006), though not as a direct result of pure shear. Another disadvantage of this type of configuration is the presence of notches, around which the fibers tend to be aligned rather than randomly distributed as would be seen in an actual structural member.

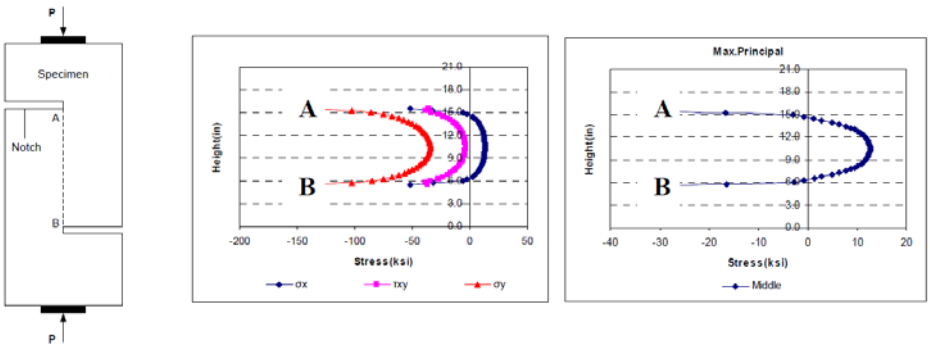

Figure 2.29 Z-type push off test and corresponding stress distributions in specimen (Cho, 2011)

Figure 2.30 and Figure 2.31 show two types of double-shear tests: One is performed on an unnotched prism based on a Japan Society for Civil Engineers (JSCE)

standard (JSCE-SF6, 1990). The other double-shear test is based on a prism with an all-around notch at the location of applied loads (Mirsayah and Banthia, 2002). Although the shear stress distribution is more uniform in the middle portion of the specimen as shown when using the JSCE test method (Figure 2.30), the failure will occur at the location having appreciable normal stresses (that is, in the vicinity of point A where maximum principal stress develops), which leads to a complicated stress field around the loading point. Indeed, experimental results indicated that the failure plane often deviated from the region under concentrated shear, and this test generally produced invalid results (Mirsayah and Banthia, 2002). Mirsayah and Banthia modified the JSCE test method by adding a 0.6-inch deep all-around notch to force the failure to occur at this predefined location. While this intervention attempted to introduce an improvement, failure initiated at the notch location (points A or B in Figure 2.31) is still evident where the normal stresses prevail, which in turn leads to a complicated failure mode as opposed to pure shear.

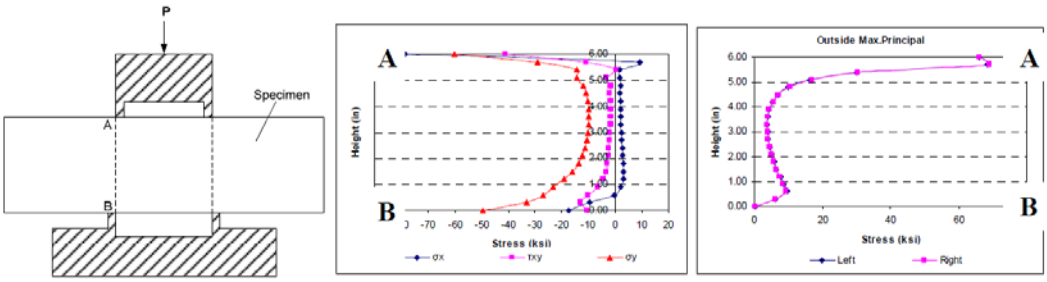

Figure 2.30 Double-shear test with unnotched prism and corresponding stress distributions in specimen (Cho, 2011)

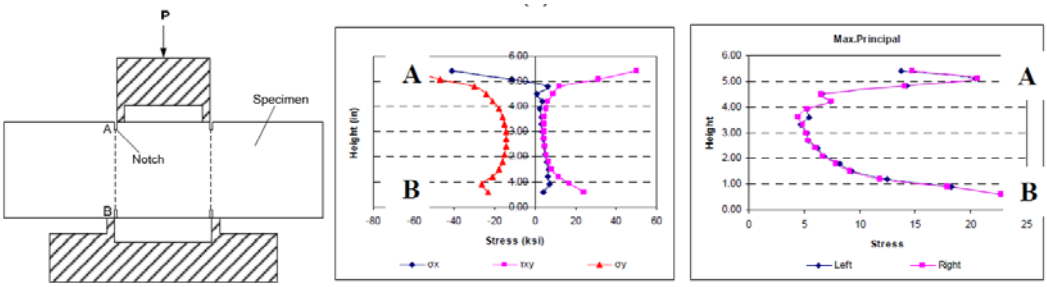

Figure 2.31 Double-shear test with notched prism and corresponding stress distributions in specimen (Cho, 2011)

Another type of shear test which can reduce the influence of normal stress was developed by Iosipescu about 40 years ago (Iosipescue, 1967; Iosipescue and Negoita, 1969), and is generally referred to as the "Iosipescu Shear Test" (Figure 2.32). By adequately adjusting the loading and support locations, a uniform shear force with zero moment is created in the vicinity of the beam's mid-span. This will technically eliminate the normal stress due to bending moment at section A-B as shown in Figure 2.32. This arrangement also prevents relative rotation of the two halves of the test specimen. The V-shaped notches are created purposely in order to produce a uniform shear stress distribution along section A-B (see the stress distributions obtained from FEA by Cho (2011) given in Figure 2.32.

The Iosipescu shear test method has been widely used in testing laminate composite materials (Iosipescue, 1967; Iosipescue and Negoita, 1969, Pierron and Vautrin, 1997) as well as in the investigation of fracture characteristics of plain concrete subjected to complex states of stress (Swartz and Taha, 1991). However, based on the stress distributions shown in Figure 2.32, initial failure will occur at the notch (point A or B) rather than the location having maximum shear stress (in the vicinity of the mid-section height). This indicates that the failure is not induced by the action of pure shear. Indeed, FRC specimens incorporating low modulus polymeric fibers tested by using the Iosipescu

shear test method showed that cracks always initiate at the notches (Van Zijl, 2007). It should also be noted that the presence of the V-shaped notches will alter the required random distribution of fibers, especially for commonly used steel fibers with a length of 1 to 2 inches.

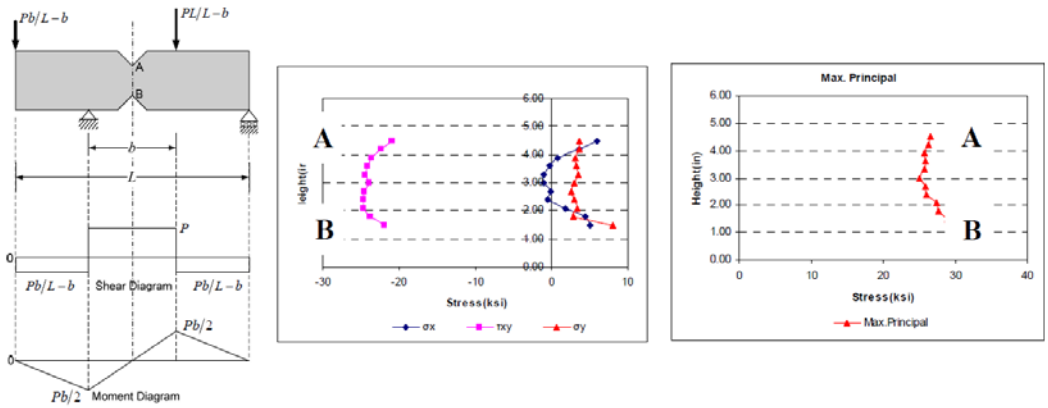

Figure 2.32 Iosipescu shear test and corresponding stress distributions in the specimen (Cho, 2011)

In order to minimize the deficiencies of existing Iosipescu test method and ensure random fiber distribution, Cho (2011) investigated a modified Iosipescu specimen as shown in Figure 2.33. The notches were removed to eliminate the localized stress concentrations. In addition, the width of cross section was reduced to induce failure to develop at the beam's mid-span where shear is the dominating force. This modification was performed by using a transitional portion where the initial cross section gradually narrowed between the end and middle of the specimen. However, the efforts to find an appropriate arrangement of flexural and shear reinforcements to achieve the desired and consistent failure mode had only moderate success. The proposed configuration of the specimen is shown in Figure 2.33.

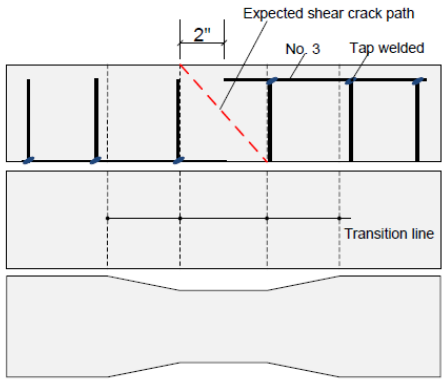

Figure 2.33 Proposed configuration of Modified Iosipescu specimen (Cho, 2011)

2.6.2.5.2 Shear strength of SFRC

Valle and Buyukozturk (1993) investigated shear strength and ductility characteristics of fiber-reinforced high strength concrete under the z-type push-off test. They found that the presence of 1% steel fiber content by volume in high strength concrete increased the shear strength by 60%, while this percentage in strength growth was reduced to 36% for the addition of the same fiber type and fiber volume fraction into normal concrete. Furthermore, they observed an 18% shear strength ascent for the high strength concrete specimens containing steel fibers alone in comparison with the normal strength concrete specimens only reinforced by stirrups. The higher effectiveness of fibers in high strength concrete was attributed to the enhanced fiber-matrix interfacial bond due to high strength concrete with silica fume. Normal-strength concrete reinforced by stirrups was observed insensitive to the addition of steel fibers in terms of the shear strength; on the contrary, the shear strength of high-strength concrete specimens containing stirrups was subjected to an enhancement in return to the fiber incorporation.

2.7 The Effectiveness of Steel Fiber in Shear Performance of SFRC Beams without Stirrup

2.7.1 Strength

In a longitudinally reinforced SFRC beam without shear reinforcement, fibers are able to clearly act as shear reinforcement. The tests conducted by Williamson and Knob (1975) on full-scale reinforced concrete beams with 1.5% steel fiber volume fraction showed that the presence of steel fibers in concrete greatly raised the shear resistance of SFRC beams such that in some cases, the SFRC beams were able to attain the full flexural capacity. In an experimental study on shear-critical mortar beams with different shapes of steel fiber such as round, flat, and crimped, Batson et al. (1972) observed that the inclusion of steel fibers greater than 0.44% volume fraction transformed the mode of failure from shear to flexure. Upon this observation, they conceived the idea of the replacement of conventional shear reinforcements with steel fibers. Indeed, the performance of steel fibers in the beams made of mortar is expected to be better than those made by concrete because the mortar fibers are free of the aggregate interference. For the lightweight concrete beams due to the inherent lower tensile strength and reduced modulus of elasticity, the influence of steel fiber on shear strength and deformation appears to be even more pronounced. The tests by Swamy et al. (1993) on I-section lightweight concrete beams confirmed that addition of 1% volume fraction of steel fibers to concrete mix proportion increases the ultimate shear strength of SFRC beams from 60 to 210% depending on the longitudinal reinforcement ratio and shear span to effective depth ratio. It should be noted that in spite of the effectiveness of steel fibers on the shear strength enhancement of SFRC beams, excessive amounts of fibers may have a contrary impact which in turn, results in a premature failure and an inconsistency in the test data. Therefore, the amount fiber to apply in SFRC beams is required to be limited by an upper bound (Muhidin and Regan, 1977).

As further example concerning the effect of steel fiber on beam shear strength, the research performed by Ashour et al. (1992) on the shear strength of high strength concrete beams showed a 96.6% increase when they are included by 1.5% steel fiber fraction. However, this increment was reduced to 32.2% when the shear span to effective depth ratio changed from 1 to 6.

In addition to the effectiveness of steel fiber in the shear-carrying capacity of SFRC beams, the presence of steel fiber allows some other behavioral aspects of SFRC beams to change as follow:

2.7.2 Stiffness and ductility

Enormous experimental studies (e.g. Swamy and Bahia, 1985; Swamy et al., 1993) on SFRC beams without stirrups illustrated a considerable reduction in the deflection and end rotations at all loading stages particularly at the post-cracking stages of a SFRC beam, regardless of the extent of longitudinal reinforcements and shear span to effective depth ratio. To elucidate, the load-deflection and load-rotation curves for SFRC and RC beams are presented in Figure 2.34, where the SFRC and RC responses to the external load are denoted by dashed and solid lines, respectively (Swamy et al., 1993). In their experimental study, the specimens were some I-beams whose shear span to effective depth ratio, a/d, and tensile reinforcement ratio, ρ, were variable. The entire SFRC beams were reinforced by crimped steel fiber with a consistent volume fraction of 1%. The values of a/d and ρ for each set of plots are shown in Figure 2.34 .

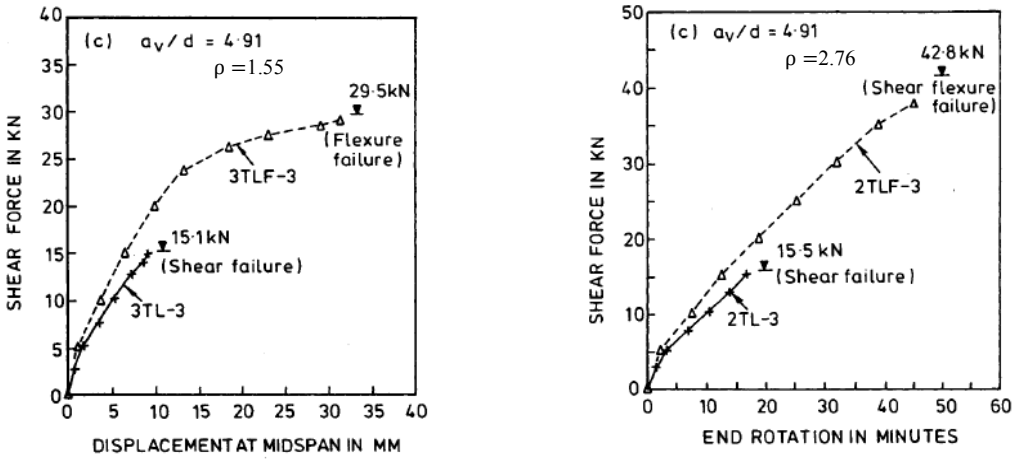

Figure 2.34 Typical load-deflection and load-end rotation curves (Swamy et al., 1993)

As indicated by the curves, the presence of steel fibers enabled the concrete beams to show substantially less deflection and end rotation compared to their counterparts with no steel fiber. However, this trend appeared to be marginal at the initial load steps, but upon the initiation of the first crack, the role of steel fibers was pronounced as it was evidenced by greater reduced deflections and rotations compared to the PC counterparts after the shear force of 1.12 kips (5 kN) (Figure 2.34). As the failure was approached, the SFRC beams exhibited a larger deformation in response to the increase in load, thereby expressing some ductility regardless of the failure mode. It was also reaffirmed by the experiments undertaken by Narayanan and Darwish (1987), where a large extent of post-peak ductility was observed such that the test could extend well into post-ultimate stage. In addition, according to Ashour et al. (1992), the incorporation of steel fibers in high strength concrete beams substantially hinders crack formation and slightly enhances the concrete tensile strength, thereby, mitigating the serious brittleness characterizing high strength concrete.

2.7.3 Cracking behavior and failure mode

The influence of fiber inclusion in concrete is significant in the cracking behavior of beams. As opposed to RC beams that the shear failure is often triggered upon formation of the first inclined crack, SFRC beams experience an increased number of shear and flexural cracks that progressively develops at closer spacing and scatters further toward the supports before the failure, Swamy et al. (1993) stated. Among those developed inclined cracks, they observed that some of them remained active even up to failure; hence, in SFRC beams, the critical crack could barely be distinguished until just before failure. Narayanan and Darwish (1987) pointed out that the formation of the several inclined cracks expressed the redistribution of internal forces after cracking. According to Swamy et al. (1993), in a cracked SFRC beam, steel fibers by holding the sides of cracks together enable the cracked tension zone to resist the shear force. Therefore, the beam undergoes smaller vertical deformation and sustains higher loads at failure than the equivalent PC beams. This capability of steel fibers was clearly noticeable through the cracking pattern of their test specimens. They recognized that steel fibers also prevent concrete spalling and bond cracking adjacent to the beam supports near the failure load. According to Narayanan and Darwish (1987), steel fibers are involved in carrying the principal tensile stresses across the crack width in the occurrence of every crack, and this action extends until all of the fibers are successfully pulled out at the so-called critical crack.

With regard to the failure mode in SFRC beams, it is wrong to expect that the presence of steel fibers transfers the mode of failure from shear to flexure, while other parameters and their interaction are significantly involved, such as shear span to effective depth ratio and longitudinal reinforcement ratio. On the other hand, as stated by Swamy et al. (1993), steel fibers can considerably mitigate the sudden and brittle nature of the conventional shear failure of concrete beams by either preventing, or reducing the

propagation of tensile splitting crack along the main reinforcements as well as increasing the stability of compression zone at failure. In 1985, Swamy and Bahia succeeded to transform the mode of failure in their specimens from diagonal tension to shear compression by adding small amounts of fiber, about 0.5% in volume. Through the strain data acquired from their tests, the strains in longitudinal bars and compression zone turned out to be well-matched with flexural failure, whereas the failure was dominated by shear failure following the formation of shear crack. This phenomenon was conceived of as ductile shear failure, where the presence of steel fibers allows the specimens to fail in shear after yielding of the steel bars. This sort of failure was emerged to be accompanied with a substantial ductility. Test observations performed by Mansur et al. (1986) on SFRC beams with rectangular section and hooked ends steel fiber revealed that inclusion of short steel fiber with the content of 1% by volume changed the mode of failure from shear to flexure irrespective of a/d. For the volume fraction less than 1%, the chance for the mode of failure to alter from shear to flexure increased for higher values of a/d. In other words, as the fiber volume fraction increases, critical a/d decreases. The critical a/d was defined as the border point less than which shear failure is to be induced (Figure 2.35). The reason was accounted for by the incremental rate distinction between the shear-load carrying capacity and bending strength of a SFRC beam due to the use of steel fibers. Based on their observation, an increase in the steel fiber volume fraction has a larger impact on the raising of the shear resistance than the bending strength of a beam if other factors are maintained constant.

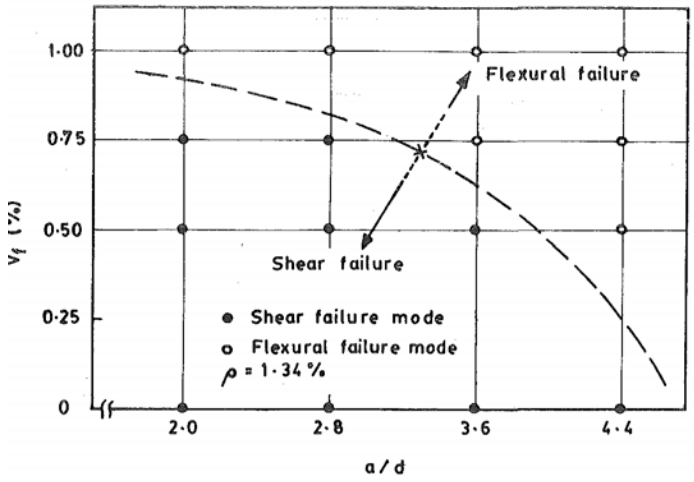

Figure 2.35 Variation of the fiber volume fraction vs. critical a/d
(Mansur et al., 1986)

2.7.4 Dowel resistance in shear

The contribution of main steel bars in the shear resistance of RC beams is not confined to only controlling the crack width, which increases the aggregate interlock capacity governing the shear failure, while they participate in shear resistance by their dowel action. However, the total shear percentage carried through dowel action is still uncertain. Swamy and Andriopoulos (1974) attributed the uncertainty to the interdependency of aggregate interlock and dowel action.

In 1968, the experimental study carried out by Baumann indicated that the shear contribution of dowel action in RC beams is tightly dependent on the flexural stiffness of tension bars and the concrete tensile strength along them where splitting crack occurs. Therefore, the general advantages of steel fibers in controlling the crack and increasing the concrete tensile strength are expected to reduce the deformation characteristic of the beam by limiting the number of cracks in the dowel zone and delaying the splitting crack formation, thereby improving the beam stiffness and dowel resistance in shear. Swamy and Bahia (1979) tested a series of conventionally reinforced T-beams with and without

steel fibers to examine potential performance improvements of dowel action in shear resistance as a result of fiber inclusion. In their study, dowel action resistance was directly induced in longitudinal bars through a preformed crack intersecting the bars. To illuminate, the specimens were constructed in two parts separated by a preformed crack at a constant distance from supports. In order to have dowel action as an only shear resistance, two parts were connected through the horizontal bars crossing the preformed crack (Figure 2.36). In these tests, the load was directly applied on the central section of the beams through two designed knife edges fitting through a couple of holes in the middle of compression flange as noticed in Figure 2.36.

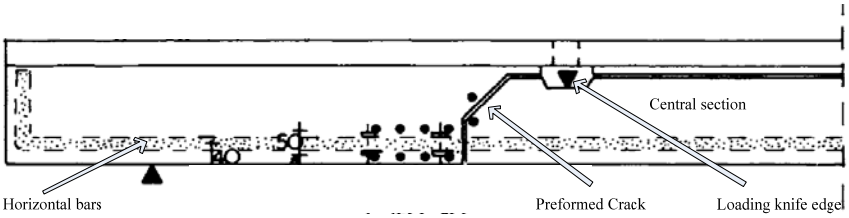

Figure 2.36 Details of the dowel test beams (Swamy and Bahia, 1979)

The dowel cracking of the tested beams indicated that the presence of steel fibers significantly slows down the propagation and widening of the dowel cracks at the level of the main bars thus, allowing the beams to undergo large deformations before failure, and they show higher ductility. In other words, steel fibers are able to preserve the adherence of concrete cover with the rest of a beam imparting ductile behavior. It should be noted that the cracking pattern for all the specimens was reported to be the same even for those without steel fiber. The load-deflection relationships for the test specimens are presented in Figure 2.37. As indicated, an increase in steel fiber volume fraction even for a marginal amount led to a growth in the stiffness of specimens. On the contrary, the immobilization of the fibers prior to the formation of first dowel crack was stated to render the initial stiffness similar for the test beams. In addition, as illustrated in Figure 1.37, a larger reduction in specimen reinforcement ratio, which clearly reflects the flexural stiffness of

horizontal bars in dowel resistance, resulted in a higher increment of specimen deflection at a given load.

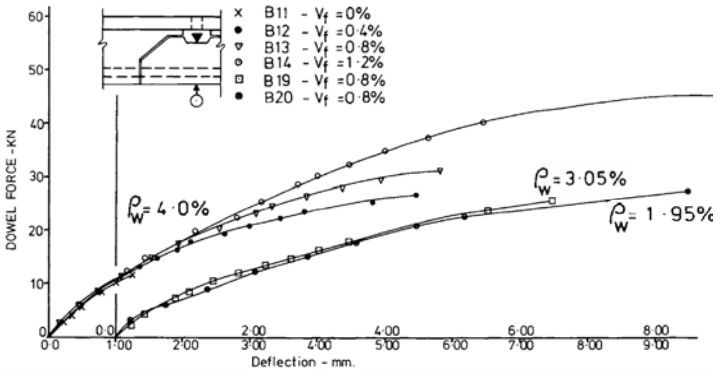

Figure 2.37 Load-deflection relationship under loading point for the beams with various steel volume fraction and reinforcement ratio (Swamy and Bahia, 1979)

Swamy and Bahia (1979) emphasized that first dowel crack strength is increased by using steel fibers in the concrete beams. This was recognized by concrete strain values between $600x10^{-6}$ and $850x10^{-6}$ measured prior to dowel cracking along the longitudinal bars that was reported to be higher than that in normal concrete ($500x10^{-6}$) as reported by Houde and Mirza (1974). Swamy and Bahia (1985) stated that the inclusion of steel fibers only into the tension zone of a concrete beam turned out to have no effect in lowering the chance of shear failure following the improvement in dowel action contribution.

2.8 Parameters Influencing the Shear Behavior Enhancement of SFRC Beams

As mentioned in the preceding section, the shear behavior of a SFRC beam could be significantly improved from various aspects due to the presence of steel fibers. The extent of improvement, however, varies from beam to beam depending on some key parameters as follows: a) beam cross section; b) beam size; c) shear span to effective depth ratio (slenderness); d). flexural reinforcement ratio; e) SFRC compressive strength; f) aggregate size; g) fiber volume fraction; h) fiber type. This section is intended to shed light on the effects each has on the shear behavior of SFRC beams based of prior research studies.

Cross section: The experimental studies investigating the shear behavior of SFRC beams have been mostly on the beams with rectangular cross sections. For flexural members, the cross section with rectangular geometry can be proved to be not an optimum section. On the contrary, members with thin web are more desired. However, the reduced width of the web hinders the placing of conventional shear reinforcement. This difficulty especially arises once the closely spaced stirrups are in demand that may result in concrete poor compactness due to the existence of voids. This inherent deficiency is addressed to a great extent by replacing conventional shear reinforcements with steel fibers. Besides, steel fibers appear to be better aligned with the direction of principal tensile stress in those sections. Therefore, the inclusion of fibers could indeed benefit the section to be more effective in carrying both flexural and shear forces. Nevertheless, there have been a very limited research in the literature focusing on the beams with thin web cross sections. Swamy and Bahia (1985) compared the shear strength of T and rectangular beams in which the amounts of fiber volume fraction and main reinforcement ratio were identical. The result of this comparison resulted in a conclusion that T-beams resisted shear force around 28% higher than that of rectangular ones. Similarly, the results of the experiments performed by Rosenbusch and Teutsch (2002) represented a 54% increment in the ultimate shear strength of the T-beam consisting of a 9 in. thick flange relative to a rectangular beam with the same height. Nevertheless, the T-beams with a flange thickness of either 4 or 6 in. carried a similar load as the corresponding rectangular beam did with the identical height. Furthermore, the load-deflection response remained almost unchanged if the flange width changes from 20 through 40 inches.

Longitudinal reinforcement ratio: The test data collected by Mansur et al. (1986) confirmed that the larger amount of main reinforcement ratio increases the bending moment capacity more than the Shear strength in SFRC beams. Therefore, increasing the

reinforcement ratio cannot alter the failure mode from shear to flexure as all the key parameters lie constant. In addition, they showed through Figure 2.38a that both first shear cracking and ultimate shear strength increased as the longitudinal reinforcement ratio was raised. However, the incremental rate in the first shear cracking was indeed marginal.

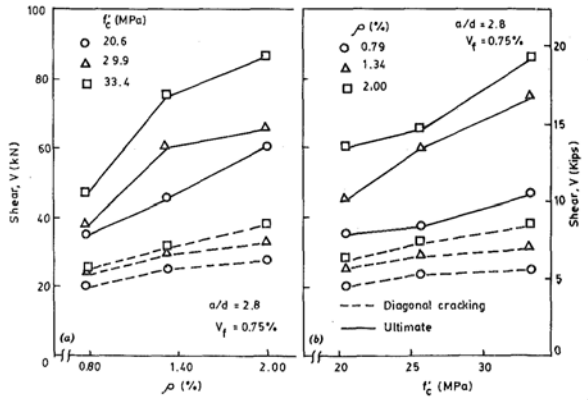

Figure 2.38 Variation of first shear cracking and ultimate shear strength vs. (a) Longitudinal steel ratio, ρ; (b) Concrete compressive strength, f'_c (Mansur et al., 1986)

In spite of the findings from the research study of Mansur et al. (1986), research done by Shoaib et al. (2014) showed that longitudinal reinforcement ratio in the range of 1.44% to 4.03% had almost no effect on the ultimate shear strength of SFRC beams with 1% steel fiber volume fraction. A similar conclusion was also drawn by Dinh et al. (2010) for longitudinal reinforcement ratio between 1.6% and 2.7%. Dinh et al. (2010) stated that longitudinal reinforcement ratio mostly dictates beam ductility.

SFRC compressive strength: In general, as viewed in Figure 2.38b, an increase in SFRC compressive strength resulted in an increase in the first shear cracking and failure load (Mansur et al., 1986). This increase rate for the first shear crack, however, was much smaller. Parra-Montesinos (2006) found no clear relationship between shear stress at failure and changes in f'_c. This conclusion was in basis of the plot in which the ultimate shear strength for 102 FRC slender beams ($a/d \geq 2.8$) with deformed steel fibers was drawn

in terms of the associated f'_c. The conclusion held the same in recognition of various ranges of steel volume fraction.

Fiber content: The effect of the fiber characteristic itself on shear strength of SFRC beam can be discussed from two primary aspects: the effect accounting for the mechanical properties of fiber such as fiber shape, length, diameter, and tensile strength and fiber volume fraction. Despite of a few research carried out on the former, the effect of fiber volume fraction in shear strength of SFRC beam has been extensively examined by Mansur et al. (1986), Ashour et al. (1992), Swamy et al. (1993), Swamy and Bahia (1985), Narayanan and Darwish(1987) and so forth. A general conclusion is that the increase of fiber content leads to an enhancement in beam shear strength irrespective of other factors such shear span to effective depth ratio, longitudinal reinforcement ratio, and concrete compressive strength. However, the incremental rate tightly depends on the aforementioned factors particularly shear span to effective depth ratio. For instance, in smaller a/d, the effect of fiber content to increase the shear strength of SFRC beams becomes highly pronounced. Narayanan and Darwish (1987) attributed the shear strength enhancement to the possible arch action improvement. In addition, the amount of fiber content could change the mode of failure. According to Sahoo and Sharma (2014), to have such change in failure mode from shear to flexure, steel fiber volume fraction requires to be at least 0.5%. In many cases of various scholarly studies, it was observed that higher fiber volume fraction more than 1% positively transformed the mode of failure. For steel fiber volume fraction less than 1%, even though the presence of fiber often is not able to alter the failure mode and causes a sudden failure at the ultimate stage, the failure is less catastrophic than counterparts without shear reinforcement (Narayanan and Darwish, 1987).

Beam size: As discussed in previous chapters under the title of size effect, the shear strength of a PC beam undergoes a significant change following the change in the effective depth, or generally the height. However, this issue requires further investigations when coming to SFRC beams. This is due to the fact that the majority of experiments on SFRC beams have been limited to the beams with the effective depths ranging from 4 to 11 inches. According to Dinh (2009), although the size effect is expected to be minor for SFRC beams, to authenticate the expectancy, there is a demand for testing more beams with larger effective depth especially in excess of 24 inches. In this order studied by Noghabai (2000), showed a 15% reduction in the average shear strength in the test SFRC beams when the effective depth was varied from 16.1 to 22.4 inches. Nevertheless, the reduction was reduced to 7% in the tests undertaken by Dinh et al. (2010) once the heights of specimens were increased from 18 to 27 inches. Minelli et al. (2014) undertook a series of tests on SFRC and companion plain concrete beams with three different heights: 20, 39, and 59 inches. For each series with the same height, the steel fiber volume fraction was varied as 0, 0.64, and 1%. The test results are replotted in Figure 2.39.

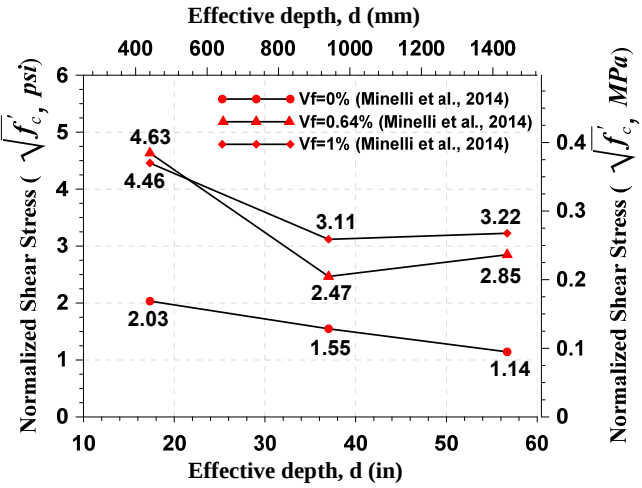

Figure 2.39 Shear stress at failure in terms of $\sqrt{f'_c}$ vs. effective depth
(Reproduced from Minelli et al., 2014)

As noticed, when the effective depth was increased about twice from 17 to 37 in., the shear strength of PC beams reduced by 30%. They concluded that the size effect could be substantially relaxed as a result of steel fiber presence. Shoaib et al. (2014) tested 12 SFRC specimens with an overall depth from 12 to 39 in. to examine the size effect in SFRC beams with 1% steel fiber volume fraction. Longitudinal reinforcement ratio was varied from 1.88 to 4.03%. In addition that they re-affirmed the existence of the size effect in SFRC beams, the size effect was attributed to a larger amount of the steel fiber pull out just before the failure as the beam height becomes larger.

Slenderness: The concept of slenderness generally originates from the difference in shear strength quantity of those equivalent beams in which all the factors affecting shear resistance remain constant with the exception of shear span to effective depth ratio, a/d. Based on this concept, the beams with lower slenderness ratio (reduced a/d) turned out to resist higher shear force. The reason was attributed to the development of arch action mechanism in shear resistance which is that of the direct transfer of external load to support by means of a compressive strut. In order to distinguish between deep and slender SFRC beams, Baston et al. (1972) suggested a value of 3 for a/d, whereas this number was reduced to 2.5 for PC beams. Figure 2.40 indicates the variation of normalized shear stress with respect to the changes in a/d for the SFRC beams tested by Ashour et al. (1992). According to them, for the a/ds less than 2, that the normalized shear stress ascended with the highest rate by a decrease in a/d signifies the involvement of arch action mechanism.

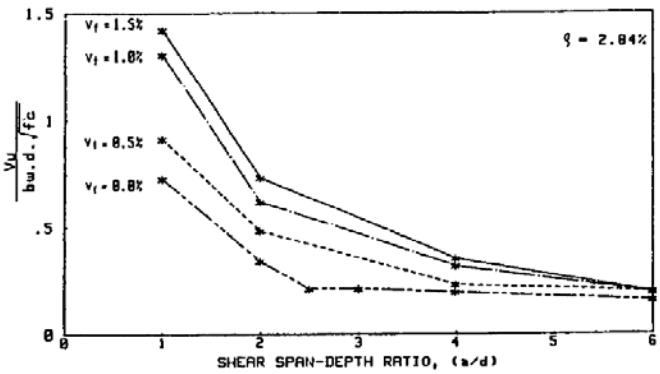

Figure 2.40 Variations of normalized shear stress vs. Shear span to effective depth ratio for SFRC beams with different fiber contents (Ashour et al., 1992)

Aggregate size: Based on the conventional acceptance associated with PC beams, aggregate interlocking constitutes the major component in shear resistance. Therefore, larger maximum aggregate size could increase the asperity of crack interface and result in improved aggregate interlocking and the consequent shear enhancement. Nevertheless, with regard to SFRC beams, aggregate interlocking and its effectiveness to ultimate shear strength has remained a controversy. This arises from the fact that in SFRC beams, the crack largely widens at the time of failure; hence, it is barely inferred that aggregate size play a role to preserve the load carrying capacity of the beam. Based on Dinh (2009), the size of aggregate comes into effect when the quality of fiber-matrix interfacial bond is concerned. In fact, smaller aggregate size tends to cause minor disturbance to the bond between fibers and concrete that may, in turn, result in a shear resistance increment.

To evaluate the effectiveness of steel fiber as minimum shear reinforcement in lieu of stirrups, a database consisting of the test results for 175 SFRC beams with deformed steel fibers and 45 companion beams without fiber was compiled by Parra-Montesinos (2006). The beams included in the data base had an effective depth ranging between 7 and 22.5 in.; a shear span to effective depth ratio from 1 to 6; a concrete compressive strength varying from 2.6 to 15.1 ksi; a fiber volume fraction lying between 0.25% and 2%;

various types of steel fiber including either hooked end or crimped with the exception five of them containing a combination of straight and hooked end fibers; a fiber length to diameter ratio of 50 to 100; and, a longitudinal tensile reinforcement ratio changing from 0.37 to 4.58%. For those beams had failed in shear, normalized shear strength was plotted vs. shear span to effective depth ratio, beam effective depth, concrete compressive strength, and steel fiber volume fraction, respectively to assess the effect of the relevant parameters on shear strength of SFRC beams (Figure 2.41a to Figure 2.41d).

By referring to Figure 2.41a, he stated that normalized shear strength turned out to decrease as a/d increases. In addition, the inclusion of steel fibers with volume fractions less than or equal to 0.5% was unable to raise the shear strength of an SFRC beam highly in excess of $2\sqrt{f'_c}$. In fact, since all the SFRC beams in the database failed in shear strength more than $2\sqrt{f'_c}$, using of deformed steel fiber in volume fractions greater than or equal to 0.5% was suggested as minimum shear reinforcement once the shear demand is less than $2\sqrt{f'_c}$. Figure 2.41b and Figure 2.41c returned no clear trend in variation of the shear strength of SFRC beams in terms of their effective depth and concrete compressive strength.

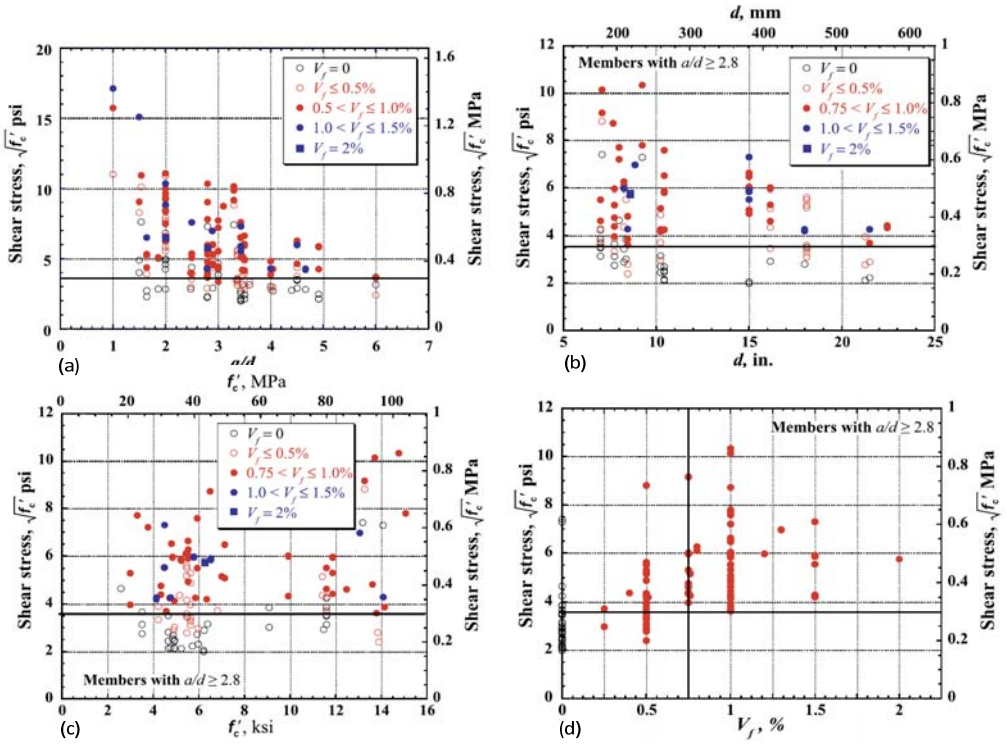

Figure 2.41 Normalized shear strength at failure versus a. shear span to effective depth ratio (a/d); b. beam effective depth (d); c. concrete compressive strength, f'_c ; d. steel fiber volume fraction (V_f) (Parra-Montesinos, 2006)

2.9 Shear Strength Prediction for SFRC Beams

To establish an equation predicting the shear strength of a SFRC beam, Mansur et al. (1986) used the ACI shear predicting expression (Equation (2.1)) to account for the contribution of concrete. In this consideration, steel fibers were assumed to influence concrete shear strength in the same way as they affect concrete compressive strength, f'_c . Meanwhile, the contribution of steel fibers as shear reinforcement was also taken into account assuming uniform residual tensile stress acting through a 45° diagonal crack. The residual tensile stress was conceived of as the post cracking tensile strength, σ_{tu}, of SFRC obtained from direct tensile test. The horizontal projection of the 45° diagonal crack was

assumed equal to beam effective depth. Therefore, the ultimate shear strength of an SFRC beam in basis of the proposed method is to estimate as follows:

$$v_c = 0.16\sqrt{f'_c} + 17.2\frac{\rho V d}{M} + \sigma_{tu} \le 0.29\sqrt{f'_c} + \sigma_{tu} \qquad (MPa) \tag{2.14}$$

The critical bending moment to shear ratio in Equation (2.14) is calculated in accordance with the following equations:

$$\frac{M}{V} = \frac{M_{max}}{V} - \frac{a}{2} \qquad when \quad a \le 2d \tag{2.15}$$

$$\frac{M}{V} = \frac{M_{max}}{V} - d \qquad when \quad a \ge 2d \tag{2.16}$$

Narayanan and Darwish (1987) developed an equation through which the ultimate shear strength of a SFRC beam, v_u, was to be determined (Equation (2.17)).

$$v_u = e\left[A' f_{cpfc} + B'\frac{\rho d}{a}\right] + v_b \qquad (MPa) \tag{2.17}$$

Equation (2.17) is compounded of three terms. The first term is ultimate split cylinder strength, f_{cpfc}, designated for taking into account the contribution of fiber concrete to the total shear and calculated through Equation (2.18). Equation (2.18) was proposed by Narayanan and Kareem-Palanjian (1984) and relates the ultimate split cylinder strength of SFRC, f_{cpfc}, to cube compressive strength, f_{cuf}, and fiber factor, F. Fiber factor, in turn, accounts for the effect of fiber characteristic including fiber volume fraction, V_f, fiber aspect ratio, L_f / D_f, and amount of matrix-fiber interfacial bond, β, on fiber concrete (Equation (2.19)).

$$f_{cpfc} = \frac{f_{cuf}}{20 - \sqrt{F}} + 0.7 + \sqrt{F} \qquad (MPa) \tag{2.18}$$

$$F = V_f \frac{L_f}{D_f} \beta \tag{2.19}$$

The bond factor β was adopted from the work of Narayanan and Kareem-Palanjian (1984) and assigned different values based on fiber geometry. β takes values of 0.5, 0.75, and 1 in case of round, crimped, and indented fibers, respectively.

The second term accounts for dowel action contribution in shear resistance as it is rendered in terms of shear span to effective depth ratio, a/d, and the amount of main steel bars, ρ. Finally, the last term is the shear resistance proportion provided by the vertical component of fiber pullout forces along a diagonal crack, v_b.

To incorporate the effect of arch action into Equation (2.17), a nondimensional coefficient, e, is introduced based on the below conditions:

$$e = 2.8 \frac{d}{a} \qquad when \qquad a \le 2.8d \tag{2.20}$$

$$e = 1.0 \qquad when \qquad a > 2.8d \tag{2.21}$$

A′ and B′ have a constant value of 0.24 and 80 MPa that resulted from a regression analysis performed on 91 test results.

v_b is the intensity of the vertical component of fiber pullout force, V_b, over the cross section of a 45° inclined crack. The total fiber pullout force normal to the diagonal crack, F_b, is basically the summation of the pullout forces each of which is denoted by F'_b and needed to induce an average fiber pullout of L/4, a quarter of the fiber length, in each fiber crossing the 45° diagonal crack.

$$F'_b = \frac{\pi D_f L}{4} . \tau \tag{2.22}$$

where τ = average fiber-matrix interfacial bond stress.

The number of fibers over a unit area, n_w, was adopted from the work of Romualdi and Mandel (1964) as follows:

$$n_w = \frac{1.64V_f}{\pi D_f^2} \tag{2.23}$$

Therefore, the total number of fibers, n, and accordingly, the total fiber pullout force, F_b, at the inclined crack section are determined based on Equation (2.24) and Equation (2.25), respectively by assuming the length of the diagonal crack as jd/sin45.

$$n = n_w . \frac{jd}{sin\,45} . b \tag{2.24}$$

$$F_b = n.F_b' = n. \frac{\pi D_f L}{4} . \tau \tag{2.25}$$

Therefore,

$$V_b = F_b . cos\,45 \tag{2.26}$$

, or

$$v_b = \frac{F_b . cos\,45}{bjd} = 0.41\tau V_f \frac{L_f}{D_f} \tag{2.27}$$

To take into account the effect of fiber geometry on bond, the aforementioned bond factor β was comprised to Equation (2.27):

$$v_b = 0.41\tau V_f \frac{L_f}{D_f} \beta = 0.41\tau F \tag{2.28}$$

The bond stress, τ, was assigned a value of 4.15 MPa as suggested by Swamy et al. (1974). In this model, the contribution of aggregate interlock was ignored.

Ashour et al. (1992) proposed two different equations to predict shear strength for HSFRC beams. The first equation was established doing some modification on ACI shear equation (Equation (2.1)). The modification was applied by incorporating the effect of shear span to effective depth ratio into both concrete compressive strength and longitudinal reinforcement terms based of a regression analysis on the test results (Equation (2.29)).

$$v_u = (0.7\sqrt{f'_c} + 7F)\frac{d}{a} + 17.2\rho\frac{d}{a} \qquad (2.29)$$

In Equation (2.29), according to them, the multiplier 0.7 is to account for the behavior of high strength concrete, while the term F is fiber factor introduced by Narayanan and Darwish (1987).

The second equation was developed by including the term F (Fiber factor) into the equation proposed by Zsutty (1968). The goal was to account for the extra strength associated with the use of steel fiber. As a matter of fact, the application of the Zsutty's equation was limited to only normal strength concrete with no fiber.

if $a/d > 2$

$$v_u = (2.11\sqrt[3]{f'_c} + 7F)(\rho\frac{d}{a})^{1/3} \quad (MPa) \qquad (2.30)$$

if $a/d < 2$

$$v_u = \left[(2.11\sqrt[3]{f'_c} + 7F)(\rho\frac{d}{a})^{1/3}\right]\left(2.5\frac{d}{a}\right) + v_b(2.5 - \frac{a}{d}) \quad (MPa) \qquad (2.31)$$

For deep beams (a/d<2), another term, v_b, was added to the original strength and believed that this component represented the additional shear resistance provided by the shear strength of fibers. The value for v_b is computed through Equation (2.32).

$$v_b = 1.7 \frac{L_f}{D_f} V_f d_f \tag{2.32}$$

Choi et al. (2007) proposed a theoretical strain-based model to account for the effect of flexural deformation on shear capacity of a FRC beam. In their model, the shear resistance from aggregate interlocking and dowel action was ignored because the intact compression zone was assumed to prevent the crack interface slip (Choi et al., 2007; Kotsovos and Pavlović, 1998). The major shear resistance in SFRC beams was assumed to be provided by the shear stress carried by the intact compression zone and the vertical component of the tensile force developed in the steel fibers crossing the diagonal cracks. Their approach to develop the model was to associate the allowable shear stress at any point across a cross section in the compression zone with the flexural normal stress at that point through the Rankin's failure criteria expressing two cases of "failure controlled by tension" and "failure controlled by compression"; hence, the allowable shear stresses acting on the cross section varies as a function of vertical distance to neutral axis in compliance with the flexural normal stress variation in the cross section. On the other hand, since the magnitude and distribution of flexural normal stress alters depending on the flexural deformation of the cross section (cross section curvature) at different loading stages, the shear capacity (i.e. the resultant of allowable shear stresses) of the section was indicated by two curves with respect to the section flexural deformation; each signifies a specific type of failure (Figure 2.42). In their study, they showed that the failure of an SFRC beam is always dominated by tension (the bottom curve in Figure 2.42). As justified, the

tension-controlled shear capacity of a cross section begins to decrease when the cross section cracks and adopts its minimum value when the crack reaches the neutral axis.

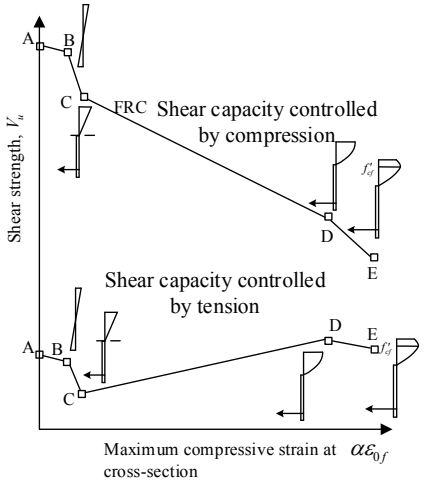

Figure 2.42 The variation of shear capacity of a cross section with respect to its flexural deformation (Reproduced from Choi et al., 2007)

Based on their model, the shear strength of SFRC beams is the point of intersection of the shear demand and the minimum shear capacity curve. The minimum shear capacity curve was introduced as a curve representing the minimum shear capacities of all the cross sections along the beam span (Figure 2.43).

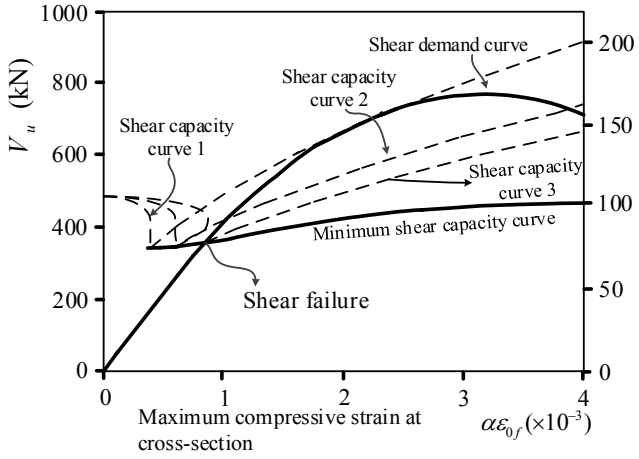

Figure 2.43 SFRC shear strength determination (Reproduced from Choi et al., 2007)

To find the location of the critical crack and subsequently the shear strength, the minimum shear capacity for all the sections was defined as a function of a single parameter (maximum compressive strain at loading point) by means of a set of strain-based equations. Eventually, by going through an iterative procedure, and at each time equating the minimum shear capacity and shear demand equations, the critical cross section and the shear strength of a SFRC beams can be determined. Dinh et al. (2011) proposed a simple model to estimate the shear capacity of SFRC beams (V_n). The shear resistance was assumed to be collectively provided by intact compression zone (V_{cc}) and the tension transferred across diagonal crack by steel fibers (V_{FRC}). Based on this model, the shear failure in SFRC beams was the consequence of flexural-shear crack development and always triggered by the crushing of concrete above the neutral axis (Figure 2.44a).

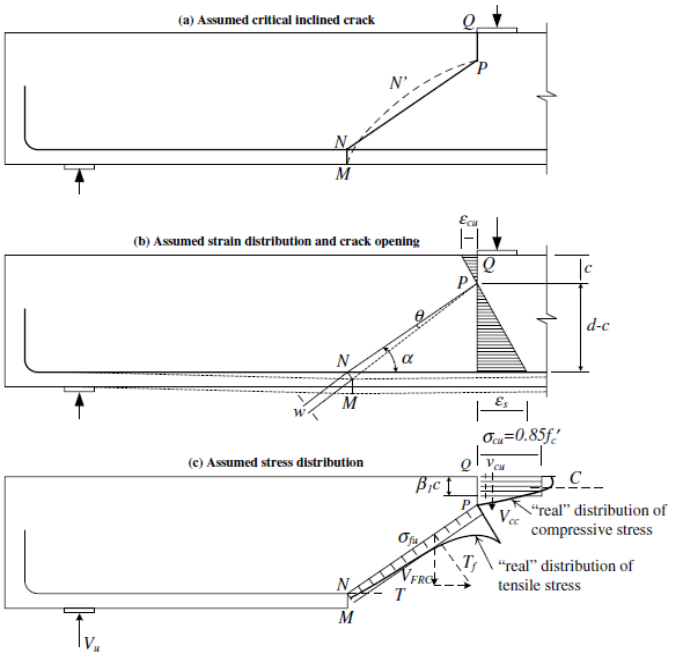

Figure 2.44 Internal stresses contributing shear resistance and their distribution (Dinh et al., 2011)

The contribution of compression zone to shear resistance was assessed by using the failure criterion for plain concrete subjected to combined compression and shear proposed by Bresler and Pister (1958) as represented by Equation (2.33).

$$\frac{v_{cu}}{f'_c} = 0.1\left[0.62 + 7.86\left(\frac{\sigma_{cu}}{f'_c}\right) - 8.46\left(\frac{\sigma_{cu}}{f'_c}\right)^2\right]^{1/2} \qquad (MPa) \qquad (2.33)$$

where v_{cu} and σ_{cu} are the shear and normal stresses at failure, respectively. Bresler and Pister assumed a uniform compressive stress of $k_1k_3f'_c$ as the average normal stress acting on beam compression zone. k_1 is a coefficient that when multiplied by the peak normal stress of $k_3f'_c$ expresses the average compressive stress (Figure 2.45a). Dinh et al. by considering (k_1k_3=0.85x1), estimated $\sigma_{cu} = 0.85f'_c$. Then, by substituting the value for σ_{cu} in Equation (2.33) and finding the ultimate shear stress acting on compression zone at failure, the shear contribution of the compression zone was rendered in form of Equation (2.34).

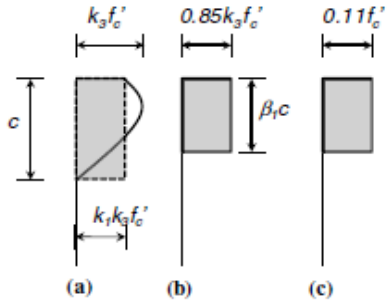

Figure 2.45 Modeling of beam compression zone: (a) actual versus average compressive stress; (b) Whitney's stress block; (c) assumed shear stress distribution in compression zone (Dinh et al., 2011)

$$V_{cc} = 0.11f'_c\beta_1cb = 0.11\frac{T_s}{0.85} = 0.13A_sf_y \qquad (MPa) \qquad (2.34)$$

where b and T_s are the beam width and the horizontal tensile force existing in the longitudinal bars at the time of failure.

The contribution of steel fibers in shear resistance was assumed to be provided by the tensile stresses transferred across the critical crack via steel fibers. However, it was noted that the tensile stress intensity varies through the length of the crack depending on the crack width. According to them, for any point along the crack, as the distance to the beam neutral axis increases, the crack width accordingly increases. This has a negative impact on the magnitude of the tensile force at that point. The suggested distribution of tensile stress is displayed in Figure 2.44c by the thick curve along line NP. Nevertheless, they considered an equivalent uniform stress distribution ($\sigma_{t_{ave}}$) with identical tensile force resultant (T_f) for simplicity. Equation (2.35) was suggested by Dinh et al. (2011) through which the shear proportion carried by steel fibers can be determined.

$$V_{FRC} = T_f \cos\alpha = \left[\sigma_{t_{ave}} b\left(\frac{d-c}{\sin\alpha}\right)\right]\cos\alpha = \sigma_{t_{ave}} b(d-c)\cot\alpha \qquad (MPa) \qquad (2.35)$$

They recommended α at 45° for the simplicity. The actual angle of α was reported between 33° and 43°. The terms included in Equation (2.35) were introduced in Figure 2.44b and Figure 2.44c. In accordance with the proposed model, the total shear force carried by a SFRC beam is to be predicted as follows:

$$V_n = V_{FRC} + V_{cc} \qquad (2.36)$$

Chapter 3

EXPRIMENTAL PROGRAM

3.1 Introduction

As reviewed in the previous chapter, a large number of experimental programs have been conducted in the last four decades to assess the shear behavior of FRC beams without web shear reinforcement, consisting of various types, geometries and fiber content. The results unanimously confirmed an enhancement in shear behavior of SFRC beams as a consequence to fiber addition. Nevertheless, some of the building codes such as ACI 318 (2014) permit the use of steel fibers only as a minimum shear reinforcement when certain criteria are met. This deficiency in the application partially arises from the lack of adequate knowledge on shear-enhancement and resisting mechanisms, as well as the influencing factors and their proportions. On the other hand, majority of research studies were carried out on laboratory-scale SFRC beams, where the effective depth mostly varied between 7 and 24 inches. For this reason, it is still unclear whether size effect should also be a concern for SFRC beams. This concern is reflected in the ACI code where the maximum SFRC beam overall depth is limited to 24 inches. Hence, an experimental program was geared to address the gap behind the ACI provisions concerning the use of steel fibers as a strength characteristic in SFRC beams. This experimental program involved the design, construction, and testing of simply supported beams subjected to a monotonically increased, concentrated load.

3.2Design of Specimens

A total of 12 simply supported SFRC and RC beams (6 pairs) were monotonically loaded up to failure. Each pair out of the first four pairs of SFRC beams consisted of two duplicated beams, whereas the last pair had two identical SFRC specimens differing in widths of 6 in. and 24 in., which allowed us to investigate the effect of width on the shear

behavior of SFRC beams. Two identical RC beams with no stirrup and an overall height of 18 in. were used as control specimens. The reason for the duplicated specimens in each pair was to increase the certainty of test data. For all the specimens, shear span to effective depth ratio, a/d, longitudinal reinforcement ratio, ρ, steel fiber volume fraction, V_f, fiber type, and concrete compressive strength were held constant. For the SFRC specimens, effective depth was selected as the only parameter varying from one pair to another which in turn led the beams to have heights of 12, 18, 24, 36, and 48 inches. Steel fibers used in this research were hooked-end fibers (l/d =67, l = 2.0 in., d = 0.03 in., f_t = 159 ksi) conforming to ASTM A820. The fiber content was fixed at 0.75% by volume, which is the minimum amount as specified by the ACI 318 (2014). The design compressive strength of concrete was 6000 psi in compliance with the maximum allowable compressive strength for SFRC (ACI 318, 2014). Table 3.1 lists the design properties of beams used in this experimental program.

Table 3.1 Design properties of the specimens

Specimen	Height (h) in.	Effective depth (d) in.	a/d	ρ (%)	V_f (%)	Targeted f'_c psi	Measured f'_c psi
SFRC12W6	12	10	3.5	2.5	0.75	6000	4235
SFRC12W24	12	10	3.5	2.5	0.75	6000	4235
SFRC18a,b	18	15.5	3.6	2.82	0.75	6000	5707
SFRC24a,b	24	21.3	3.45	2.64	0.75	6000	7210
SFRC36a,b	36	32	3.5	2.72	0.75	6000	7210
SFRC48a,b	48	44	3.5	2.65	0.75	6000	7210
RC18a,b	18	15.5	3.6	2.82	0	6000	5514

3.2.1 Shear span to effective depth

Depending on the selected shear span to effective depth ratio, equivalent reinforced concrete beams without conventional shear reinforcement (PC beams) indicate different shear stress at failure. Herein, the term of equivalent beams refers to those beams

that resemble one another in terms of their geometry and all the parameters influencing the shear behavior (i.e. a/d, f'_c , d, ρ, maximum aggregate size (a_g)). In fact, the different shear strengths due to the variable a/d arises from the various involved shear carrying mechanisms. For a very short beam with a/d less than 1, the development of direct load transfer through a compression strut from loading point to support (arch action mechanism) allows the beam to sustain additional loads and gain higher shear strength (Figure 3.1).

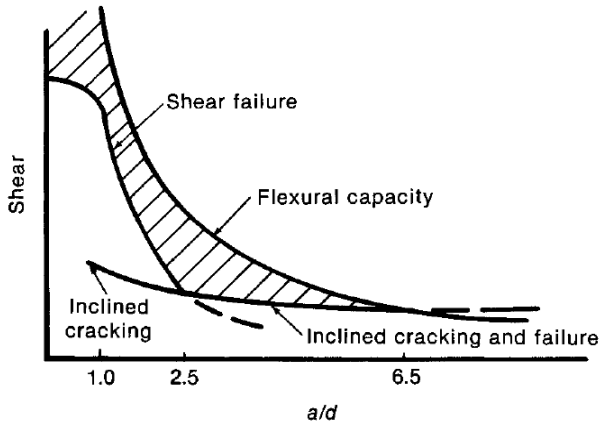

Figure 3.1 The influence of shear span to effective depth ratio on shear strength of PC beams (Wight and MacGregor, 2009)

Figure 3.1 compares the shear strength at failure for PC beams as a function of a/d. The enhanced shear strength resulting from arc action involvement seems to diminish as a/d increases such that it descends to the minimum value at 2.5 (Wight and MacGregor, 2009) as noticed in Figure 3.1. For beams with a/d greater than 2.5 and less than 6.5, which is the distinguishing characteristic of slender beams, the shear capacity is dominated by occurrence of an inclined crack disturbing the formation of arch action. The shear strength is predicted to be almost invariable for equivalent slender beams, irrespective of a/d. To isolate the effect of beam height on shear strength of SFRC beams, shear strength improvement resulting from arch action was required to be minimized. Therefore, by

expecting the same shear behavior for SFRC beams as that of established for PC ones, a/d was selected at 3.5.

3.2.2 Beam size

As described before, inadequate shear test data for SFRC beams with a height of over 24 in. and the relevant concern that size effect causes shear strength degradation prompted the ACI-318 committee to limit the maximum height of SFRC beams to 24 inches beginning in 2008. Therefore, to fill the data base gap and investigate size effect in SFRC beams, an extensive height range was considered for the test specimens from 12 to 48 inches.

The width of each specimen pair was determined by the following required tasks: 1) to ensure that required longitudinal steel bars can be accommodated with a proper cover thickness; 2) to ensure that the shear capacity of specimens (loading) does not exceed the capacity of the equipment and setup (550 kips); 3) to minimize the respective width and consequent reduced weight to ease the transportation and disposal.

Prior research has shown that the shear strength (in terms of stress) of PC beams is not a function of beam width (Kani et al., 1979; Lubell et al., 2004). Despite the fact that this finding had not been explored in the case of SFRC beams, it constituted a premise and was initially considered in the design of the test specimens. However, the validity of this premise was verified later by allocating a pair of duplicated 12-inch high SFRC specimens with different widths of 6 and 24 inches.

Shear span length for each specimen were adopted based on the constant shear span to effective depth ratio (a/d) of 3.5 and the designated effective depth. The shear span refers to a segment of the total length of a beam along which shear failure is designed to occur. Eventually, the total length of SFRC specimens was adjusted at twice the sum of the shear span and sufficient flexural bar developing length avoiding anchorage failure.

However, in the case of the PC specimens, the shear span to total length was assigned at 0.6. To induce shear failure in the intended shear span under investigation, the other span was reinforced with stirrups. Figure 3.2 displays the boundary conditions and basic terms signifying the geometry of the specimens. Table 3.2 summarizes the geometrical dimensions of the specimens.

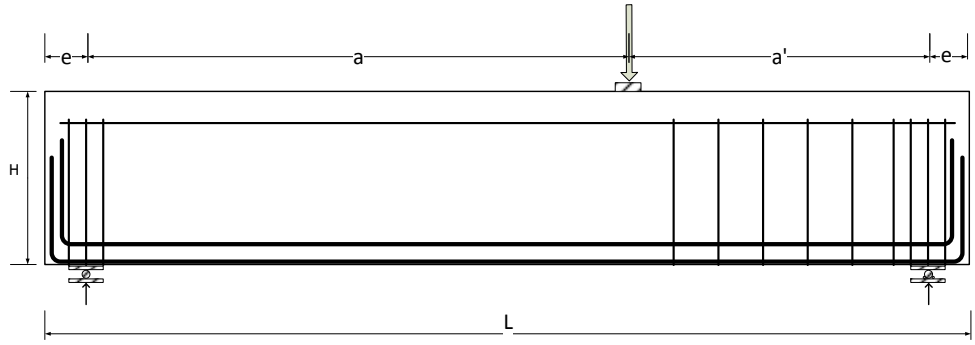

Figure 3.2 Basic dimensions, loading location, and boundary conditions of a specimen

Table 3.2 Geometrical dimensions of the specimens

Specimens	Total Length (L) in.	Total Height (h) in.	Width (b) in.	Shear span length (a) in.	a′ in.	e in.
SFRC12W6	78	12	6	35	35	4
SFRC12W24	78	12	24	35	35	4
SFRC18a,b	120	18	6	56	56	4
SFRC24a,b	195	24	8	73.5	73.5	24
SFRC36a,b	278	36	10	112	112	27
SFRC48a,b	370	48	12	154	154	31
RC18a,b	96	18	6	56	32	4

3.2.3 Longitudinal reinforcing bar

As discussed in the last chapter, the inclusion of steel fiber in concrete improves both flexural and shear resistance of a beam. However, depending on the fiber volume fraction, the extent of enhancement varies from beam to beam. In general, presence of steel fiber in concrete more effectively contributes to shear resistance than a flexural one. This might in turn, lead to a transformation in the failure mode from shear to flexure (Narayanan and Darwish, 1987). Therefore, to ensure that the failure would be governed

by shear rather than flexure, a sufficient flexural reinforcement ratio (ρ_{ave} = 2.66%) was provided for both SFRC and PC specimens. The amount of the longitudinal reinforcement was calculated according to the highest shear capacity ($6\sqrt{f'_c}$ psi) reported by Parra-Montesinos (2006) for SFRC beams with V_f =0.75%. Note that research done by Shoaib et al. (2014) showed that longitudinal reinforcement ratio in the range of 1.44 to 4.03% had almost no effect on the ultimate shear strength of SFRC beams. A similar conclusion was also drawn by Dinh et al. (2010) for longitudinal reinforcement ratio between 1.6% and 2.7%. The considered values corresponding to the required parameters for the design of longitudinal bars as well as the used number and size of the reinforcing bars and the consequent nominal flexural capacity for each specimen are illustrated in Table 3.3.

The nominal moments reported in Table 3.3 was based on the equilibrium equations of a cross section in PC beams. In other words, the effect of steel fiber was not taken into account in calculation of flexural capacity of SFRC beams. A sample of the calculations for the pair of SFRC24 are presented below:

$$V_u = 6\sqrt{f'_c}bd = 6\sqrt{6000}\,psi \times 8in. \times 21.3in. = 79195lbs = 79.2kips$$

$$P_{us} = \frac{V_u L}{a} = \frac{79.2 \times 147in.}{73.5in.} = 158.4kips \qquad Ans.$$

$$a_c = \frac{A_s f_y}{0.85 f'_c b} = \frac{(4.43in.^2) \times 75ksi}{0.85 \times 6ksi \times 8in.} = 8.14in.$$

$$M_n = A_s f_y (d - \frac{a_c}{2}) = 4.43in.^2 \times 75ksi \times (21.3in. - \frac{8.14in.}{2}) = 5724kips.in$$

$$P_{nm} = \frac{M_n \times 4}{L} = \frac{5724kips.in \times 4}{147in.} = 155.8kips \qquad Ans.$$

Table 3.3 Required parameters for longitudinal bar design and the used reinforcements

Specimens	$v_u / \sqrt{f'_c}$	f'_c (ksi)	f_y (ksi)	b (in.)	d (in.)	Shear capacity load (P_{us}, kips)	A_s (in^2)	ρ_s (%)	M_n (kips.in)	Flexural capacity load (P_{nm}, kips)
SFRC12W6	6	6	75	6	10	55.8	1.5 (2-#5+2-#6)	2.5	918	52.5
SFRC12W24	6	6	75	6	10	223	6 (8-#5+8-#6)	2.5	3673	209.9
SFRC18a,b	6	6	75	6	15.5	86.4	2.64 (6-#6)	2.8	2428	87.0
SFRC24a,b	6	6	75	8	21.3	158.4	4.43 (4-#8+1-#6)	2.6	5724	155.8
SFRC36a,b	6	6	75	10	32.0	297.4	8.69 (11-#8)	2.72	16692	298.1
SFRC48a,b	6	6	75	12	44.0	490.8	13.97 (11-#10)	2.65	37132	482.2
RC18a,b	6	6	75	6	15.5	39.6	2.64 (6-#6)	2.8	2428	119.2

For some cases in Table 3.3, the flexural capacity seems to be lower than the associated shear capacity. This perhaps brings to the attention that the specimens with the forgoing characteristic would adversely fail in flexure before the shear capacity is achieved. In fact, the evaluation of flexural capacities was performed in accordance with the equations established for PC beams, thus neglecting the effect of fiber existence. In reality, the ultimate flexural loads therefore, were positively higher than the assessed values. In the worst case, the longitudinal bars would yield prior to shear failure.

For all of the specimens, two No. 4 mild steel bars were placed in compression zone as compression reinforcement and extended along the total length. It is worth mentioning that the reinforcement ratio corresponding to RC18a and RC18b was selected 2.8% with the same layer and size of bars in order to be consistent with the SFRC counterparts and render the comparison possible. The reinforcement details, specimen geometries, and cross sections are depicted in Figure 3.3 and Figure 3.4.

3.2.4 Stirrups and end anchorage

As pointed out before, to ensure that shear failure would initiate in the instrumented shear span under investigation, the contrary span was reinforced with a closed shape stirrup. That how many stirrups were in need was found unnecessary for the SFRC beams, where the two spans on both sides of the loading point were identical in length. Therefore, the existence of stirrups with any rational spacing provided a larger shear capacity than that of the targeted shear span. Unlike the SFRC beams, the number of stirrups was required to be designed for the pair of PC beams. This proceeded from the fact that in the PC beams, the two spans differed in length (Table 3.2), and in particular, the larger span was designated as shear span. For this reason, an inadequate number of stirrups in the smaller span would cause failure within the smaller span.

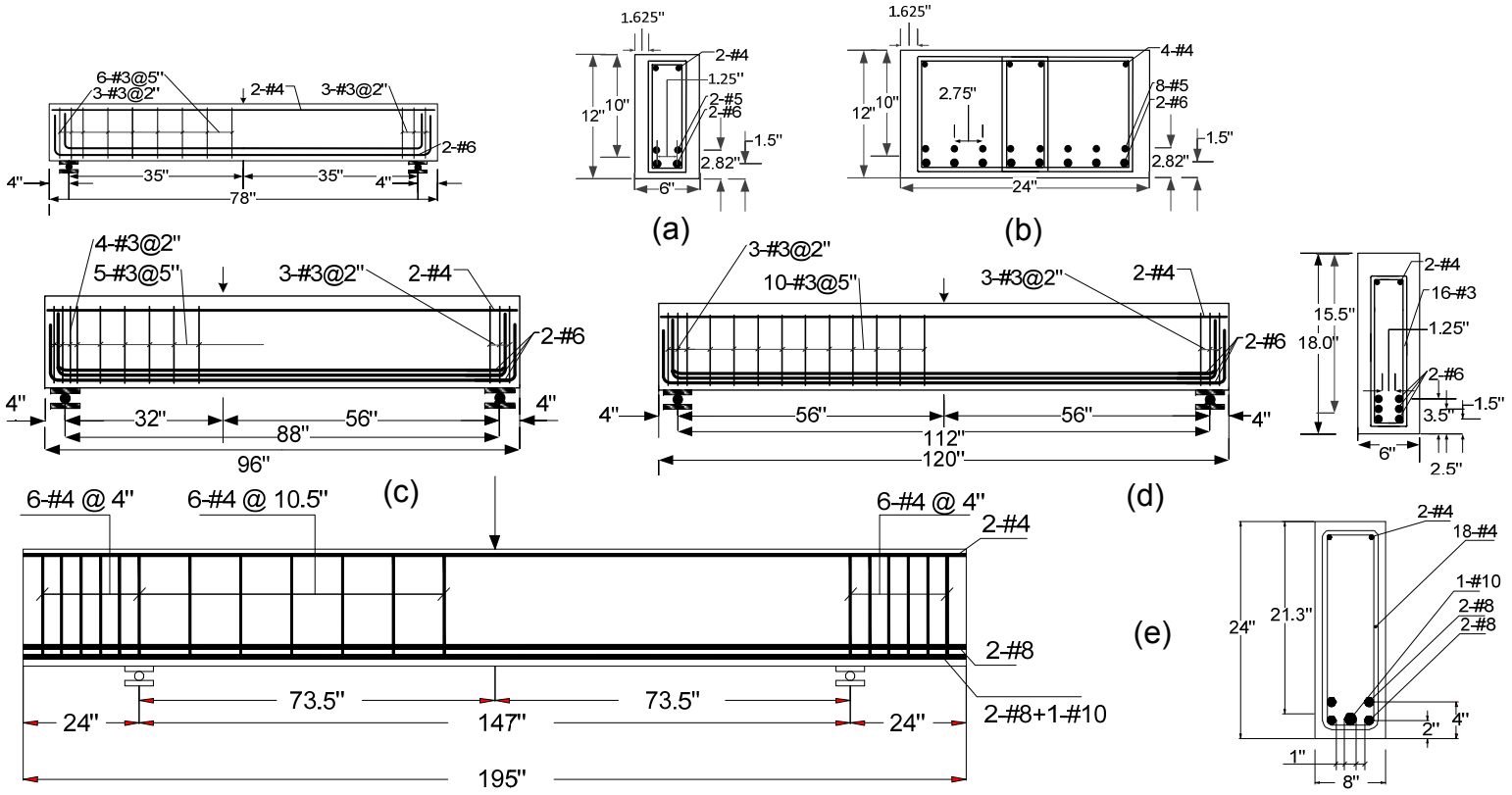

Figure 3.3 Geometry and reinforcement details of the large-scale RC and SFRC beams; (a) SFRC12W6; (b) SFRC12W24; (c) RC18; (d) SFRC18; (e) SFRC24 (in. = 25.4 mm).

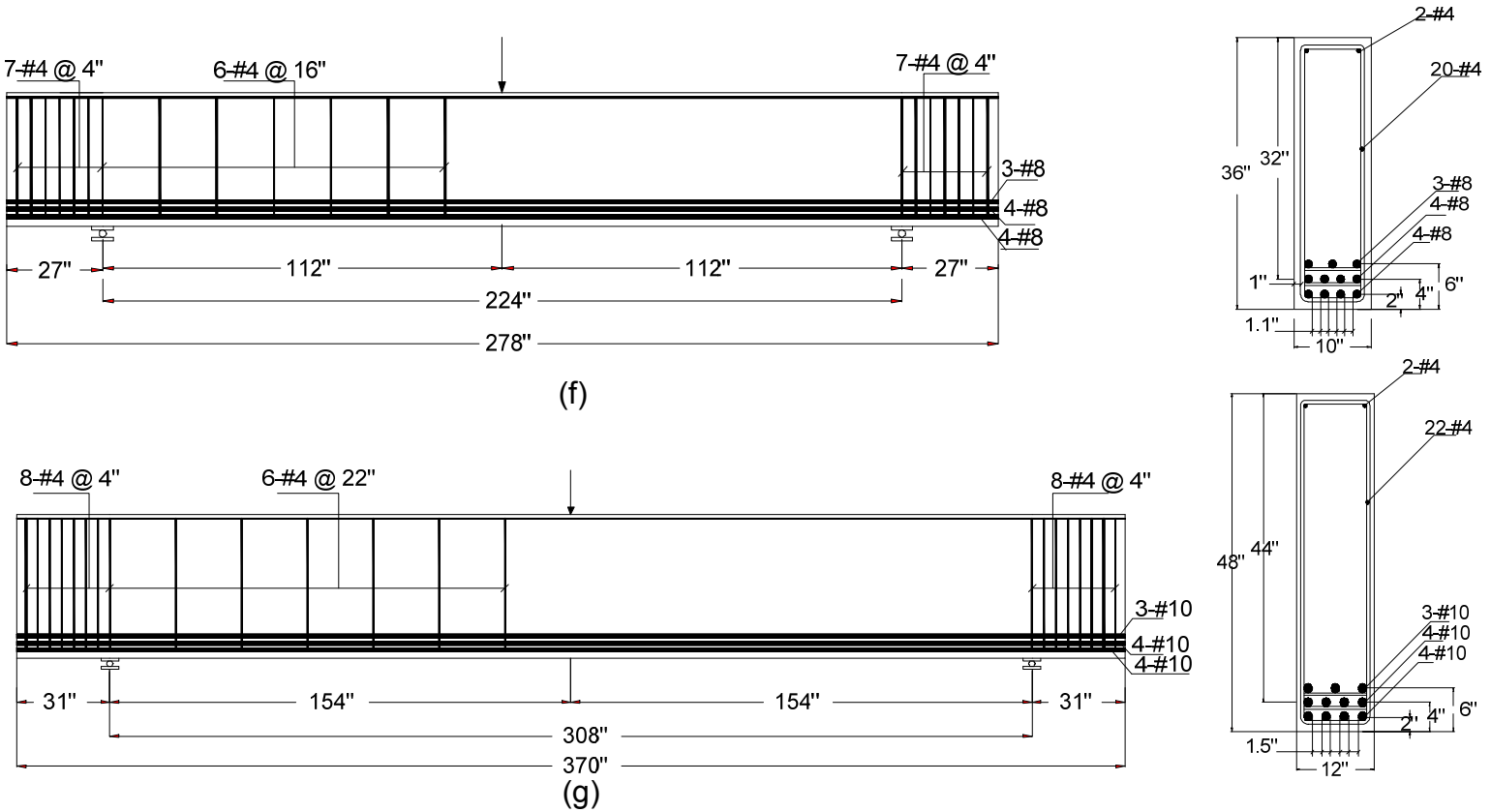

Figure 3.4 Geometry and reinforcement details of the large-scale RC and SFRC beams; (f) SFRC36; (g) SFRC48 (in. = 25.4 mm).

For the PC beams, the shorter span was conventionally reinforced in shear by a series of evenly spaced double legs #3 stirrups which were 5 in. apart. Stirrups and the relating spaces are displayed in Figure 3.3 and Figure 3.4 for all of the specimens. The sufficient shear strength of the shear span was verified for the PC beams as follows:

The shear force (V_{usa}) and accordingly the applied force (P_{us}) required for failure in the larger span and the shorter span shear demand ($V_{usa'}$) were computed below.

$$V_{usa} = 2\sqrt{f_c'}bd = 2\sqrt{6000}\,psi \times 6in. \times 15.5in. = 14..4kips$$

$$P_{us} = \frac{V_{usa}L}{a'} = \frac{14.41 \times 88in.}{32in.} = 39.6kips$$

$$*V_{usa'} = P_{us} - V_{usa} = 39.6 - 14.4 = 25.22kips$$

The nominal shear capacity of the shorter span was:

$$*V_{nsa'} = V_s + V_s = 2\sqrt{f_c'}bd + A_v f_y \frac{d}{s} = 2\sqrt{6000\,psi} \times 6in. \times 15.5in. + 0.22in.^2 \times 75ksi \times \frac{15.5in.}{5in.} = 65.6kips$$

$$*V_{nsa'} > V_{usa'} \qquad Ok$$

As noticed above, the nominal shear capacity of the shorter span was much greater than its shear demand indicating that shear failure is not expected to take place in the short span.

Mechanical terminators (headed bars) were employed at the end of the longitudinal bars (Figure 3.5) to alleviate congestion except for the 18 in. deep PC, and 12 in. and 18 in. SFRC beams in which the longitudinal bars were bent 90° at the ends to provide anchorage.

Figure 3.5 A view of Mechanical terminators (headed bars)

3.2.5 Fiber type and fiber volume fraction

In steel fiber industry, there are two different types of discrete and bundled hooked-end steel fibers currently available (Figure 3.6). The latter refers to the steel fibers which are bundled together through a dissolvable adhesion. The bundled end-hooked steel fibers are promoted by the manufacturer to impede fiber balling in a way that the adhesion is gradually dissolved in concrete water during the mixing process. This allows the fibers to be uniformly distributed in the mixture. Nevertheless, the research carried out by Cho (2011) evidenced quite the contrary, where the adhesion between the fibers was not properly dissolved and the steel fibers remained in bundles, thereby causing ununiformed distribution of steel fibers as found out after testing of the beams (Figure 3.7). Steel fibers used in this study were discrete hooked-end steel fibers with a commercial name of “FF3” and a product of MACCAFERRI incorporation. These fibers had mechanical properties of L/d =67, L = 2.0 in., d = 0.03 in., and f_t = 159 ksi conforming to ASTM A820 (Table 3.4). The fiber content was fixed at 0.75% by volume, which is the minimum amount as specified by the ACI 318 (2014).

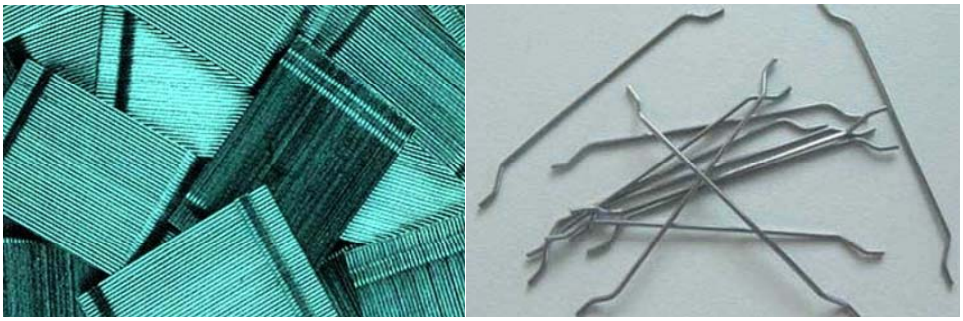

Figure 3.6 A view of bundled vs. discrete steel fibers

Figure 3.7 Unevenly distributed steel fibers as a result of undissolved adhesion (Cho, 2011)

Table 3.4 Mechanical properties of FF3 steel fiber provided by manufacturer

Type of Fiber	Length (L) (in.)	Diameter (D) (in.)	Aspect Ratio (L/D)	Tensile Strength (f_t) (ksi)
Hooked-end	2.00	0.03	67	159

3.2.6 SFRC and PC mix design

SFRC mix needs to be workable enough to permit the steel fibers to uniformly scatter in the mix. On the other hand, the compressive strength of the mixture must not exceed 6000 psi as specified by ACI 318 (2014). Therefore, the mix proportions was designed in a manner to fulfill these two factors. The design compressive strength of concrete was considered at 6000 psi. However, the measured compressive strengths (Table 3.1) varied in the range of +20% and -29% of the targeted strength. The variation in the strength primarily originated from the fact that the specimens were tested in different

ages; the concrete was provided from different suppliers; and specimen castings were not performed at the same circumstances. Table 3.5 gives the SFRC mix proportions used in this research study.

Table 3.5 Mix proportions by weight

Type of Mix	Cement (Type I)	Fly Ash (Class C)	Sand	Coarse Aggregate 3/8"	Water[1]	Steel Fiber	Total Weight
SFRC	1.00	0.5	1.7	1.00	0.60	0.117[2]	4.92
RC	1.00	0.5	1.7	1.00	0.60	0	4.80

[1]: W/CM = 0.4; [2]: V_f = 0.75%

3.3Construction of Specimens

Construction of each specimen was conducted in various phases including strain gage installation, reinforcement caging, formwork fabrication, concrete casting, and specimen curing.

3.3.1 Strain gage installation

For each specimen with the exception of specimens SFRC12W6 and SFRC12W24, two pairs of foil-type strain gauges were mounted on the bottom layer reinforcing bars under the loading point and mid-shear span, respectively. Each strain gauge out of the two ones at each particular location was placed on the nearest bar to each side of the beam so that if one of them malfunctioned, the data would still be acquired through the remaining one.

Arch action is an alternative shear-strength enhancement mechanism that might develop in a PC beam after beam action disturbance depending on the shear span to effective depth ratio. According to Park and Paulay (1975), arch action development is contingent upon the complete interfacial bond loss or yielding of the longitudinal bars. Therefore, to investigate the involvement of arch action in the tested SFRC beams, a series of additional strain gages was mounted on one of the bottom layer reinforcing bars within the shallowest specimens (SFRC12W6 and SFRC12W24). The first 12 gauges were

spaced 3 inches apart starting from mid-span up to the support center, while the remaining two were spaced evenly at 1.5 inches passing the support center toward the anchorage (Figure 3.8).

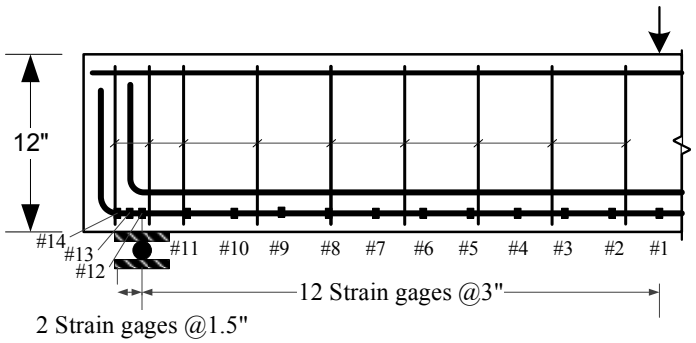

Figure 3.8 Locations of strain gages for SFRC12W6 and SFRC12W24

To install a strain gage, a number of ribs on a rebar at the selected place were grinded to create a flat surface a bit larger than the strain gage to be installed. Then, after degreasing the surface, the strain gage was glued to the surface and protected by three different layers of coating, namely, polyurethane, nitrile, and rubber mastic tape. At the end, the whole thing was sealed by electric liquid tape to avoid the penetration of concrete water into that (Figure 3.9).

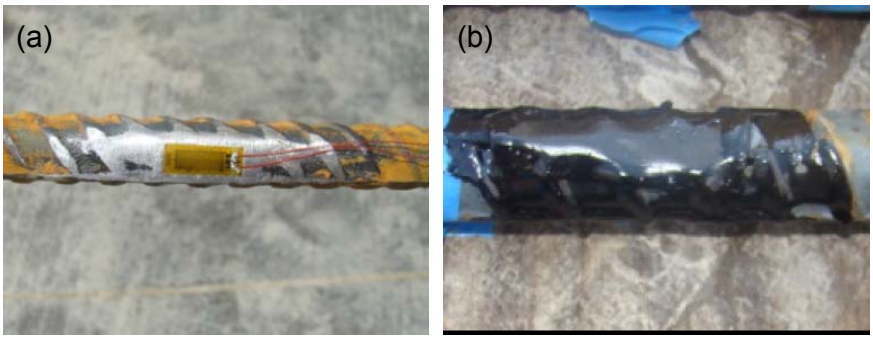

Figure 3.9 Strain gage installation; (a) glued strain gage to the degreased flat surface; (b) sealed strain gage by electric liquid tape

3.3.2 Caging and formwork fabrication

Reinforcing bar cage and formwork for the specimens with the height of 24 in. and beyond were fabricated by professional workers at Hanson Pipe and Precast Plant under the author's supervision as depicted in Figure 3.10. However, for the shallower specimens, the cages and formworks were constructed at the University of Texas at Arlington Civil Engineering Laboratory Building (Figure 3.11).

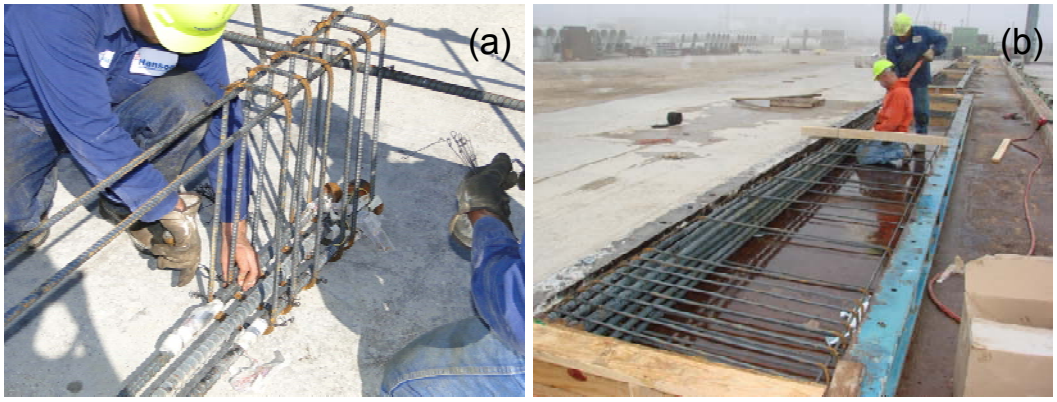

Figure 3.10 Typical photo of reinforcement caging and formwork for SFRC beams with the height greater than 24″ at Hanson Pipe & Precast Plant

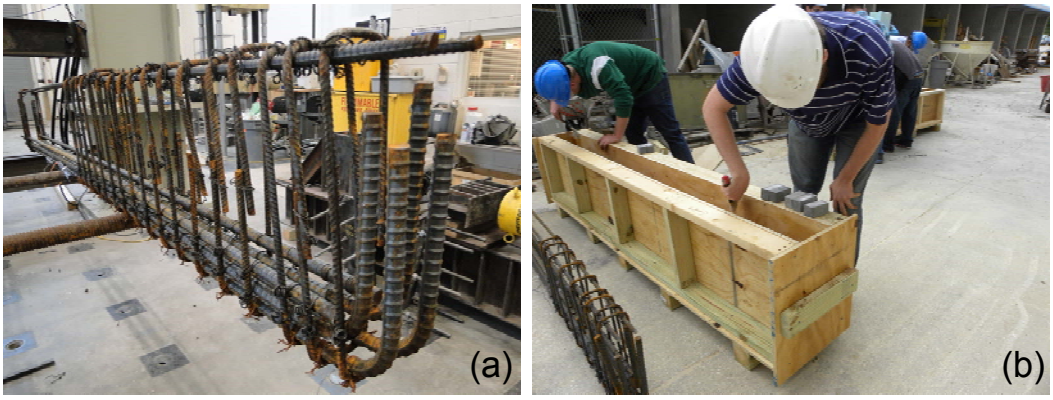

Figure 3.11 Typical photo of reinforcement caging and formwork for SFRC and PC beams at the University of Texas at Arlington Civil Engineering Lab

To fabricate the reinforcement cages in the Civil Engineering Laboratory Building (CELB), the first layer of longitudinal bars was laid apart at the specified clear spaces on

two transverse and parallel stiff rods. The rods were spaced at a distance slightly less than the length of the supported longitudinal bars and constituted a work support for the cage fabrication. Then, stirrups were slid in one after the other across the designated span length and tied to the longitudinal bars at the determined location by means of double loop steel wire ties. Subsequently, compression bars were longitudinally slid into and tied to the assembled stirrups at the compression side corners. At the tension side of the stirrups, the second and third layers of longitudinal bars were tied to the inner sides of the stirrups, respectively at the specified clear space to the last layer of bars (Figure 3.11a). After reinforcement assembly, the inside of formworks was oiled, and the reinforcement cages were placed into the formworks in a manner that the reinforcing bars were not stained with the oil. To provide a 1-inch concrete cover, multiple one-in.-high concrete chairs were inserted between reinforcement cages and formworks. In addition, for lifting purposes and movement of the specimens, two hoops were attached at top and both ends of the cages.

3.3.3 Mixing of concrete and SFRC; Casting; and curing of the specimens

SFRC mixing for beams 24 in. and higher was achieved using the local Hanson Pipe and Precast's facilities. To mix SFRC, all the materials, with the exception of steel fibers, were measured through an automated system and in basis of the mix proportion listed in Table 3.5 and dumped into a pan mixer. On the other hand, the amount of steel fibers required to produce SFRC mixture with 0.75% volume fraction was separately measured and added to the mix through a hatch on the mixing pan as shown in Figure 3.12b, indeed, after observing a uniform color throughout the mix. Once the mix was completely prepared, it was loaded into a Tuckerbilt and transferred to the casting plant (Figure 3.13). The fiber-reinforced concrete in the Tuckerbilt was poured in the formworks and compacted by vibrator as showed in Figure 3.14.

Figure 3.12 (a) a view of pan mixer in local Hanson Pipe & Precast Plant; (b) dumping of steel fibers into the mixer through the intended hatch

Figure 3.13 Loading of concrete into the Tuckerbilt

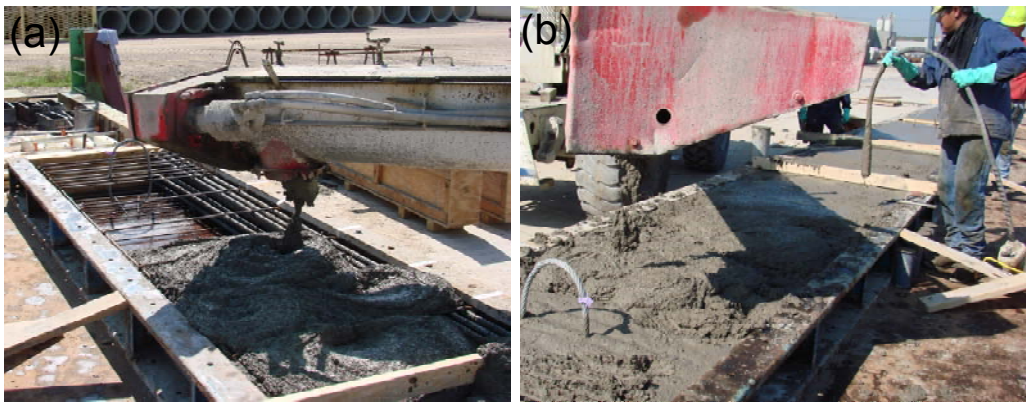

Figure 3.14 Concrete pouring and compacting

Figure 3.15 shows steel fibers lying uniformly on top of the SFRC mix after compactness. Despite the intense compacting process, the steel fibers didn't sink in the concrete, thereby, ensuring the lack of steel fiber segregation from the concrete.

Figure 3.15 A view of uniform distribution of fibers and fiber desegregation from concrete

After casting, all the specimens were covered by a plastic sheet to improve the hydration process and accordingly, expedite curing of the beams. After 7 days, the specimens were removed from the formworks and retained until the test date.

Mixing and casting process for the shallower SFRC specimens were performed in CELB, where concrete was delivered to and from a local ready mix supplier. The pre-measured amount of steel fibers was then, dumped into the truck mixing drum (Figure 3.16a) and allowed to mix with the concrete until reaching a consistent distribution of fibers. As mentioned before, the amount of steel fiber was determined based on the concrete batch volume and fiber volume fraction of 0.75%. Eventually, concrete was shot into the formworks (Figure 3.16b) and sufficiently compacted (Figure 3.16c) without any steel fiber segregation. For the curing purpose, the casted specimens were covered by a plastic sheet for 7 days prior to demolding.

(a) (b)

(c)

Figure 3.16 (a) dumping of steel fibers into the truck mixing drum; (b) shooting of SFRC mixture into formworks; (c) SFRC compactness

3.4Test Setup and Instrumentation

Testing of the specimens was conducted under one of the steel reaction frames established in the University of Texas at Arlington. Loading was applied through a 650 kips hydraulic cylinder that had a moving capability across the frame horizontal beam. Each specimen was supported by a concrete block at each end. Considering the fixed location of the frame horizontal beam, the heights of blocks were adjusted for each test depending on the overall depth of the specimen. The specimens were intended to test under simply supported boundary conditions. To this end, at one end of the test beams, a 2 in. roller with

a sufficient length longer than the beam width was placed between two bearing plates. Then, the entire assemblage was laid between the concrete block top and beam bottom surfaces such that the roller axes be parallel with the beam width (roller support). At the other end, the same set of roller and plates was employed, while the horizontal translation of the roller was restrained by welding a bar against each side of the roller on the bottom plate (Hinge support). Figure 3.17 shows a typical view of roller and hinge supports.

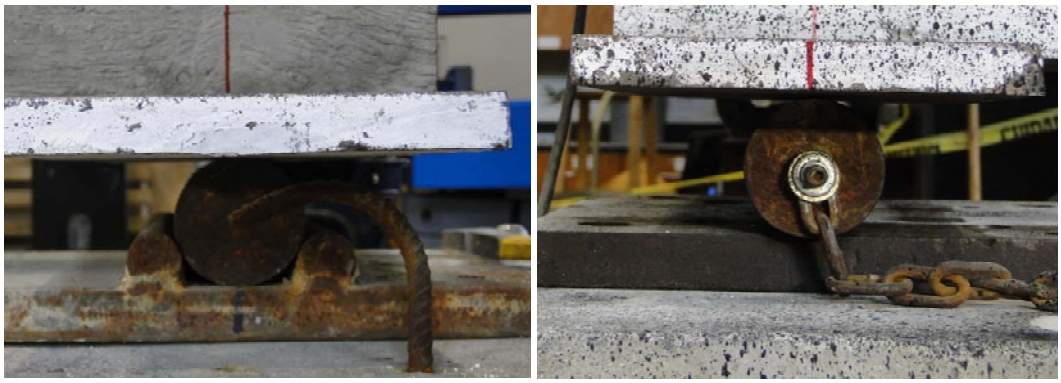

(a) (b)

Figure 3.17 (a) hinge support; (b) roller support

For each test, a total of three bearing plates were used at the supports and loading point. Dimensions of the bearing plate are illustrated in Figure 3.18. To provide a uniform interface contact, a layer of non-shrink grout was used between concrete and bearing plate at the loading point.

With regard to the 24 in. wide specimen (SFRC12W24), in order to have the point load uniformly distributed across the width of the specimen, the load from hydraulic cylinder was transferred through a stiffened W12×87 steel beam to a 2×6×48 in. bearing plate (Figure 3.19). A schematic view of test setup, instrumentations, and loading configuration is depicted in Figure 3.18.

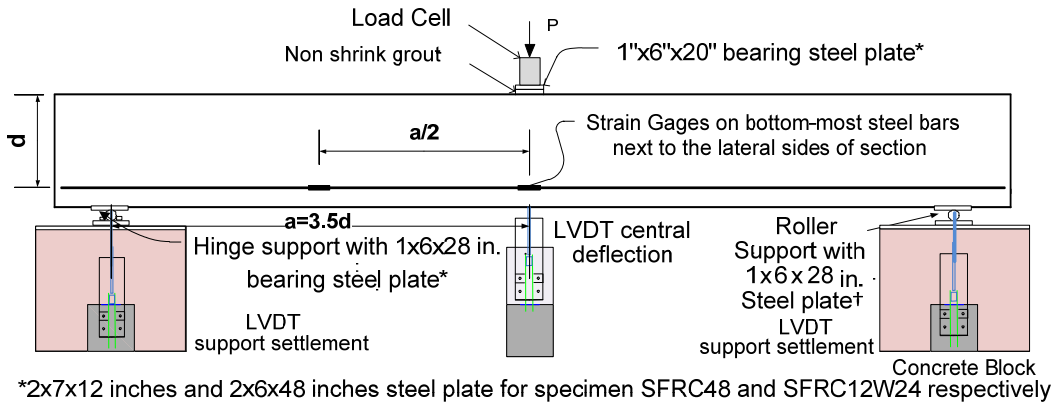

*2x7x12 inches and 2x6x48 inches steel plate for specimen SFRC48 and SFRC12W24 respectively at loading point

†2x6x48 inches steel plates for specimens SFRC48 at supports

Figure 3.18 Schematic view of the test setup, loading configuration, and instrumentations

Figure 3.19 Uniformly distributed load across the specimen width (SFRC12W24)

For each specimen, two pairs of strain gauges were mounted on the bottom layer reinforcing bars at the location shown in Figure 3.18 with the exception of specimens SFRC12W6 and SFRC12W24. For each of those excluded specimens, 14 strain gages were mounted on one of the bottom layer reinforcing bars. The first 12 gauges were spaced 3 inches apart starting from mid-span up to the support center, while the remaining two were spaced evenly at 1.5 inches passing the support center toward the anchorage as displayed in Figure 3.8. Three linear variable differential transformers (LVDTs) were employed to measure the deflections under the loading point and the settlement of each

support. During the tests, the applied load was measured by a load cell. To collect the test data and monitor their variations in real time, all the sensors were connected to Vishay 5000 Data Acquisition (DAQ) system. The rate of data acquisition for all the tests was set on 5 data points per second.

A DIC (Digital Image correlation) non-contact deformation measurement system with the measuring strain accuracy of 0.01% (in./in.) was used to visualize the full field strains and displacements, as they developed on the surface. DIC is an optical metrology supported by digital image processing and numerical computing. In general, DIC detects displacements directly from digital images of the surface of a specimen. Figure 3.20 shows a schematic view of an experimental setup for digital image correlation.

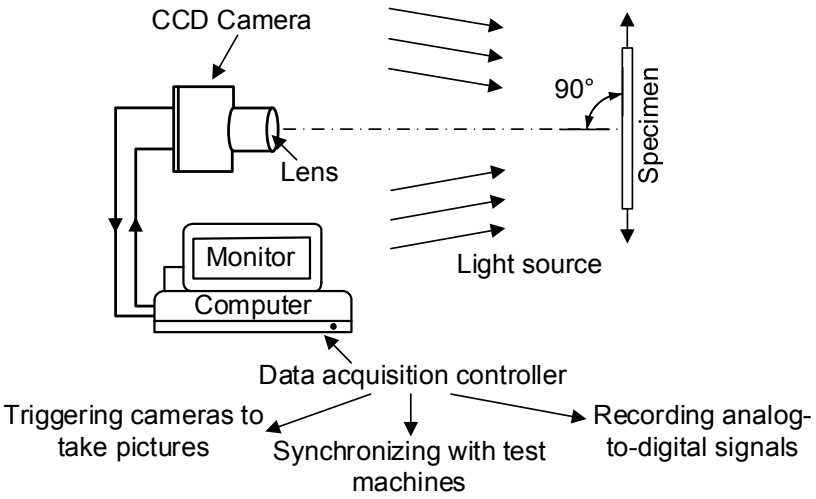

Figure 3.20 A schematic view of an experimental setup for digital image correlation

A CCD camera captures the picture of the test specimen's surface one before and another after deformation. The images, then, are digitized and stored in a computer as digital images. To detect displacements, the two images are compared by searching a matched point from one image to another. Since finding of the matched point using a single pixel is impossible, an area containing multiple pixel points (e.g. 9 × 9 pixels) is used to perform the matching process. This area is called subset, and has a unique light intensity

(gray level) distribution inside itself. This light intensity distribution is assumed to remain unchanged during the deformation. Figure 3.21 shows a part of the digital images before and after deformation.

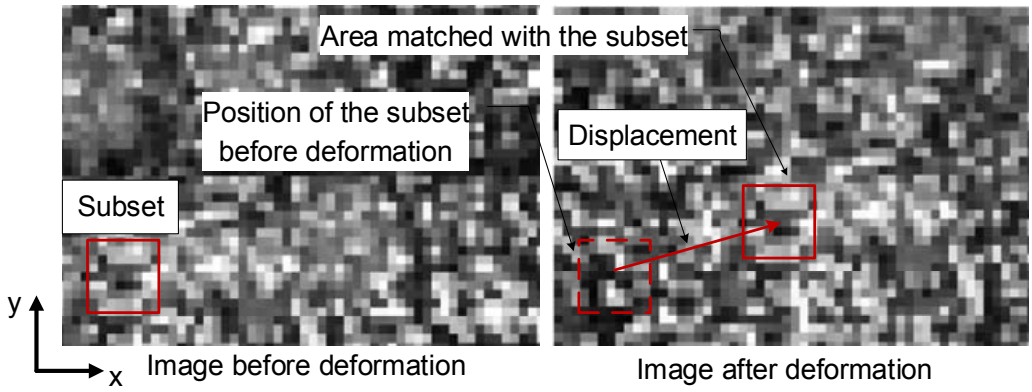

Figure 3.21 Matching the subset before and after deformation

After the specimen deforms, the new position of the subset on the deformed image can be recognized by finding an area with the same light intensity distribution as that of the subset on the undeformed image. Therefore, by knowing the locations of the subset before and after deformation, the associated displacement can be determined. Proceeding to this stage involves doing a particular treatment on the specimen surface, what in fact, raises contrast on the surface. This could be achieved by creating a random spackle pattern on the surface by stamping or spraying black paint dots on the white base. Figure 3.22 shows an example of the random pattern produced by stamping.

DIC equipment used in this experimental program consisted of: a pair of 5 mega pixels CCD cameras (no internal moving parts) to capture frequent shots at desired intervals from specimens' surface where having the full field deformation is in need (region of interest) while load is increasing; a data acquisition controller that triggers cameras to take pictures, synchronizes with test machines, and records analog-to-digital signals; and a high-speed computer with an installed DIC 3D software (ARAMIS) to process the data.

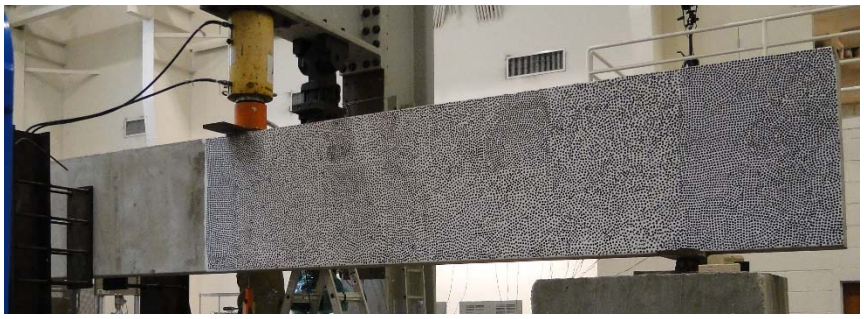

Figure 3.22 Spackle pattern created by stamping black paint dot on white base (specimen SFRC36b)

One side of each specimen across the targeted shear span facing toward the cameras (ROI) was spackled by either stamping black paint dots or spraying can on a white base. It was essential that each black dot contained at least 3 to 5 pixels in order for the DIC software to process the strain data with sufficient accuracy. Therefore, larger size specimens, with the same camera (five mega pixel camera), would require larger black dots in order to contain the required number of larger pixels.

Specimens were loaded by a concentrated force at mid-span. For the RC beams, however, the load was applied at one third of the span length (Figure 3.3c). In each test, the beam was initially loaded until the first visible flexural crack surfaced. Then, loads were monotonically increased and paused at a few loadings to trace the cracks and take photos. The process continued until failure. For safety purposes, lateral supports were provided for specimens with depths of 36 in. (915 mm) and 48 in. (1220 mm). The lateral supports were not in contact with the specimen surface. A typical photo of lateral support bracing SFRC36b is indicated in Figure 3.23. It is noteworthy that testing was carried out 502 to 1005 days after casting. The specimens were exposed to weather during this period.

Figure 3.23 A typical photo of lateral support bracing SFRC36b

3.5Material Testing and Properties

3.5.1 SFRC flexural strength

The flexural performance of SFRC mixes used in this research study was determined in accordance with ASTM C1609 (2012) *("Standard Test Method for Flexural Performance of Fiber-Reinforced Concrete (Using Beam with Third-Point Loading").* The specimens had dimensions of 20x6x6 inches. Since at each end of the specimens, the support was located 1 inch apart from that end, the specimens had a span length of 18 inches. Figure 3.24 clearly depicts the third-point loading test setup. The test was a displacement-control test, where the loading was performed in form of displacement with a rate of 0.002 in./min. The mid-span deflection of the specimens was measured through a pair of LVDTs. The tests proceeded until the mid-span deflection reached 0.12 in. as it was 1/150 of the span length. Since the results from the tests were intended to reflect the flexural performance of SFRC, failure was required to be induced by pure flexure rather than any other forces. For this reason, crack location needed to fall in the 6 in. middle region, where the bending moment was invariable due to zero shear. Third-point loading test setup is illustrated in Figure 3.24.

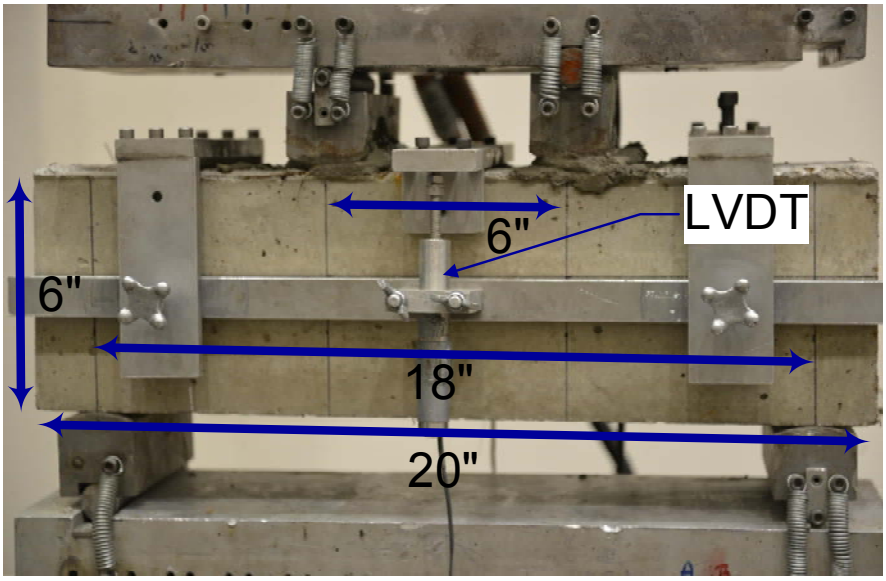

Figure 3.24 ASTM C1609 test setup

The two typical load versus mid-span deflection relationships for a SFRC specimen under third-point loading test are schematically presented in Figure 3.25 in conjunction with the key parameters defined by ASTM C1609 (2012) for SFRC flexural assessment. In both cases, the specimen exhibits linear - elastic behavior up to the first flexural cracking which mostly causes a sudden drop in the applied load. After this point, the major difference between the two cases arises. For the first one as depicted in Figure 3.25a, the dropping in the load progresses in a very low and steady rate up to the end of the test. However, for the latter (Figure 3.25b), the specimen experiences some deflection hardening such that the load rises to some extent and after reaching a peak, starts descending in nearly the same way as explained for the former. The first peak load (P_1) corresponds to the first point at which the load-deflection curve has a zero slope. Similarly, the peak load (P_p) is the largest load on the load-deflection curve. For the load-deflection curve shown in Figure 3.25a, P_1 and P_p lies at the same point.

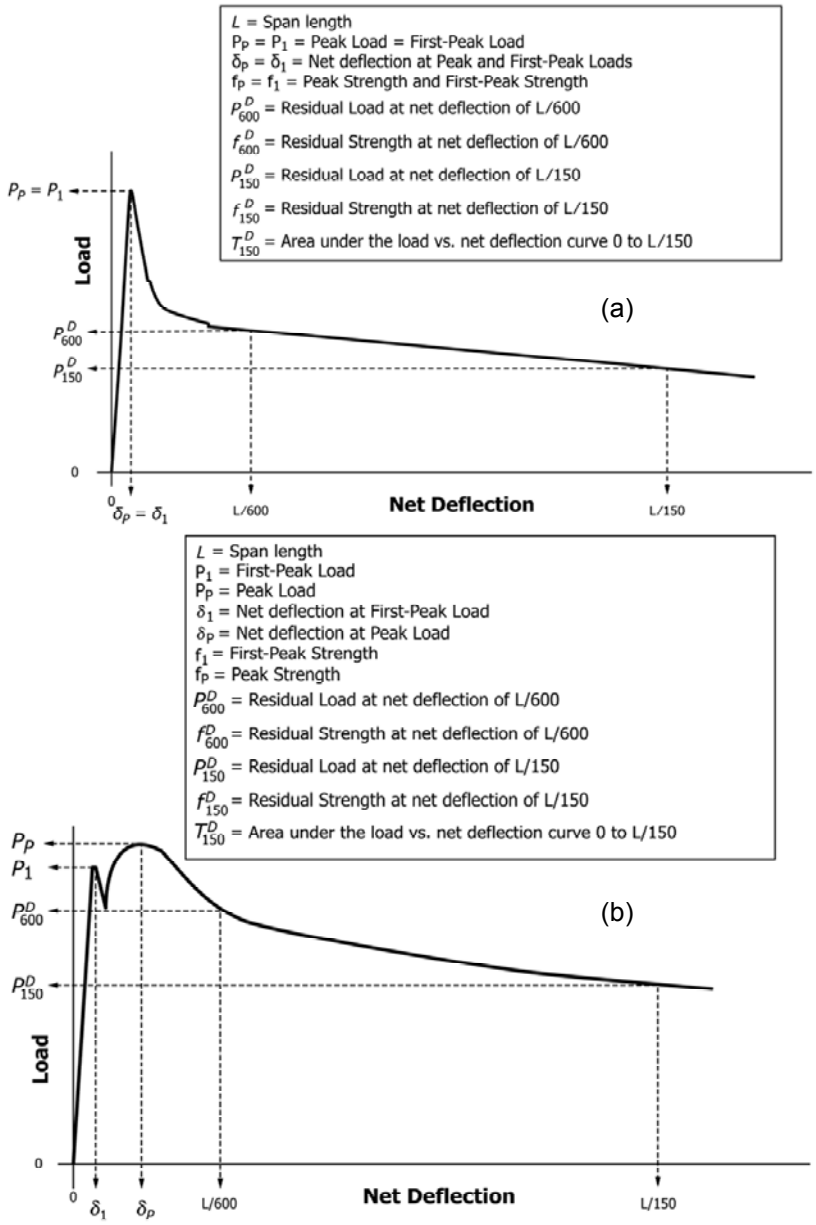

Figure 3.25 Typical load versus mid-span deflection relationships for a SFRC specimen under third-point loading test; (a) the first peak load matching the peak load; (b) the first peak load is lower than the peak load (ASTM C1609, 2012)

Load–deflection curves for the SFRC specimens sampled from the SFRC batches applied in casting of 24 in. and higher specimens are shown in Figure 3.26. Likewise, the flexural

test results for the SFRC mix used to cast the specimens with overall depth less than 24 in. are plotted in Figure 3.27.

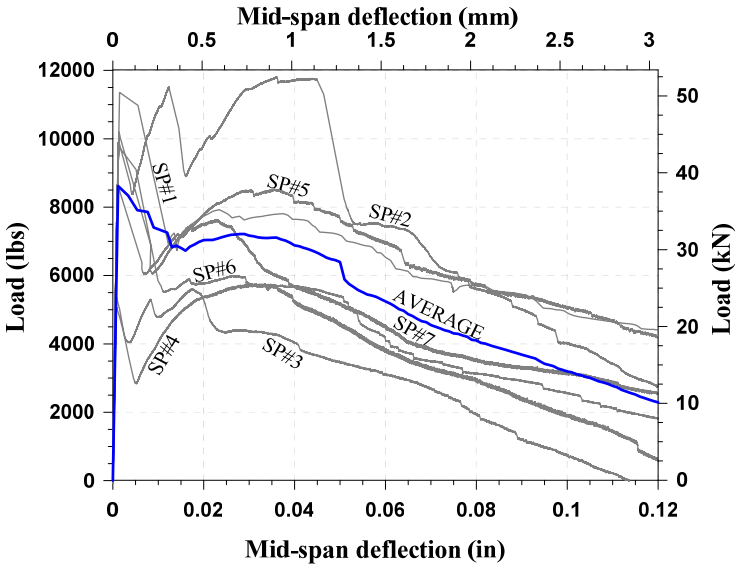

Figure 3.26 SFRC flexural test results (sampled at Hanson Pipe & Precast Plant)

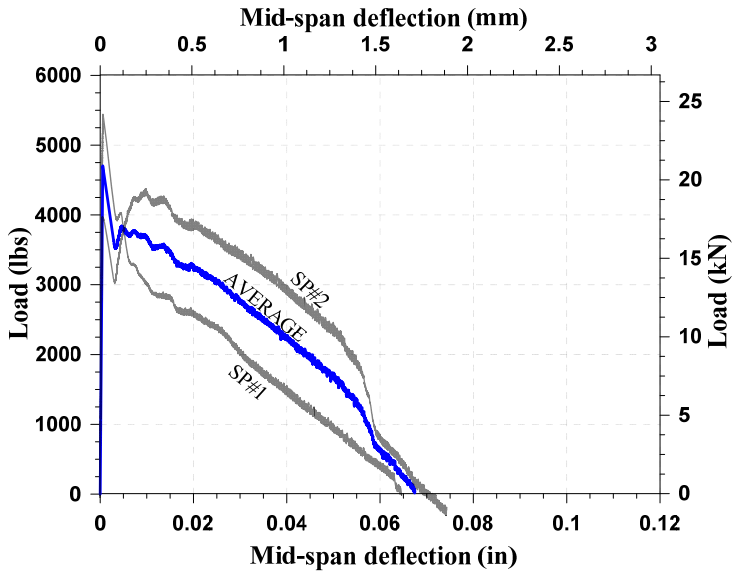

Figure 3.27 SFRC flexural test results (sampled at CELB)

The load values at some of the key deflections were pulled out of each plotted curves and summarized in Table 3.6.

Table 3.6 Summary of ASTM C1609 Test: Load at various deflection

Mix	Specimen	First-Peak Load, P_1	Peak Load, P_p	Load at 0.03 in. (L/600)[1] Deflection	Load at 0.06 in. (L/300) Deflection	Load at 0.12 in. (L/150) Deflection
CELB	#1	5442	5442	2000	350	N.A
	#2	3976	4376	3510	854	N.A
	Mean	6209	4909	2755	602	N.A
	Standard Deviation	3158	754	1068	356	N.A
	Coefficient of Variation	50.9%	15.4%	38.8%	59.1%	N.A
Hanson Pipe & Precast Plant	#1	11354	7926	7654	6662	4410
	#2	9920	11802	11454	7432	2746
	#3	5362	5604	4374	3122	N.A
	#4	5048	5756	5704	3828	574
	#5	8666	8522	8488	7002	4216
	#6	9798	5994	5760	4182	1816
	#7	10192	7634	6734	4526	2560
	Mean	8620	7605	7167	5251	2720
	Standard Deviation	2463	2182	2326	1733	1452
	Coefficient of Variation	28.6%	28.7%	32.5%	33%	53.4%

[1] L is the span length (18 in.). Unit for the load: lbf. [1.0 lbf = 4.448 N; 1 in. = 25.4 mm]

At this point, the following question arose: if the consumed SFRC mixes had qualified for being used as shear reinforcement in compliance with ACI requirements? Section 26.12.5.1 of ACI 318 (2014) states that steel fiber reinforced concrete shall be considered acceptable for shear resistance if the following two criteria from ASTM C1609 are satisfied (Figure 3.28):

(1) The residual strength obtained from flexural testing in accordance with ASTM C1609 at a mid-span deflection of 1/300 of the span length is greater than or equal to 90 percent of the measured first-peak strength obtained from a flexural test or 90 percent of the strength corresponding to f_r from Equation (3.1), whichever is larger:

$$f_r = 7.5\sqrt{f_c'} \qquad (Modulus\ of\ Rupture) \qquad f_c'\ in\ psi \tag{3.1}$$

(2) The residual strength obtained from flexural testing in accordance with ASTM C1609 at a mid-span deflection of 1/150 of the span length is greater than or equal to 75 percent of the measured first-peak strength obtained from a flexural test or 75 percent of the strength corresponding to f_r from Equation (3.1), whichever is larger.

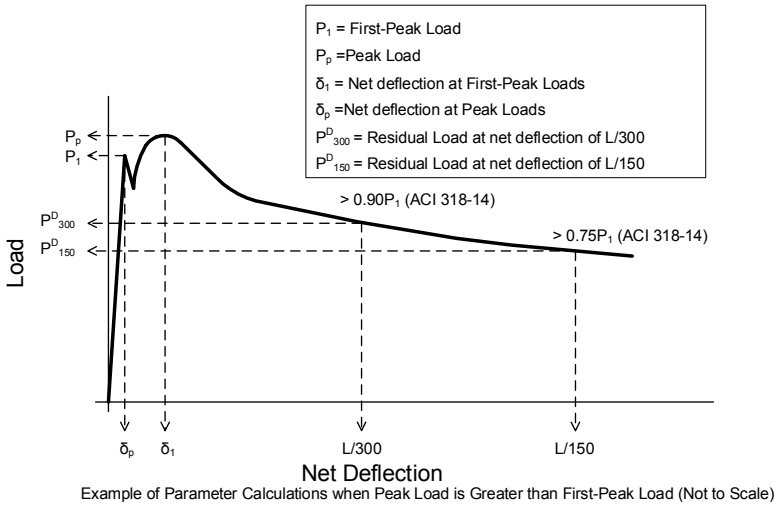

Figure 3.28 Shear performance criteria of SFRC under ASTM C1609 test required by ACI 318 (2014)

The first and second ACI performance criteria were examined for the SFRC specimens and shown in Table 3.7 and Note: [1] Pr=fr.bh2/L, b=h=6 in., L=18 in., Unit for the load: lbf. [1.0 lbf = 4.448 N; 1 in. = 25.4 mm]

Table 3.8, respectively. The data clearly indicates that none of the specimens met the two ACI criteria, and therefore this SFRC mix could not be used to replace conventional shear reinforcement. However, as demonstrated in the next chapter, the large-scale SFRC beams tested in this program showed a significantly improved shear performance in terms of ultimate shear strength and ductility (deflection at failure) as a result to fiber addition.

Table 3.7 Summary of ASTM C1609 Tests: ACI requirement comparison-I

Mix	Specimen	90% P_r[1]	90% of the first peak load	Maximum (90% P_r, 90% P_1)	Load at 0.06 in. (L/300) Deflection	Difference	Note
CELB	#1	6119	4898	6119	350 (5.7%)	-5769	Not pass
	#2	6119	3578	6119	854 (14.0%)	-5265	Not pass
Hanson Pipe & Precast Plant	#1	6878	10218	10218	6662 (65.2%)	-3556	Not pass
	#2	6878	8928	8928	7432 (83.24%)	-1496	Not pass
	#3	6878	4826	6878	3122 (45.4%)	-3756	Not pass
	#4	6878	4544	6878	3828 (55.7%)	-3050	Not pass
	#5	6878	7800	7800	7002 (89.8%)	-798	Not pass
	#6	6878	8818	8818	4182 (47.4%)	-4636	Not pass
	#7	6878	9160	9160	4526 (49.4%)	-4634	Not pass

Note: [1] $P_r=f_r.bh^2/L$, b=h=6 in., L=18 in., Unit for the load: lbf. [1.0 lbf = 4.448 N; 1 in. = 25.4 mm]

Table 3.8 Summary of ASTM C1609 Test: ACI requirement comparison-II

Mix	Specimen	75% P_r[1]	75% of the first peak load	Maximum (75% P_r, 75% P_1)	Load at 0.12 in. (L/150) Deflection	Difference	Note
CELB	#1	5099	4082	5099	N.A	N.A	Not pass
	#2	5099	2982	5099	N.A	N.A	Not pass
Hanson Pipe & Precast Plant	#1	5731	8516	8516	4410 (51.8%)	-4106	Not pass
	#2	5731	7440	7440	2746 (36.9%)	-4694	Not pass
	#3	5731	4022	5731	N.A	N.A	Not pass
	#4	5731	3786	5731	574 (10.0%)	-5157	Not pass
	#5	5731	6500	6500	4216 (64.9%)	-2284	Not pass
	#6	5731	7348	7348	1816 (24.7%)	-5532	Not pass
	#7	5731	7644	7644	2560 (33.5%)	-5084	Not pass

Note: [1] $P_r=f_r.bh^2/L$, b=h=6 in., L=18 in., Unit for the load: lbf. [1.0 lbf = 4.448 N; 1 in. = 25.4 mm]

3.5.2 SFRC compressive strength

To examine the solo effect of depth on shear strength of SFRC beams, all the parameters affecting shear resistance with the exception of depth must be considered consistent among the beams. However, the only factor which an individual has a limited control on its variations among the beams is concrete/SFRC compressive strength (f'_c) despite the same assigned mix design. For this reason, knowing the exact amount of SFRC/concrete compressive strength at the time of beam testing is necessary. By this way, the effect of concrete compressive strength can be taken out of the shear strength assessment by normalizing the test-obtained shear strength values by $\sqrt{f'_c}$. To this end, a total of three 4×8 in. cylinders was sampled for each pair of beams at the time of the casting, removed from the mold after one day, and held in curing room up to the beam test date. To break the samples, the top and bottom faces were first capped using a sulfur compound. Figure 3.29 briefly represents the capping process before testing of cylinders.

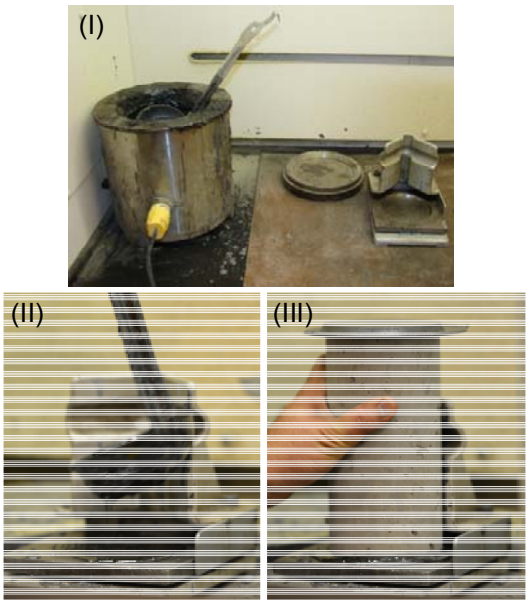

Figure 3.29 Capping setup and process

Generally, this action induces the breakage of concrete cylinders by pure compression as well as the compressive force uniformly applied on the surface.

The cylinder test was conducted in accordance with ASTM C39 / C39M (2012), “Standard Test Method for Compressive Strength of Cylindrical Concrete Specimens.” The average SFRC/concrete compressive strength for all tested specimens was presented in Table 1.1. The compression test machine and setup as well as a photo of the typical crushing of SFRC are depicted in Figure 3.30.

(a) (b)

Figure 3.30 (a) the compression test machine and setup; (b) typical crushing of SFRC cylinder

To quantify the shear capacity and contributing percentage of compression zone for each tested SFRC beam, the magnitude and distribution of horizontal compressive stresses developed across the failure path in compression zone were in a need for evaluation at the failure (the procedure will be detailed in Chapter 5). Since the required data collected by DIC system were in the form of strains, to find the corresponding stresses, an SFRC average stress-strain relationship was obtained by testing of a few SFRC cylinders through 100 kips MTS machine. To capture the peak and softening branch of the

stress-strain curve for each specimen, the loading was controlled by displacement with a rate of 0.002 in/min. The strains of the cylinders were also measured by the DIC system. A photo of the compression test setup using 100 kips MTS and DIC cameras are displayed in Figure 3.31.

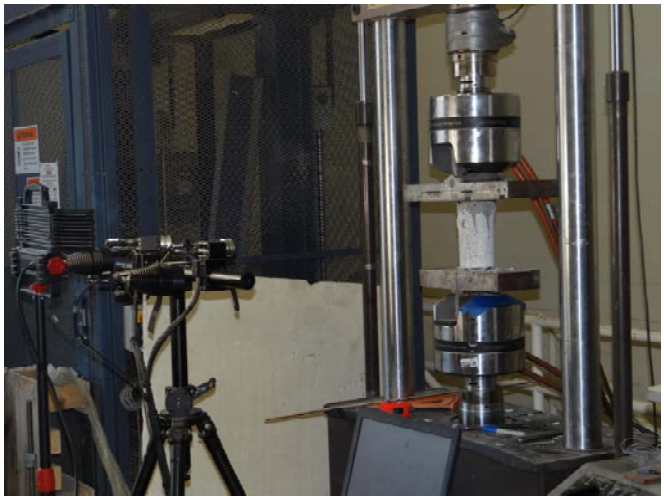

Figure 3.31 A photo of compression test setup using 100 kips MTS and DIC cameras

To reach a completely smooth surface at each end of the cylinders, the specimens were cut for 0.5 in. from the top and bottom through a concrete saw. Also, to minimize the possible shear force generated due to the interface friction between the setup and the end faces of the specimens, friction grease was adequately rubbed on the end surfaces. In some previous pilot tests, it was observed that even though the compressive strains at the specimen mid-height were still very small even in elastic range, the specimens failed resulting from the early crushing at the ends. Nevertheless, after eliminating the capping compound and applying all those aforementioned treatments, the problem seemed thoroughly resolved. Figure 3.32 clearly distinguishes the crushing in a capped SFRC specimen from a treated one. The resulted average stress-strain correlation is illustrated in Figure 3.33.

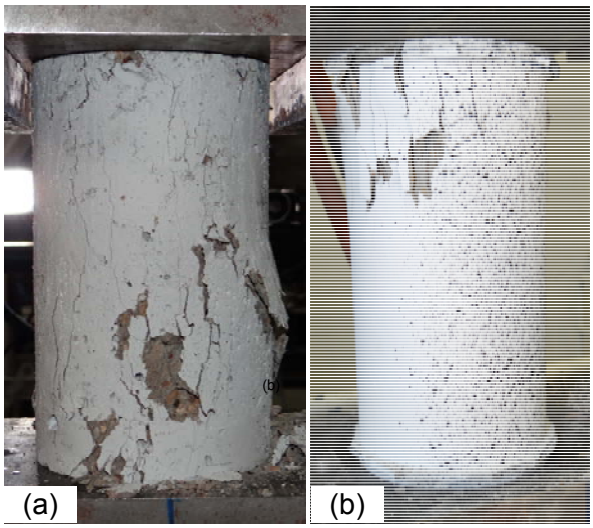

Figure 3.32 (a) Typical crushing in treated SFRC cylinders; (b) Crushing in regular SFRC cylinders

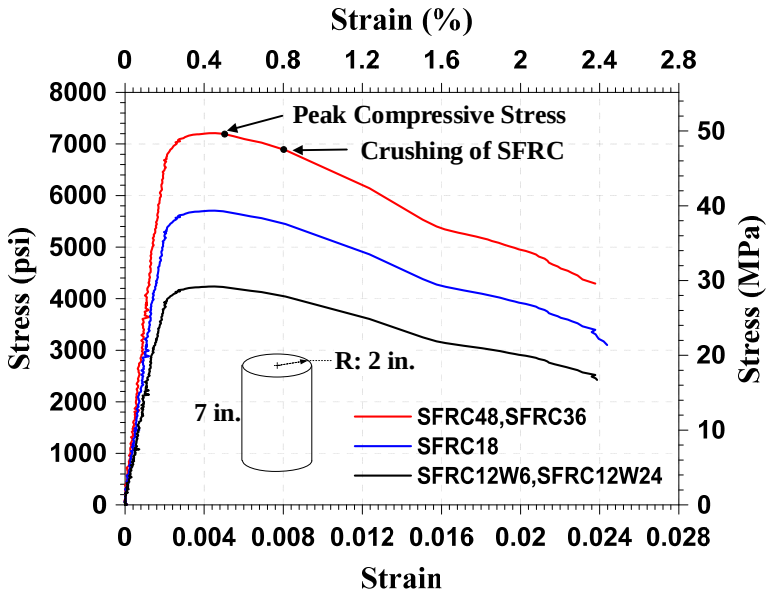

Figure 3.33 The average stress-strain relationships for the sampled SFRC cylinders

3.5.3 SFRC direct tensile test

To quantify tension in the steel fibers bridging the critical crack at the failure of SFRC beams and accordingly the proportion of shear force resisted by them, the post cracking tensile stress distribution is to be determined all the way through the critical crack

in tension zone (elaborated in Chapter 5). To address this issue, the post-cracking tensile strength of SFRC was obtained as a function of crack width by testing a few SFRC dog-bone shape specimens under direct tensile test. The dog-bone shape specimen mold and direct tensile test setup are shown in Figure 3.34.

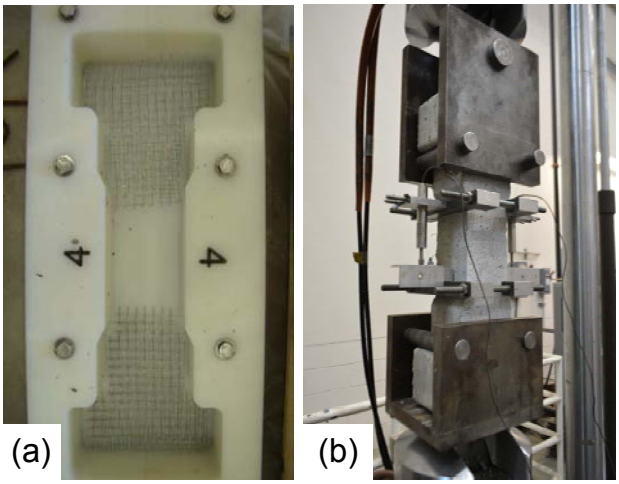

Figure 3.34 (a) dog-bone shape specimen mold; (b) direct tensile test setup

The dog-bone specimens were loaded in tension by 100 kips MTS testing machine. The tensile displacement in the specimen gage length was measure using a pair of LVDTs. In addition, after cracking, the width of crack was measured by DIC system (Figure 3.35). The variation of tensile stress for two SFRC tensile specimens under direct tensile test is plotted with respect to crack width and strain in Figure 3.36 as well as their average curves.

Figure 3.35 DIC system measuring the width of crack for dog-bone shape specimen

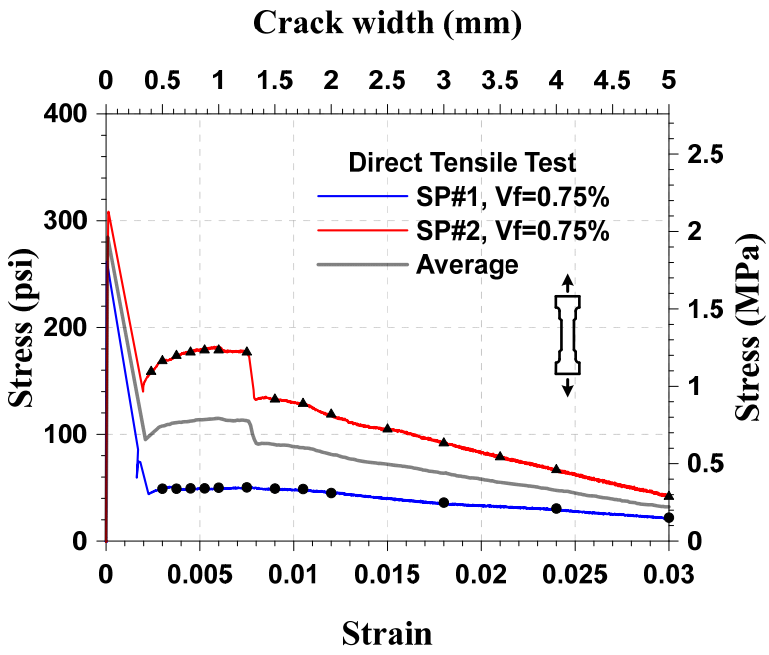

Figure 3.36 SFRC responses to direct tensile test

Chapter 4

EXPRIMENTAL RESULTS-LARGE SCALE BEAMS

4.1 General

In this chapter, the behavior of each large scale beam (10 SFRC and 2 PC beams) is separately examined in terms of cracking pattern, failure mode, load-deflection response, load-steel strain relationship, distribution and magnitude of different strain components developed on specimen surface, and the maximum width of critical crack. The test results including ultimate load (P_u), ultimate shear force (V_u), average shear stress at failure (v_u), shear strength normalized by $\sqrt{f'_c}$, the first observed shear cracking load (V_{cr}), first shear crack strength (v_{cr}), and the maximum critical crack width at peak load (C_w) for all specimens are summarized in Table 4.1.

4.1Behavior of the Test Plain Concrete Beams with no Transvers Reinforcement (Stirrup)

A pair of plain concrete (PC) beams with a height of 18 in. was constructed and experimented for a comparison purpose with the geometrically identical SFRC beams. As pointed out in the preceding chapter, all primary shear parameters were held constant for all the specimens.

4.1.1 Beam RC18a

4.1.1.1 Load-deflection relationship, crack pattern, and failure mode

Load-deflection curve and crack pattern at various load stages for beam RC18a are plotted in Figure 4.1 and Figure 4.2, respectively. The first visible flexural crack initiated at 20 kips from the bottom surface of the beam in the region under the loading point, where the maximum bending moment generally develops. At this load, in contrast to the typical behavior of PC beams, no sudden drop in load or change in the curve slope was observed (Figure 4.1). This could be due the fact that the reinforcement ratio in the PC beams was required to match up the higher amount of reinforcements used in the SFRC beams to

avoid flexural failure. Therefore, at the occurrence of the first flexural crack, the initial stiffness of the beam was well maintained.

By increasing the applied load, flexural cracks started developing along the shear span toward the support. At load about 35 kips (corresponding to shear load 13 kips), a non-linear behavior with gradually decreasing slope was noticed in the load-deflection curve, as it continued up to failure. For this reason, the load was inferred to be the beginning of shear crack development. This was also confirmed by checking the full-field maximum principal strains measured by DIC system. The first inclined crack was flexural-shear crack that became visible at the distance of 1.34d away from the loading point (Figure 4.2). “d” is effective depth, and the distance was measured at the beam mid-height level. At load 50 kips (shear force of 18.1 kips), the beam developed the second flexure-shear crack. However, instantly after 1 kips increase in the external load (at 51 kips corresponding to shear force 19 kips), the shear crack significantly and in a sudden movement, advanced and extended back toward the loading point and level of longitudinal bars, respectively, thereby resulting in an abrupt drop in the applied load by nearly 12 kips. The critical crack position at the middle of the beam depth was 1.77d away from the loading point. Figure 4.3 depicts cracking pattern for beam RC18a right after the peak load and failure. As viewed on Figure 4.1, after the pick load drop at point D, the beam gained some strength up to point E. Eventually, the fully extension of the critical crack to the edge of concrete in compression zone at the face of bearing plate led to failure (Figure 4.3b). The mode of failure was recognized as diagonal-tension failure, as displayed in Figure 4.3b and clearly identified through the DIC image processed for major strain in Figure 4.19, where the significant opening of critical crack at nearly middle depth triggered the peak load dropping. The residual strength after the peak load drop is suggested to be potentially induced by compressive confinement developed in the vicinity of the loading point.

4.1.1.2 Strain in longitudinal rebars

Figure 4.4 shows load versus average strain response for each pair of strain gages mounted on longitudinal rebars at the points under the applied load and mid-shear span, respectively. As noticed, both curves followed the same trend. The strains in rebars at these locations, was initially observed to linearly vary as the external load increases. However, the initiation of adjacent flexural crack to each strain gauge caused an abrupt strain increment in the corresponding load-strain curve.

The first sudden change in the load-strain response recorded at the point under the external load represents that the first flexural crack occurred at about 11 kips. However, the crack was likely such tiny that was not recognizable with bare eyes. Likewise, after the strain gauges located at the mid-shear span implied the formation of a flexural crack in their vicinity, the strains at both locations seemed to ascend with the same rate until the first inclined cracking load (35 kips). Beyond this load, the mid-shear span gauges exhibited higher strains for the same amount of increase in the applied load. This arose from the fact that the first shear cracks appeared in a close distance to the mid-shear span gauges and locally influenced the measured strains. As clearly indicated by Figure 4.4, none of the reinforcement rebars yielded by the time of failure.

4.1.1.3 Full-field visualization of strain components developed on the shear span concrete surface

As discussed in the previous chapter, full-filed strain components developed on concrete surface throughout shear span for specimen RC18a were captured with the aid of DIC technology at different load values and illustrated in Figure 4.5 through Figure 4.24. For better evaluation of the relationship between cracking pattern and the state of developed stresses acquired by DIC system, the cracks on the other side of the beam at each desired load were integrated into the corresponding DIC processed images.

The significance of longitudinal compressive strain distribution in recognition of neutral axis, the depth and extension of compression zone along shear span, and consequently shear behavior of the specimens, prompted the author to alter the displaying scale of compressive strain ranges. Through this strategy, various small ranges of compressive strain values were distinguishable by different colors from yellow to dark blue. On the other hand, since in the tension zone, the tensile strain magnitudes are generally misrepresented by crack opening, only knowing the points subjected to tension seemed to be quite enough rather than their strain quantities. Hence, tension was solo denoted by red color regardless of the magnitude. Furthermore, for the comparison purpose of compressive strains at different loads and among all specimens, the total range of strain was fixed from -0.129% to 0.020%. The scaled full-field concrete longitudinal strain (ε_x) distributions across shear span at different loads for specimen RC18a were visualized from Figure 4.25 to Figure 4.29.

Table 4.1 Test results

Specimen	(P_u) *kips*	(V_u) *kips*	(v_u) *psi*	($v_u/\sqrt{f'_c}$) $\sqrt{psi}$	(V_{cr}) *kips*	(v_{cr}) *psi*	(C_w)$^{\Im}$ *in.*
SFRC12W6	54	27	449.4	6.9	21	350.0	0.052
SFRC12W24	215	108	448.1	6.9	73	304.0	0.129
SFRC18a	73	36	389.7	5.2	23	241.9	0.054
SFRC18b	88	44	470.2	6.2	16	166.7	0.066
SFRC24a	120	60	352.3	4.2	40	234.7	0.060
SFRC24b	171	85	500.9	5.9	30	176.1	0.080
SFRC36a	307	154	479.6	5.7	40	125.0	0.080
SFRC36b	317	158	494.5	5.8	60	187.5	0.041
SFRC48a	470	235	445.1	5.2	80	151.5	0.077
SFRC48b	454	227	429.4	5.1	70	132.6	0.101
RC18a	51	19	198.5	2.7	13	139.8	0.001
RC18b	45	17	177.3	2.4	11	118.3	0.014

$\Im$: Maximum crack width at peak load

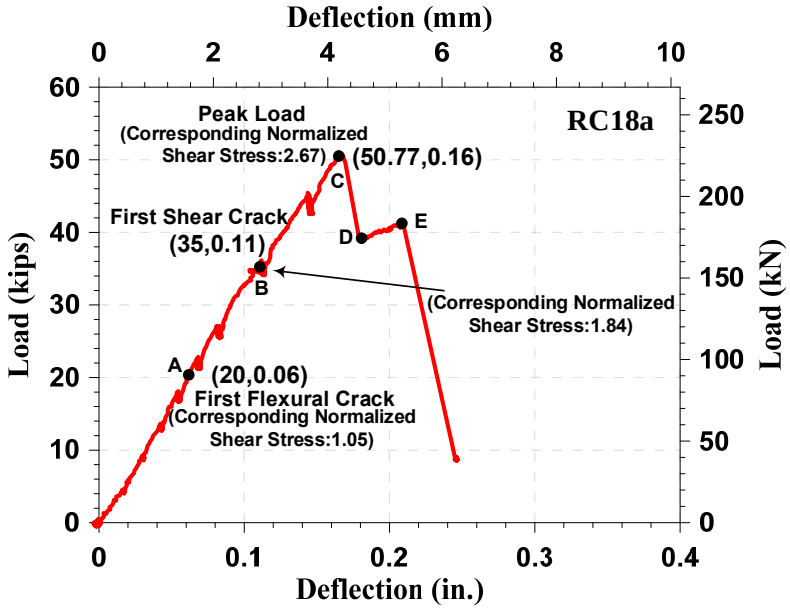

Figure 4.1 load-deflection response for beam RC18a

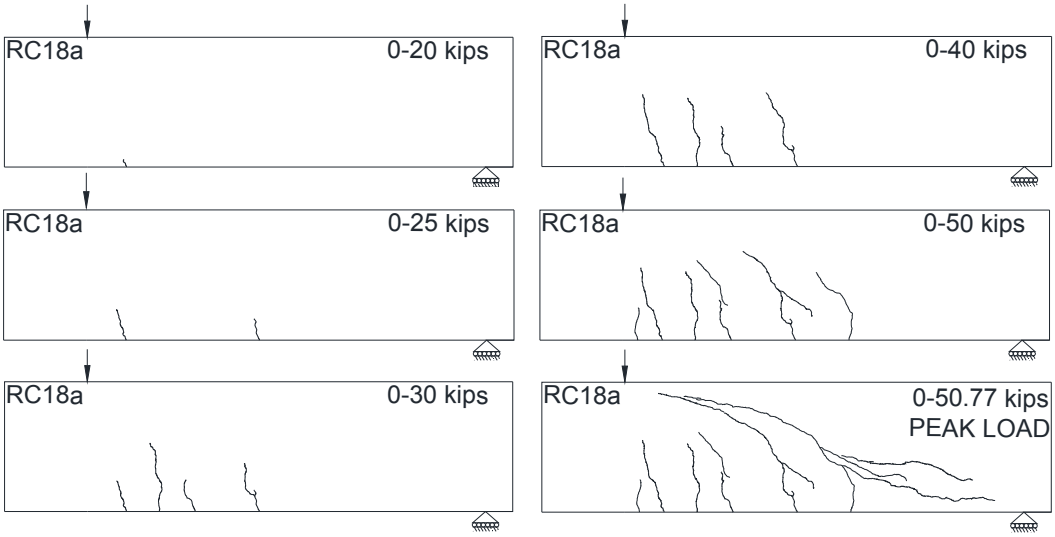

Figure 4.2 Cracking pattern for RC18a at different load stages

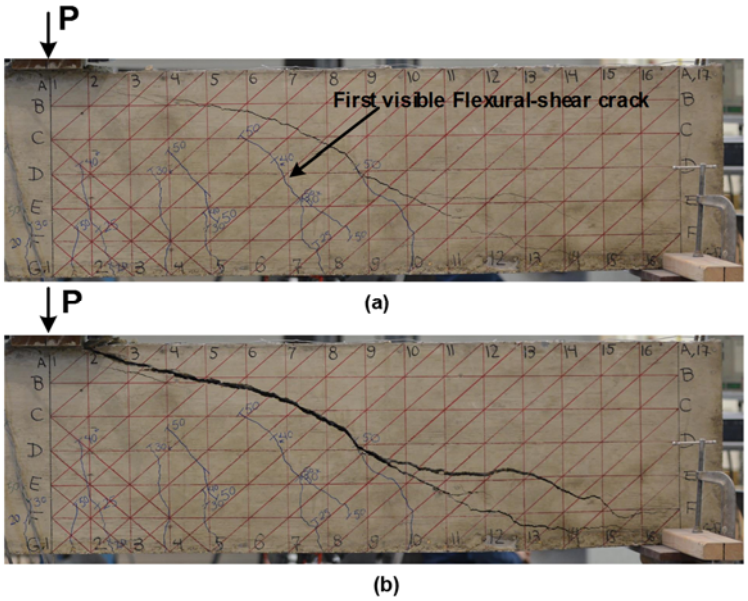

Figure 4.3 Cracking patter for beam RC18a at: (a) right after peak load; (b) failure

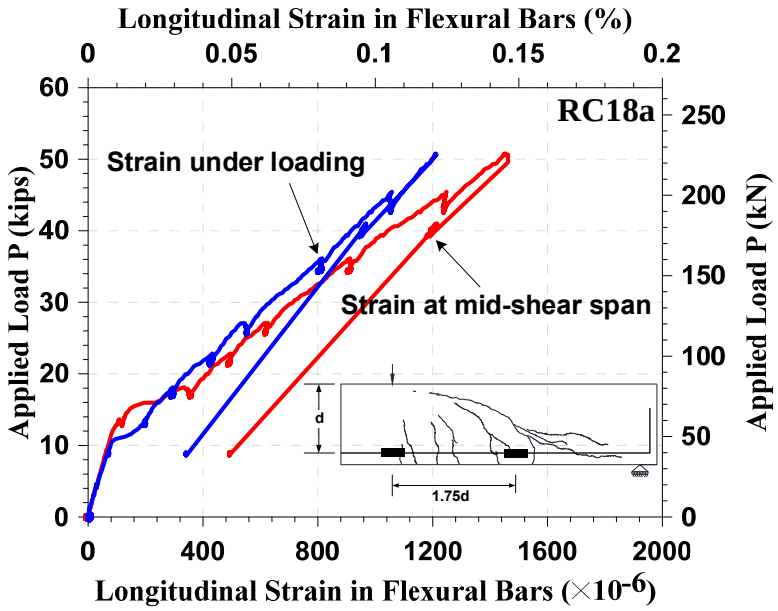

Figure 4.4 Load versus reinforcement strain relationships for beam RC18a

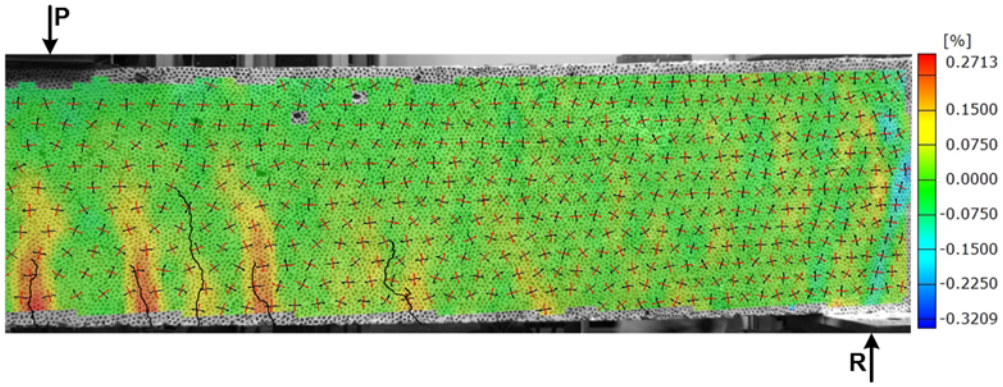

Figure 4.5 Full-field concrete longitudinal strain (ε_x) across shear span for specimen RC18a at load 35 kips

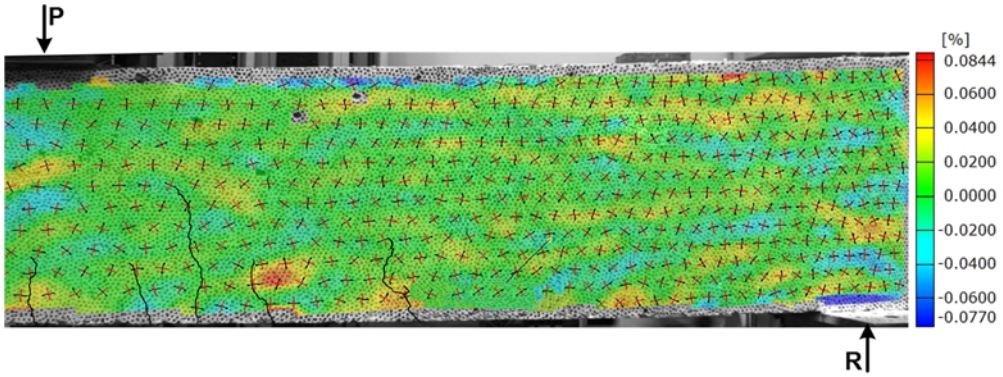

Figure 4.6 Full-field concrete transvers strain (ε_y) across shear span for specimen RC18a at load 35 kips

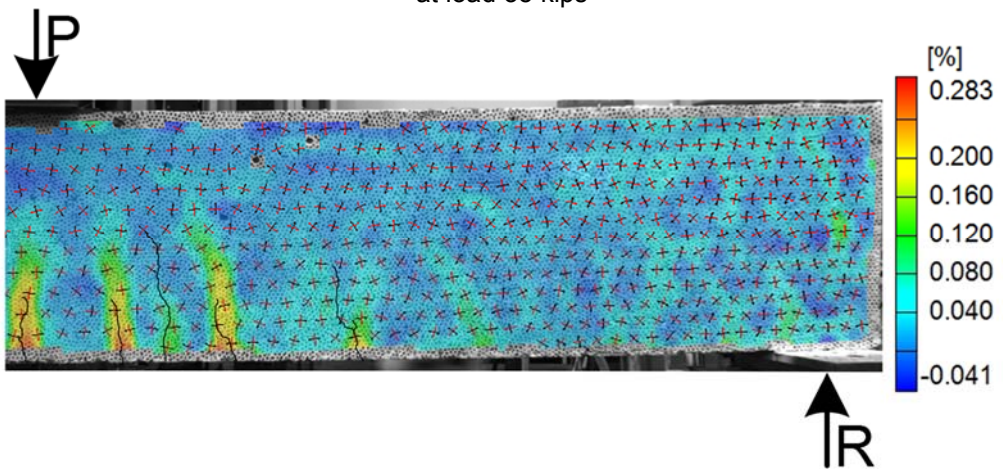

Figure 4.7 Full-field concrete maximum principal strain (σ_1) across shear span for specimen RC18a at load 35 kips

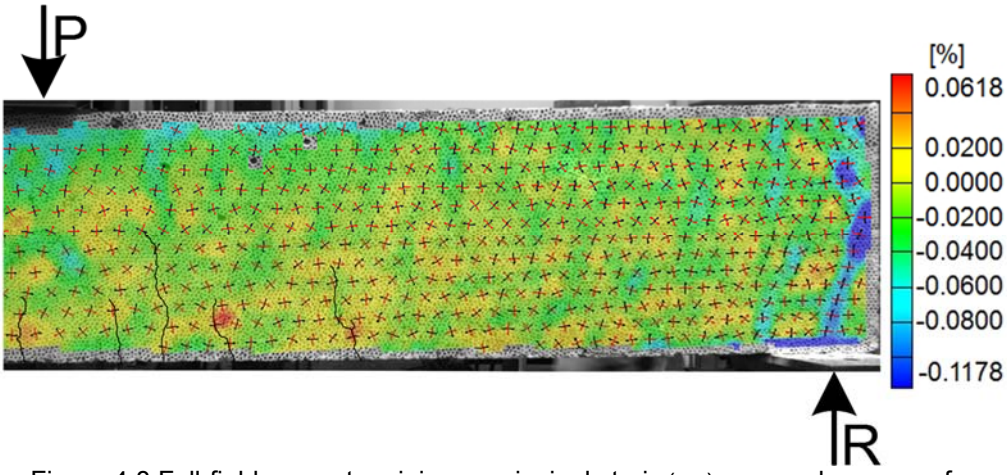

Figure 4.8 Full-field concrete minimum principal strain (σ_2) across shear span for specimen RC18a at load 35 kips

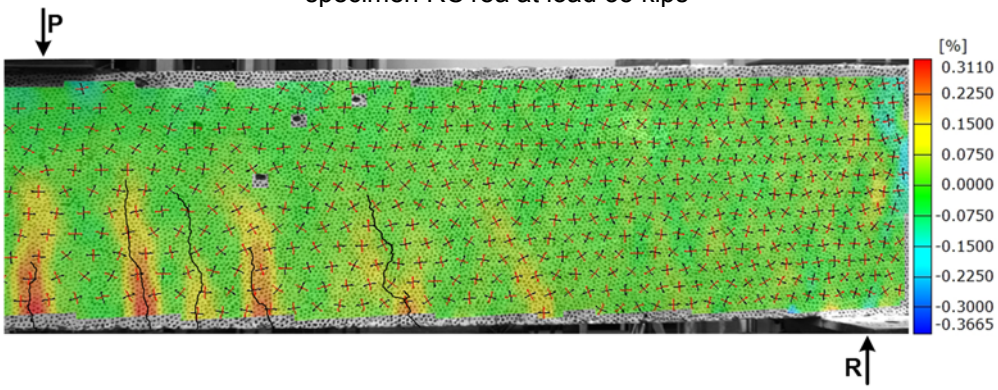

Figure 4.9 Full-field concrete longitudinal strain (ε_x) across shear span for specimen RC18a at load 40 kips

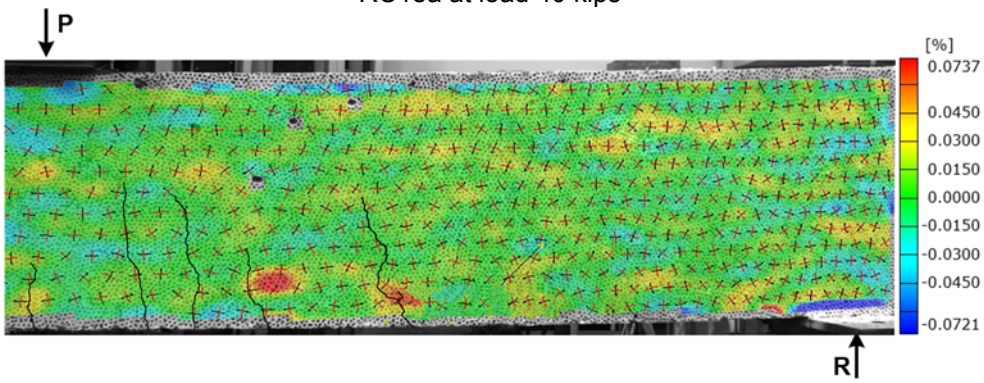

Figure 4.10 Full-field concrete transvers strain (ε_y) across shear span for specimen RC18a at load 40 kips

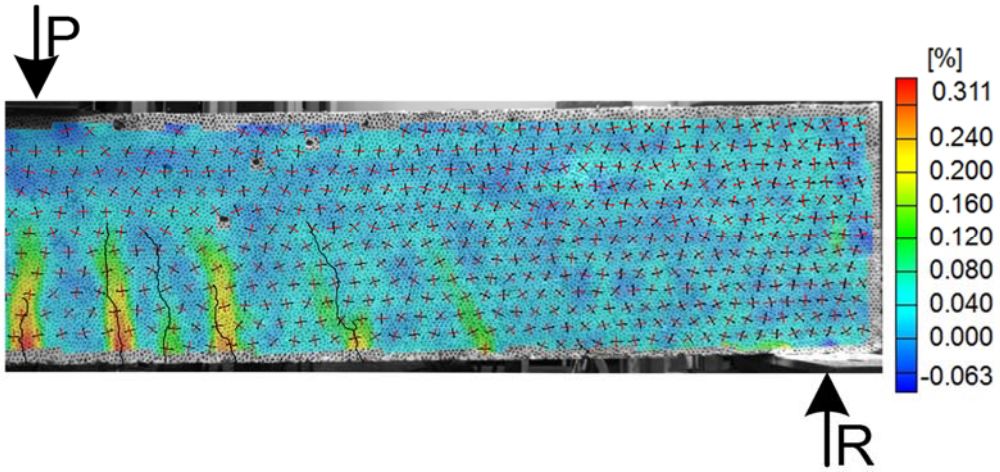

Figure 4.11 Full-field concrete maximum principal strain (σ_1) across shear span for specimen RC18a at load 40 kips

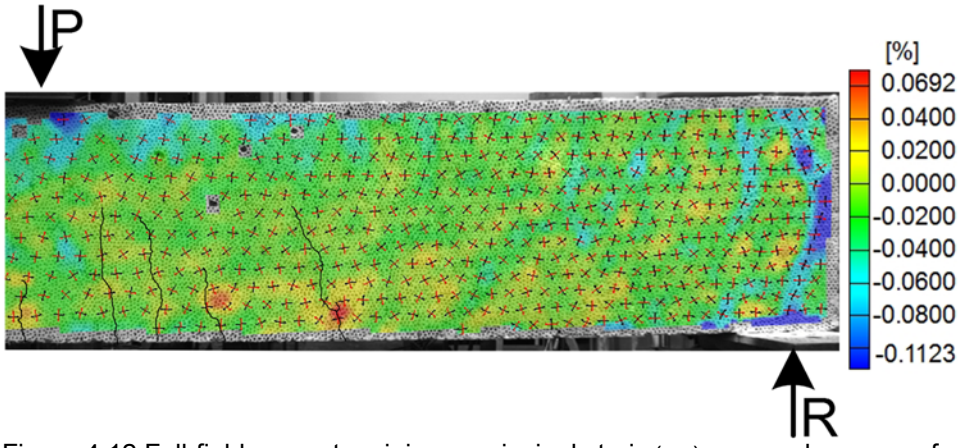

Figure 4.12 Full-field concrete minimum principal strain (σ_2) across shear span for specimen RC18a at load 40 kips

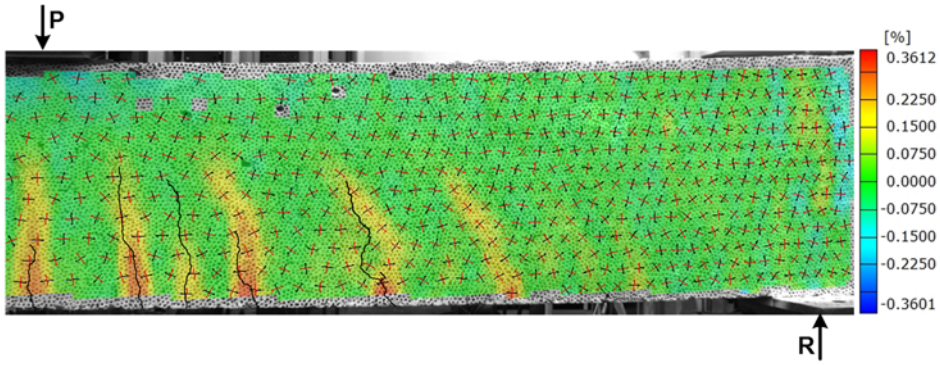

Figure 4.13 Full-field concrete longitudinal strain (ε_x) across shear span for specimen RC18a at load 45 kips

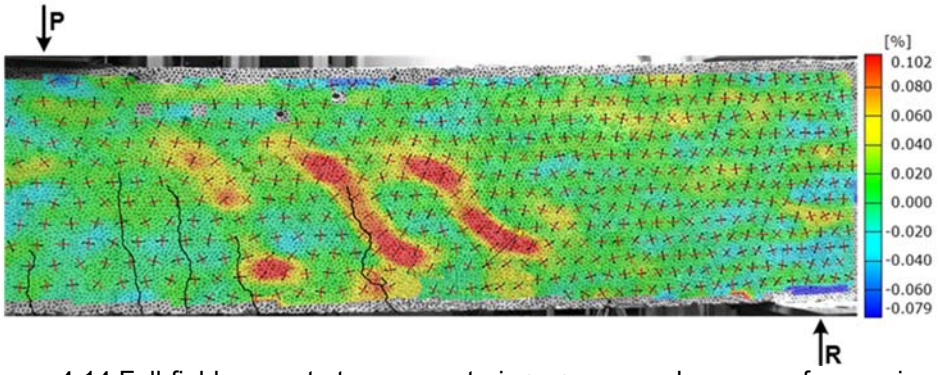

Figure 4.14 Full-field concrete transvers strain (ε_y) across shear span for specimen RC18a at load 45 kips

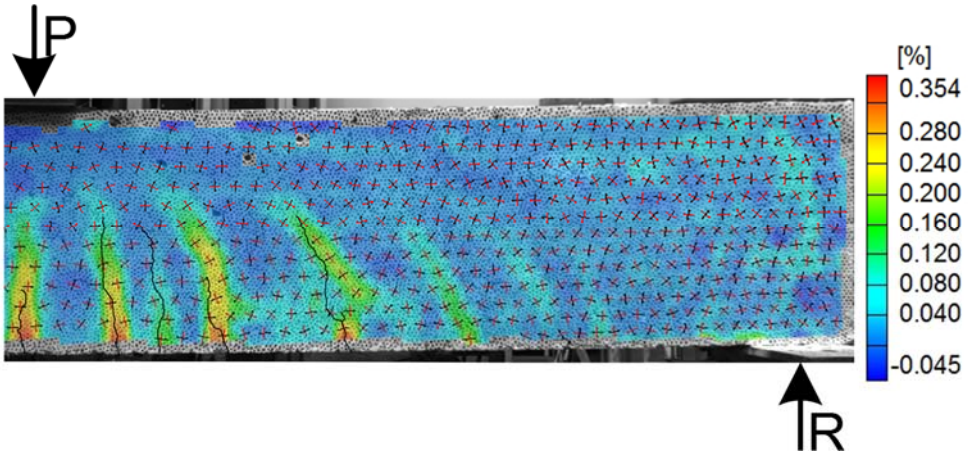

Figure 4.15 Full-field concrete maximum principal strain (σ_1) across shear span for specimen RC18a at load 45 kips

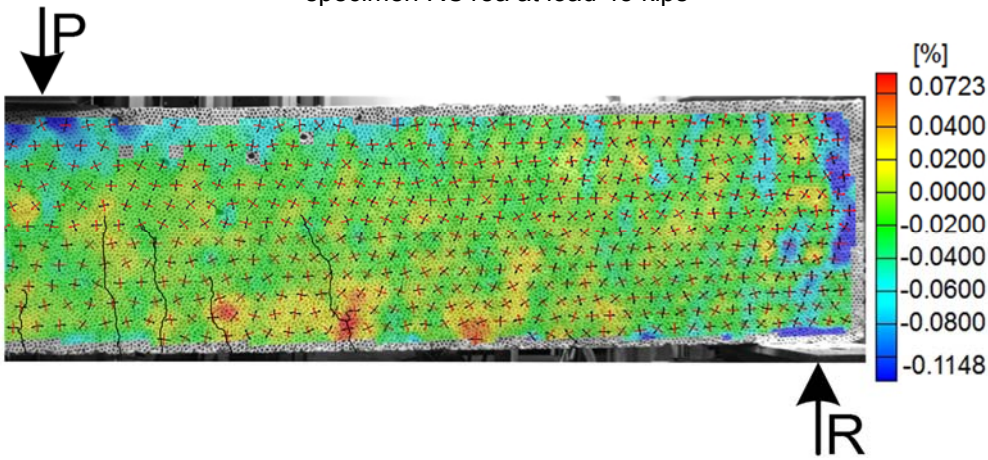

Figure 4.16 Full-field concrete minimum principal strain (σ_2) across shear span for specimen RC18a at load 45 kips

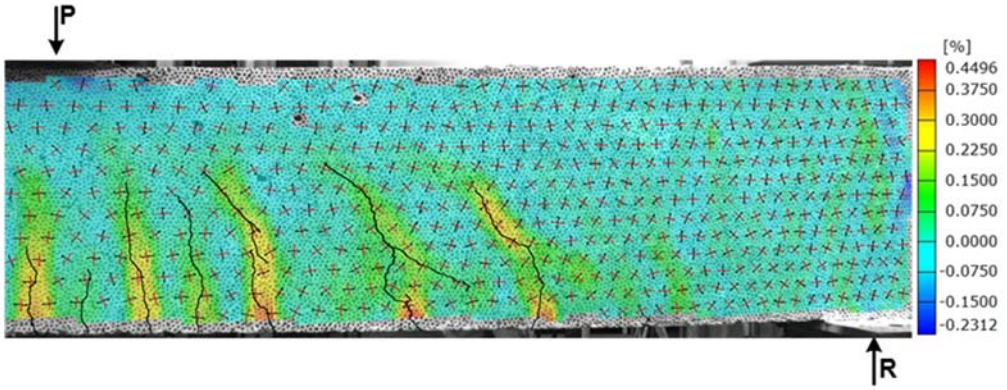

Figure 4.17 Full-field concrete longitudinal strain (ε_x) across shear span for specimen RC18a at load 50.77 kips (Peak load)

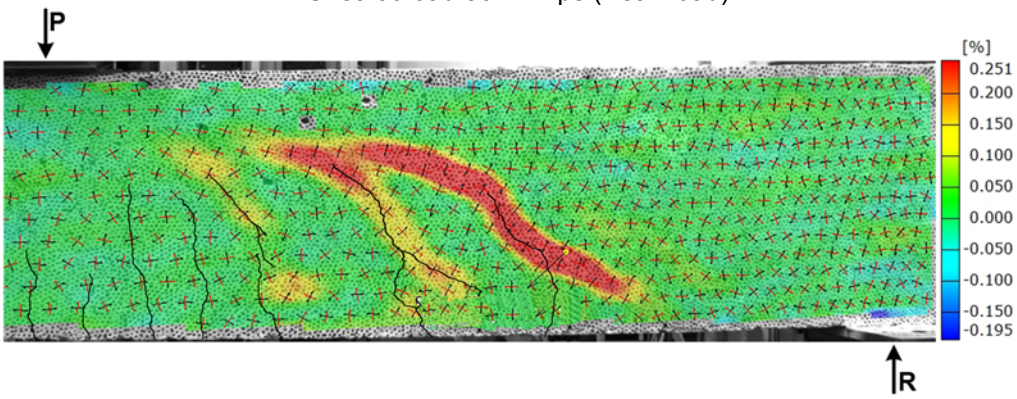

Figure 4.18 Full-field concrete transvers strain (ε_y) across shear span for specimen RC18a at load 50.77 kips (Peak load)

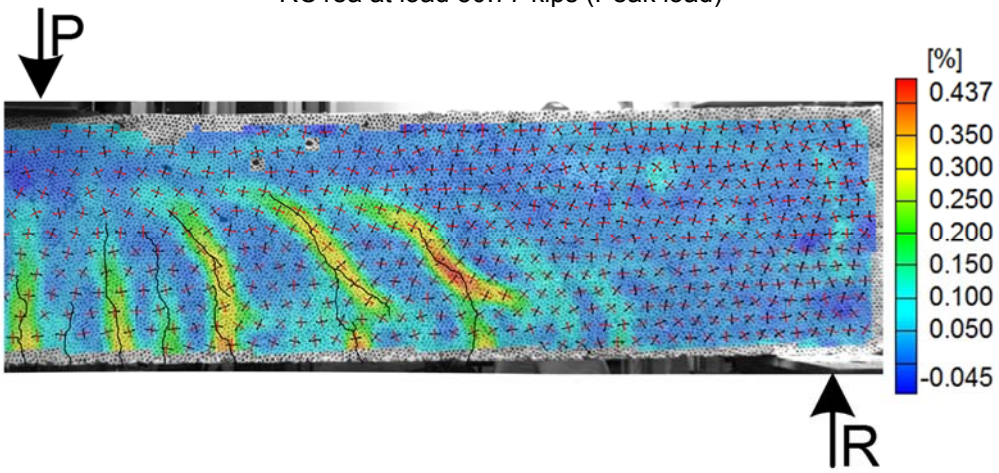

Figure 4.19 Full-field concrete maximum principal strain (σ_1) across shear span for specimen RC18a at load 50.77 kips (Peak Load)

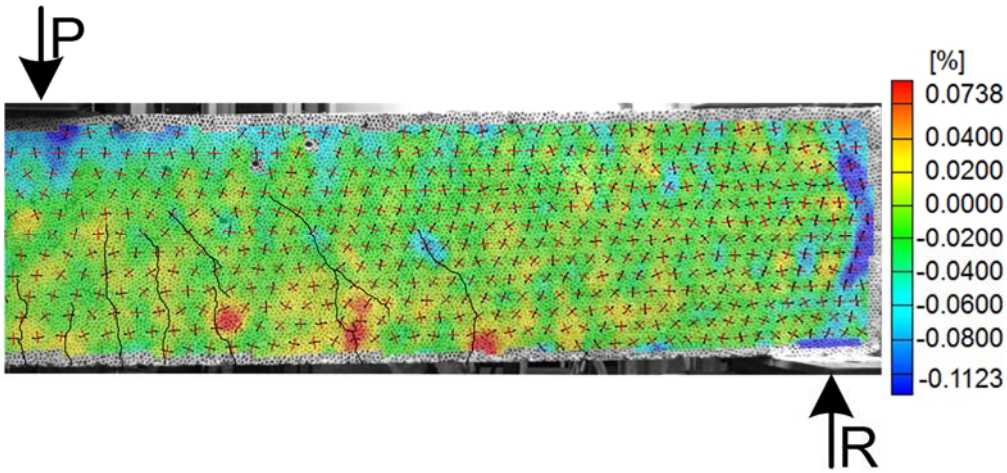

Figure 4.20 Full-field concrete minimum principal strain (σ_2) across shear span for specimen RC18a at load 50.77 kips (Peak Load)

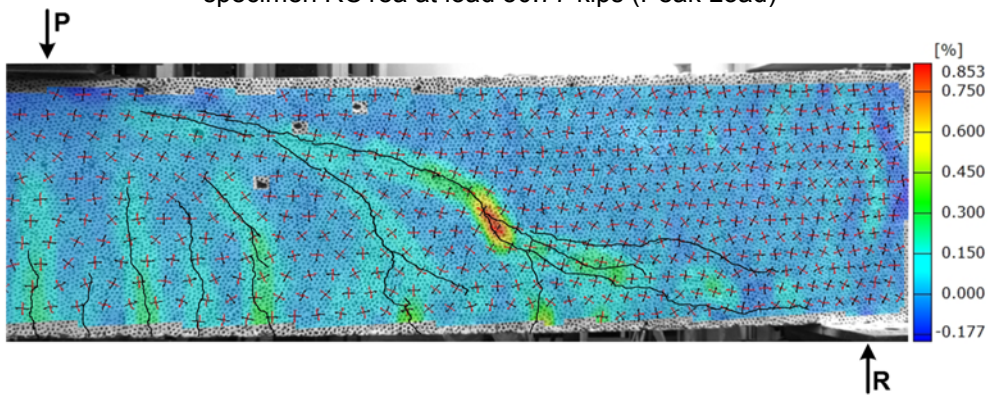

Figure 4.21 Full-field concrete longitudinal strain (ε_x) across shear span for specimen RC18a just after the peak load drop (post-peak load)

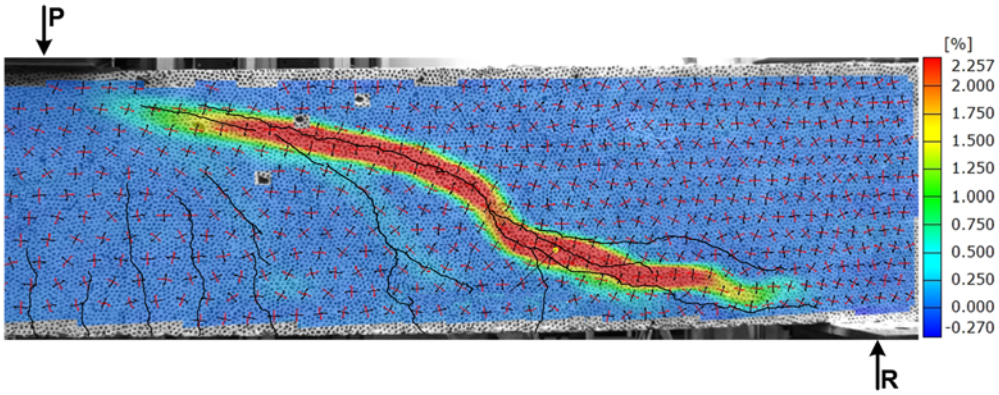

Figure 4.22 Full-field concrete transvers strain (ε_y) across shear span for specimen RC18a just after the peak load drop (post-peak load)

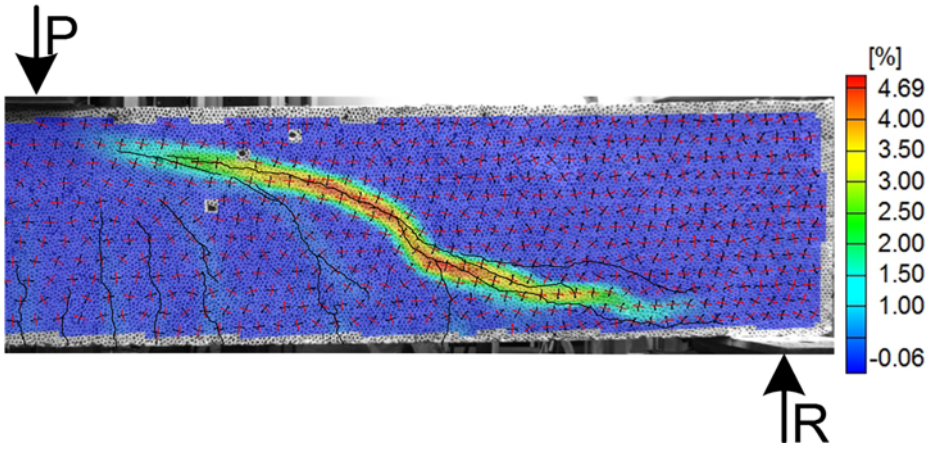

Figure 4.23 Full-field concrete maximum principal strain (σ_1) across shear span for specimen RC18a just after the peak load drop (post-peak load)

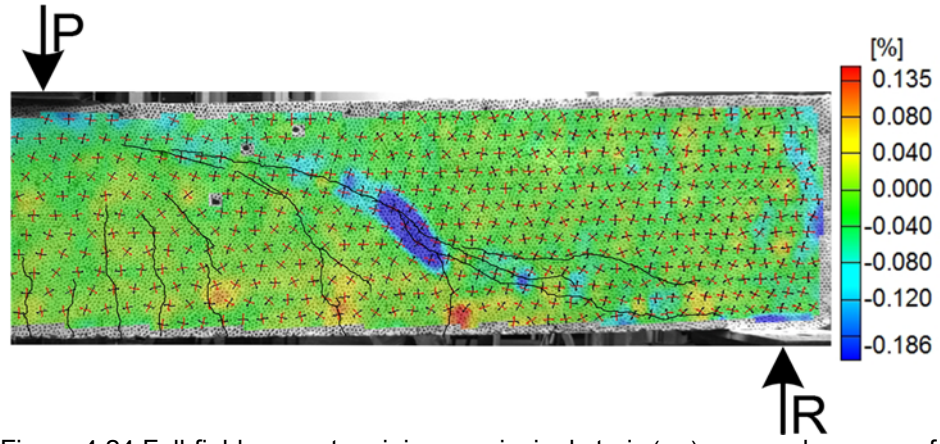

Figure 4.24 Full-field concrete minimum principal strain (σ_2) across shear span for specimen RC18a just after the peak load drop (post-peak load)

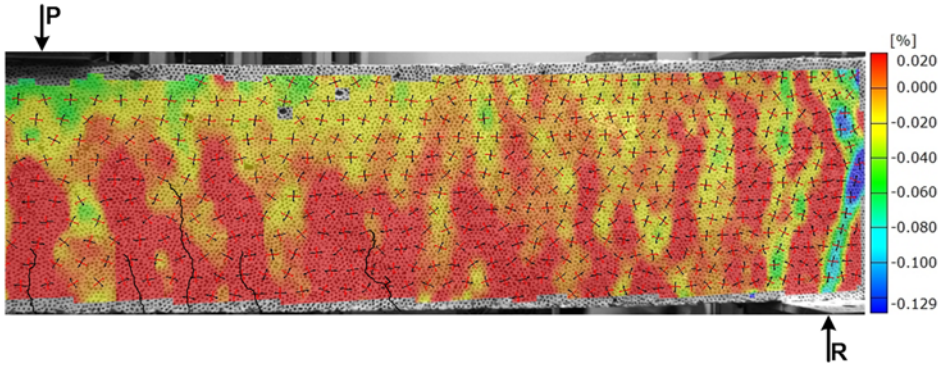

Figure 4.25 Scaled full-field concrete longitudinal strain (ε_x) across shear span for specimen RC18a at load 35 kips

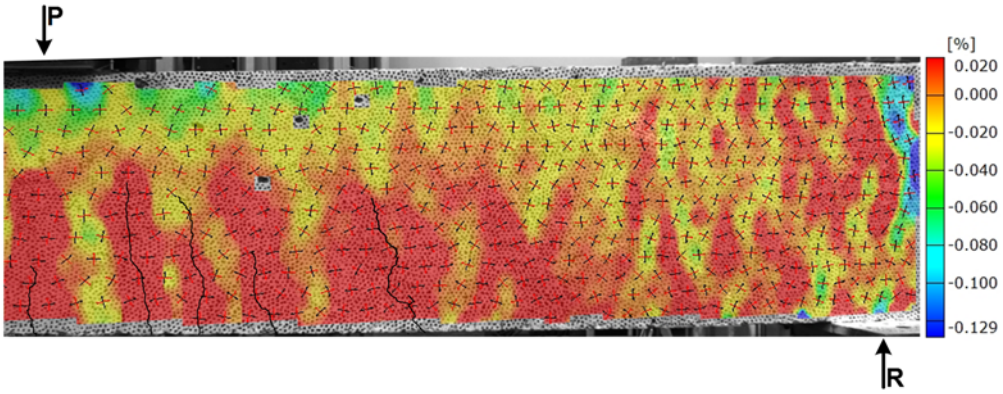

Figure 4.26 Scaled full-field concrete longitudinal strain (ε_x) across shear span for specimen RC18a at load 40 kips

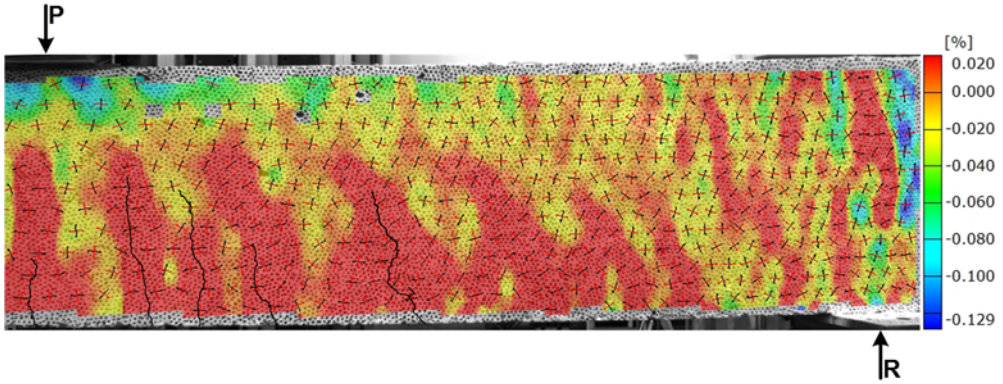

Figure 4.27 Scaled full-field concrete longitudinal strain (ε_x) across shear span for specimen RC18a at load 45 kips

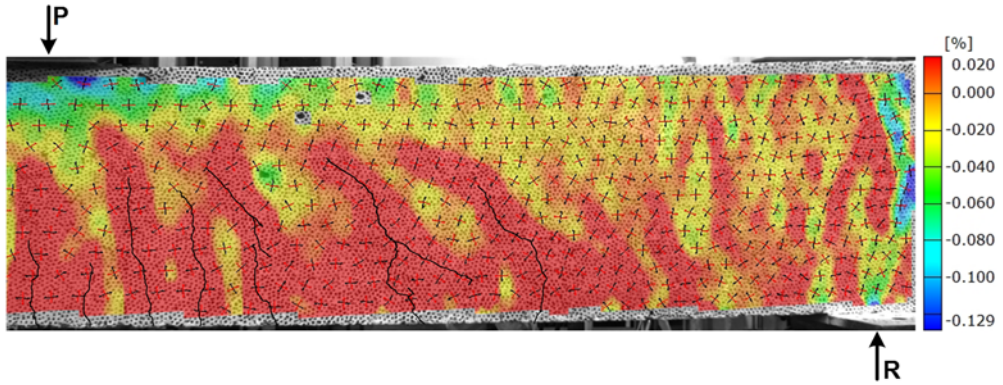

Figure 4.28 Scaled full-field concrete longitudinal strain (ε_x) across shear span for specimen RC18a at load 50 kips

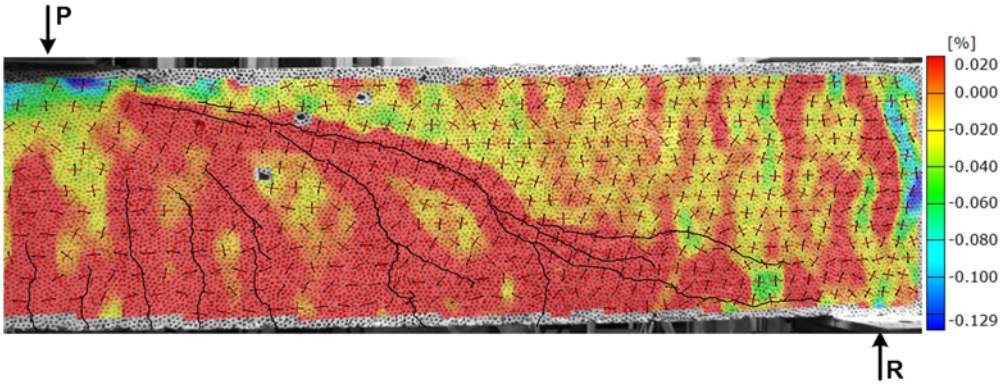

Figure 4.29 Scaled full-field concrete longitudinal strain (ε_x) across shear span for specimen RC18a just after the peak load drop (post-peak)

4.1.2 Beam RC18b

4.1.2.1 Load-deflection relationship, crack pattern, and failure mode

RC18b beam was the duplication of beam RC18a.The relationship between applied load and deflection under the external load as well as the cracking patterns at various load steps were plotted in Figure 4.30 and Figure 4.31. In this test, the load was raised at 5 kips intervals after the first visible flexural crack development.

First flexural crack was noticed at load 25 kips from the bottom surface of the beam, nearly under the external load. The formation of flexural crack caused no change in the beam stiffness. Gradually, by an increase in the applied load, the formation of flexural crack extended to the other points along the shear span toward the supports, while the curve slope still remained steady. When the load reached 30 kips corresponding the shear force of 11 kips, the last flexural crack in the targeted shear span became deviated from its original direction toward the loading point. At the same time, another shear crack developed in a form of web shear cracking in the shear span at a further distance from the loading point than the other cracks (Figure 4.31).

At load 45.3 kips corresponding to shear force of 17 kips, the sudden extension of a new significant diagonal tension crack from the top layer of longitudinal rebars to loading point

triggered failure of the beam (Figure 4.32). On the other side of the beam, the critical crack was observed to develop all the way and intersected the beam edge in the compression zone. The cracking patterns at failure on both sides of the beam are compared in Figure 4.32. Note, the critical crack lay 2.3d away from the loading point, as it measured at the beam middle depth. The failure mode for beam RC18b was defined as diagonal-tension failure.

4.1.2.2 Strains measured in reinforcing Bars

Figure 4.33 reflects the averages of longitudinal strain variation curves recorded from flexural reinforcing bars under the loading point and the middle of the shear span, respectively during the loading process. As seen in Figure 4.33, the strain variation at both locations were of the same order up to load 10 kips. However, at this load, the reinforcing bars suddenly experienced a larger amount of strain under the loading point without having any increase in the applied load. As a matter of fact, the development of a flexural crack possibly accounts for such abrupt strain increment in the reinforcing bar, while in specimen RC18b, no flexural crack had been visually observed up to that loading point. Nevertheless, checking the full-filed concrete longitudinal strain distributions (ε_x) obtained from DIC for different loads revealed the accurate load corresponding to the first flexural crack initiation at 10 kips, as visualized by Figure 4.34. To be in consistence with prior research studies, in our analysis, the load at which the flexural crack became visible (25 kips) was considered as the first visible flexural cracking load. At a higher load, the load-strain curve obtained from the mid-shear span strain gauges exhibited the same trend, yet larger abruptly increased strain when it attained a strain magnitude as equal as that causing the first flexural crack under the loading point. The greater sudden change in the strain perhaps proceeded from multiple flexural cracking in vicinity of the mid-shear span. Beyond an

approximate load of 14 kips, the straining rate seemed rather identical at the two locations along the shear span up to the load of 22.8 kips. After that, the reinforcement strain at mid-shear span nonlinearly increased by elevating the applied load. As opposed to the first visible shear cracking load at 30 kips, load 22.8 kips (corresponding to shear force of 8.2 kips) turned out to be the initiation of the first shear crack, as emerged by Figure 4.38. Since the first shear crack was quite close to the mid-shear span, it induced extra tensile strain in the reinforcements due to shear deformation.

As clearly indicated by Figure 4.33, the measured tensile strains did not exceed the nominal yielding strain of grade 60 steel (0.0021 in./in.). Therefore, none of the longitudinal reinforcements yielded by the time of failure.

4.1.2.3 Full-field visualization of strain components developed on the shear span concrete surface

Full-filed strain components developed on concrete surface throughout shear span for specimen RC18b were obtained with the aid of DIC technology at different load values and illustrated in Figure 4.34 through Figure 4.57. For better evaluation of the relationship between cracking pattern and the state of developed stresses acquired by DIC system, the cracks on the other side of the beam at each desired load were integrated into the corresponding DIC processed images.

The scaled full-field concrete longitudinal strain (ε_x) distributions across shear span at different loads for specimen RC18b were visualized from Figure 4.58 to Figure 4.63. Tensile strains are denoted by red, while other colors (yellow to dark blue) represent various magnitudes of compressive strain in the compression zone.

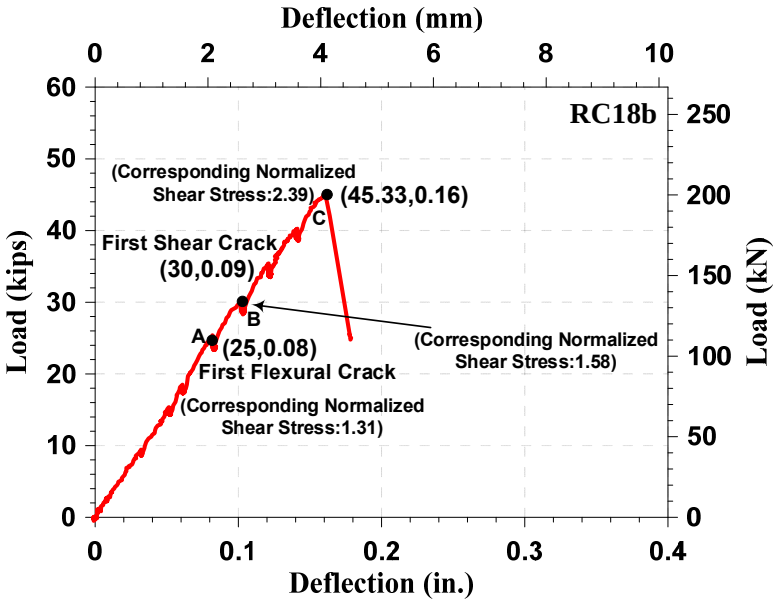

Figure 4.30 load-deflection response for beam RC18b

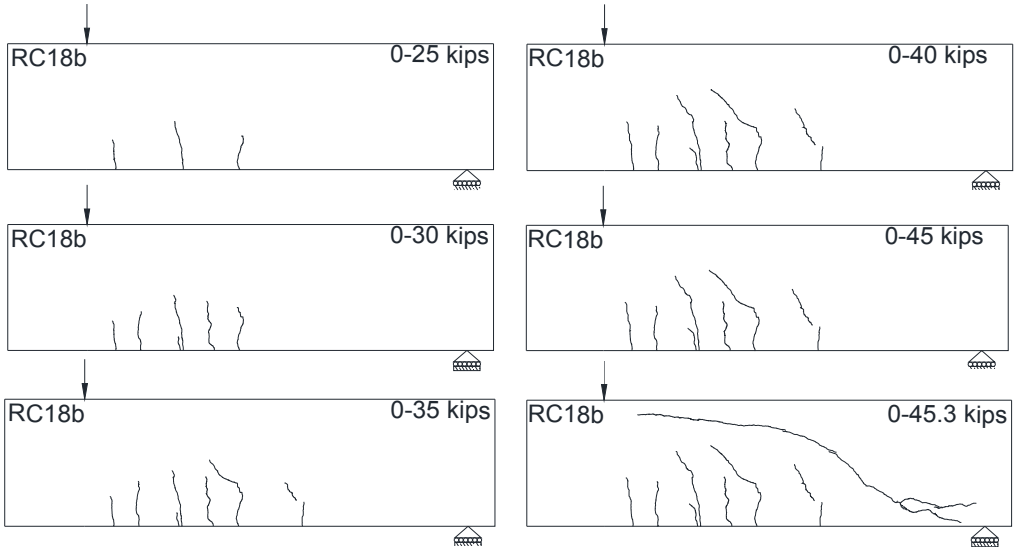

Figure 4.31 Cracking pattern for RC18b at different load stages

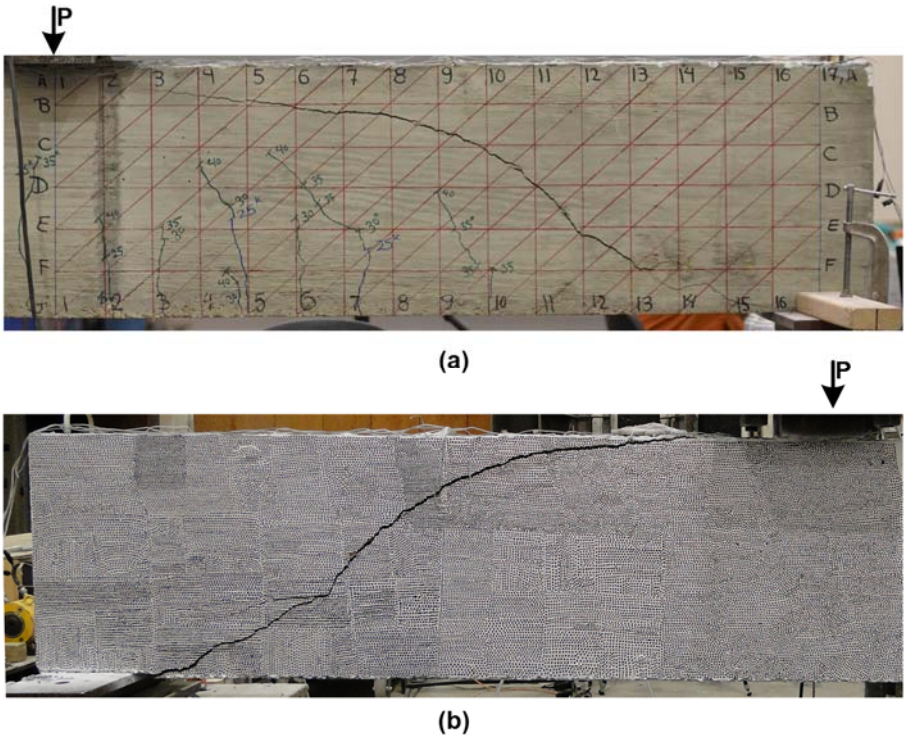

Figure 4.32 Two different views of the critical crack from the two sides of beam RC18b at failure

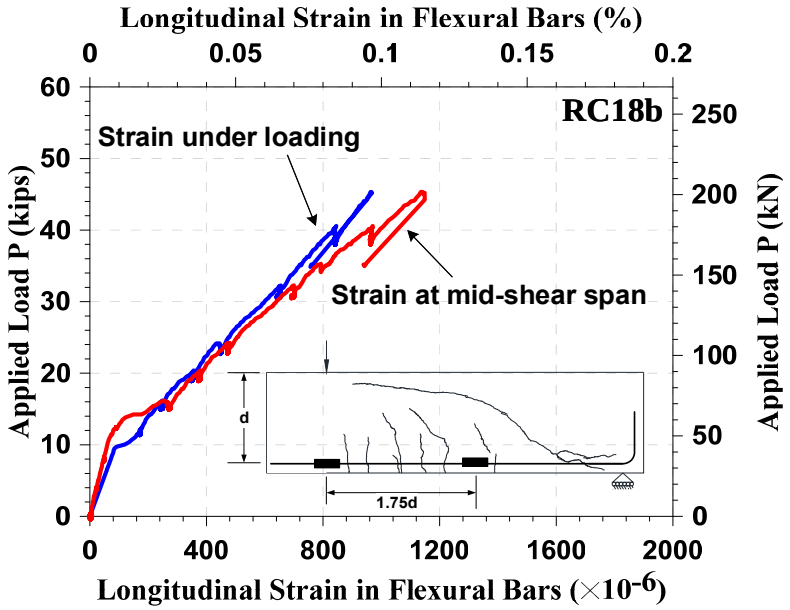

Figure 4.33 Load versus reinforcement strain relationships for beam RC18b

Figure 4.34 Full-field concrete longitudinal strain (ε_x) across shear span for specimen RC18b at load 10 kips

Figure 4.35 Full-field concrete transvers strain (ε_y) across shear span for specimen RC18b at load 10 kips

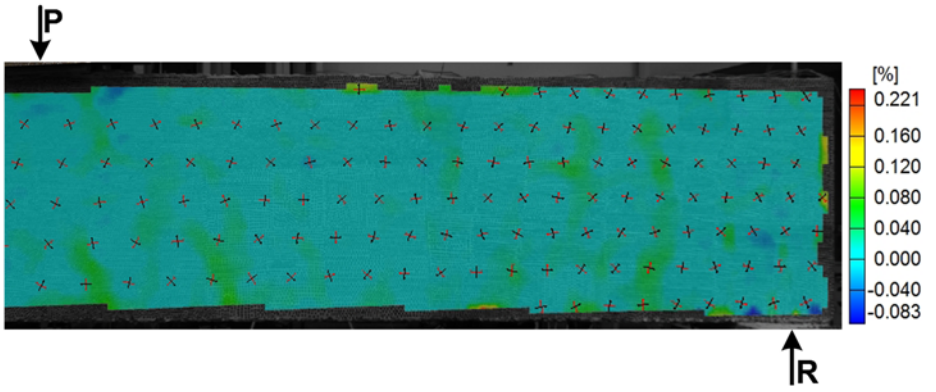

Figure 4.36 Full-field concrete maximum principal strain (σ_1) across shear span for specimen RC18b at load 10 kips

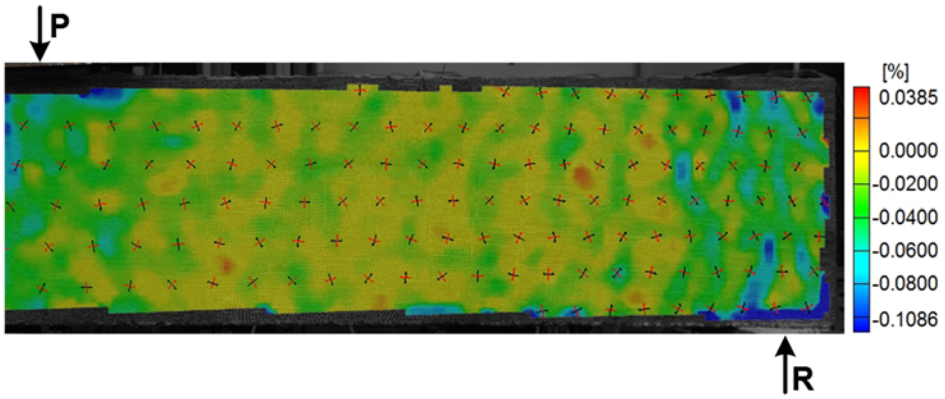

Figure 4.37 Full-field concrete minimum principal strain (σ_2) across shear span for specimen RC18b at load 10 kips

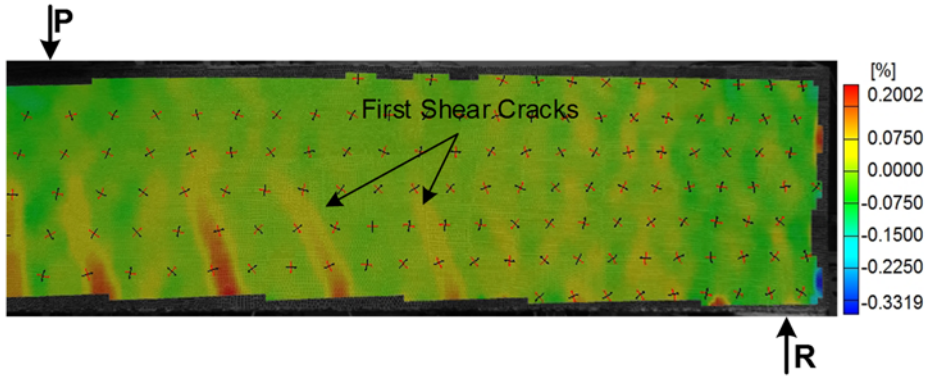

Figure 4.38 Full-field concrete longitudinal strain (ε_x) across shear span for specimen RC18b at load 22.8 kips

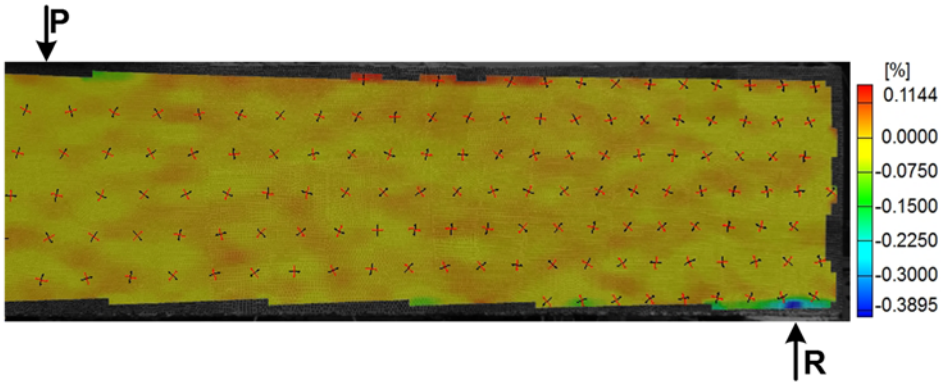

Figure 4.39 Full-field concrete transvers strain (ε_y) across shear span for specimen RC18b at load 22.8 kips

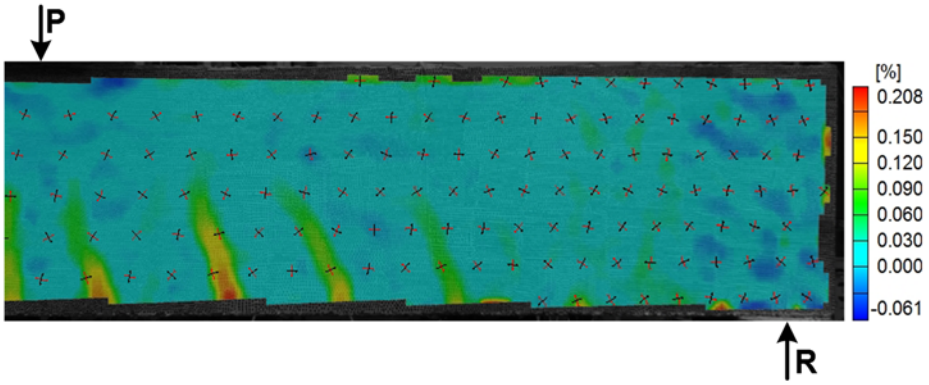

Figure 4.40 Full-field concrete maximum principal strain (σ_1) across shear span for specimen RC18b at load 22.8 kips

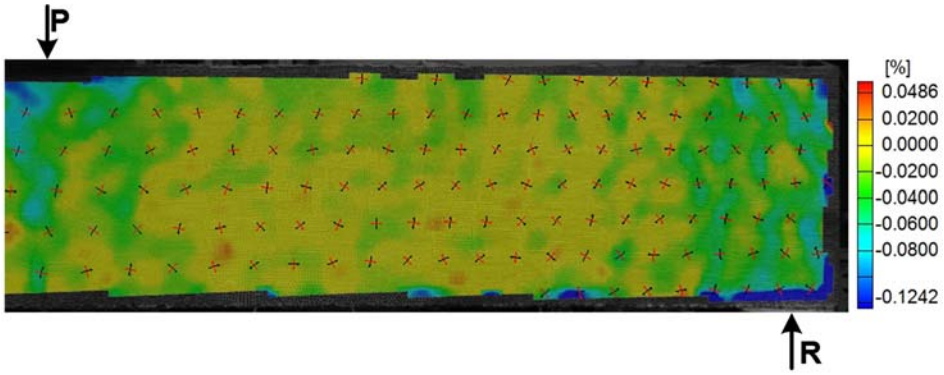

Figure 4.41 Full-field concrete minimum principal strain (σ_2) across shear span for specimen RC18b at load 22.8 kips

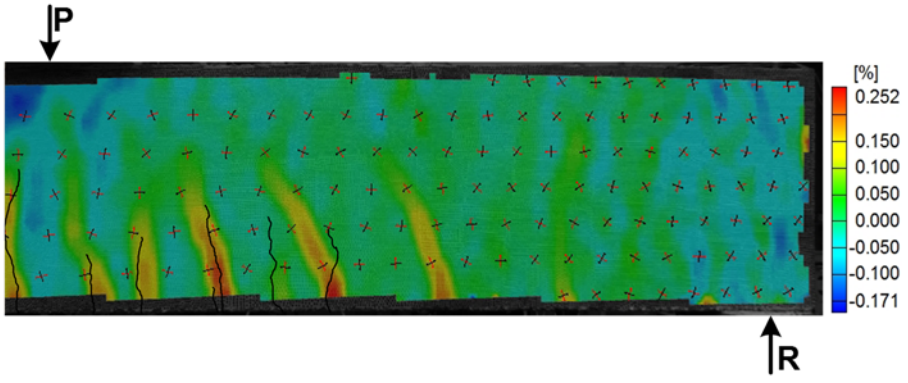

Figure 4.42 Full-field concrete longitudinal strain (ε_x) across shear span for specimen RC18b at load 30 kips

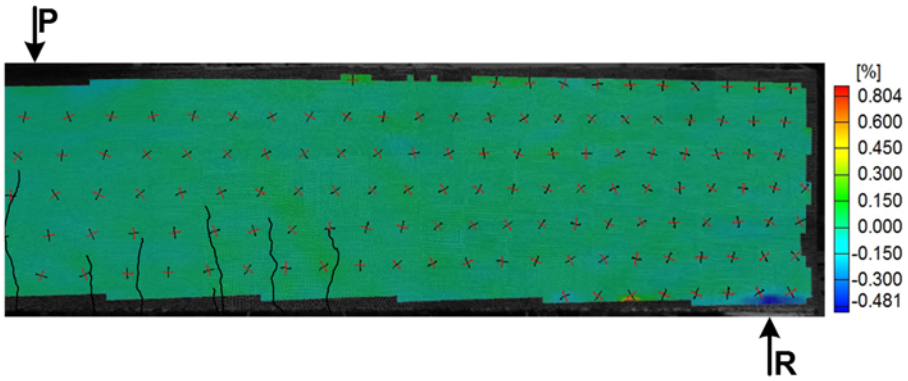

Figure 4.43 Full-field concrete transvers strain (ε_y) across shear span for specimen RC18b at load 30 kips

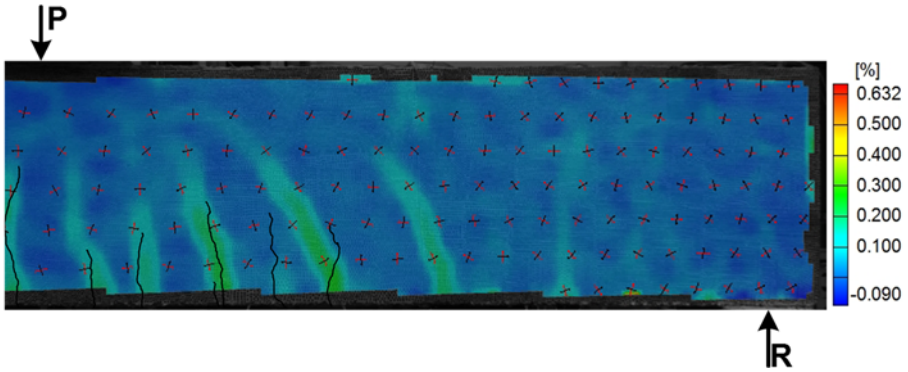

Figure 4.44 Full-field concrete maximum principal strain (σ_1) across shear span for specimen RC18b at load 30 kips

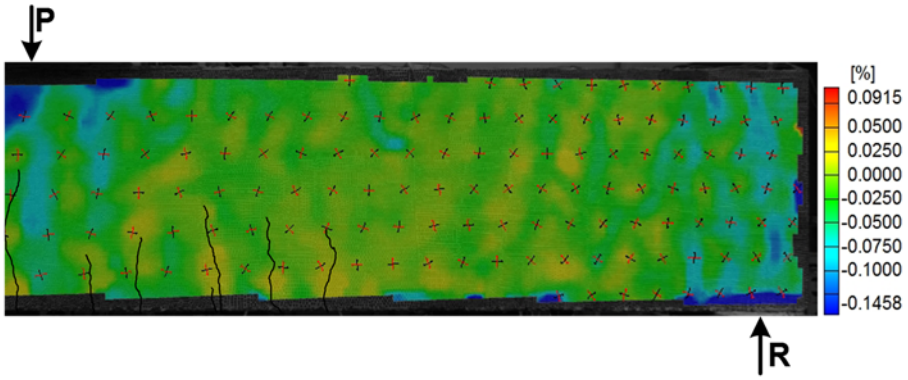

Figure 4.45 Full-field concrete minimum principal strain (σ_2) across shear span for specimen RC18b at load 30 kips

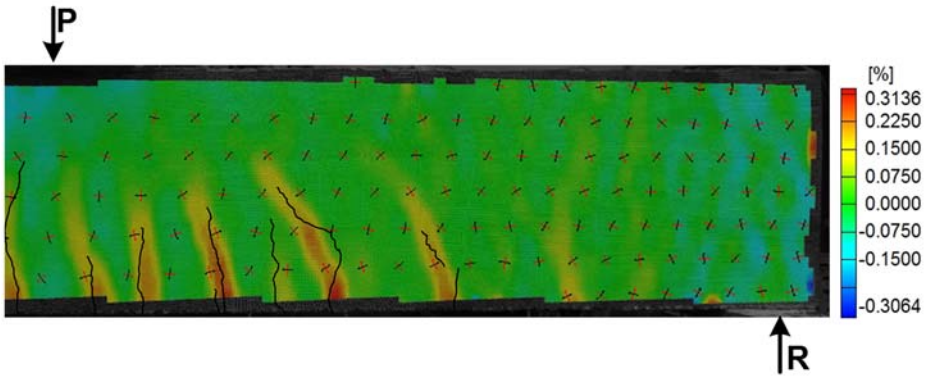

Figure 4.46 Full-field concrete longitudinal strain (ε_x) across shear span for specimen RC18b at load 35 kips

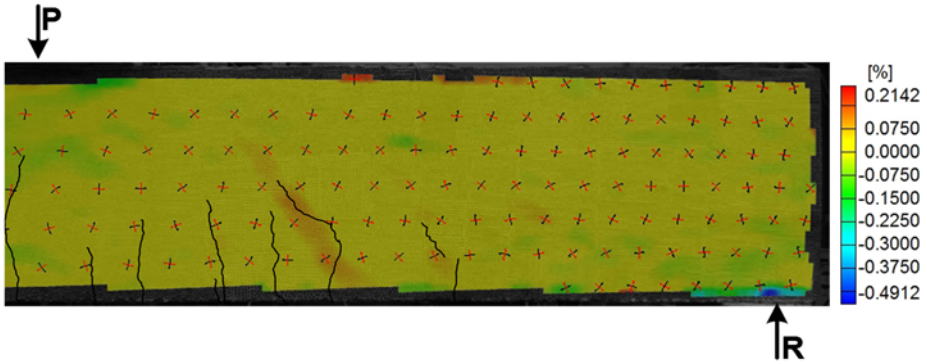

Figure 4.47 Full-field concrete transvers strain (ε_y) across shear span for specimen RC18b at load 35 kips

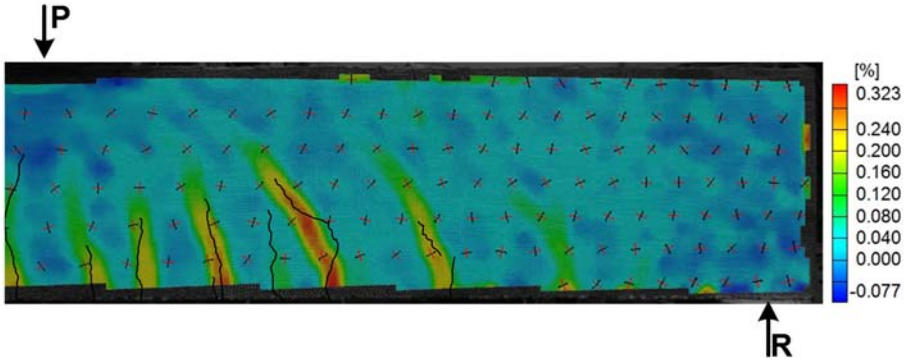

Figure 4.48 Full-field concrete maximum principal strain (σ_1) across shear span for specimen RC18b at load 35 kips

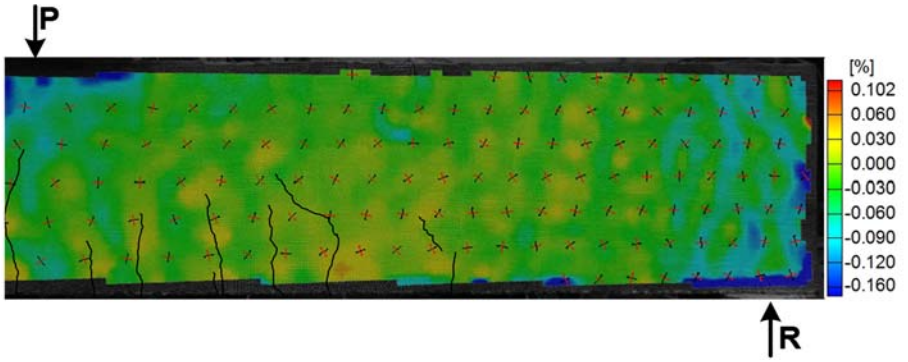

Figure 4.49 Full-field concrete minimum principal strain (σ_2) across shear span for specimen RC18b at load 35 kips

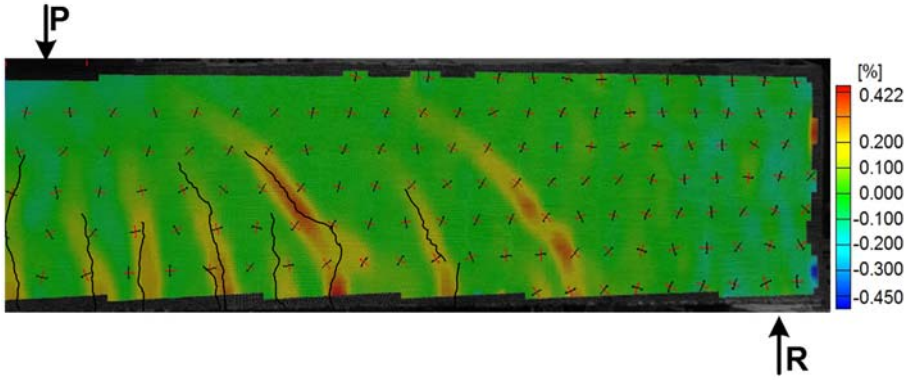

Figure 4.50 Full-field concrete longitudinal strain (ε_x) across shear span for specimen RC18b at load 45.33 kips (Peak Load)

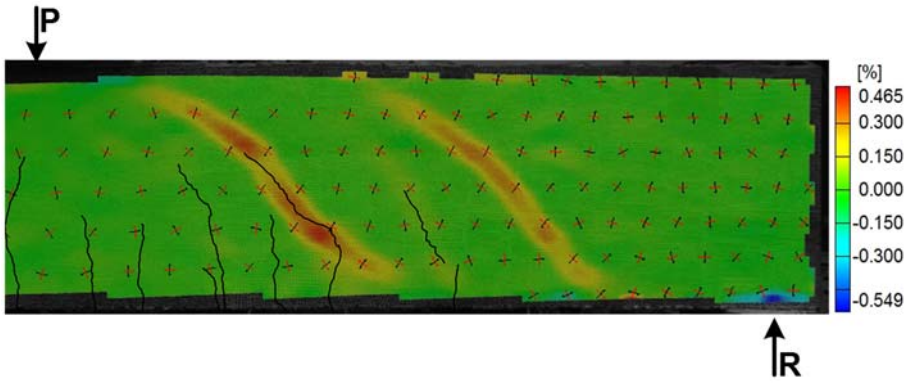

Figure 4.51 Full-field concrete transvers strain (ε_y) across shear span for specimen RC18b at load 45 kips (Just before Peak Load)

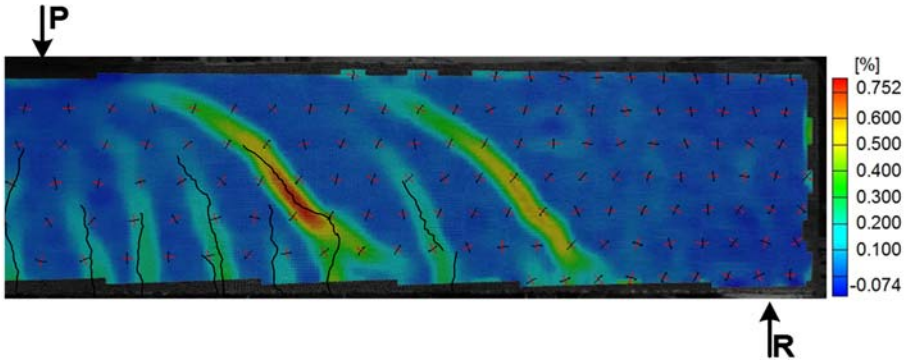

Figure 4.52 Full-field concrete maximum principal strain (σ_1) across shear span for specimen RC18b at load 45.33 kips (Just before Peak Load)

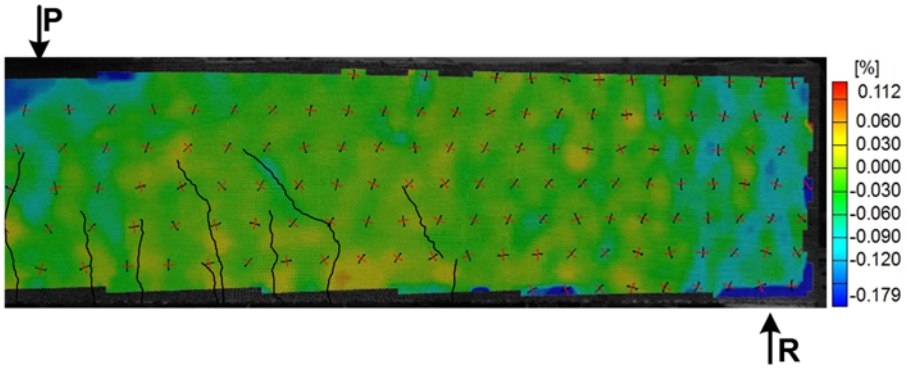

Figure 4.53 Full-field concrete minimum principal strain (σ_2) across shear span for specimen RC18b at load 45.33 kips (Just before Peak Load)

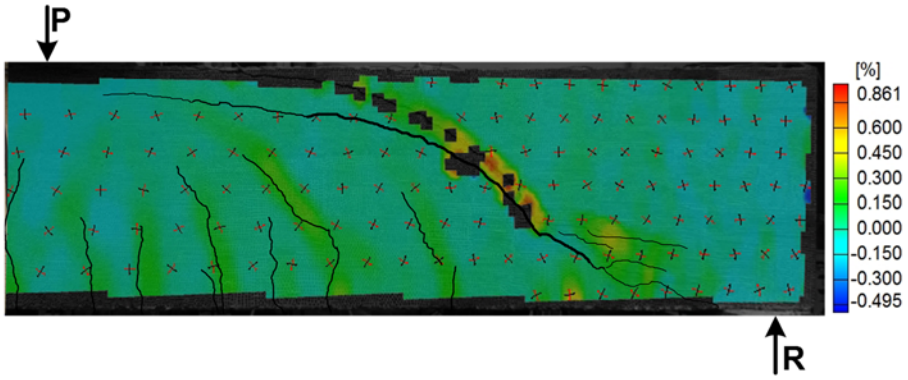

Figure 4.54 Full-field concrete longitudinal strain (ε_x) across shear span for specimen RC18b after failure

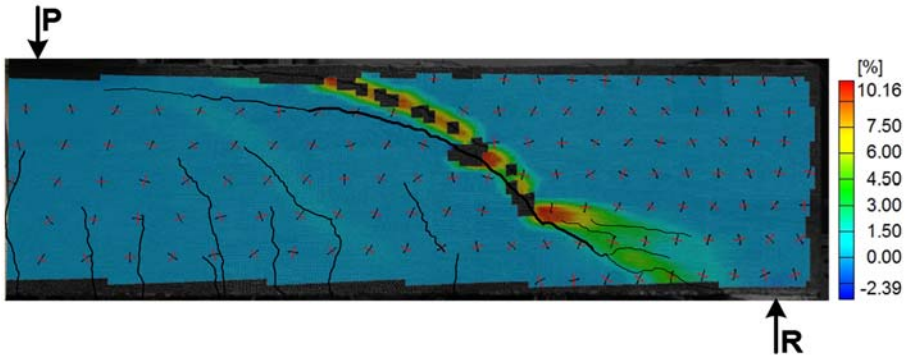

Figure 4.55 Full-field concrete transvers strain (ε_y) across shear span for specimen RC18b after failure

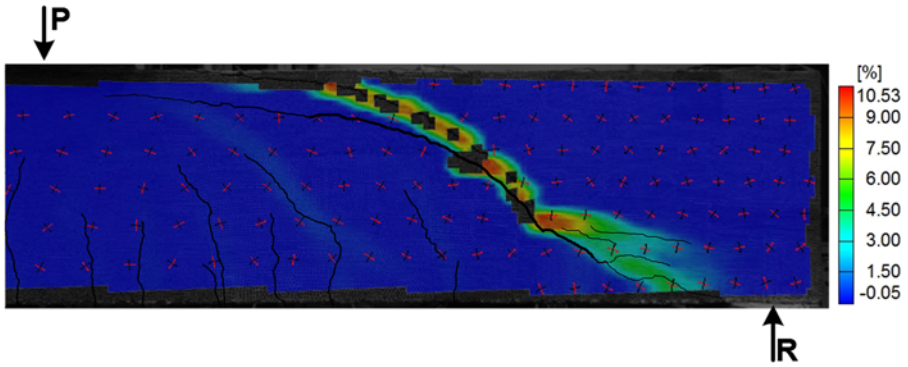

Figure 4.56 Full-field concrete maximum principal strain (σ_1) across shear span for specimen RC18b after failure

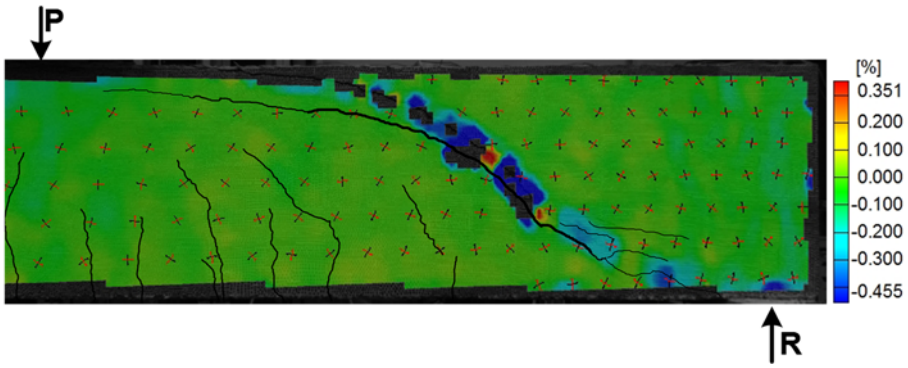

Figure 4.57 Full-field concrete minimum principal strain (σ_2) across shear span for specimen RC18b after failure

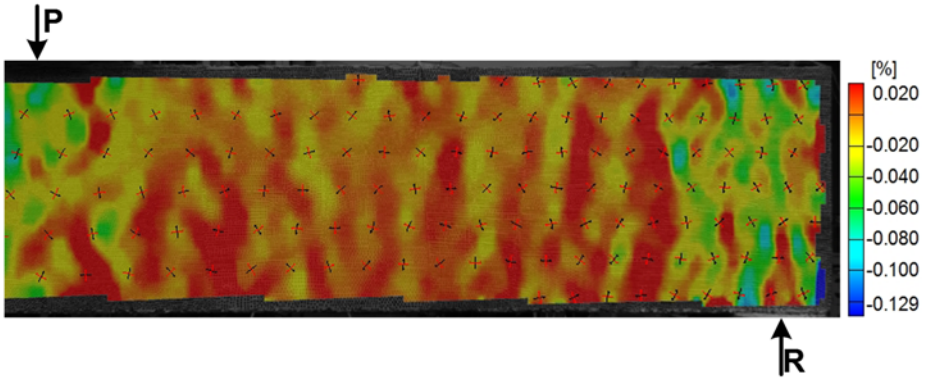

Figure 4.58 Full-field concrete longitudinal strain (ε_x) across shear span for specimen RC18b at load 10 kips

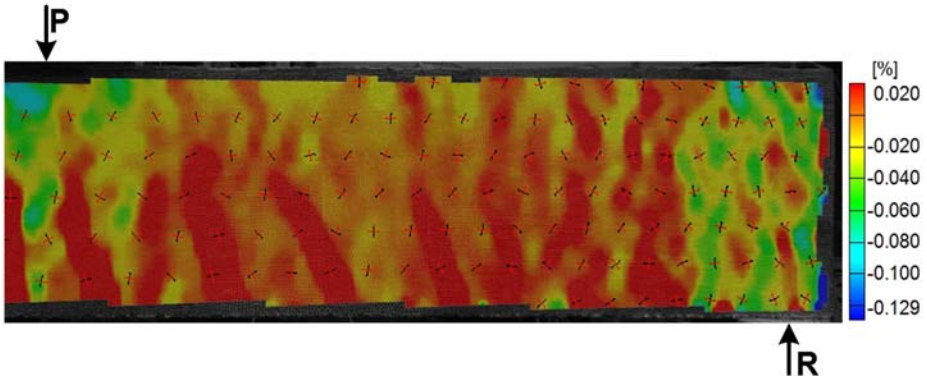

Figure 4.59 Scaled full-field concrete longitudinal strain (ε_x) across shear span for specimen RC18b at load 22.8 kips

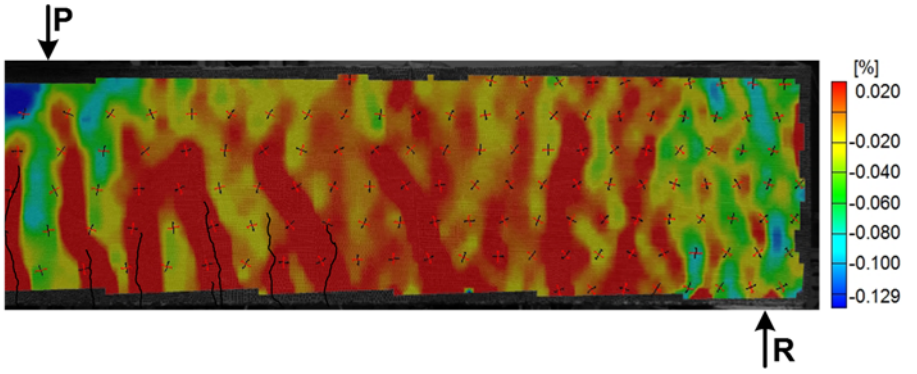

Figure 4.60 Scaled full-field concrete longitudinal strain (ε_x) across shear span for specimen RC18b at load 30 kips

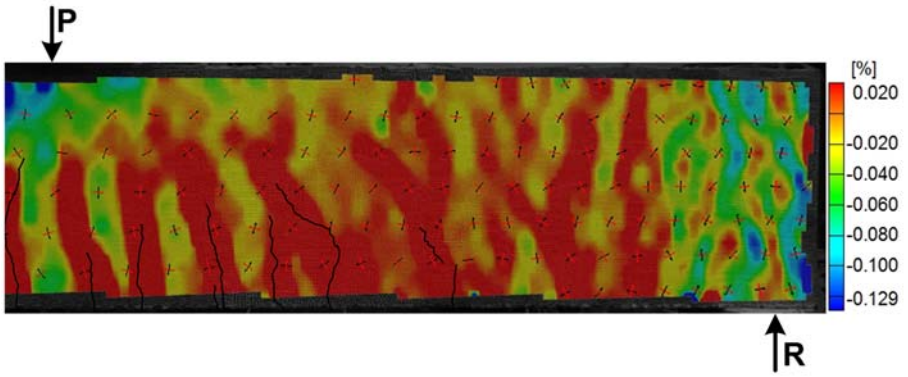

Figure 4.61 Scaled full-field concrete longitudinal strain (ε_x) across shear span for specimen RC18b at load 35 kips

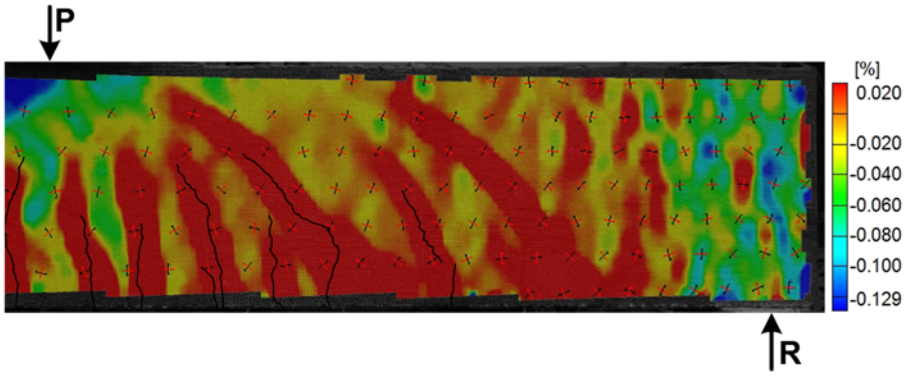

Figure 4.62 Scaled full-field concrete longitudinal strain (ε_x) across shear span for specimen RC18b at load 45.33 kips (Peak Load)

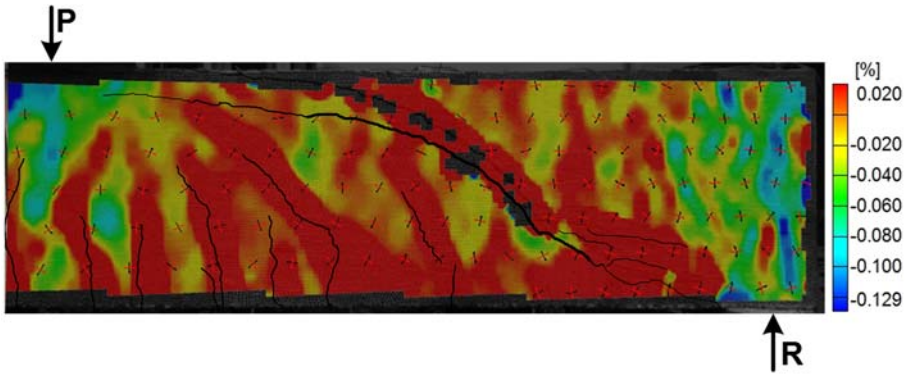

Figure 4.63 Scaled full-field concrete longitudinal strain (ε_x) across shear span for specimen RC18b after failure

4.2 Behavior of the Steel Fiber-Reinforced Concrete (SFRC) Specimens

4.2.1 Beam SFRC12W6

4.2.1.1 Load-deflection relationship, crack pattern, and failure mode

Figure 4.64 and Figure 4.65, respectively show the load versus deflection relationship of beam SFRC12W6 and the corresponding cracking pattern at various loading stages.

At 17 kips corresponding to the shear stress of $2.18\sqrt{f'_c}$ psi as indicated by Figure 4.65, first flexural cracking was noticed, though it didn't signify in the beam load-deflection response. Therefore, the load kept picking up linearly with the curve initial slope. At load 41 kips corresponding to the shear stress of $5.28\sqrt{f'_c}$ psi, multiple web shear cracks developed on the shear span, as displayed by Figure 4.65.

Beyond load 41 kips, the beam stiffness decreased gradually until reaching the peak load of 54 kips corresponding to the shear stress of $6.9\sqrt{f'_c}$ psi. Then, the sudden opening of critical crack in the compression zone toward the beam edge caused the peak load to drop to 49 kips (10% of the maximum load) and triggered the failure. It is noteworthy that at the time of the failure, the critical crack fully developed all the way to the beam edge (Figure 4.66). Therefore, the failure mode is suggested to be diagonal tension failure of the compression zone. By a further increase in the beam displacement, a major crack slipping was observed along the critical crack following to the widening of a splitting crack along the top layer of longitudinal rebars (Figure 4.67). That led to a slight concrete spalling at the face of the loading bearing plate in vicinity of the critical crack tip. As revealed by Figure 4.64, after failure, the beam still exhibited some residual strength and underwent a significant post-peak displacement, as illustrated by Figure 4.68.

4.2.1.2 Strain distribution along reinforcement in SFRC12W6

Longitudinal strain distribution at various shear stresses was measured along a reinforcing bar located at the lower left corner of the beam cross section by means of a series of strain gauges at the desired locations shown in Figure 4.69. As clearly indicated by Figure 4.69, at lower shear stresses prior to the development of shear cracks, strain had almost a linear distribution along the longitudinal bar in compliance with the dominating linier variation of bending moment. At shear stress of $5.0\sqrt{f'_c}$ psi (applied load of 39 kips), the sudden change in the magnitude of strain shown by gauge 7 evidenced the formation of shear crack intersecting the longitudinal bar at that location. Likewise, the relative jump in the strain values in gauges 8 and 10 at shear stresses above $5.0\sqrt{f'_c}$ psi arose from the additional shear deformation induced by shear cracking. As it can be viewed through the strain variation curve in Figure 4.69, the large distinction in shear strain quantities recorded through gauges 6 to 12 at each current shear stress evidenced that the bar-SFRC interface bonding strength had not been achieved along that length of the shear span. Moreover, the longitudinal strain at the interior face of the support, where the bending moment faded away was negligible. Through all these two above evidences, it emerged that no tied arch was involved in the shear resistance. Considering the yielding strain at 2750 με for #6 bars as reported by Dinh (2009), the reinforcement yielded no where along the shear span in beam SFRC12W6 (Figure 4.69).

4.2.1.3 Full-field visualization of strain components developed on the shear span concrete surface

Full-filed strain components developed on concrete surface throughout shear span for specimen SFRC12W6 were obtained with the aid of DIC technology at different load values and illustrated in Figure 4.70 through Figure 4.97. For the better evaluation of the

relationship between cracking pattern and the state of developed stresses acquired by DIC system, the cracks on the other side of the beam at each desired load were integrated into the corresponding DIC processed images.

The scaled full-field concrete longitudinal strain (ε_x) distributions across shear span at different loads for specimen SFRC12W6 were visualized from Figure 4.98 to Figure 4.104. Tensile strains are denoted by red, while other colors (yellow to dark blue) represent various magnitudes of compressive strain in the compression zone.

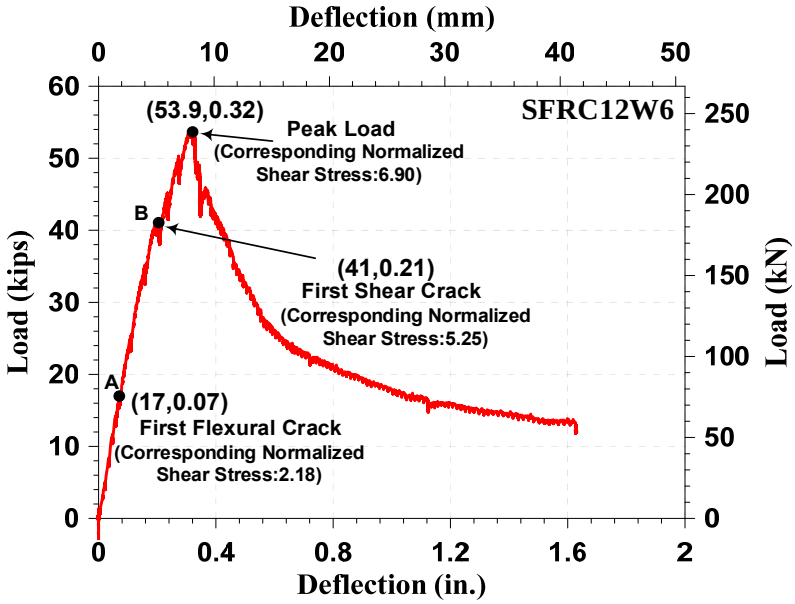

Figure 4.64 load-deflection response for beam SFRC12W6

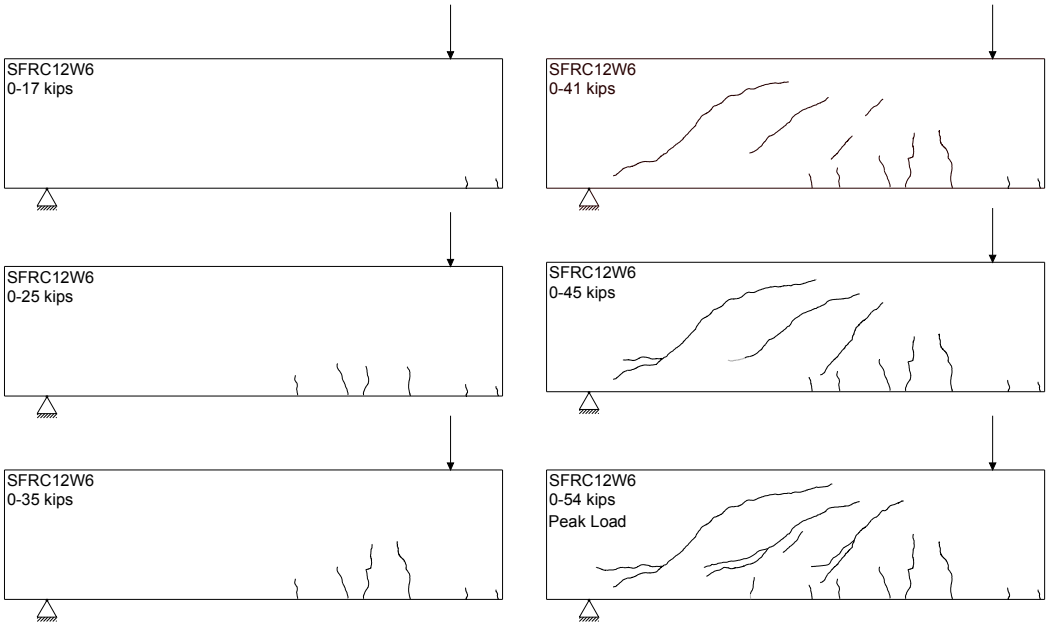

Figure 4.65 Cracking pattern for SFRC12W6 at different load stages

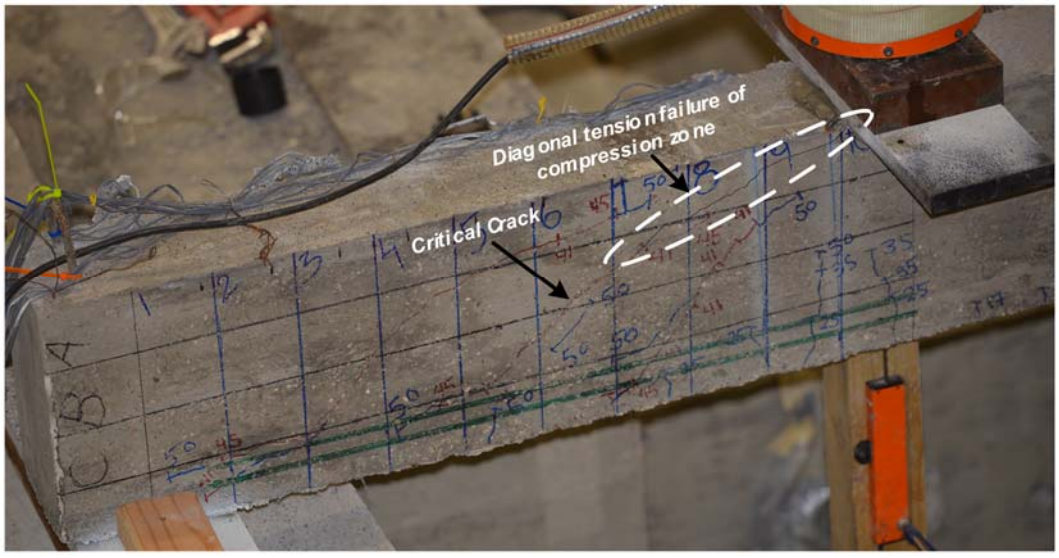

Figure 4.66 A view of failure mode for beam SFRC12W6 (just after peak)

Figure 4.67 Formation of splitting crack at the level of flexural bars as a post-peak phenomenon

Figure 4.68 Significant post-peak displacement (External load: 26% of the peak load)

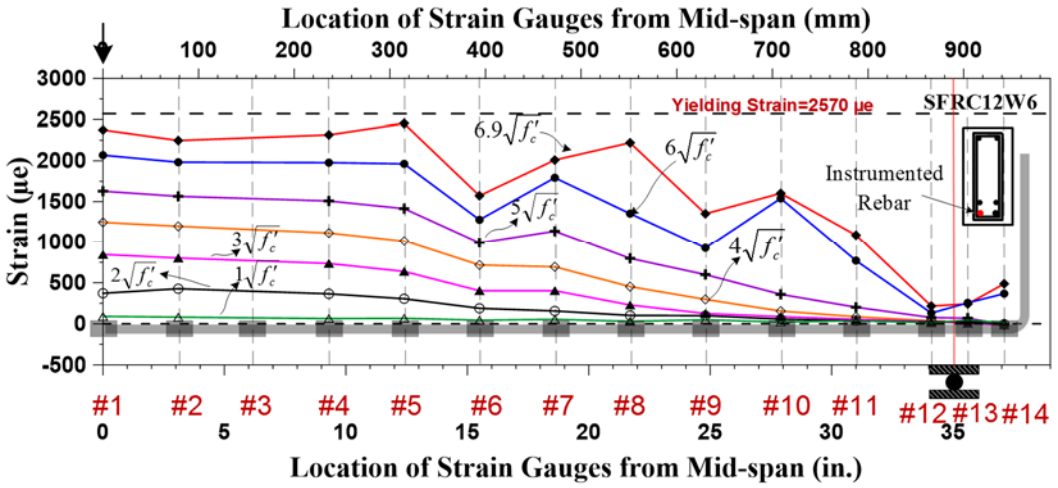

Figure 4.69 Strain variation along an instrumented longitudinal rebar at different normalized shear stresses

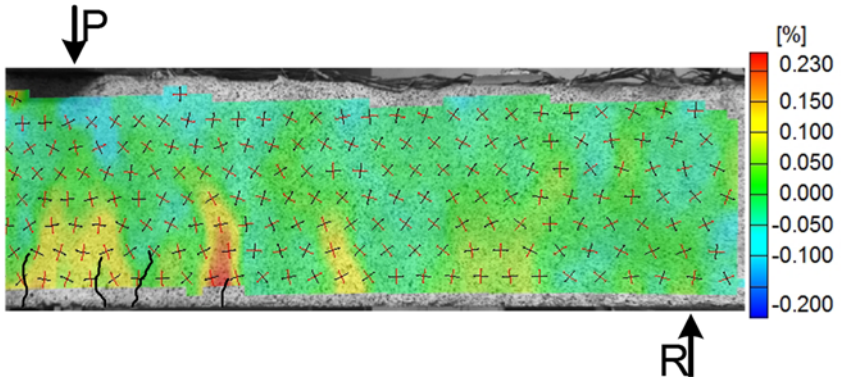

Figure 4.70 Full-field concrete longitudinal strain (ε_x) across shear span for specimen SFRC12W6 at normalized shear stress of $2.5\sqrt{f'_c}$.

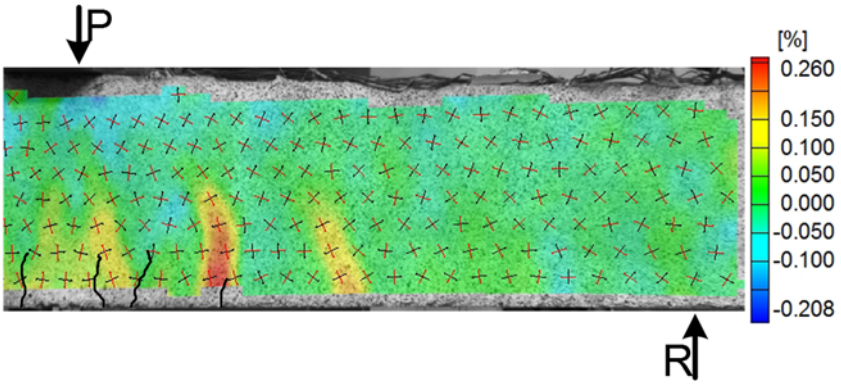

Figure 4.71 Full-field concrete longitudinal strain (ε_x) across shear span for specimen SFRC12W6 at normalized shear stress of $3.0\sqrt{f'_c}$.

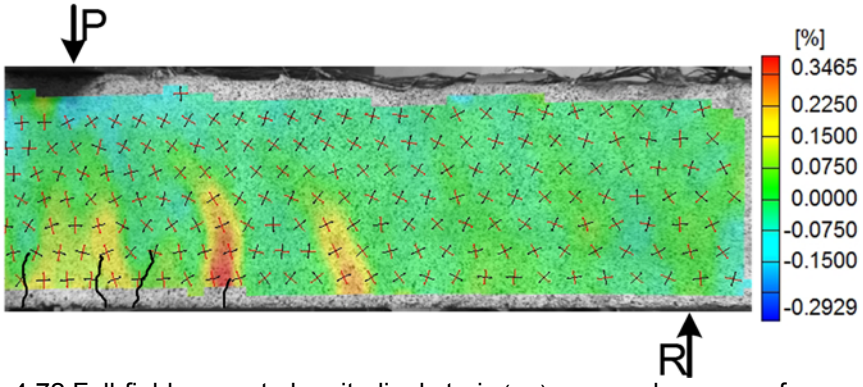

Figure 4.72 Full-field concrete longitudinal strain (ε_x) across shear span for specimen SFRC12W6 at normalized shear stress of $4.0\sqrt{f'_c}$.

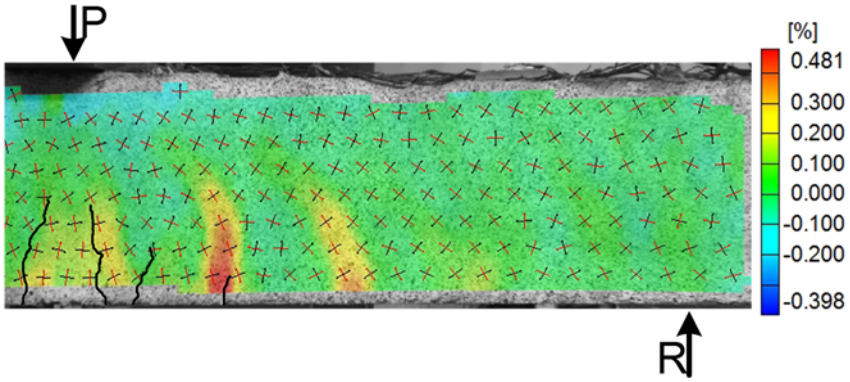

Figure 4.73 Full-field concrete longitudinal strain (ε_x) across shear span for specimen SFRC12W6 at normalized shear stress of $5.0\sqrt{f'_c}$.

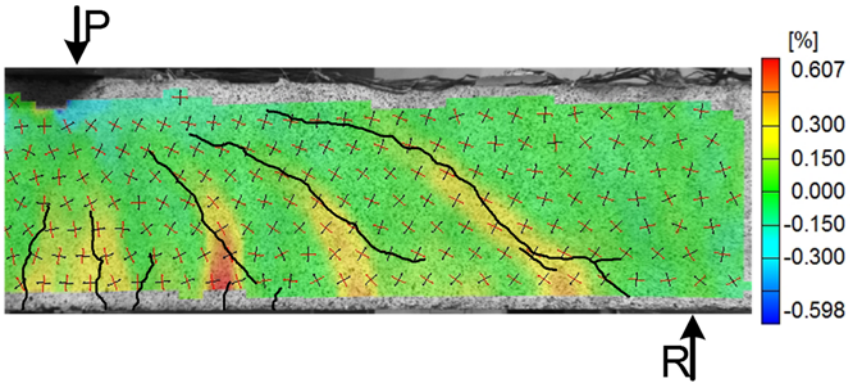

Figure 4.74 Full-field concrete longitudinal strain (ε_x) across shear span for specimen SFRC12W6 at normalized shear stress of $6.0\sqrt{f'_c}$.

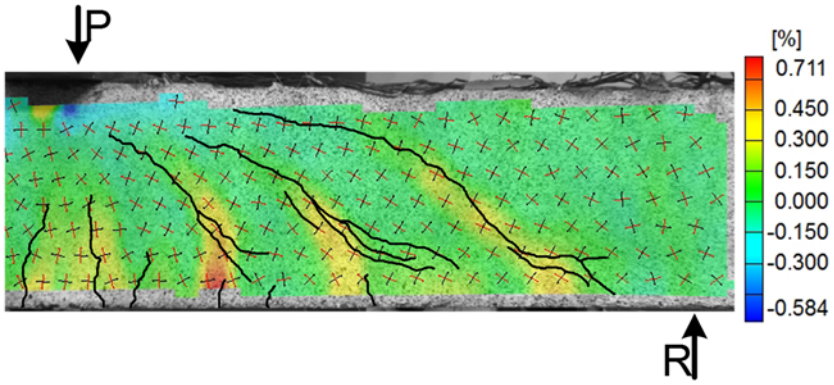

Figure 4.75 Full-field concrete longitudinal strain (ε_x) across shear span for specimen SFRC12W6 at normalized shear stress of $6.5\sqrt{f'_c}$.

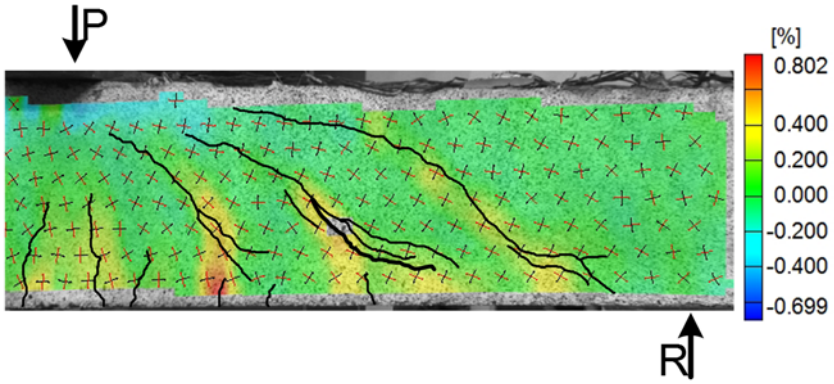

Figure 4.76 Full-field concrete longitudinal strain (ε_x) across shear span for specimen SFRC12W6 at normalized shear stress of $6.9\sqrt{f'_c}$.

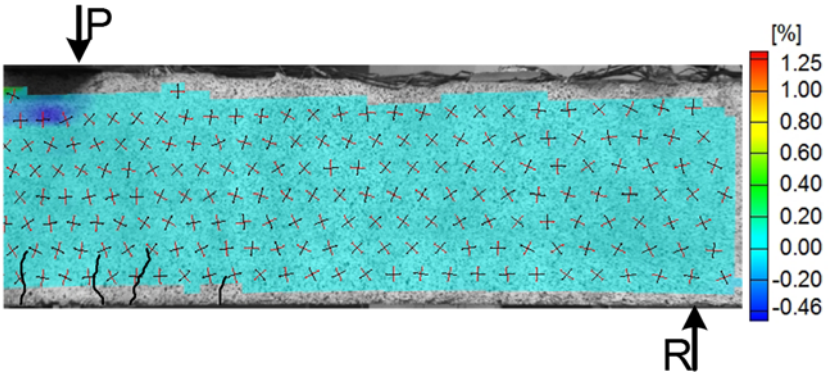

Figure 4.77 Full-field concrete transvers strain (ε_y) across shear span for specimen SFRC12W6 at normalized shear stress of $2.5\sqrt{f'_c}$.

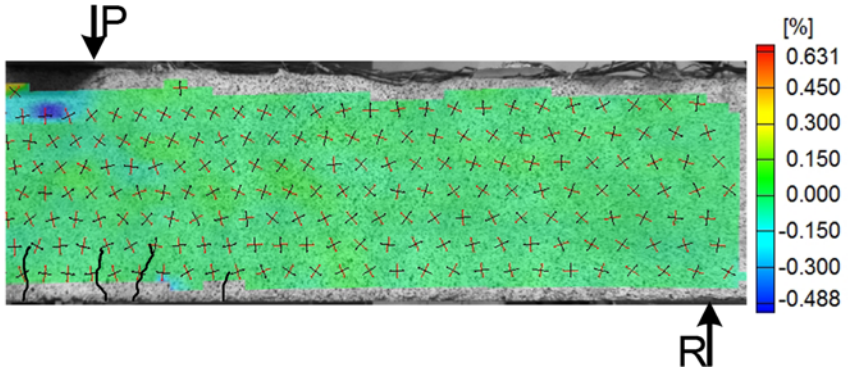

Figure 4.78 Full-field concrete transvers strain (ε_y) across shear span for specimen SFRC12W6 at normalized shear stress of $3.0\sqrt{f'_c}$.

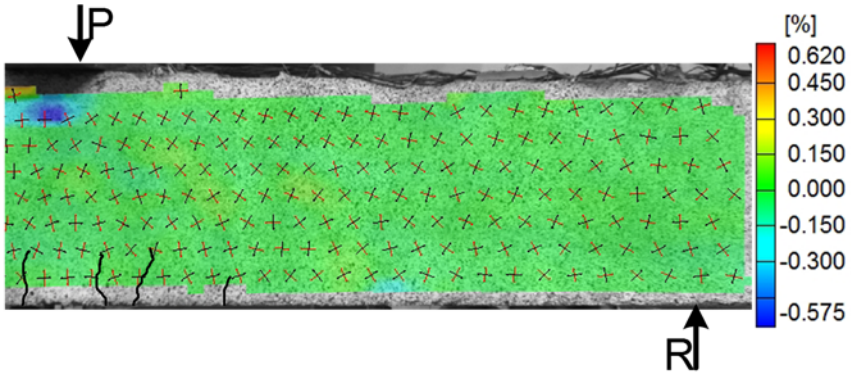

Figure 4.79 Full-field concrete transvers strain (ε_y) across shear span for specimen SFRC12W6 at normalized shear stress of $4.0\sqrt{f'_c}$.

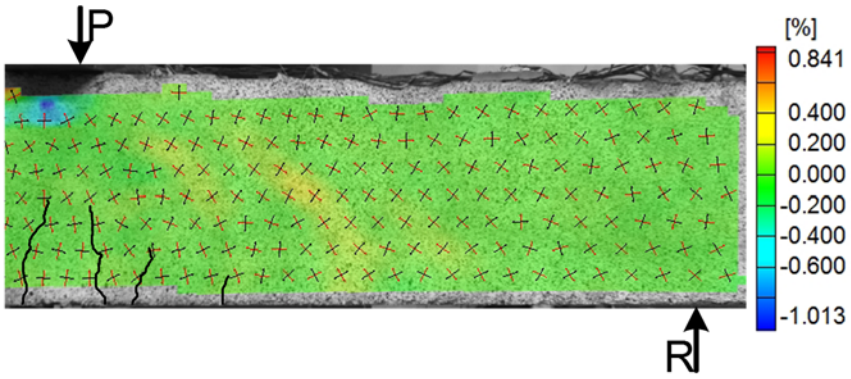

Figure 4.80 Full-field concrete transvers strain (ε_y) across shear span for specimen SFRC12W6 at normalized shear stress of $5.0\sqrt{f'_c}$.

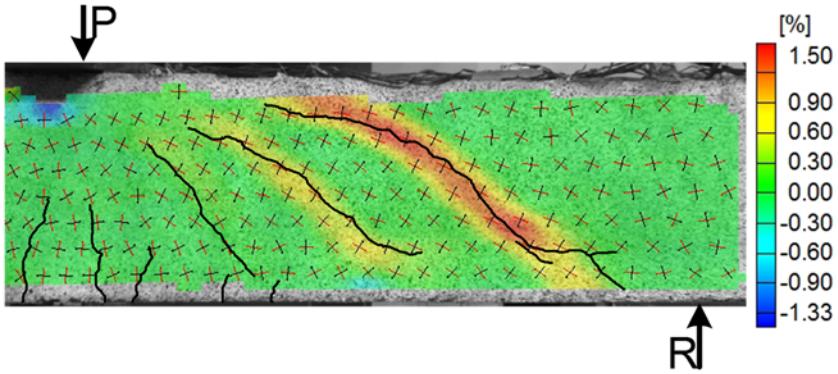

Figure 4.81 Full-field concrete transvers strain (ε_y) across shear span for specimen SFRC12W6 at normalized shear stress of $6.0\sqrt{f'_c}$.

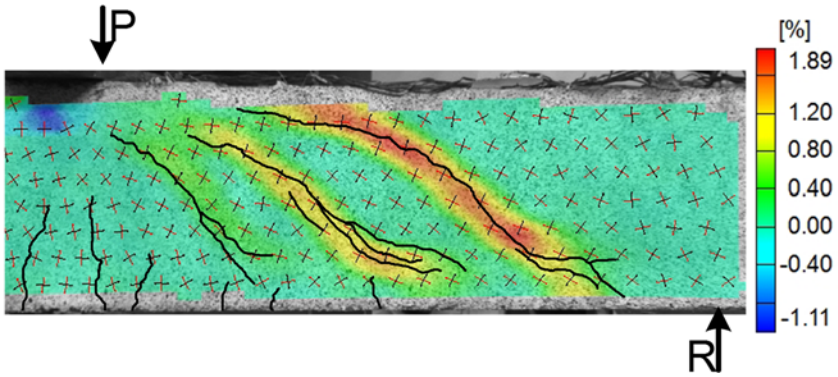

Figure 4.82 Full-field concrete transvers strain (ε_y) across shear span for specimen SFRC12W6 at normalized shear stress of $6.5\sqrt{f'_c}$.

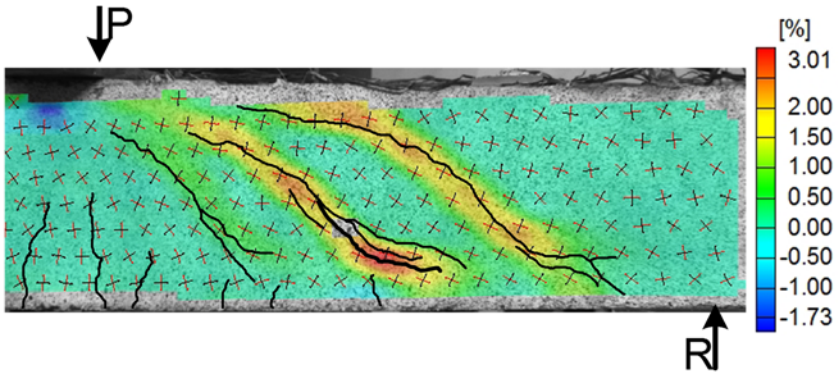

Figure 4.83 Full-field concrete transvers strain (ε_y) across shear span for specimen SFRC12W6 at normalized shear stress of $6.9\sqrt{f'_c}$.

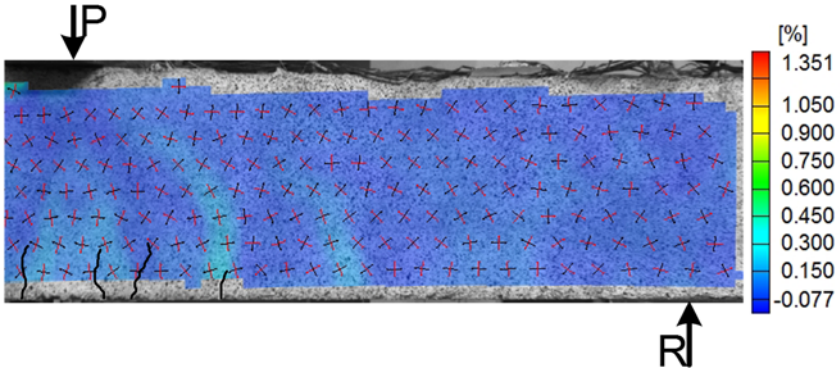

Figure 4.84 Full-field concrete maximum principal strain (σ_1) across shear span for specimen SFRC12W6 at normalized shear stress of $2.5\sqrt{f'_c}$.

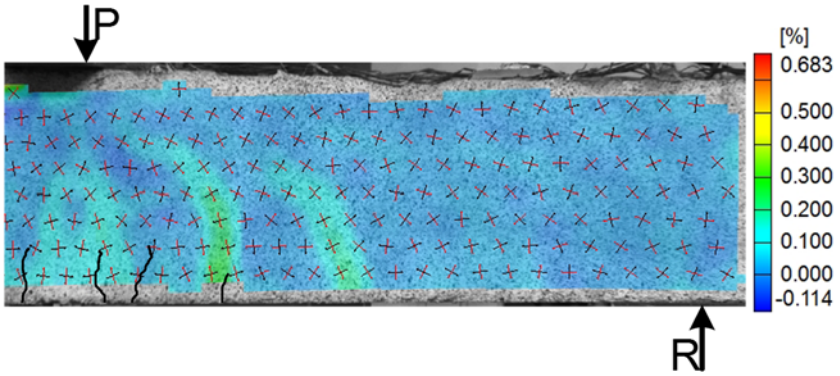

Figure 4.85 Full-field concrete maximum principal strain (σ_1) across shear span for specimen SFRC12W6 at normalized shear stress of $3.0\sqrt{f'_c}$.

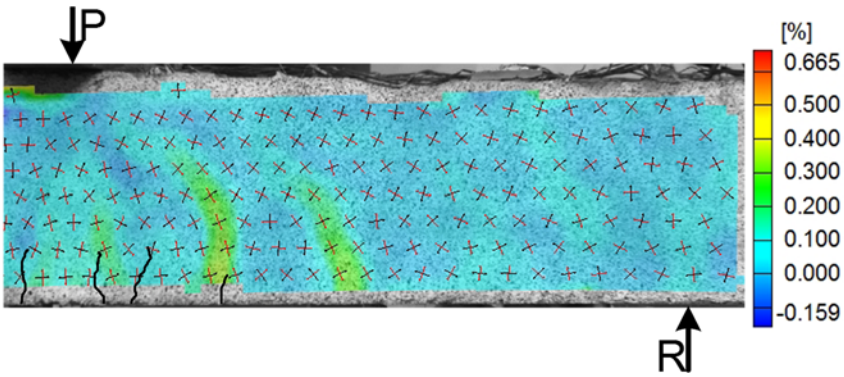

Figure 4.86 Full-field concrete maximum principal strain (σ_1) across shear span for specimen SFRC12W6 at normalized shear stress of $4.0\sqrt{f'_c}$.

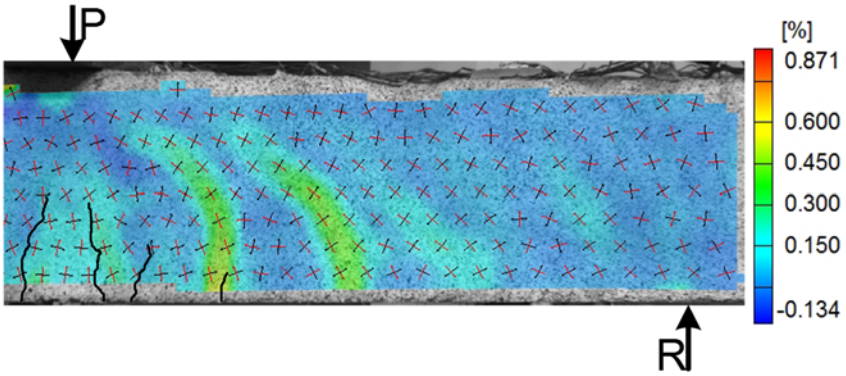

Figure 4.87 Full-field concrete maximum principal strain (σ_1) across shear span for specimen SFRC12W6 at normalized shear stress of $5.0\sqrt{f'_c}$.

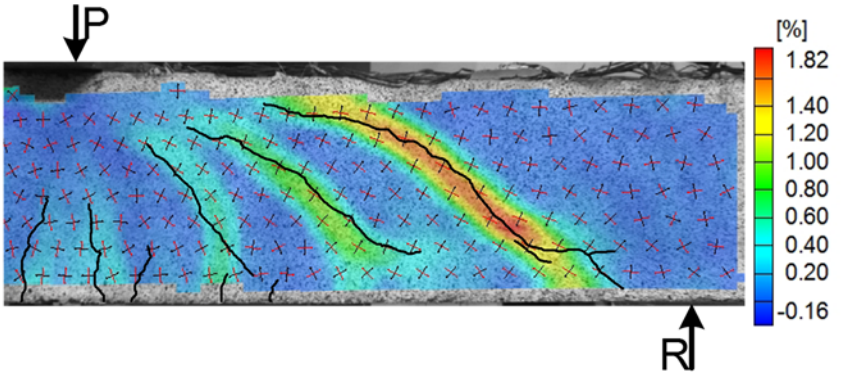

Figure 4.88 Full-field concrete maximum principal strain (σ_1) across shear span for specimen SFRC12W6 at normalized shear stress of $6.0\sqrt{f'_c}$.

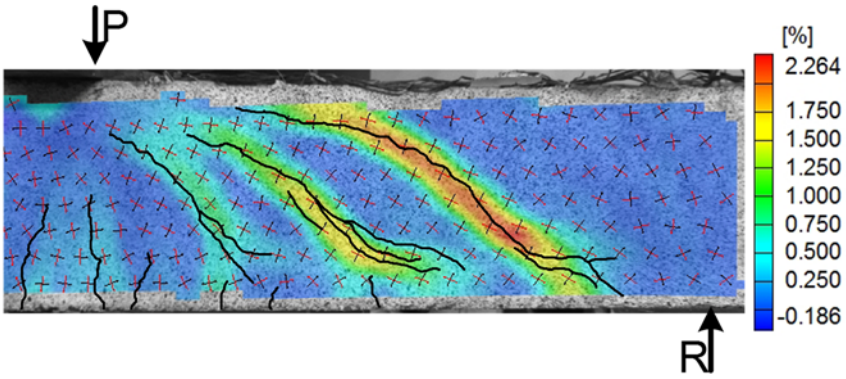

Figure 4.89 Full-field concrete maximum principal strain (σ_1) across shear span for specimen SFRC12W6 at normalized shear stress of $6.5\sqrt{f'_c}$.

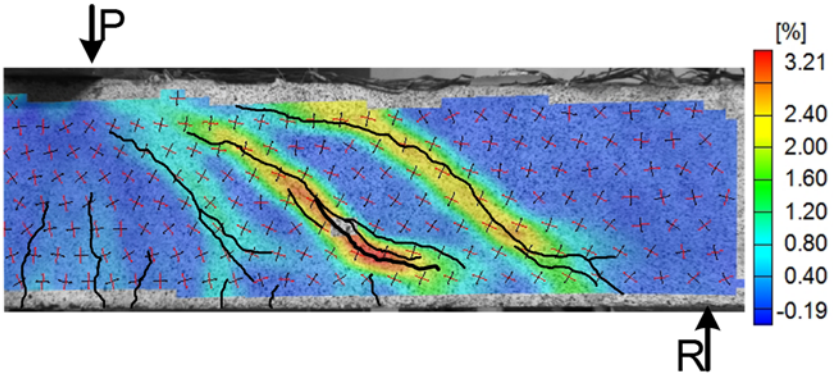

Figure 4.90 Full-field concrete maximum principal strain (σ_1) across shear span for specimen SFRC12W6 at normalized shear stress of $6.9\sqrt{f'_c}$.

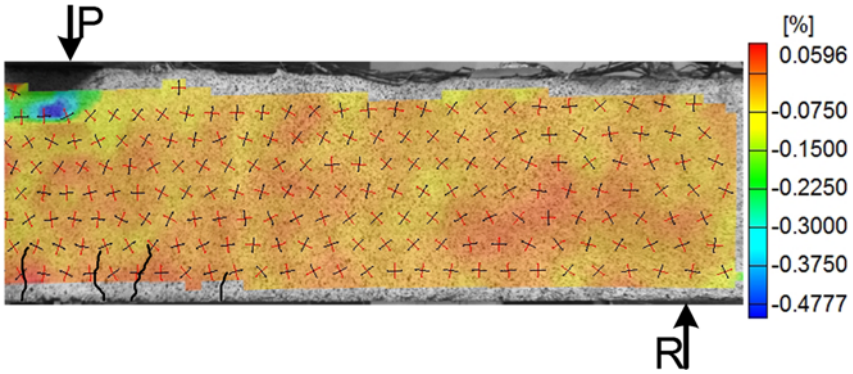

Figure 4.91 Full-field concrete minimum principal strain (σ_2) across shear span for specimen SFRC12W6 at normalized shear stress of $2.5\sqrt{f'_c}$.

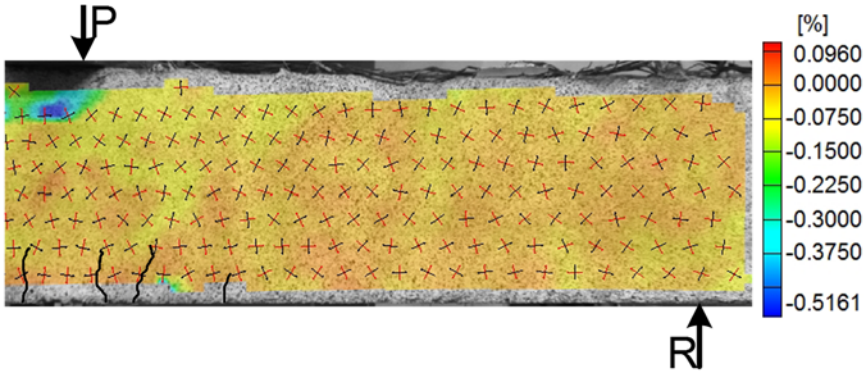

Figure 4.92 Full-field concrete minimum principal strain (σ_2) across shear span for specimen SFRC12W6 at normalized shear stress of $3.0\sqrt{f'_c}$.

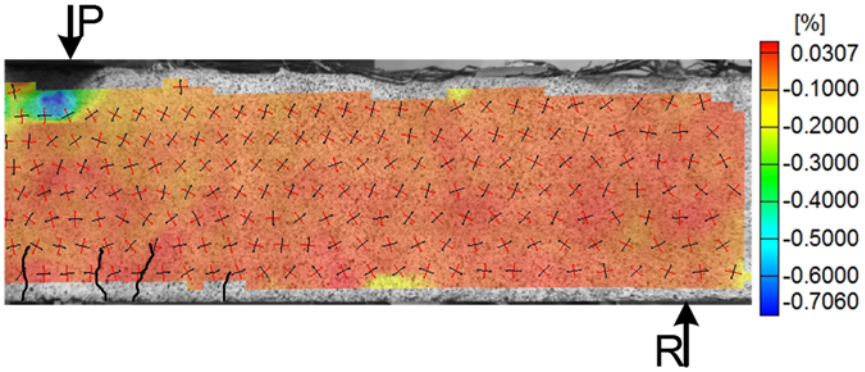

Figure 4.93 Full-field concrete minimum principal strain (σ_2) across shear span for specimen SFRC12W6 at normalized shear stress of $4.0\sqrt{f'_c}$.

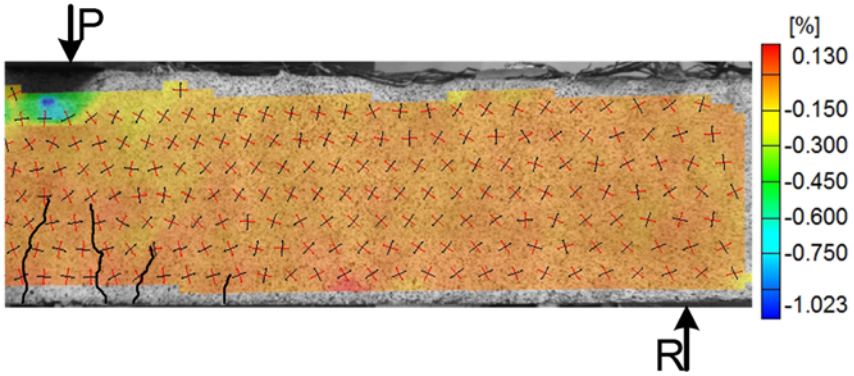

Figure 4.94 Full-field concrete minimum principal strain (σ_2) across shear span for specimen SFRC12W6 at normalized shear stress of $5.0\sqrt{f'_c}$.

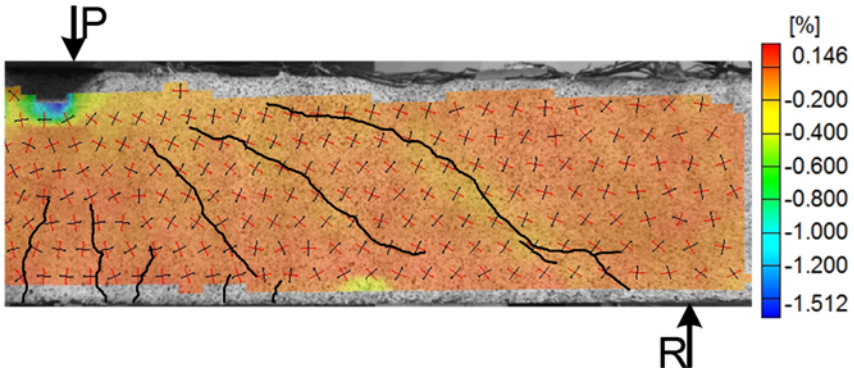

Figure 4.95 Full-field concrete minimum principal strain (σ_2) across shear span for specimen SFRC12W6 at normalized shear stress of $6.0\sqrt{f'_c}$.

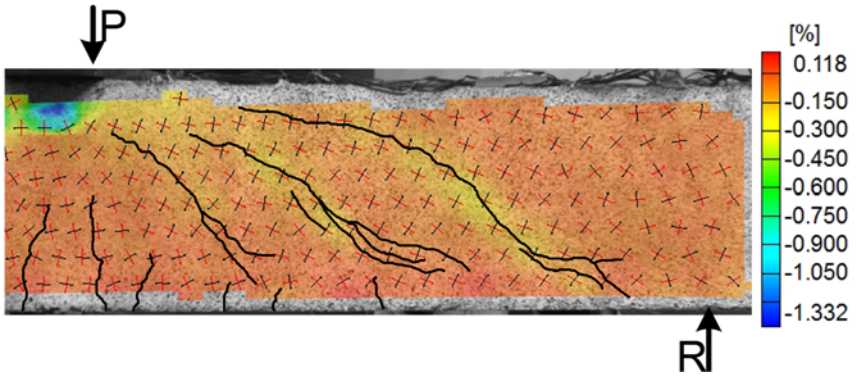

Figure 4.96 Full-field concrete minimum principal strain (σ_2) across shear span for specimen SFRC12W6 at normalized shear stress of $6.5\sqrt{f'_c}$.

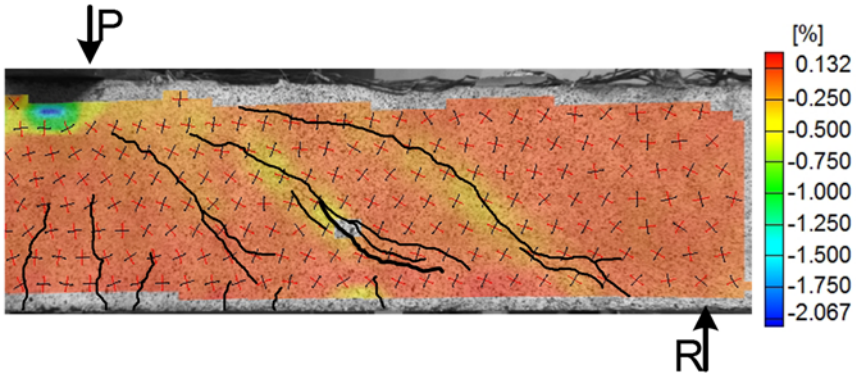

Figure 4.97 Full-field concrete minimum principal strain (σ_2) across shear span for specimen SFRC12W6 at normalized shear stress of $6.9\sqrt{f'_c}$.

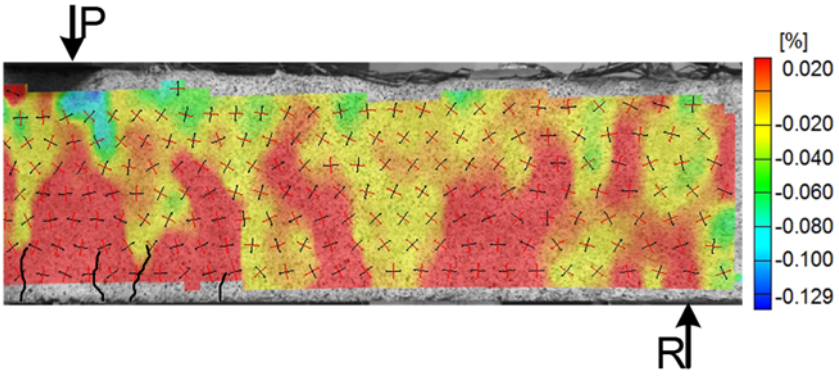

Figure 4.98 Scaled full-field concrete longitudinal strain (ε_x) across shear span for specimen SFRC12W6 at normalized shear stress of $2.5\sqrt{f'_c}$.

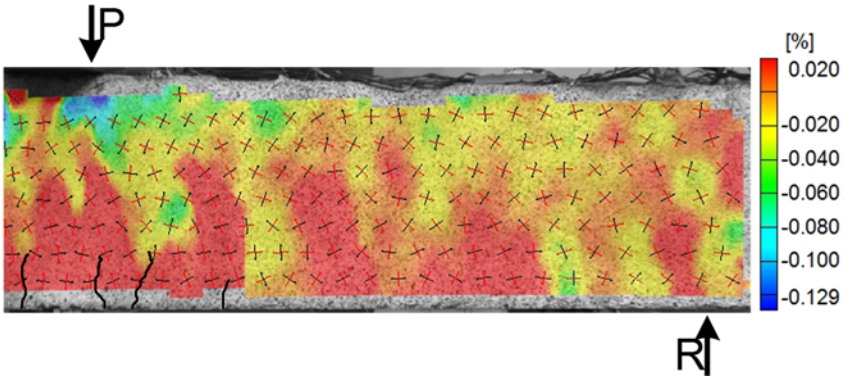

Figure 4.99 Scaled full-field concrete longitudinal strain (ε_x) across shear span for specimen SFRC12W6 at normalized shear stress of $3.0\sqrt{f'_c}$.

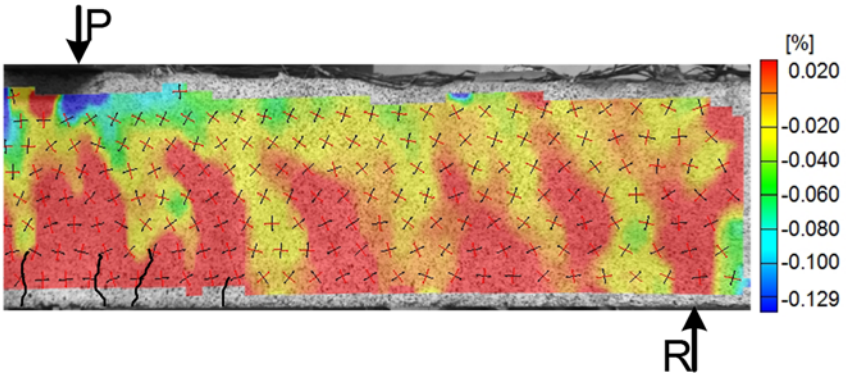

Figure 4.100 Scaled full-field concrete longitudinal strain (ε_x) across shear span for specimen SFRC12W6 at normalized shear stress of $4.0\sqrt{f'_c}$.

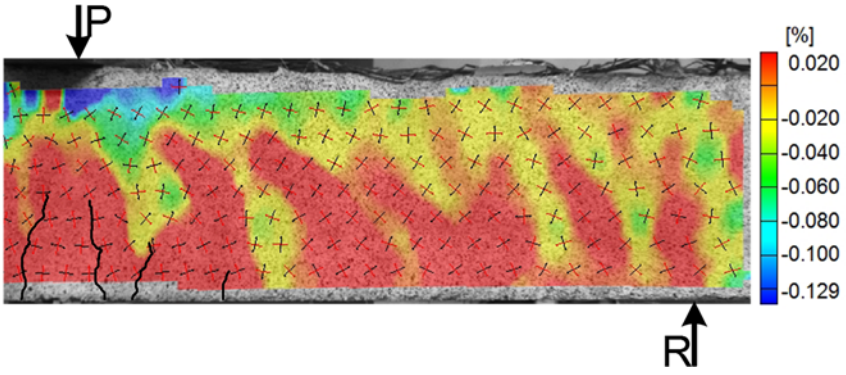

Figure 4.101 Scaled full-field concrete longitudinal strain (ε_x) across shear span for specimen SFRC12W6 at normalized shear stress of $5.0\sqrt{f'_c}$.

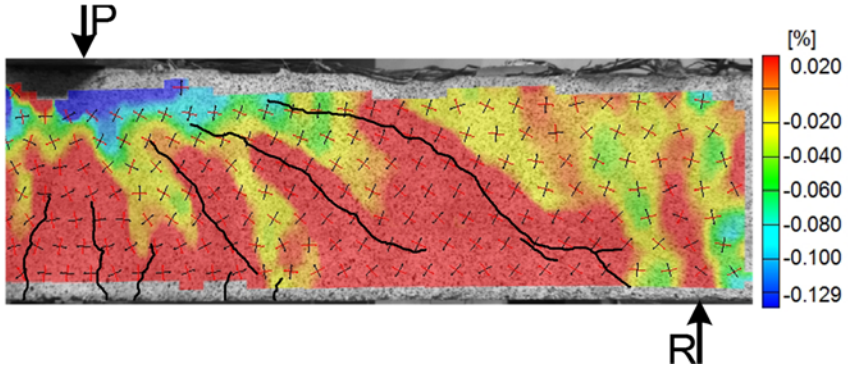

Figure 4.102 Scaled full-field concrete longitudinal strain (ε_x) across shear span for specimen SFRC12W6 at normalized shear stress of $6.0\sqrt{f'_c}$.

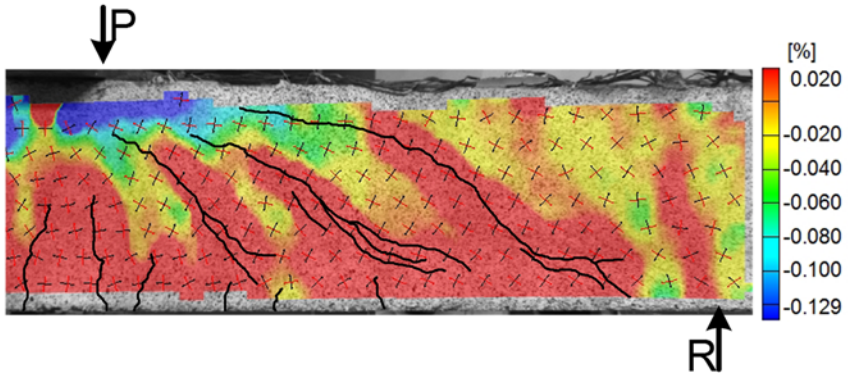

Figure 4.103 Scaled full-field concrete longitudinal strain (ε_x) across shear span for specimen SFRC12W6 at normalized shear stress of $6.5\sqrt{f'_c}$.

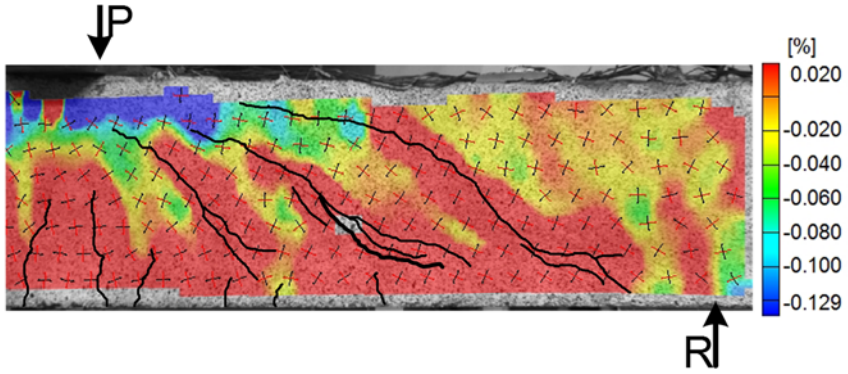

Figure 4.104 Scaled full-field concrete longitudinal strain (ε_x) across shear span for specimen SFRC12W6 at normalized shear stress of $6.9\sqrt{f'_c}$.

4.2.2 Beam SFRC12W24

4.2.2.1 Load-deflection relationship, crack pattern, and failure mode

Figure 4.105 and Figure 4.106, respectively picture the load versus deflection relationship of beam SFRC12W24 and the corresponding cracking pattern at various loading stages. The first visible flexural crack appeared at the middle zone of the beam when the external load attained 40 kips corresponding to shear stress of $1.28\sqrt{f'_C}$ psi. As seen from Figure 4.105, the formation of the first flexural crack slightly reduced the beam stiffness. Nevertheless, the increase in the applied load linearly continued up to load 145 kips. In the meantime, a number of flexural cracks gradually developed one after the other along the shear span to the support, and those being already developed further propagated in the beam web (Figure 4.106). At Load 145 kips corresponding to shear stress of $4.6\sqrt{f'_c}$ psi, the first shear crack emerged in the form of flexural-shear crack that resulted in a further reduction in the load-deflection curve slope. Beyond this load, the beam showed a non-linear behavior with gradually decreasing slope up to the failure. While the load increased, the specimen developed multiple web shear cracks that propagated toward the loading point. The multiple shear cracking characterizing SFRC beams could be in fact, attributed to the internal stress redistribution resulting from fiber bridging effect. This is contrary to RC beams, where the failure mostly occurs immediately after the development of first inclined crack. As illustrated by Figure 4.106, after the load reached 160 kips (shear stress of $5.12\sqrt{f'_c}$ psi), the propagation of the existing cracks seemed to slow down or totally vanish at a certain radius from the loading point. Finally, at load 215 kips (shear stress of $6.9\sqrt{f'_c}$ psi), the sudden propagation of critical crack all the way to the edge of the beam in compression zone caused the two concrete portions at the both sides of the critical crack to become separated and have a vertical movement relative to one another.

This was identified as a primary reason for the peak load to drop and the consequent beam failure. The mode of failure was classified as tension failure in compression zone. Note, at failure, no sign of concrete crushing or dowel action destruction were observed on the beam side facing to the DIC cameras. On the other hand, on the opposite side, the significant interface-slipping of the critical crack due to the compression zone fracture led the critical crack to advance downward from the lower end and propagate along the bottom layer of the reinforcement. A view of failure on both sides of the beam is shown in Figure 4.107. As inferred, beams SFRC12W6 and SFRC12W24 resembled in their overall shear behavior in terms of cracking patter, mode of failure, and ultimate shear strength. The identical ultimate shear strength recorded for the two specimens ($6.9\sqrt{f'_c}$ psi) implies that width has no effect on ultimate shear strength of SFRC beams. This finding was already validated for plain concrete beams by Kani et al. (1979) and Lubell et al. (2004).

4.2.2.2 Strain in reinforcing bars

Figure 4.108 illustrates load-reinforcement strain response for beam SFRC12W24. Among all the applied gauges, strain gauges 3, 4, and 11 malfunctioned from the beginning of the experiment. Two Strain gauges, S1 and S2 showed similar strain pattern up to the beam failure. The reinforcement strain in these two locations varied in a linear relationship with the external load. Similarly, after the initiation of the first flexural crack, the strains still increased linearly, though with a higher rate. The variation of strains at the locations of gauges S5 to S10 followed also rather the same trend by an increase in the applied load except that at each of those locations, the strain variation rate was not constant and altered in the recognition of any new adjacent shear crack. The strain responses shown by gauges S12 and S14 were nearly of the same order up to the first shear cracking at 145 kips. Prior to the first shear cracking, the strains at these locations were excessively small near to zero. This is due to the fact that gauges S12 and S14 were measuring the reinforcement

strains above the center and exterior face of the support, respectively, where the bending moment was zero. When the load exceeded 145 kips, the strain began to escalade in the two locations due to the developing shear cracks in the vicinity of the gauges. As illustrated by Figure 4.108, the load-strain relationship curves recorded by gauges S6, S7, and S9 indicated a lower incremental strain rate approximately beyond load160 kips than what would have been expected to be based on the trend observed for the curves before that load. This phenomenon can be attributed to the fact that the reinforcement became locally unbonded at the gauge positions at load 160 kips due to the local cracking.

At the peak load, the strains measured by gauges S1 through S6 and S8 were in excess of the yielding strain reported by Dinh (2009) for #6 bars at 2570 με. The reinforcement at the rest of the locations did not yield. This can be also inferred by Figure 4.109. Figure 4.109 indicates the distribution of longitudinal strain along the reinforcement at different average shear stresses normalized by $\sqrt{f'_c}$. Like specimen SFRC12W6, for the lower range of average shear stresses before shear cracking, the strains were linearly distributed along the reinforcement, as it can be analogized closely with the shape of the moment diagram. After the beam cracked in shear, however, the increase in the reinforcement strain was localized at those adjacent sections to shear cracks that can be explained by the additional strain generated by the shear cracks. In Figure 4.109, strain gauge 13 was noted to reflect a compressive strain at higher loads corresponding to the average shear stresses of $6.0\sqrt{f'_c}$ and $6.9\sqrt{f'_c}$ psi, respectively, what in fact, was in conflict with the tensile strains observed anywhere else along the bar. That can be accounted for by the fact that at such higher loads, the anchorage strength was likely approaching. This can be deduced by a few very tiny cracks appearing over the anchorage zone. Therefore, the bar was bent

downward at that location, and since the strain gauges were mounted on the bottom surface of the bar, the strain gauge measurements were in compression.

4.2.2.3 Full-field visualization of strain components developed on the shear span concrete surface

Full-filed strain components developed on concrete surface throughout shear span for specimen SFRC12W24 were obtained with the aid of DIC technology at different load values and illustrated in Figure 4.110 through Figure 4.137. For the better evaluation of the relationship between cracking pattern and the state of developed stresses acquired by DIC system, the cracks on the other side of the beam at each desired load were integrated into the corresponding DIC processed images.

The scaled full-field concrete longitudinal strain (ε_x) distributions across shear span at different loads for specimen SFRC12W24 were visualized from Figure 4.138 to Figure 4.144. Tensile strains are denoted by red, while other colors (yellow to dark blue) represent various magnitudes of compressive strain in the compression zone.

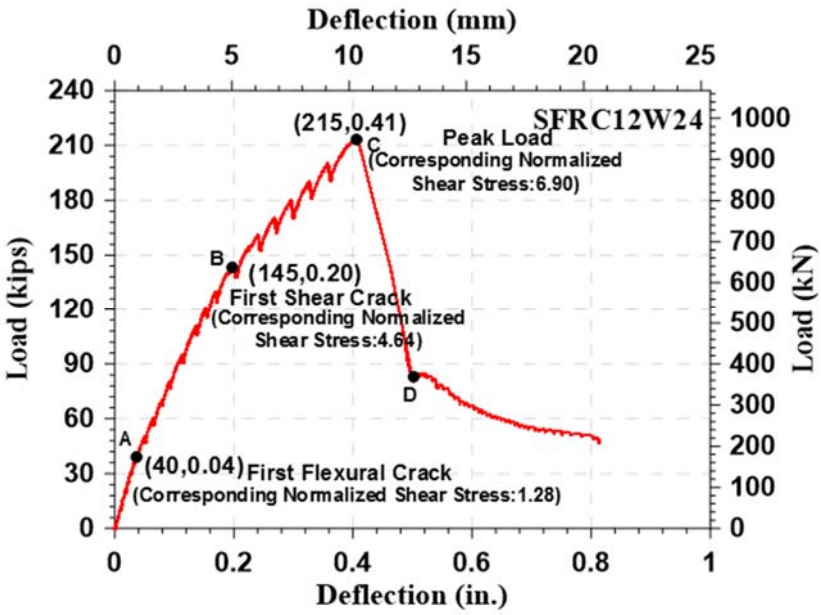

Figure 4.105 load-deflection response for beam SFRC12W24

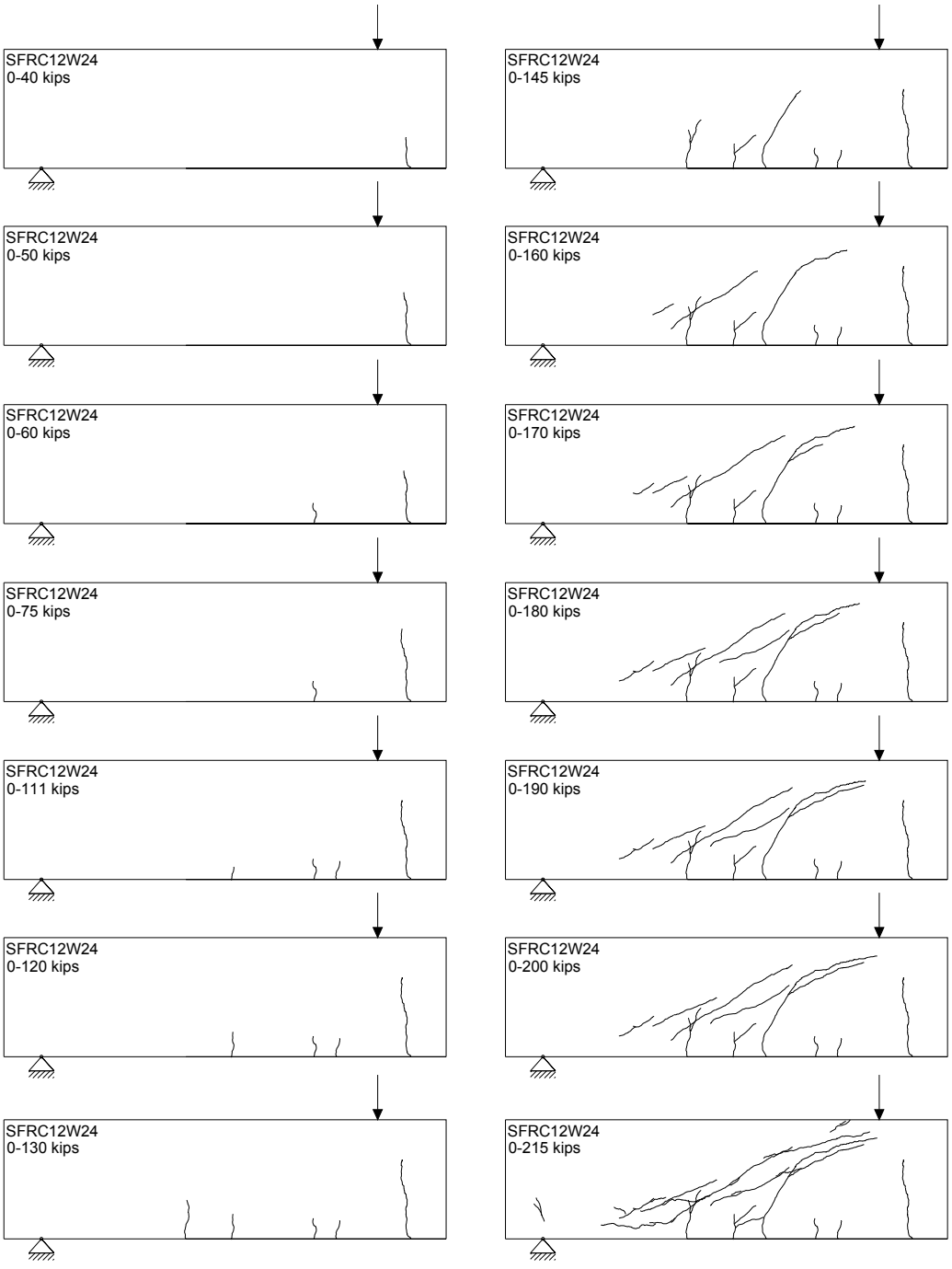

Figure 4.106 Cracking pattern for SFRC12W24 at different load stages

Figure 4.107 A view of failure on both sides of beam SFRC 12W24

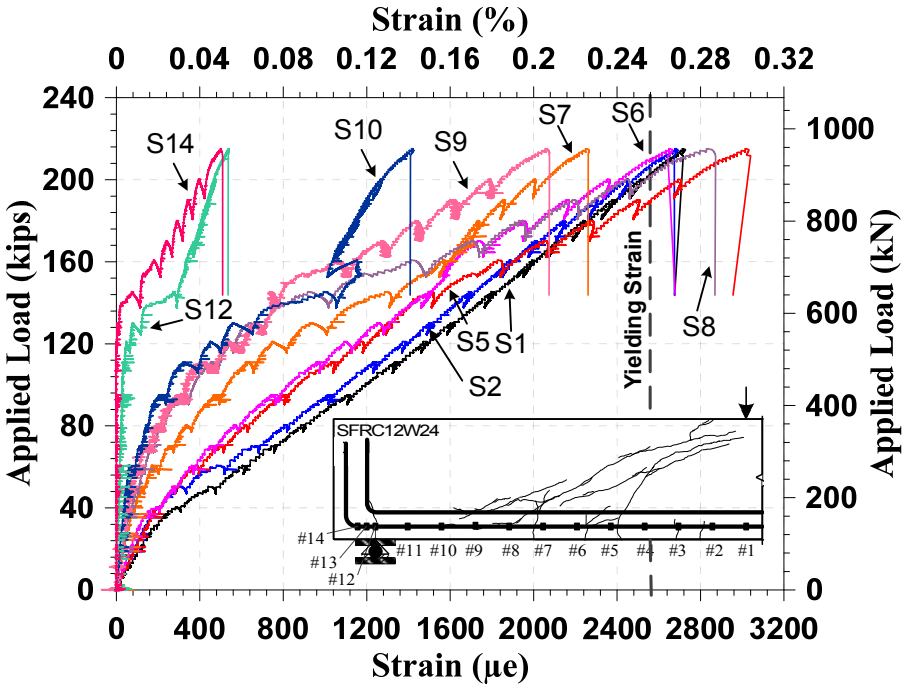

Figure 4.108 Load versus reinforcement strain relationships for beam SFRC12W24

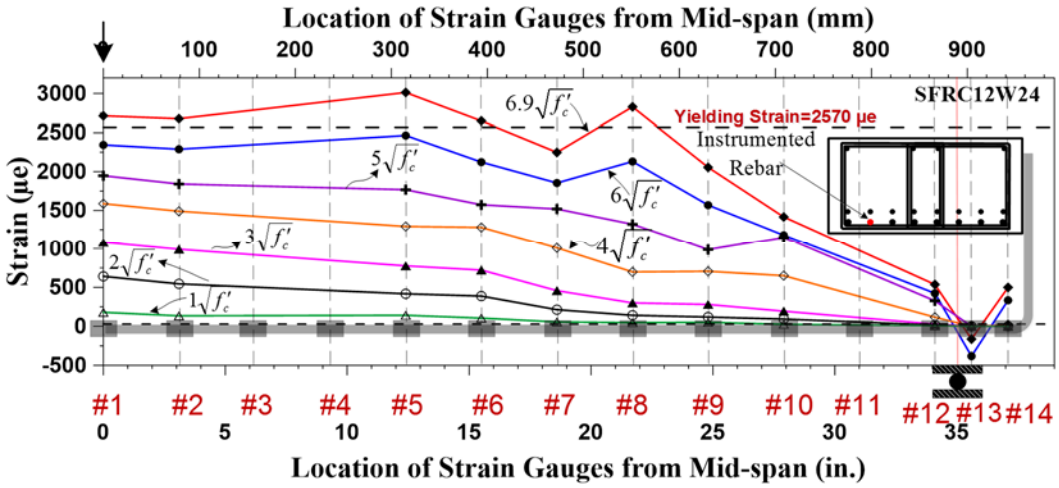

Figure 4.109 Strain variation along an instrumented longitudinal rebar at different normalized shear stresses

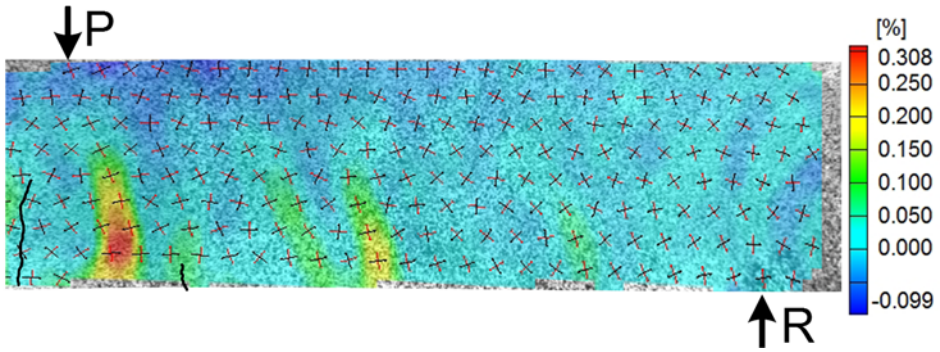

Figure 4.110 Full-field concrete longitudinal strain (ε_x) across shear span for specimen SFRC12W24 at normalized shear stress of $2.5\sqrt{f'_c}$.

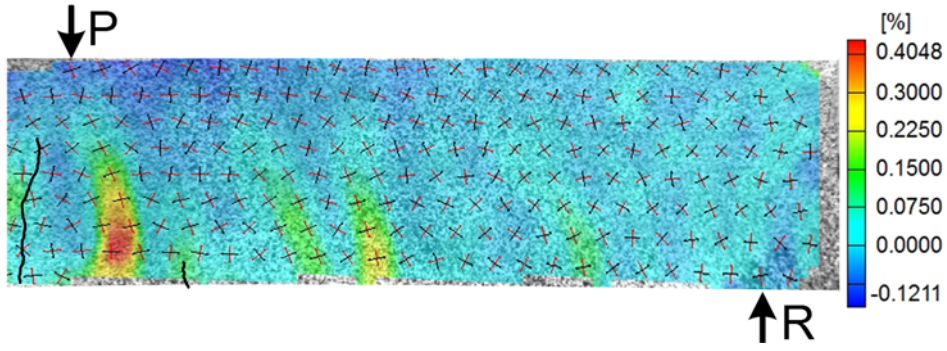

Figure 4.111 Full-field concrete longitudinal strain (ε_x) across shear span for specimen SFRC12W24 at normalized shear stress of $3.0\sqrt{f'_c}$.

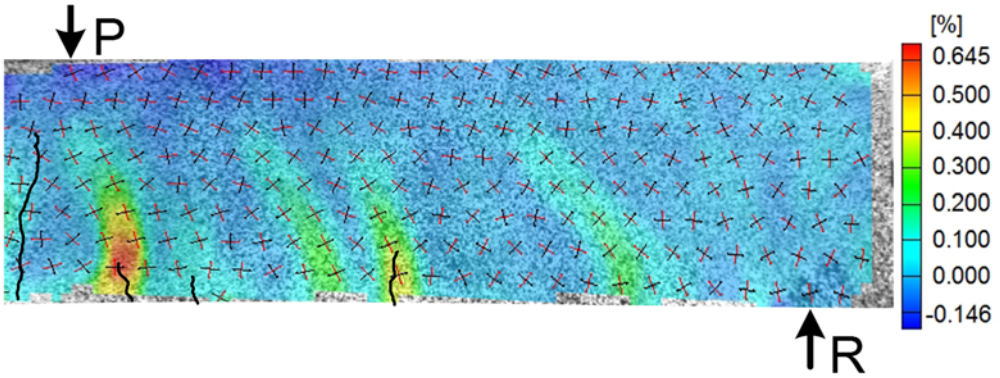

Figure 4.112 Full-field concrete longitudinal strain (ε_x) across shear span for specimen SFRC12W24 at normalized shear stress of $4.0\sqrt{f'_c}$.

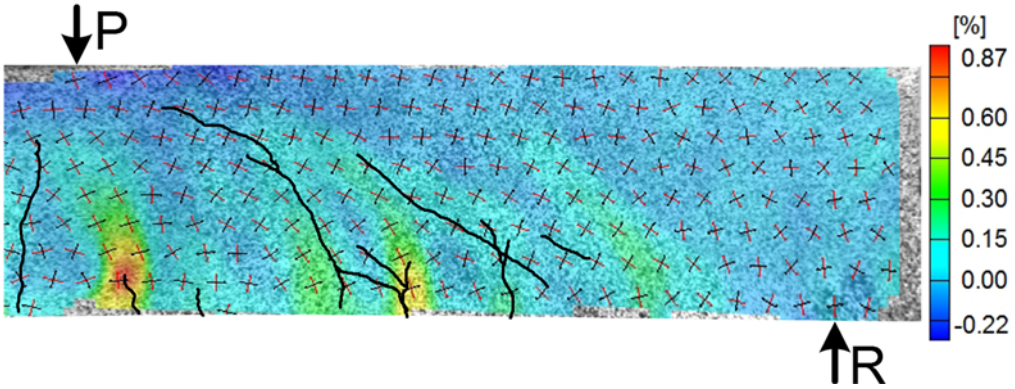

Figure 4.113 Full-field concrete longitudinal strain (ε_x) across shear span for specimen SFRC12W24 at normalized shear stress of $5.0\sqrt{f'_c}$.

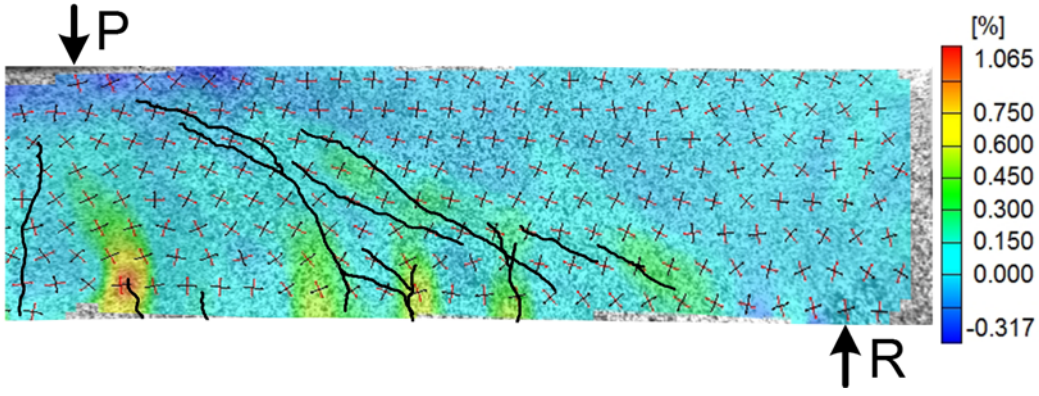

Figure 4.114 Full-field concrete longitudinal strain (ε_x) across shear span for specimen SFRC12W24 at normalized shear stress of $6.0\sqrt{f'_c}$.

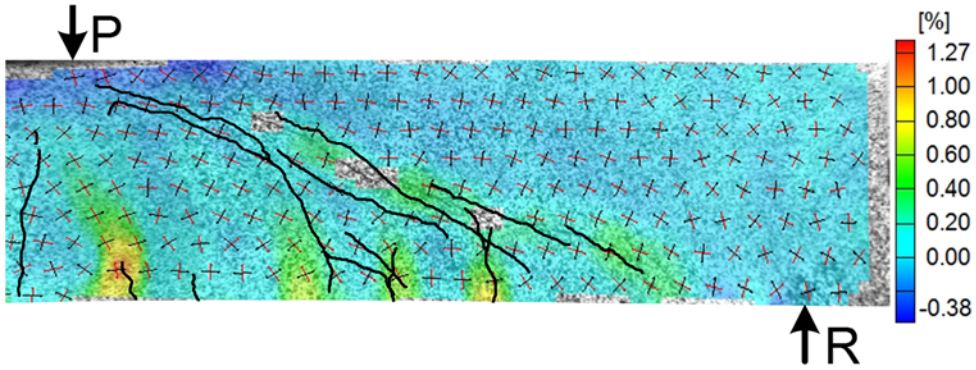

Figure 4.115 Full-field concrete longitudinal strain (ε_x) across shear span for specimen SFRC12W24 at normalized shear stress of $6.5\sqrt{f'_c}$.

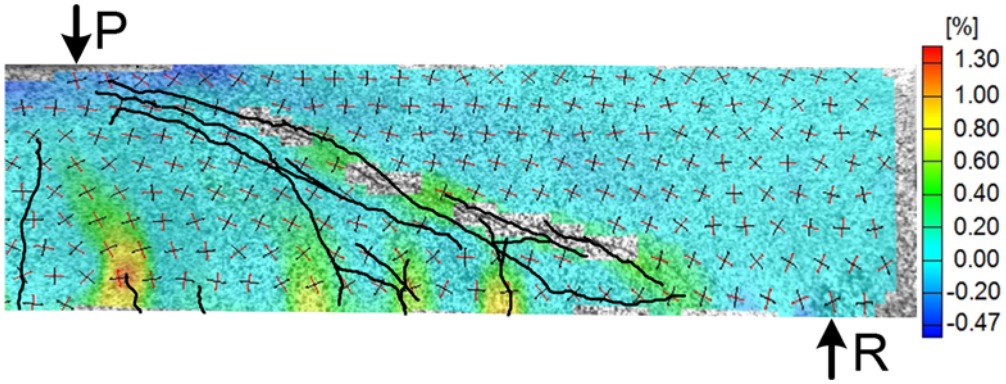

Figure 4.116 Full-field concrete longitudinal strain (ε_x) across shear span for specimen SFRC12W24 at normalized shear stress of $6.9\sqrt{f'_c}$.

Figure 4.117 Full-field concrete transvers strain (ε_y) across shear span for specimen SFRC12W24 at normalized shear stress of $2.5\sqrt{f'_c}$.

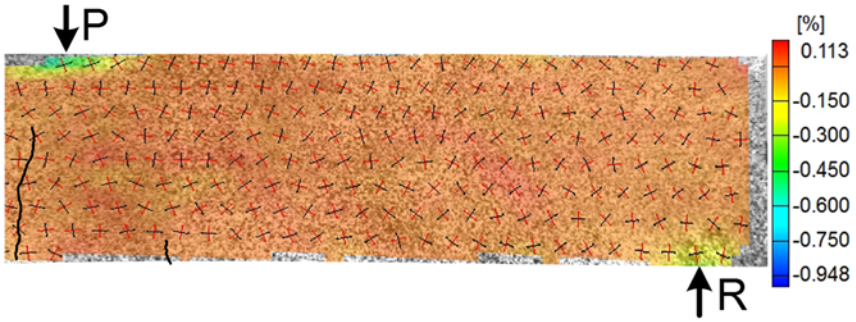

Figure 4.118 Full-field concrete transvers strain (ε_y) across shear span for specimen SFRC12W24 at normalized shear stress of $3.0\sqrt{f'_c}$.

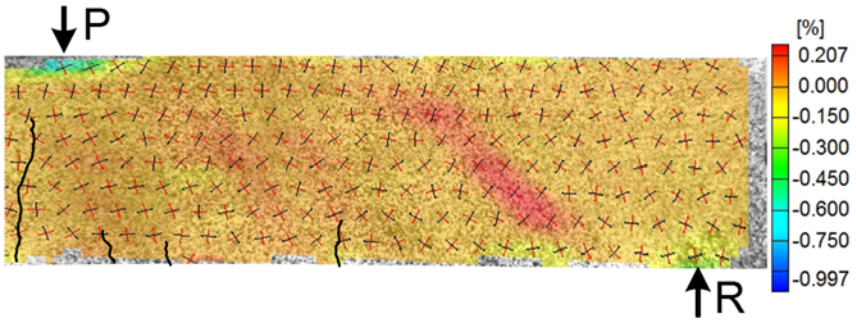

Figure 4.119 Full-field concrete transvers strain (ε_y) across shear span for specimen SFRC12W24 at normalized shear stress of $4.0\sqrt{f'_c}$.

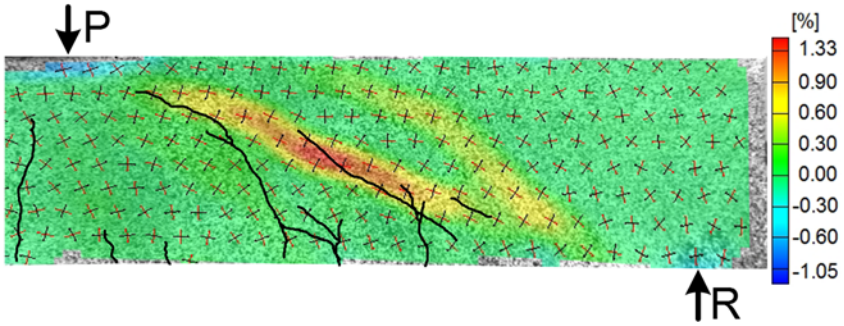

Figure 4.120 Full-field concrete transvers strain (ε_y) across shear span for specimen SFRC12W24 at normalized shear stress of $5.0\sqrt{f'_c}$.

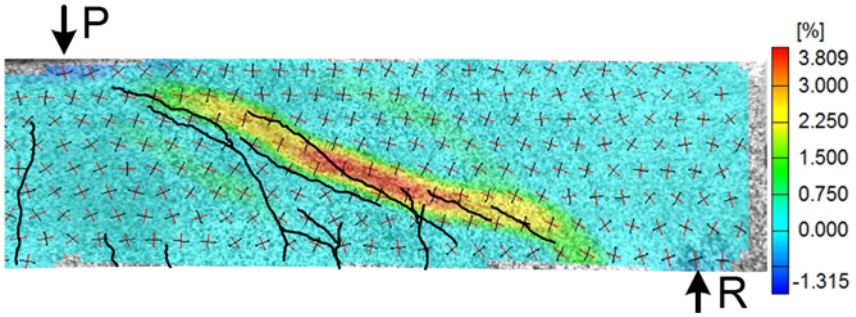

Figure 4.121 Full-field concrete transvers strain (ε_y) across shear span for specimen SFRC12W24 at normalized shear stress of $6.0\sqrt{f'_c}$.

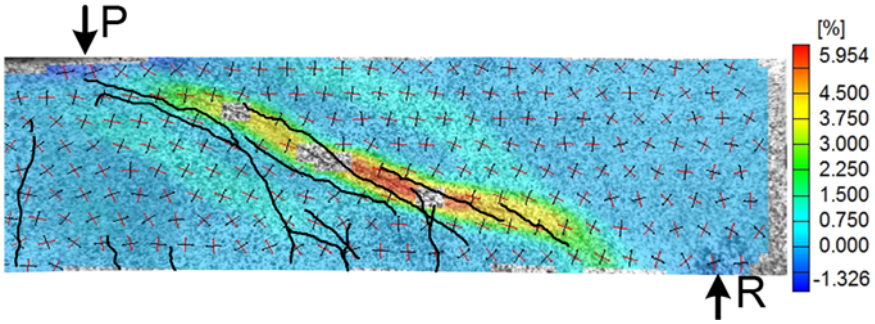

Figure 4.122 Full-field concrete transvers strain (ε_y) across shear span for specimen SFRC12W24 at normalized shear stress of $6.5\sqrt{f'_c}$.

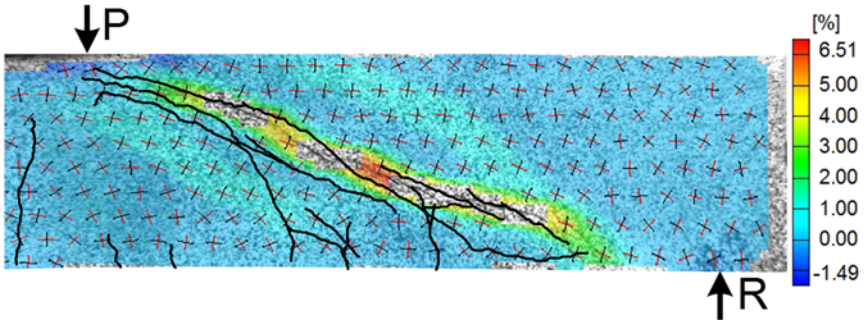

Figure 4.123 Full-field concrete transvers strain (ε_y) across shear span for specimen SFRC12W24 at normalized shear stress of $6.9\sqrt{f'_c}$.

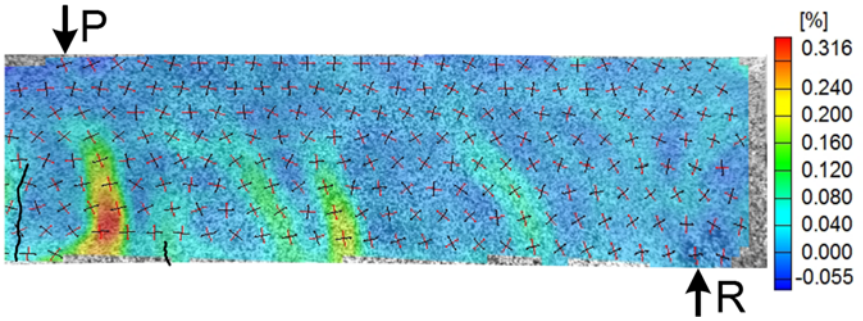

Figure 4.124 Full-field concrete maximum principal strain (σ_1) across shear span for specimen SFRC12W24 at normalized shear stress of $2.5\sqrt{f'_c}$.

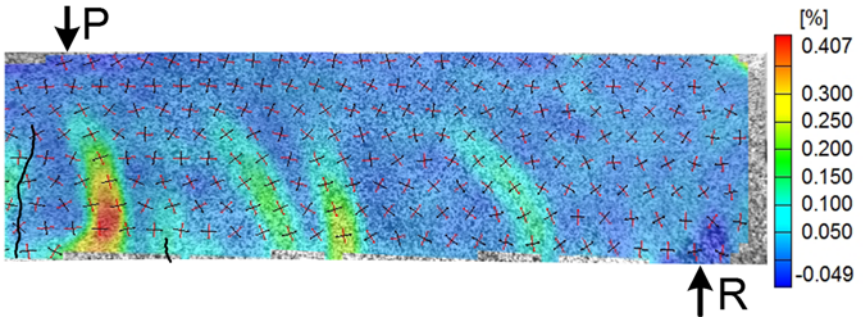

Figure 4.125 Full-field concrete maximum principal strain (σ_1) across shear span for specimen SFRC12W24 at normalized shear stress of $3.0\sqrt{f'_c}$.

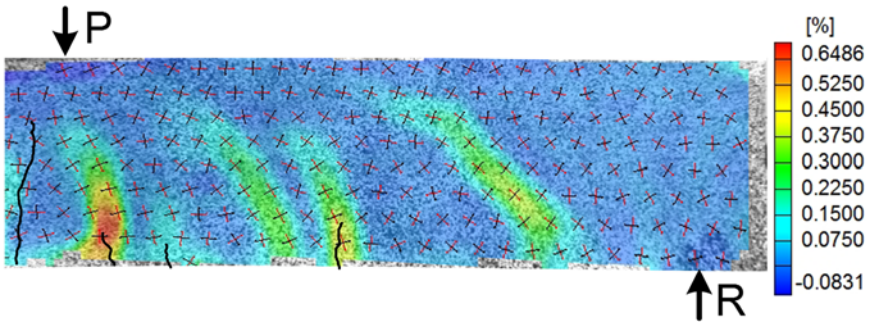

Figure 4.126 Full-field concrete maximum principal strain (σ_1) across shear span for specimen SFRC12W24 at normalized shear stress of $4.0\sqrt{f'_c}$.

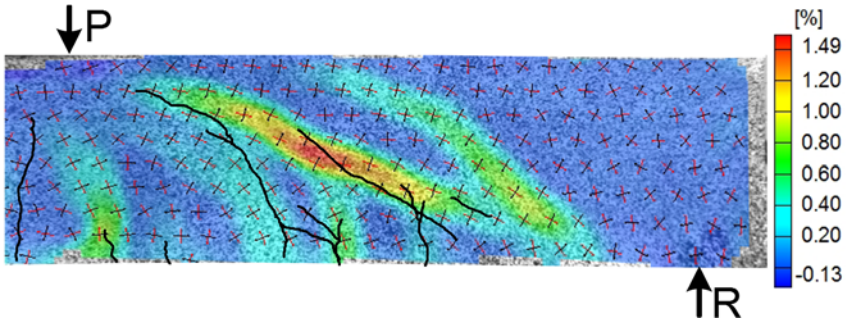

Figure 4.127 Full-field concrete maximum principal strain (σ_1) across shear span for specimen SFRC12W24 at normalized shear stress of $5.0\sqrt{f'_c}$.

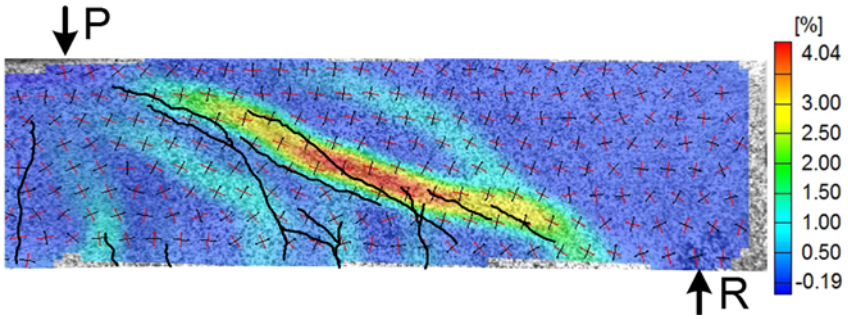

Figure 4.128 Full-field concrete maximum principal strain (σ_1) across shear span for specimen SFRC12W24 at normalized shear stress of $6.0\sqrt{f'_c}$.

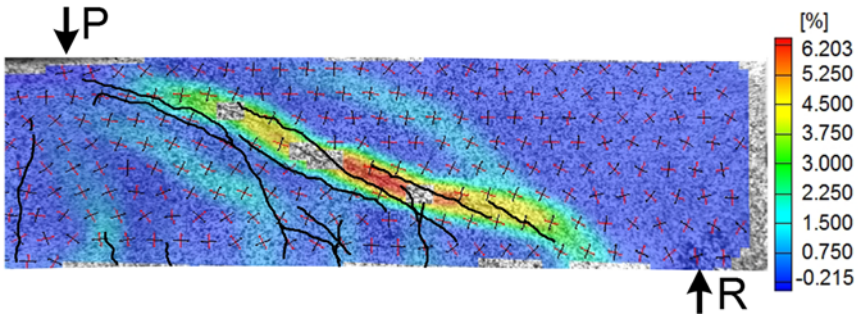

Figure 4.129 Full-field concrete maximum principal strain (σ_1) across shear span for specimen SFRC12W24 at normalized shear stress of $6.5\sqrt{f'_c}$.

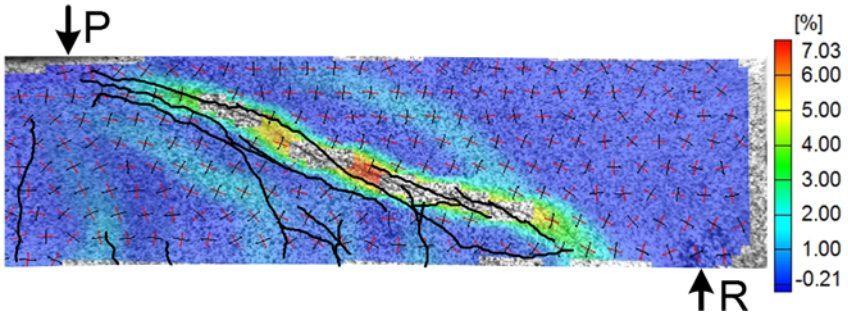

Figure 4.130 Full-field concrete maximum principal strain (σ_1) across shear span for specimen SFRC12W24 at normalized shear stress of $6.9\sqrt{f'_c}$.

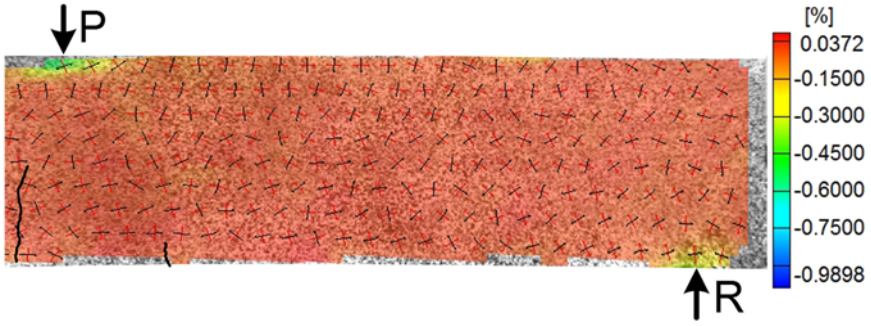

Figure 4.131 Full-field concrete minimum principal strain (σ_2) across shear span for specimen SFRC12W24 at normalized shear stress of $2.5\sqrt{f'_c}$.

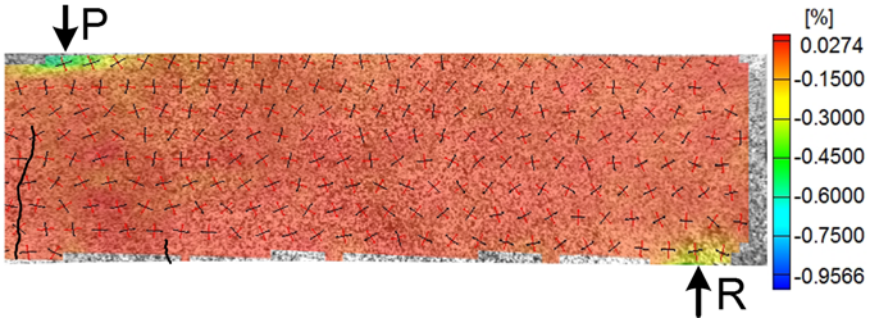

Figure 4.132 Full-field concrete minimum principal strain (σ_2) across shear span for specimen SFRC12W24 at normalized shear stress of $3.0\sqrt{f'_c}$.

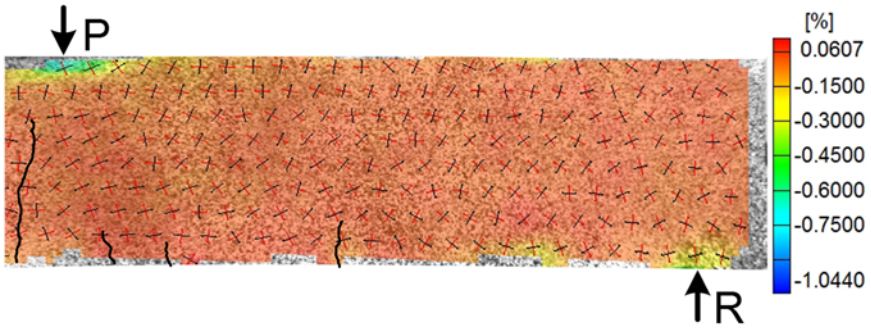

Figure 4.133 Full-field concrete minimum principal strain (σ_2) across shear span for specimen SFRC12W24 at normalized shear stress of $4.0\sqrt{f'_c}$.

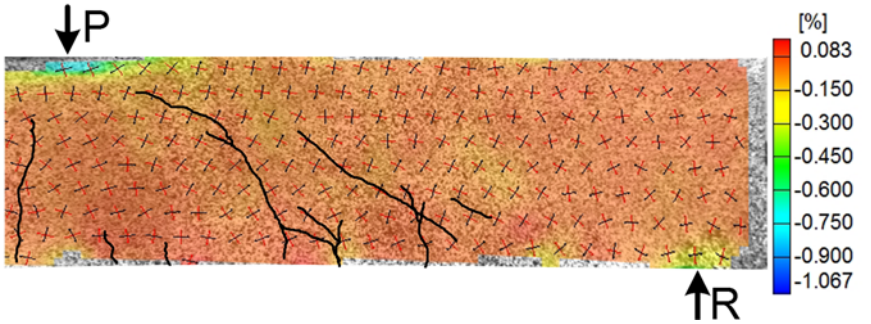

Figure 4.134 Full-field concrete minimum principal strain (σ_2) across shear span for specimen SFRC12W24 at normalized shear stress of $5.0\sqrt{f'_c}$.

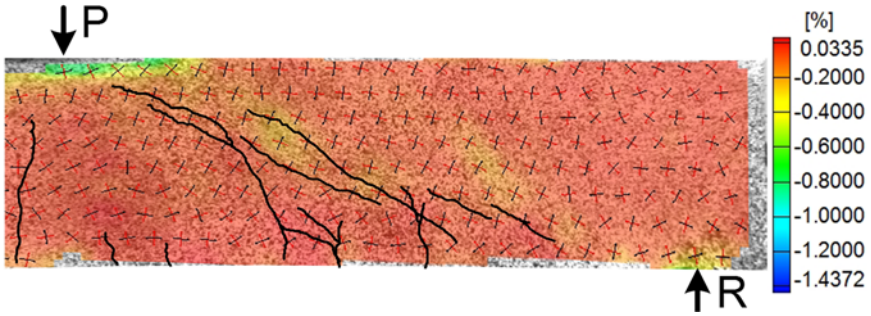

Figure 4.135 Full-field concrete minimum principal strain (σ_2) across shear span for specimen SFRC12W24 at normalized shear stress of $6.0\sqrt{f'_c}$.

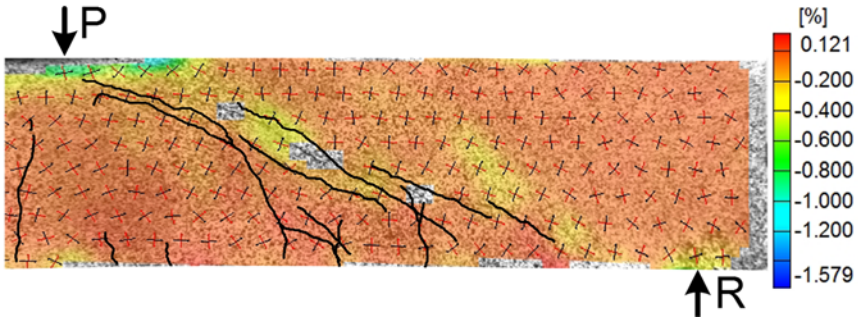

Figure 4.136 Full-field concrete minimum principal strain (σ_2) across shear span for specimen SFRC12W24 at normalized shear stress of $6.5\sqrt{f'_c}$.

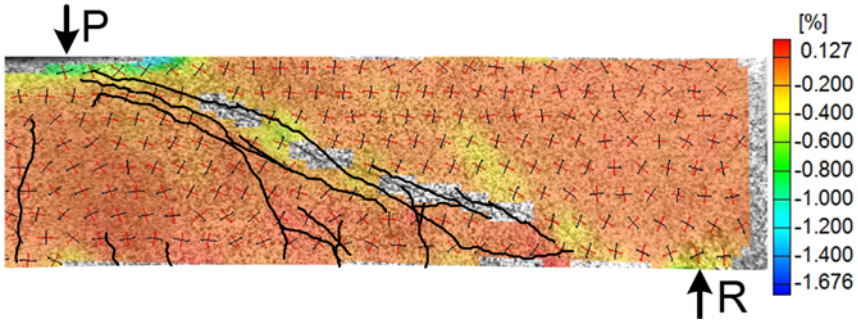

Figure 4.137 Full-field concrete minimum principal strain (σ_2) across shear span for specimen SFRC12W24 at normalized shear stress of $6.9\sqrt{f'_c}$.

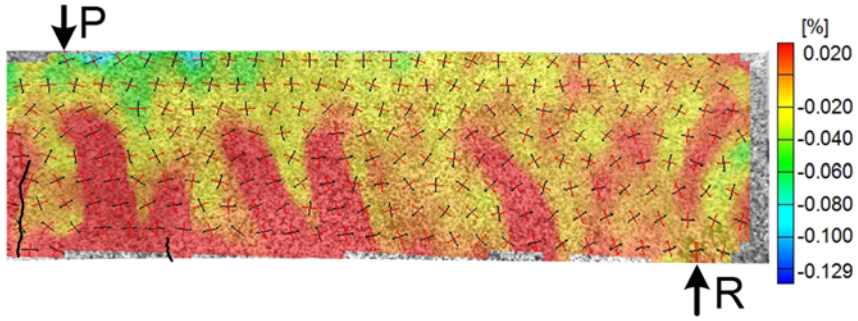

Figure 4.138 Scaled full-field concrete longitudinal strain (ε_x) across shear span for specimen SFRC12W24 at normalized shear stress of $2.5\sqrt{f'_c}$.

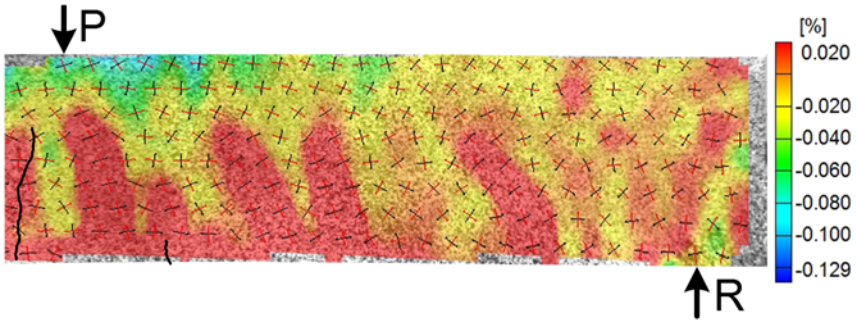

Figure 4.139 Scaled full-field concrete longitudinal strain (ε_x) across shear span for specimen SFRC12W24 at normalized shear stress of $3.0\sqrt{f'_c}$.

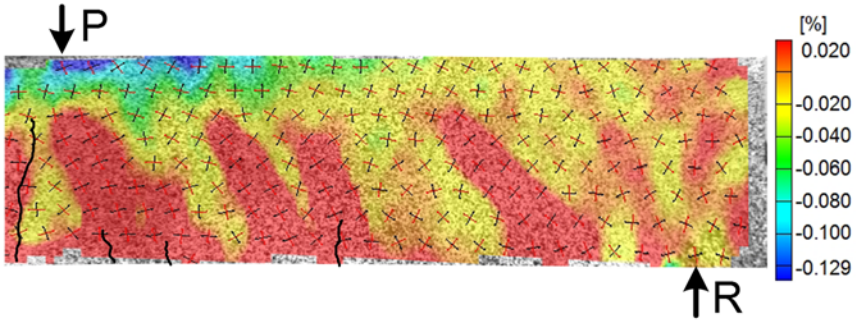

Figure 4.140 Scaled full-field concrete longitudinal strain (ε_x) across shear span for specimen SFRC12W24 at normalized shear stress of $4.0\sqrt{f'_c}$.

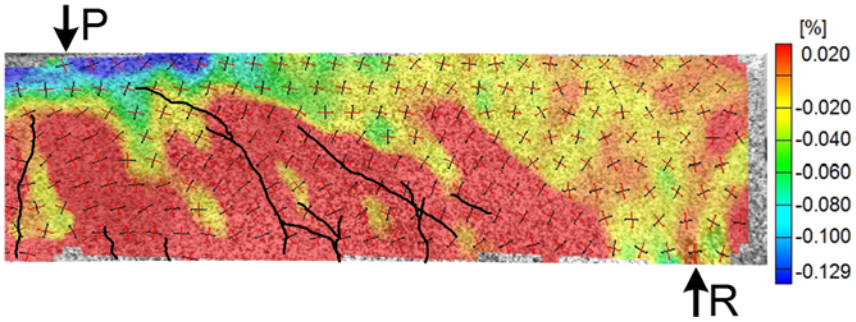

Figure 4.141 Scaled full-field concrete longitudinal strain (ε_x) across shear span for specimen SFRC12W24 at normalized shear stress of $5.0\sqrt{f'_c}$.

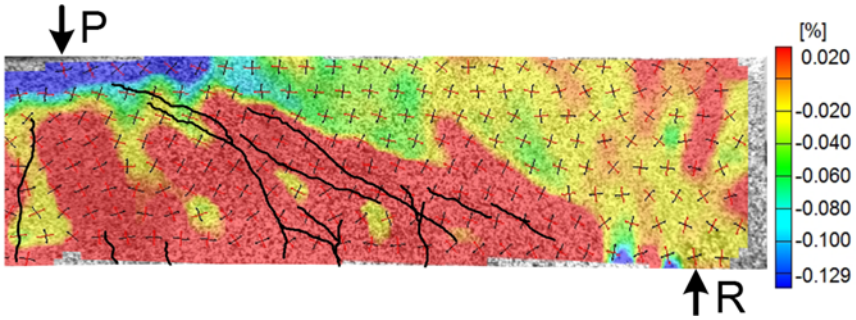

Figure 4.142 Scaled full-field concrete longitudinal strain (ε_x) across shear span for specimen SFRC12W24 at normalized shear stress of $6.0\sqrt{f'_c}$.

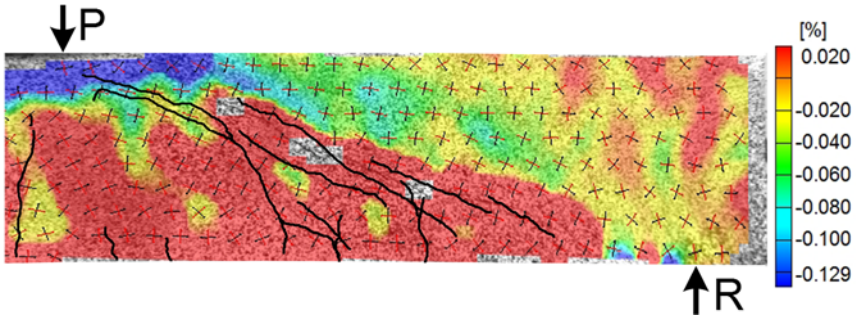

Figure 4.143 Scaled full-field concrete longitudinal strain (ε_x) across shear span for specimen SFRC12W24 at normalized shear stress of $6.5\sqrt{f'_c}$.

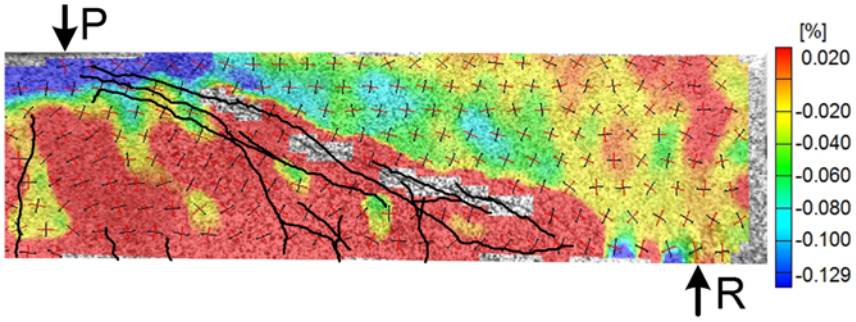

Figure 4.144 Scaled full-field concrete longitudinal strain (ε_x) across shear span for specimen SFRC12W24 at normalized shear stress of $6.9\sqrt{f'_c}$.

4.2.3 Beam SFRC18a

4.2.3.1 Load-deflection relationship, crack pattern, and failure mode

Figure 4.145 and Figure 4.146 represent load versus mid-span deflection response and cracking pattern at diverse loads, respectively for specimen SFRC18a. Flexural crack was first observed at 20 kips (corresponding to shear stress of $1.42\sqrt{f'_c}$ psi). According to Figure 4.145, the external load was linearly varied with respect to the mid-span deflection up to the first shear crack occurrence. As noticed, the flexural cracking was not reflected in the beam stiffness. By increasing the applied load, the beam progressively cracked in flexure at further locations from the loading point. The first shear crack became visible at 45 kips (shear stress of $3.20\sqrt{f'_c}$ psi) in a form of web shear cracking. The shear cracking did not impose a large nonlinearity into the load-deflection curve. At load 55 kips (shear stress of $3.91\sqrt{f'_c}$ psi), one of the existing flexural cracks turned into an inclined shear crack. As depicted by Figure 4.146, except the new flexural-shear crack development, almost no progression had been observed in any of the developed shear and flexural cracks up to load 65 kips, meaning the crack propagation was ceased for about 20 kips above the first shear cracking load. However, at 65 kips (shear stress of $4.63\sqrt{f'_c}$ psi), the leftmost significant shear crack from the loading point suddenly jumped into the compression zone and substantially reduced the intact compression zone depth (Figure 4.146). At that time, the intact compression zone depth was measured at 0.5 inches. Nevertheless, no failure took place, and the beam could even carry a further 8 kips load despite such extremely reduced intact compression zone depth. It is important mentioning that all the cracks, except for the critical crack, were observed to stop at a certain radius from the loading point. At load 73 kips (shear stress of $5.20\sqrt{f'_c}$ psi), eventually the extension of the critical

crack to the beam edge caused the peak load to drop and the consequent failure. Therefore, the failure initiated by tension failure of the compression zone. Point D on Figure 4.145 represents the dowel action breakdown following to the opening of splitting crack along the top layer of the flexural bars. A view of beam SFRC18a at failure is shown in Figure 4.147.

4.2.3.2 Strain in reinforcing bars

Two pairs of strain gauges were installed in the middle of the targeted shear span and under the loading point, respectively. The load versus the average of strains measured by each pair of the gauges is shown in Figure 4.148. The strains measured at the two locations seemed to have the same pattern up to the failure. However, for the entire range of the external load, the reinforcing bar experienced higher strains under the loading point than those measured at the mid-shear span. That could be explained by the fact that no shear crack developed in vicinity of the mid-shear span gauges. Up to the first flexural crack, the strains at both locations rose with the same rate, while after that, the strains under the loading point increased with a higher rate. the formation of shear cracks was not reflected by the gauge measurements irrespective of the mounted locations.

4.2.3.3 Full-field visualization of strain components developed on the shear span concrete surface

Full-filed strain components developed on concrete surface throughout shear span for specimen SFRC18a were obtained with the aid of DIC technology at different load values and illustrated in Figure 4.149 through Figure 4.168. For the better evaluation of the relationship between cracking pattern and the state of developed stresses acquired by DIC system, the cracks on the other side of the beam at each desired load were integrated into the corresponding DIC processed images.

The scaled full-field concrete longitudinal strain (ε_x) distributions across shear span at different loads for specimen SFRC18a were visualized from Figure 4.169 to Figure 4.173. Tensile strains are denoted by red, while other colors (yellow to dark blue) represent various magnitudes of compressive strain in the compression zone.

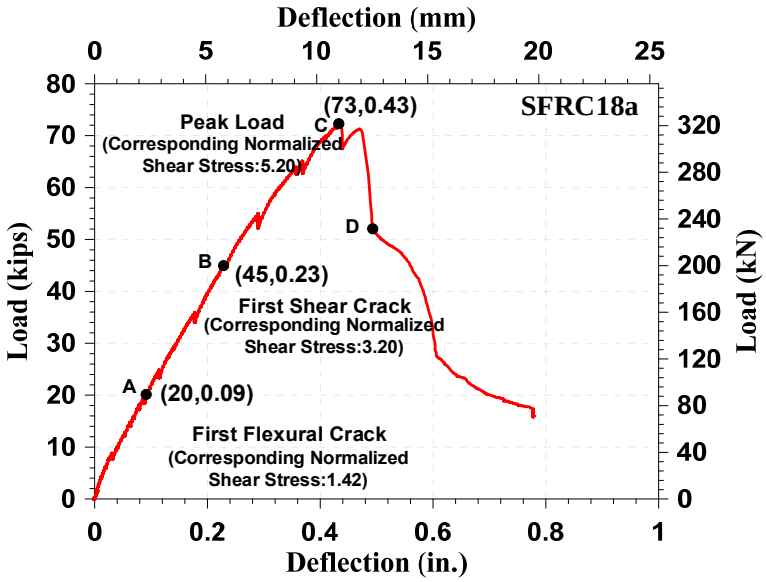

Figure 4.145 load-deflection response for beam SFRC18a

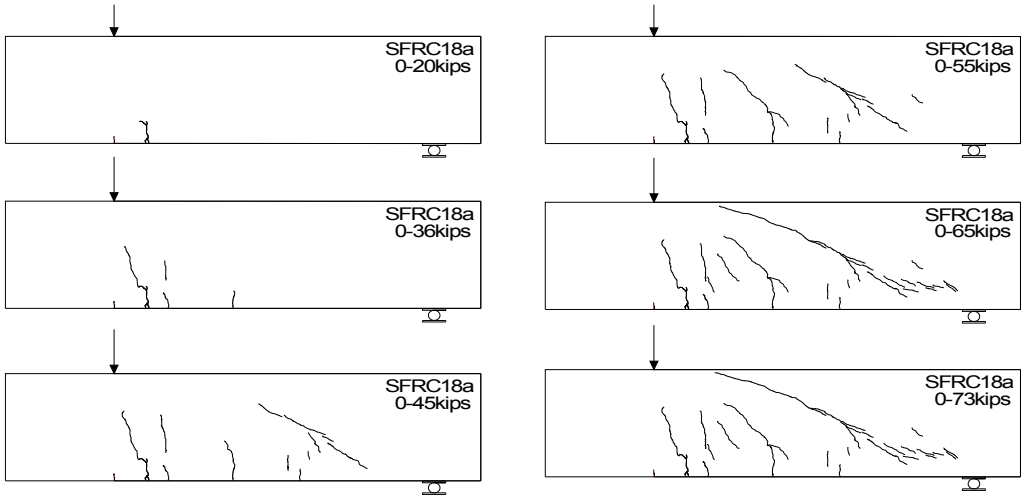

Figure 4.146 Cracking pattern for SFRC18a at different load stages

Figure 4.147 A view of beam SFRC18a at failure

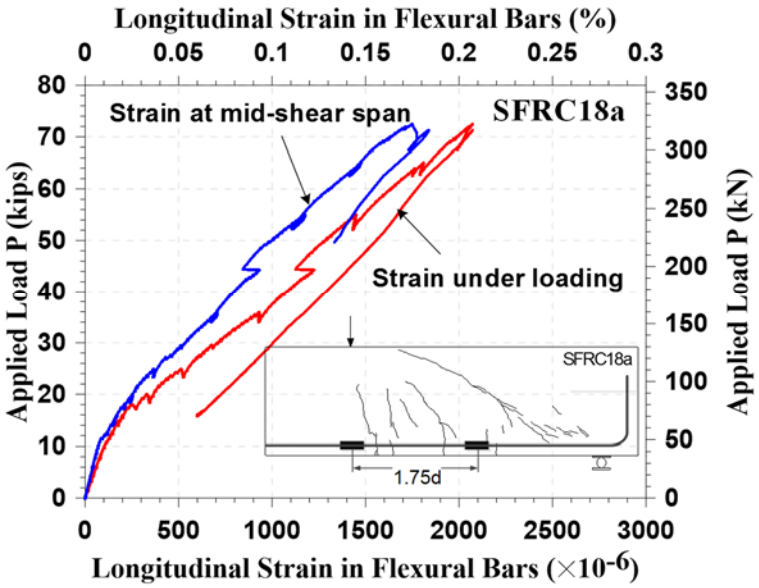

Figure 4.148 Load versus reinforcement strain relationships for beam SFRC18a

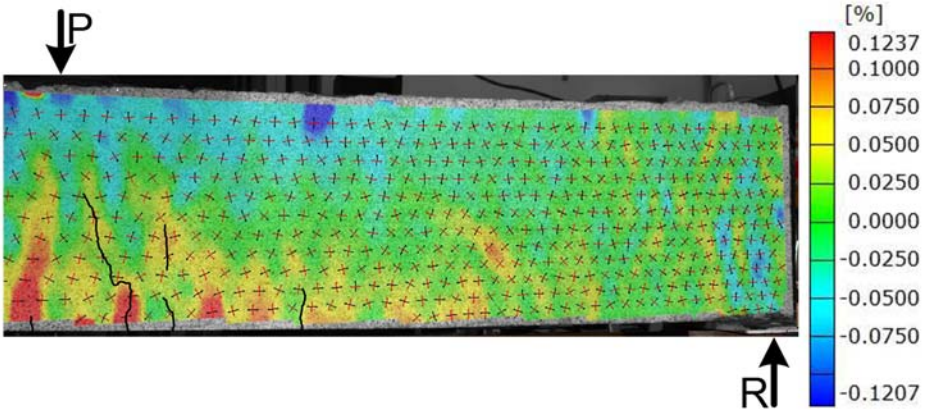

Figure 4.149 Full-field concrete longitudinal strain (ε_x) across shear span for specimen SFRC18a at normalized shear stress of $2.5\sqrt{f'_c}$

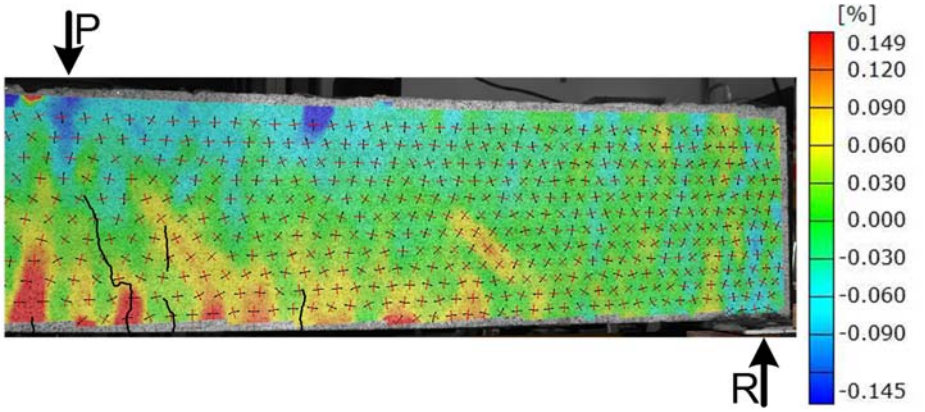

Figure 4.150 Full-field concrete longitudinal strain (ε_x) across shear span for specimen SFRC18a at normalized shear stress of $3.0\sqrt{f'_c}$

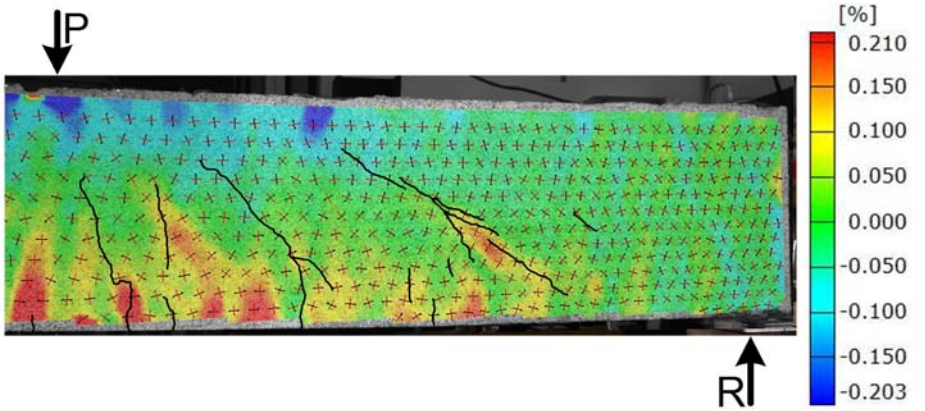

Figure 4.151 Full-field concrete longitudinal strain (ε_x) across shear span for specimen SFRC18a at normalized shear stress of $4.0\sqrt{f'_c}$

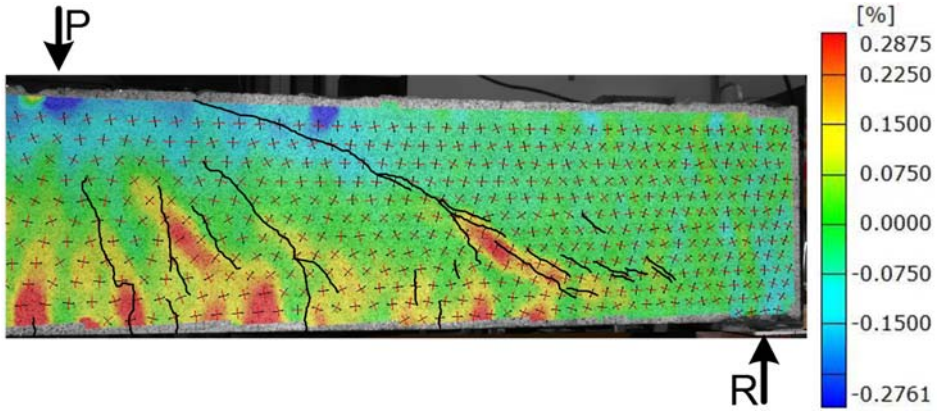

Figure 4.152 Full-field concrete longitudinal strain (ε_x) across shear span for specimen SFRC18a at normalized shear stress of $5.0\sqrt{f'_c}$

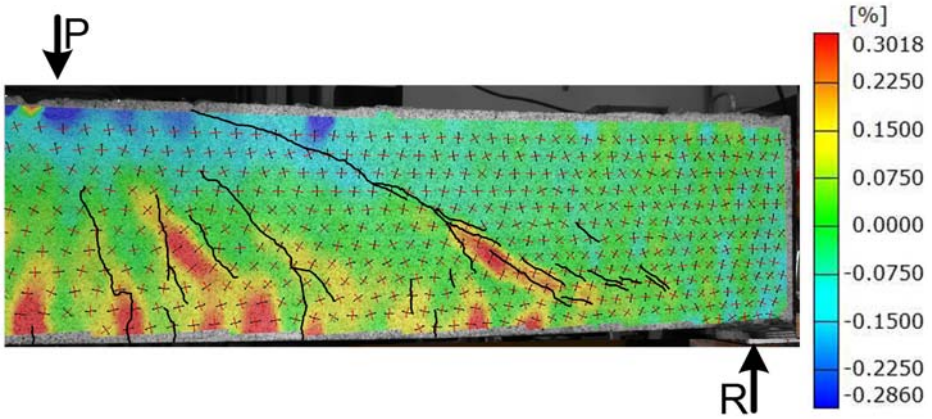

Figure 4.153 Full-field concrete longitudinal strain (ε_x) across shear span for specimen SFRC18a at normalized shear stress of $5.2\sqrt{f'_c}$

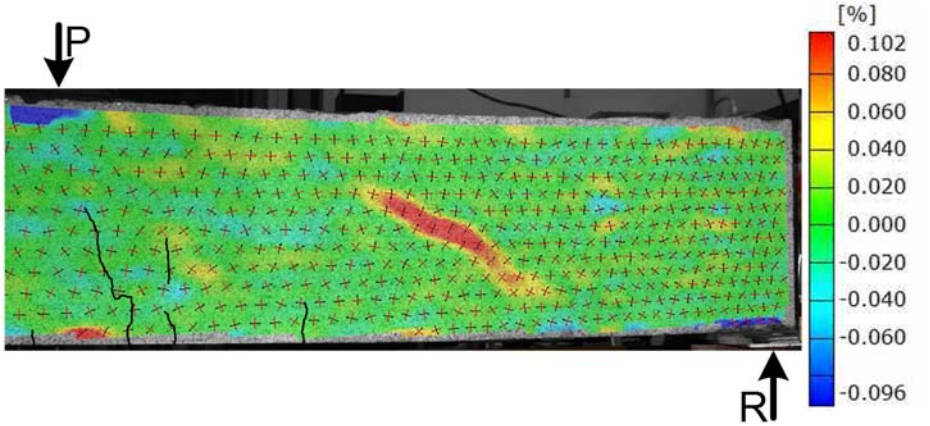

Figure 4.154 Full-field concrete transvers strain (ε_y) across shear span for specimen SFRC18a at normalized shear stress of $2.5\sqrt{f'_c}$

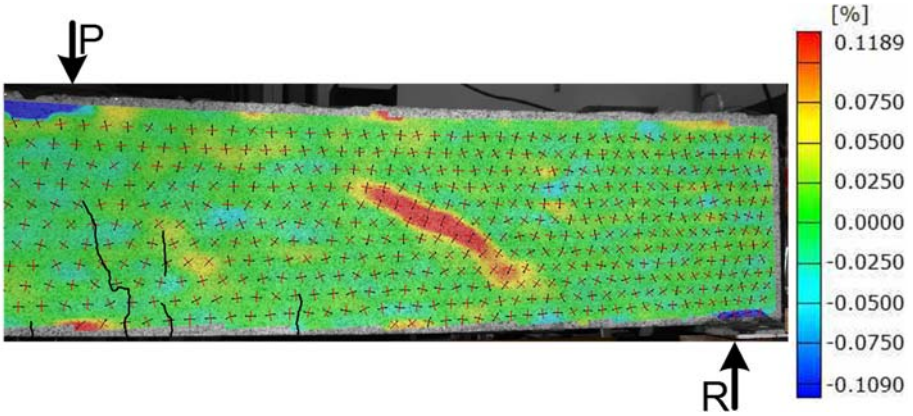

Figure 4.155 Full-field concrete transvers strain (ε_y) across shear span for specimen SFRC18a at normalized shear stress of $3.0\sqrt{f'_c}$

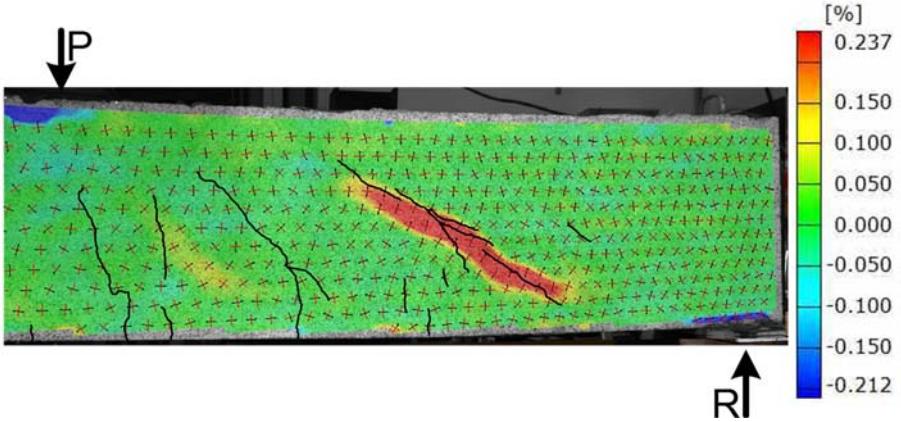

Figure 4.156 Full-field concrete transvers strain (ε_y) across shear span for specimen SFRC18a at normalized shear stress of $4.0\sqrt{f'_c}$

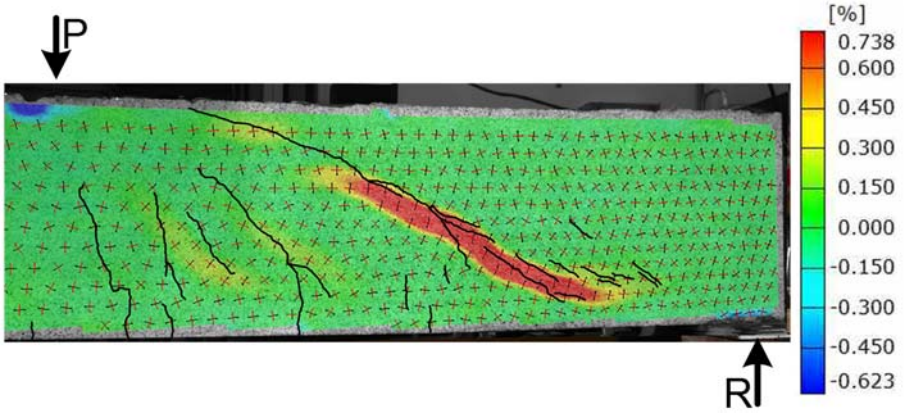

Figure 4.157 Full-field concrete transvers strain (ε_y) across shear span for specimen SFRC18a at normalized shear stress of $5.0\sqrt{f'_c}$

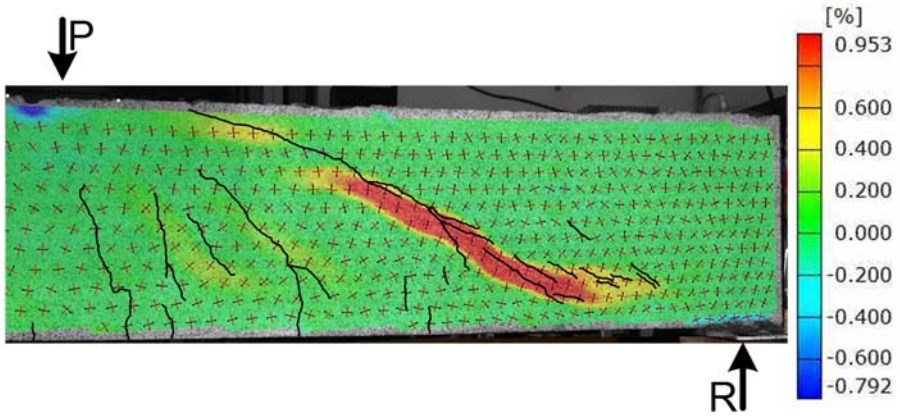

Figure 4.158 Full-field concrete transvers strain (ε_y) across shear span for specimen SFRC18a at normalized shear stress of $5.2\sqrt{f'_c}$

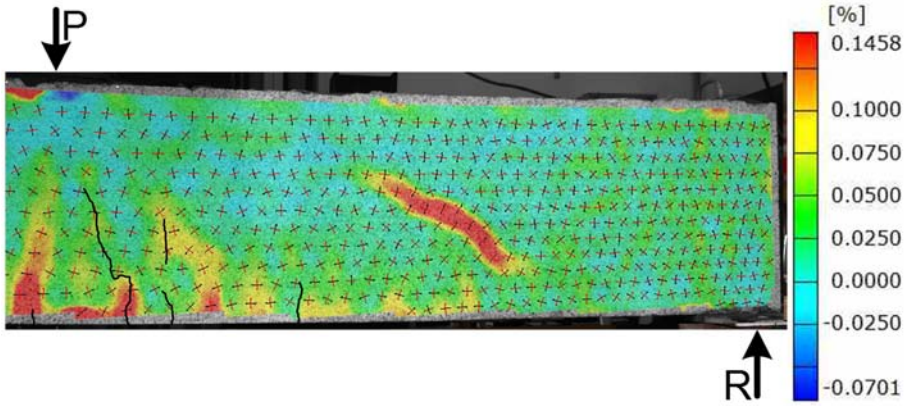

Figure 4.159 Full-field concrete maximum principal strain (σ_1) across shear span for specimen SFRC18a at normalized shear stress of $2.5\sqrt{f'_c}$

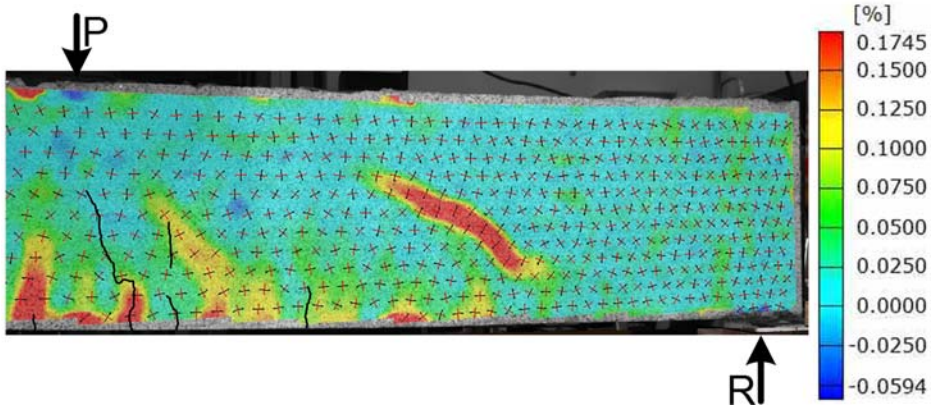

Figure 4.160 Full-field concrete maximum principal strain (σ_1) across shear span for specimen SFRC18a at normalized shear stress of $3.0\sqrt{f'_c}$

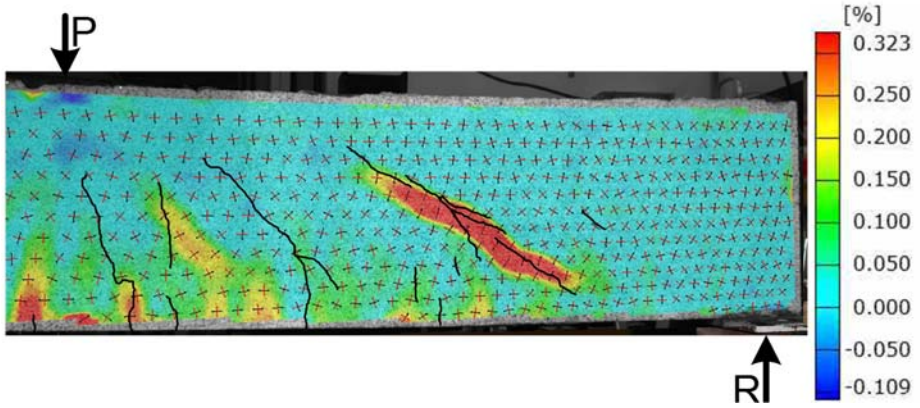

Figure 4.161 Full-field concrete maximum principal strain (σ_1) across shear span for specimen SFRC18a at normalized shear stress of $4.0\sqrt{f'_c}$

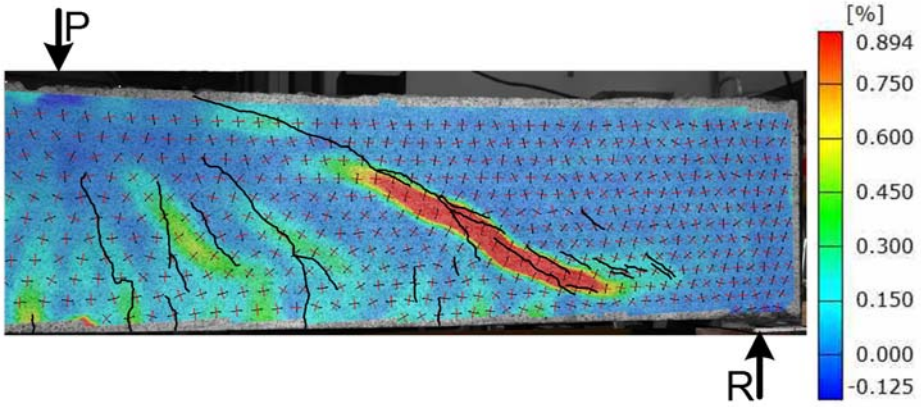

Figure 4.162 Full-field concrete maximum principal strain (σ_1) across shear span for specimen SFRC18a at normalized shear stress of $5.0\sqrt{f'_c}$

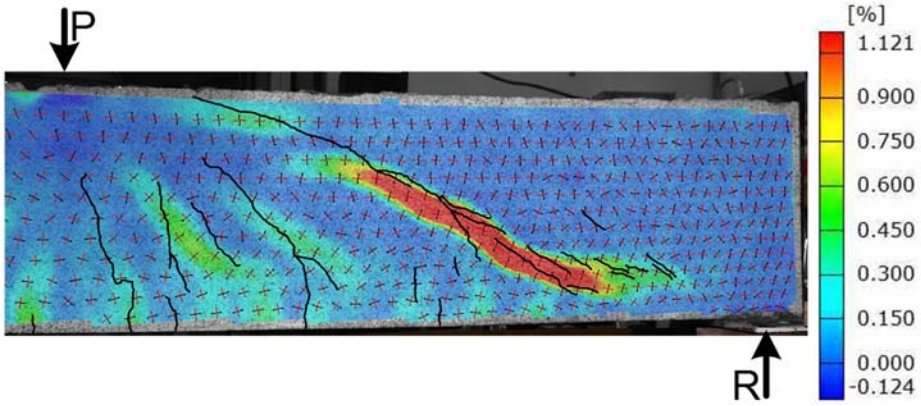

Figure 4.163 Full-field concrete maximum principal strain (σ_1) across shear span for specimen SFRC18a at normalized shear stress of $5.2\sqrt{f'_c}$

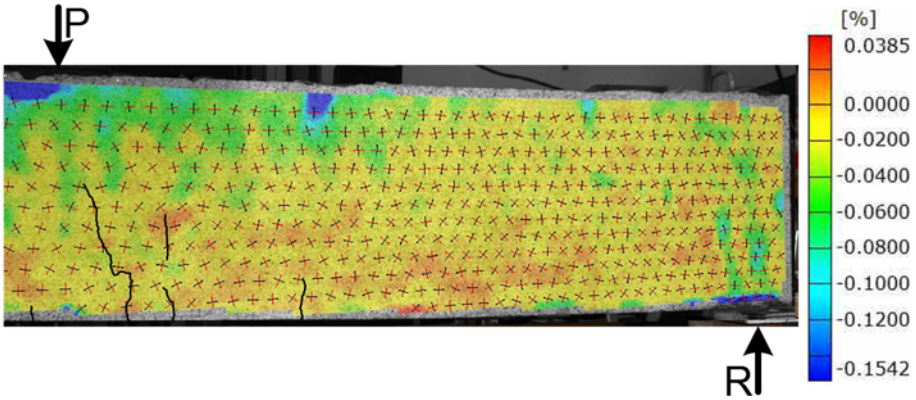

Figure 4.164 Full-field concrete minimum principal strain (σ_2) across shear span for specimen SFRC18a at normalized shear stress of $2.5\sqrt{f'_c}$

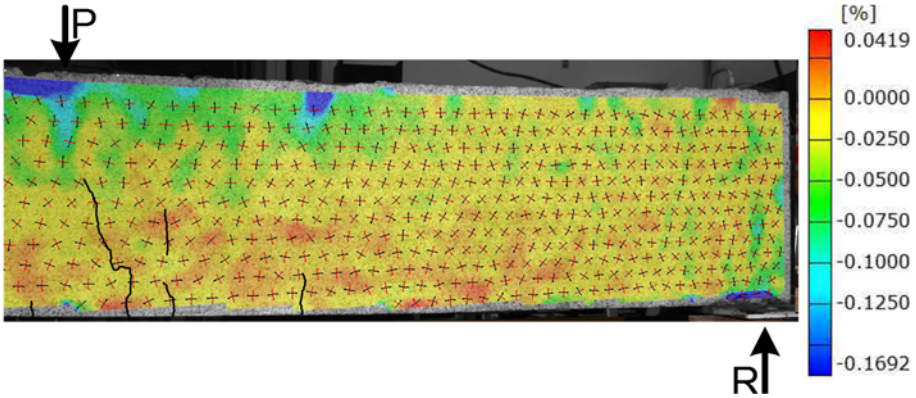

Figure 4.165 Full-field concrete minimum principal strain (σ_2) across shear span for specimen SFRC18a at normalized shear stress of $3.0\sqrt{f'_c}$

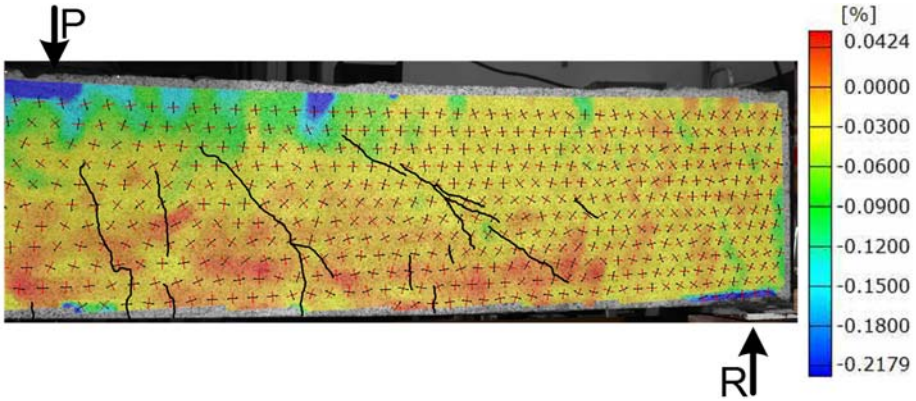

Figure 4.166 Full-field concrete minimum principal strain (σ_2) across shear span for specimen SFRC18a at normalized shear stress of $4.0\sqrt{f'_c}$

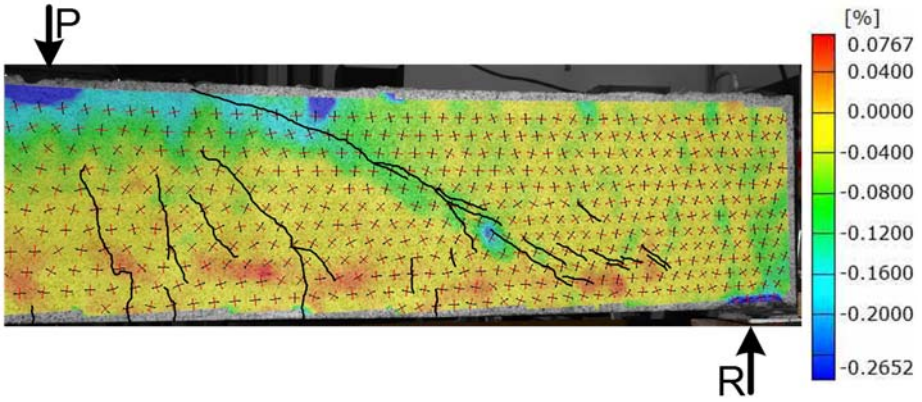

Figure 4.167 Full-field concrete minimum principal strain (σ_2) across shear span for specimen SFRC18a at normalized shear stress of $5.0\sqrt{f'_c}$

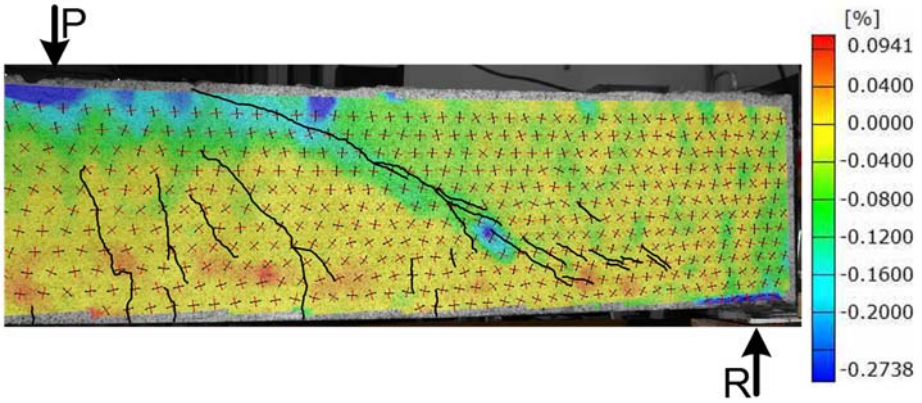

Figure 4.168 Full-field concrete minimum principal strain (σ_2) across shear span for specimen SFRC18a at normalized shear stress of $5.2\sqrt{f'_c}$

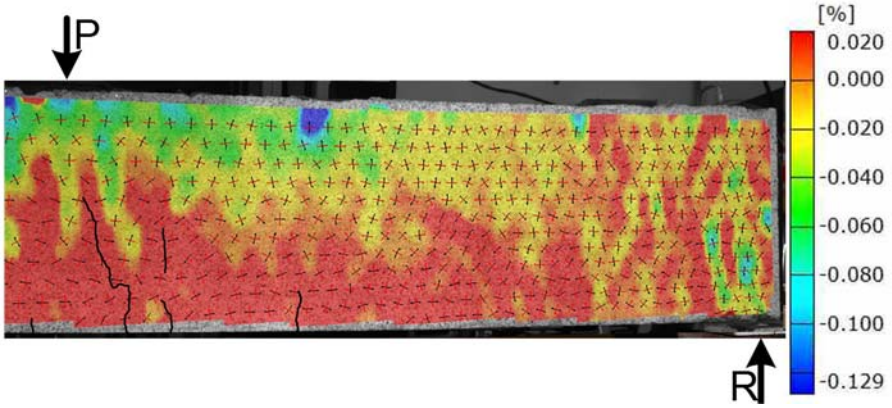

Figure 4.169 Scaled full-field concrete longitudinal strain (ε_x) across shear span for specimen SFRC18a at normalized shear stress of $2.5\sqrt{f'_c}$

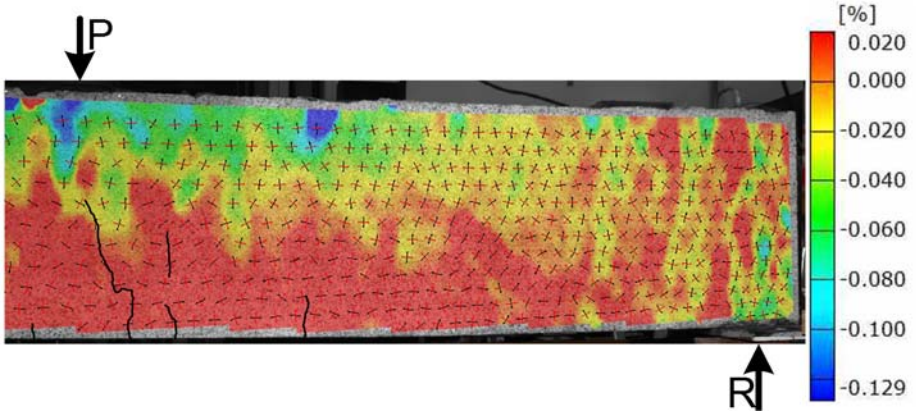

Figure 4.170 Scaled full-field concrete longitudinal strain (ε_x) across shear span for specimen SFRC18a at normalized shear stress of $3.0\sqrt{f'_c}$

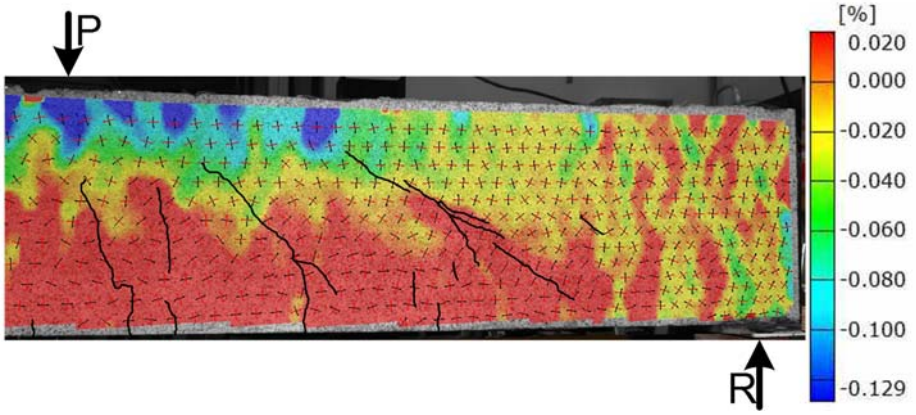

Figure 4.171 Scaled full-field concrete longitudinal strain (ε_x) across shear span for specimen SFRC18a at normalized shear stress of $4.0\sqrt{f'_c}$

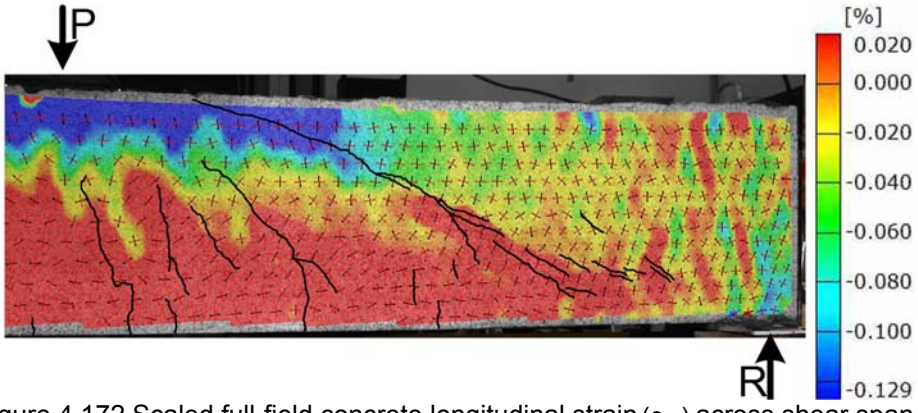

Figure 4.172 Scaled full-field concrete longitudinal strain (ε_x) across shear span for specimen SFRC18a at normalized shear stress of $5.0\sqrt{f'_c}$

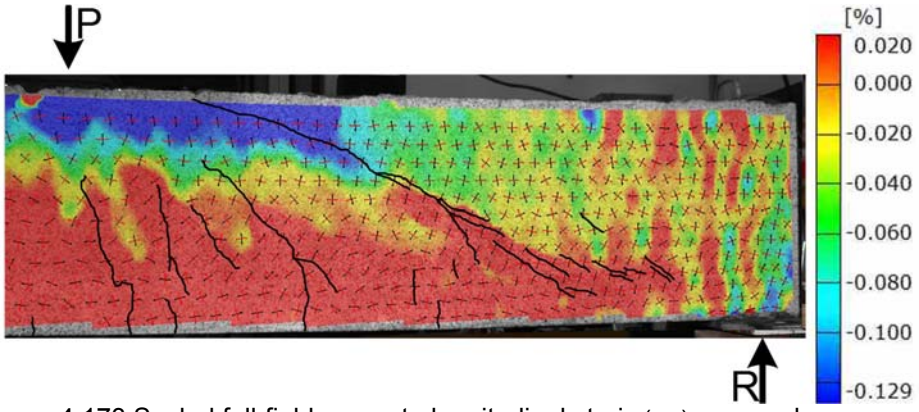

Figure 4.173 Scaled full-field concrete longitudinal strain (ε_x) across shear span for specimen SFRC18a at normalized shear stress of $5.2\sqrt{f'_c}$

4.2.4 Beam SFRC18b

4.2.4.1 Load-deflection relationship, crack pattern, and failure mode

Beam SFRC18b was a duplication of beam SFRC18a. The graph displayed in Figure 4.174 shows the load versus deflection response for the specimen. The curve was linear up to 20 kips (shear stress of $1.42\sqrt{f'_c}$), where the first visible flexural crack was developed. The first shear crack became visible at 31 kips (shear stress of $2.21\sqrt{f'_c}$) in a form of flexural-shear crack. The shear cracking did not introduce a substantial nonlinearity into the load-deflection curve. The maximum load that the beam could sustain was measured at 88 kips (shear stress of $6.22\sqrt{f'_c}$), as it was slightly higher than the load carried by SFRC18a at the failure (i.e. 73 kips). Figure 4.175 displays the cracking patterns of beam SFRC18b at different loads. As seen, the first visible crack occurred in vicinity of the loading point due to flexural bending moment. At load 31 kips, the first shear crack occurred, and then while the load increased, the beam developed multiple shear cracking. The multiple shear cracks proceeded from the stress redistribution due to the fiber bridging effect; this mechanism was not available for the controlling PC beams. As opposed to the tested PC beams, the existing of steel fibers considerably slowed down and stabilized the

propagation of the developed cracks. That enabled the internal stresses to redistribute and led the other cracks to progressively develop and scatter all over the shear span length until the failure. Beyond a certain loading stage (45 kips), the developed cracks being sufficiently close to the loading point stopped moving forward. At this load, a web shear crack also occurred that compared to the other shear cracks, it had a much greater extension within the compression zone. For this reason, it was initially conceived of as the critical crack. Nevertheless, its advance almost ceased after load 60 kips. At this moment, the compression zone depth above the top end of the crack was excessively small (less than 0.75 in.), yet it did not precipitate the failure. The reason could be attributed to the high compressive confinement of the compression zone due to the bending moment at such considerable external load. Note, our controlling PC beams failed when shear force reached 19 and 17 kips, respectively in their shear span, as compared to the current shear force of 30 kips in SFRC18b. In SFRC18b shear failure occurred when the closest significant inclined crack to the support intersected the compression edge of the beam at load 88 kips. At the same time, dowel action contribution to shear resistance was terminated as a result to the kinking of the flexural bars. The evaluation of the DIC full-field major strain visualization at failure evidenced that the compression zone failure preceded the dowel action breakdown. This will be later discussed in the next chapter. Therefore, the shear failure of the beam was classified as the compression zone failure dominated by tension. A view of failure in beam SFRC18b is presented in Figure 4.176.

4.2.4.2 Strain in reinforcing bars

The applied load versus reinforcement longitudinal strain relationships at under the loading point and middle of the shear span are plotted in Figure 4.177. At the both locations, the reinforcement strain varied linearly due to bending moment. For this reason, the strain at each load was measured lower at the mid-shear span. At the first flexural cracking, a

marginal jump can be noticed in the curves. Afterward, the strains kept ascending with a constant slope because the strain measurements at those aforementioned locations were not interfered by the local shear cracks.

4.2.4.3 Full-field visualization of strain components developed on the shear span concrete surface

Full-filed strain components developed on concrete surface throughout shear span for specimen SFRC18b were obtained with the aid of DIC technology at different load values and illustrated in Figure 4.178 through Figure 4.201. For the better evaluation of the relationship between cracking pattern and the state of developed stresses acquired by DIC system, the cracks on the other side of the beam at each desired load were integrated into the corresponding DIC processed images.

The scaled full-field concrete longitudinal strain (ε_x) distributions across shear span at different loads for specimen SFRC18b were visualized from Figure 4.202 to Figure 4.207. Tensile strains are denoted in red, while other colors (yellow to dark blue) represent various magnitudes of compressive strain in the compression zone.

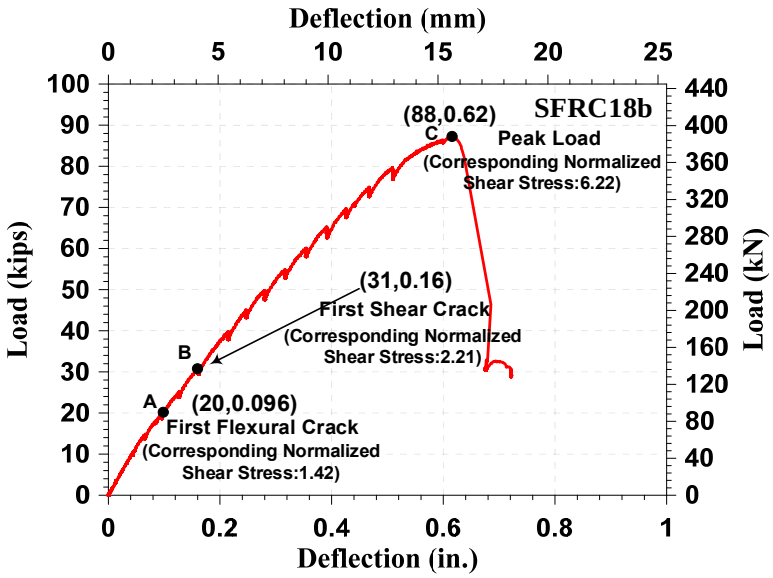

Figure 4.174 load-deflection response for beam SFRC18b

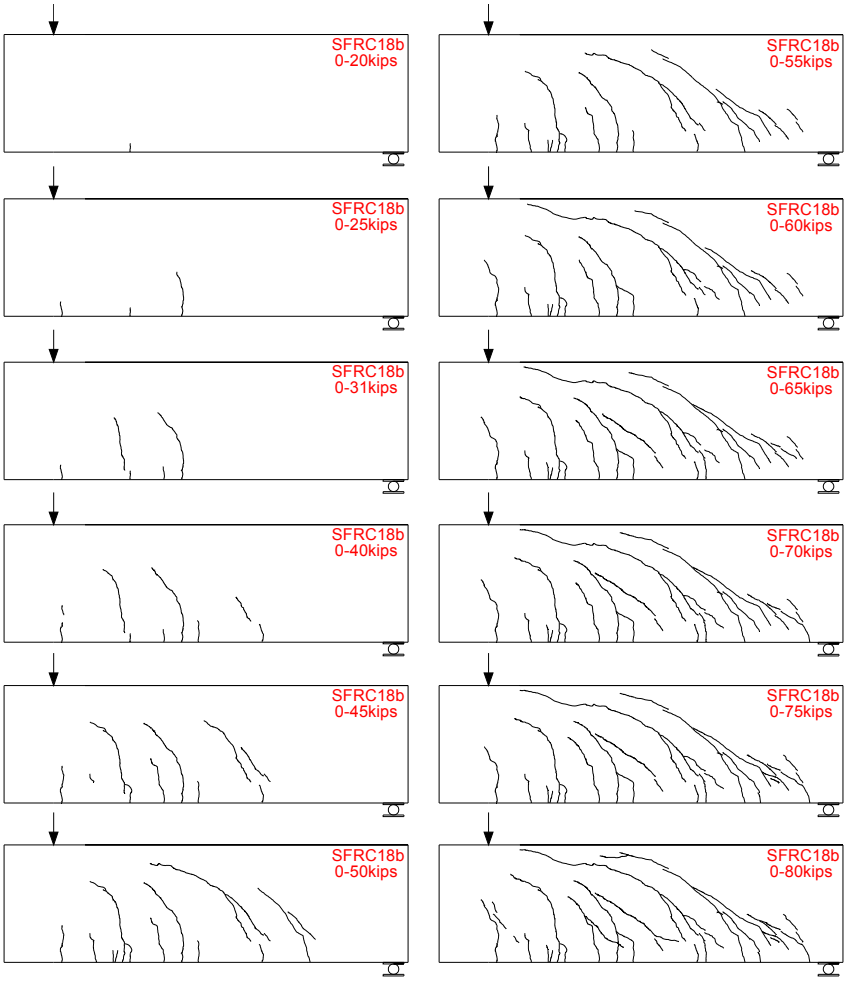

Figure 4.175 Cracking pattern for SFRC18b at different load stages

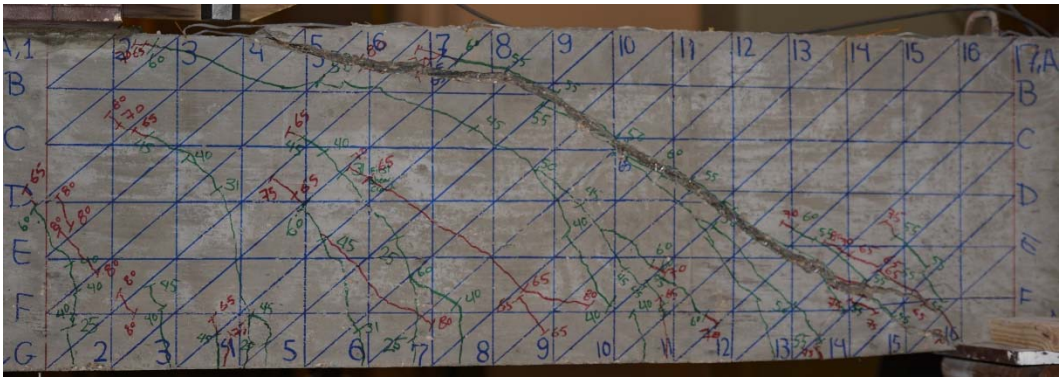

Figure 4.176 A view of failure in beam SFRC18b

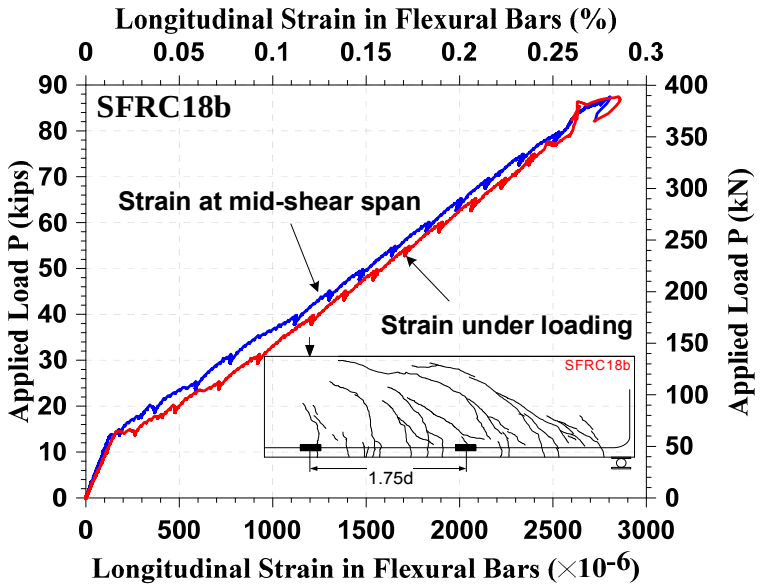

Figure 4.177 Load versus reinforcement strain relationships for beam SFRC18b

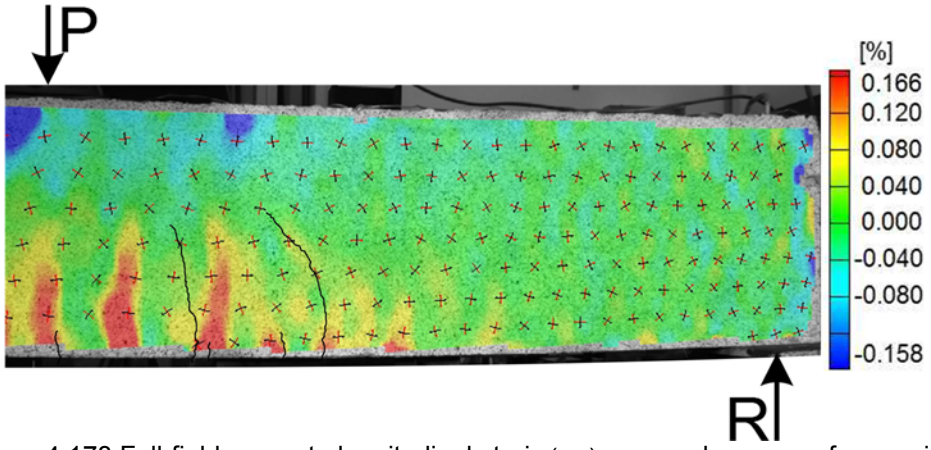

Figure 4.178 Full-field concrete longitudinal strain (ε_x) across shear span for specimen SFRC18b at normalized shear stress of $2.5\sqrt{f'_c}$

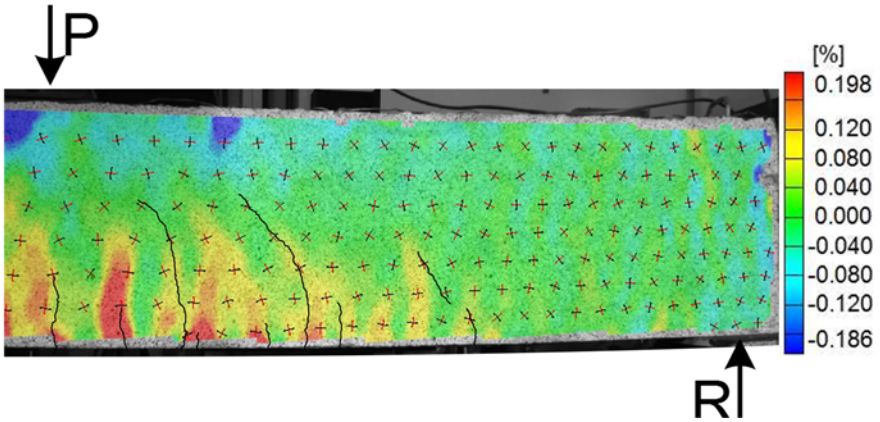

Figure 4.179 Full-field concrete longitudinal strain (ε_x) across shear span for specimen SFRC18b at normalized shear stress of $3.0\sqrt{f'_c}$

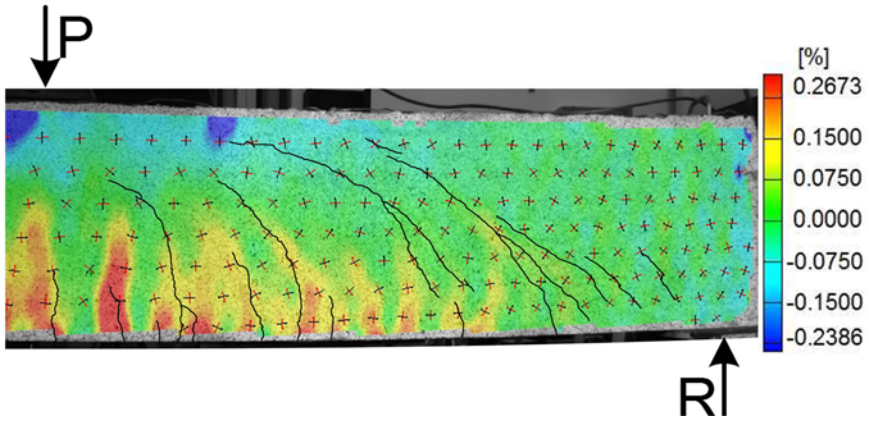

Figure 4.180 Full-field concrete longitudinal strain (ε_x) across shear span for specimen SFRC18b at normalized shear stress of $4.0\sqrt{f'_c}$

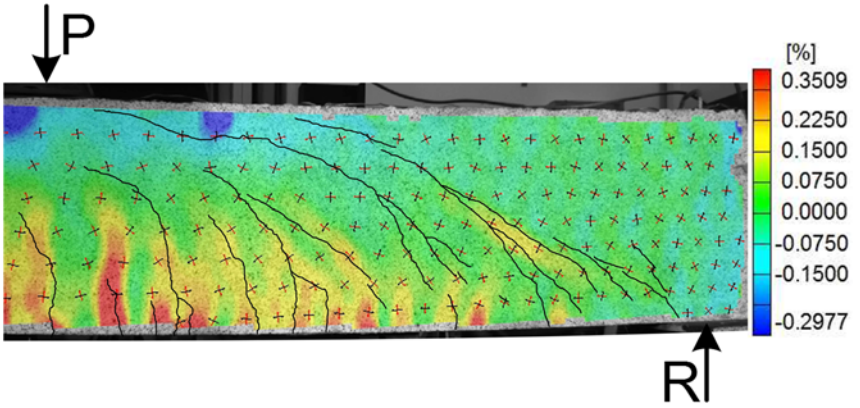

Figure 4.181 Full-field concrete longitudinal strain (ε_x) across shear span for specimen SFRC18b at normalized shear stress of $5.0\sqrt{f'_c}$

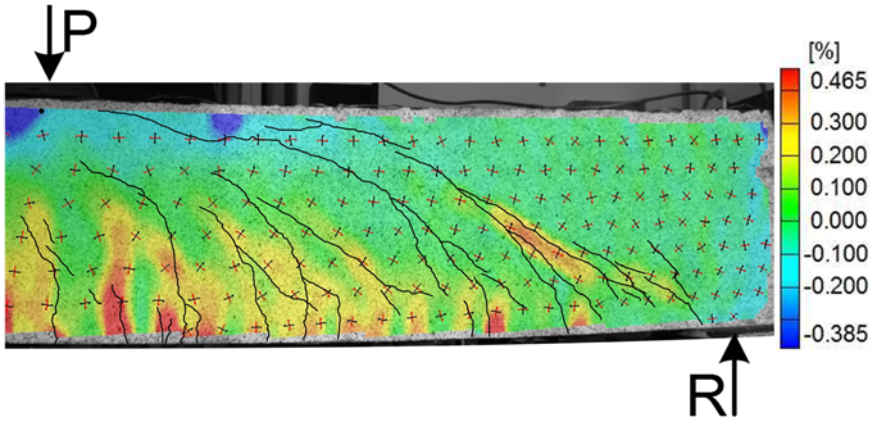

Figure 4.182 Full-field concrete longitudinal strain (ε_x) across shear span for specimen SFRC18b at normalized shear stress of $6.0\sqrt{f'_c}$

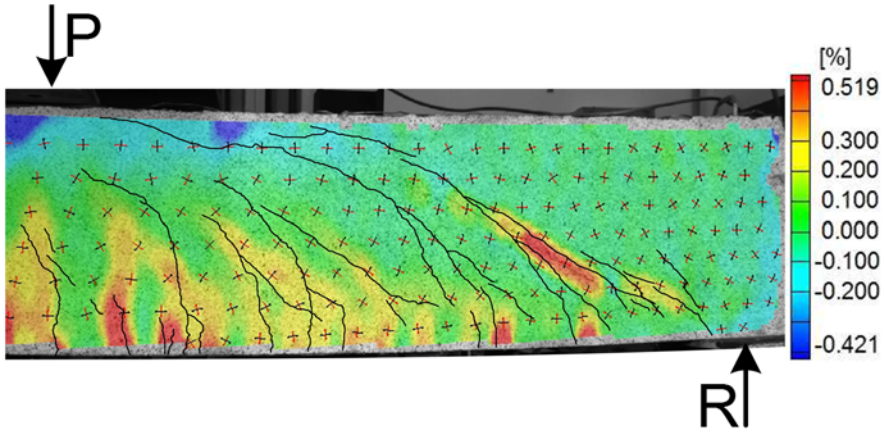

Figure 4.183 Full-field concrete longitudinal strain (ε_x) across shear span for specimen SFRC18b at normalized shear stress of $6.2\sqrt{f'_c}$

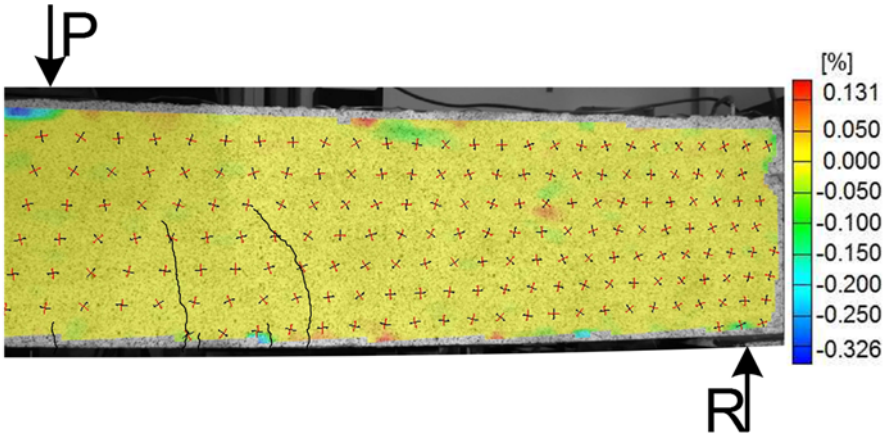

Figure 4.184 Full-field concrete transvers strain (ε_y) across shear span for specimen SFRC18b at normalized shear stress of $2.5\sqrt{f'_c}$

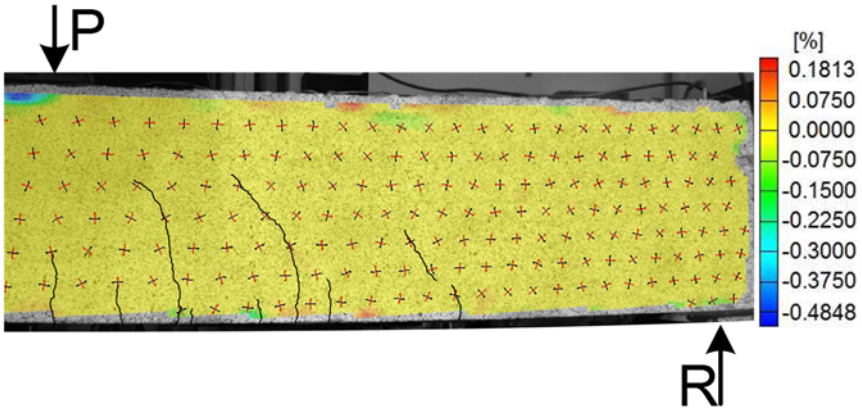

Figure 4.185 Full-field concrete transvers strain (ε_y) across shear span for specimen SFRC18b at normalized shear stress of $3.0\sqrt{f'_c}$

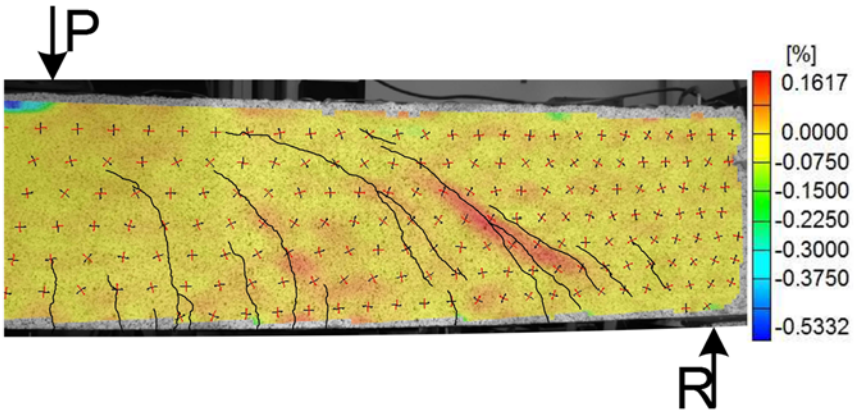

Figure 4.186 Full-field concrete transvers strain (ε_y) across shear span for specimen SFRC18b at normalized shear stress of $4.0\sqrt{f'_c}$

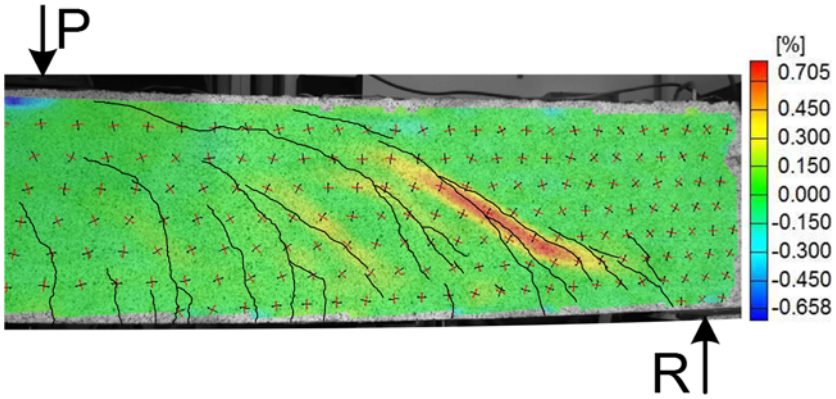

Figure 4.187 Full-field concrete transvers strain (ε_y) across shear span for specimen SFRC18b at normalized shear stress of $5.0\sqrt{f'_c}$

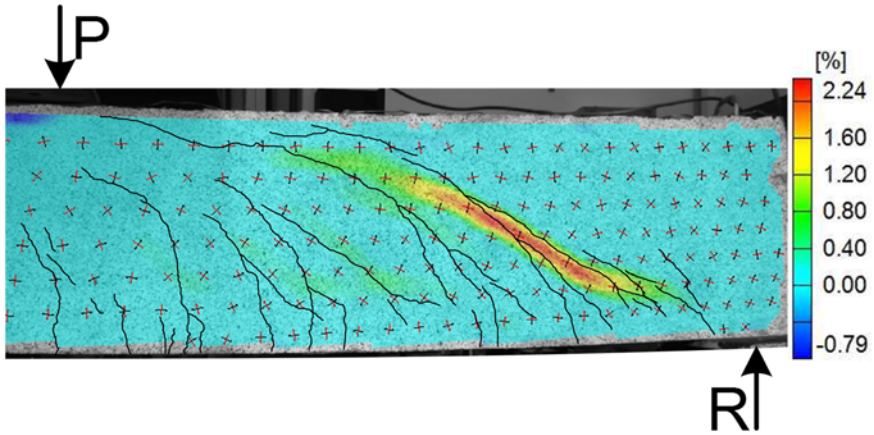

Figure 4.188 Full-field concrete transvers strain (ε_y) across shear span for specimen SFRC18b at normalized shear stress of $6.0\sqrt{f'_c}$

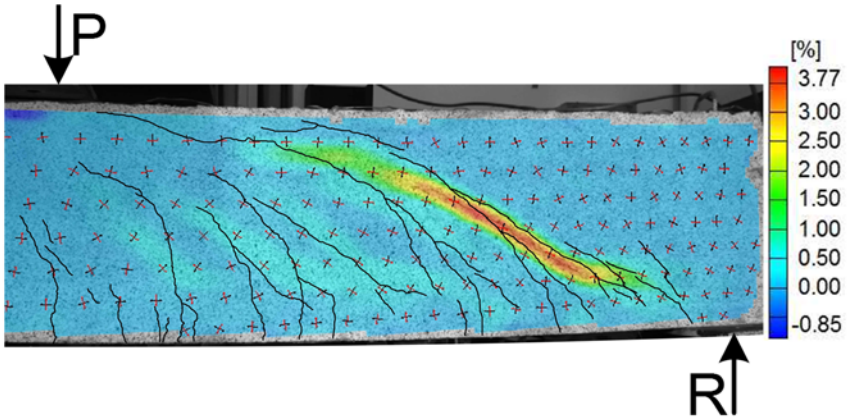

Figure 4.189 Full-field concrete transvers strain (ε_y) across shear span for specimen SFRC18b at normalized shear stress of $6.2\sqrt{f'_c}$

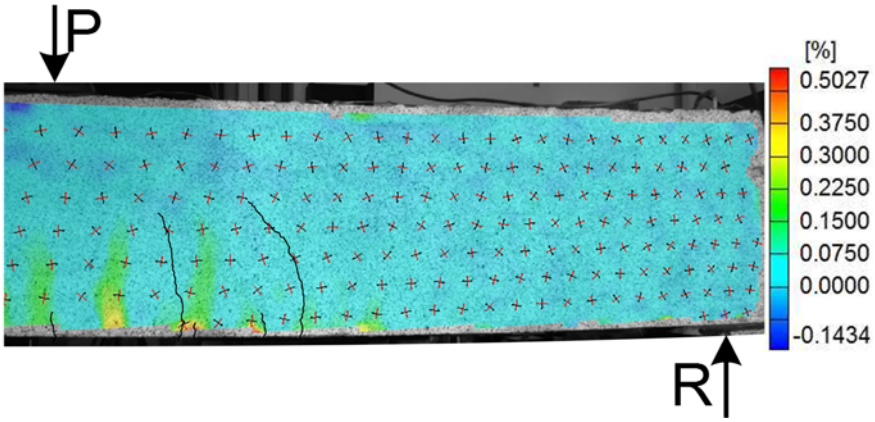

Figure 4.190 Full-field concrete maximum principal strain (σ_1) across shear span for specimen SFRC18b at normalized shear stress of $2.5\sqrt{f'_c}$

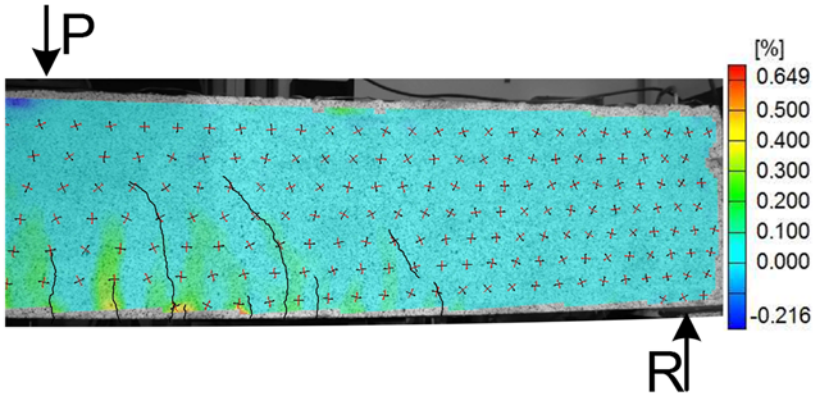

Figure 4.191 Full-field concrete maximum principal strain (σ_1) across shear span for specimen SFRC18b at normalized shear stress of $3.0\sqrt{f'_c}$

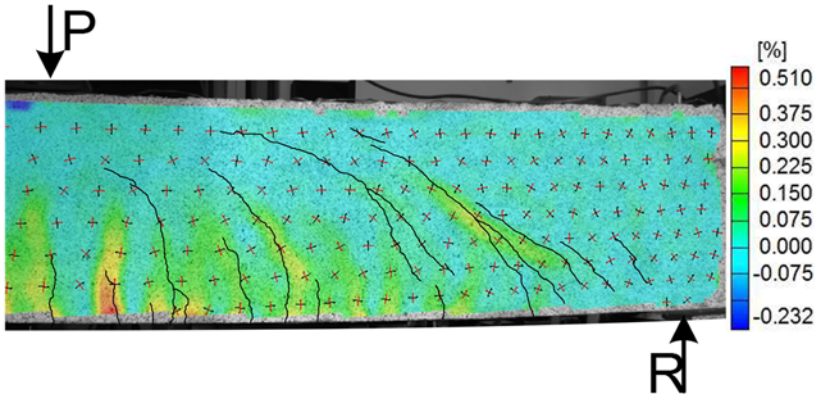

Figure 4.192 Full-field concrete maximum principal strain (σ_1) across shear span for specimen SFRC18b at normalized shear stress of $4.0\sqrt{f'_c}$

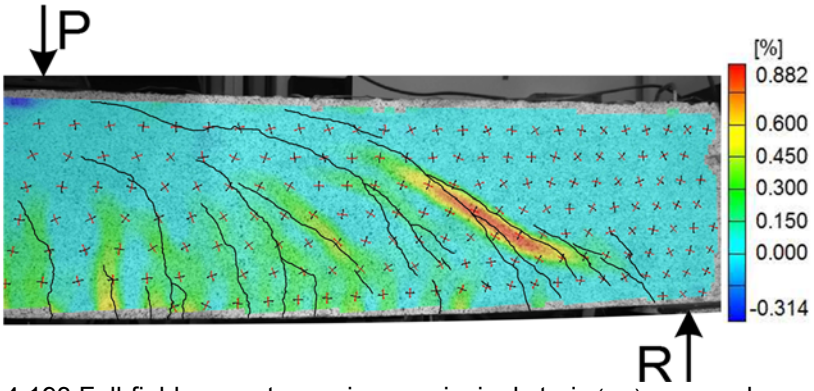

Figure 4.193 Full-field concrete maximum principal strain (σ_1) across shear span for specimen SFRC18b at normalized shear stress of $5.0\sqrt{f'_c}$

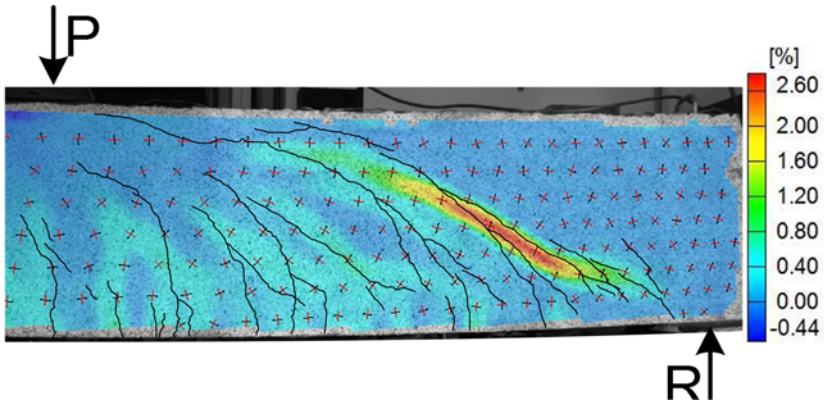

Figure 4.194 Full-field concrete maximum principal strain (σ_1) across shear span for specimen SFRC18b at normalized shear stress of $6.0\sqrt{f'_c}$

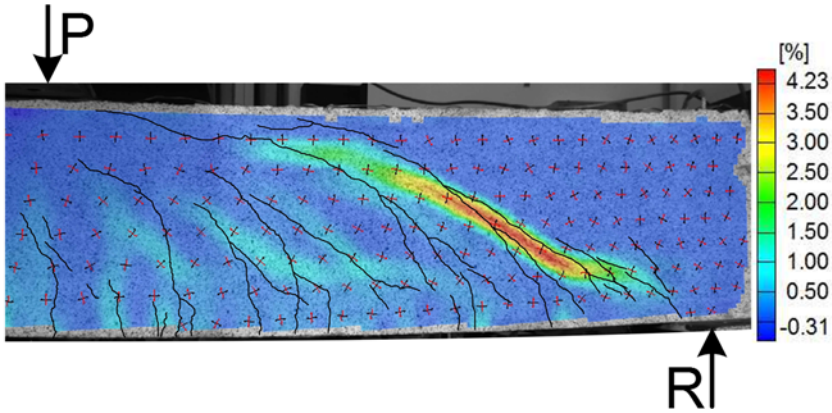

Figure 4.195 Full-field concrete maximum principal strain (σ_1) across shear span for specimen SFRC18b at normalized shear stress of $6.2\sqrt{f'_c}$

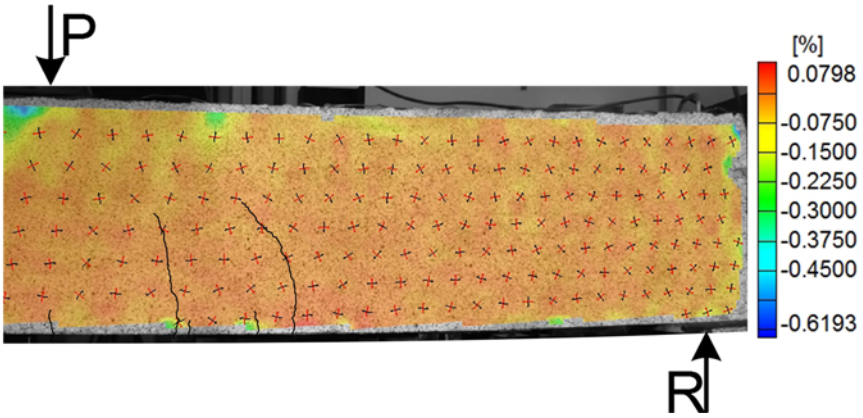

Figure 4.196 Full-field concrete minimum principal strain (σ_2) across shear span for specimen SFRC18b at normalized shear stress of $2.5\sqrt{f'_c}$

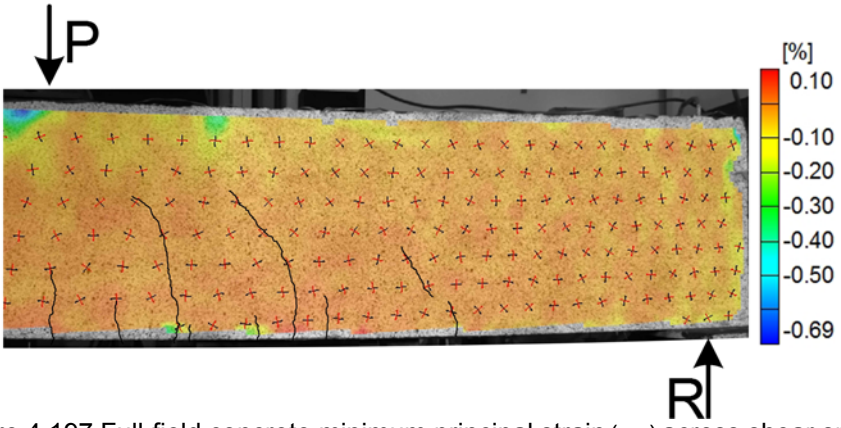

Figure 4.197 Full-field concrete minimum principal strain (σ_2) across shear span for specimen SFRC18b at normalized shear stress of $3.0\sqrt{f'_c}$

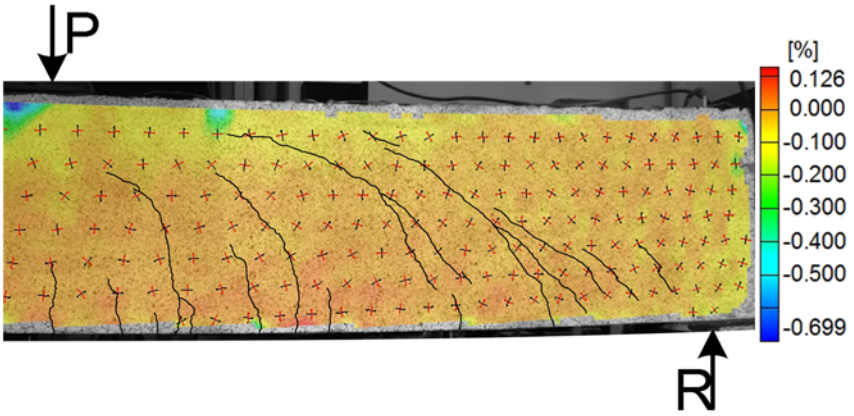

Figure 4.198 Full-field concrete minimum principal strain (σ_2) across shear span for specimen SFRC18b at normalized shear stress of $4.0\sqrt{f'_c}$

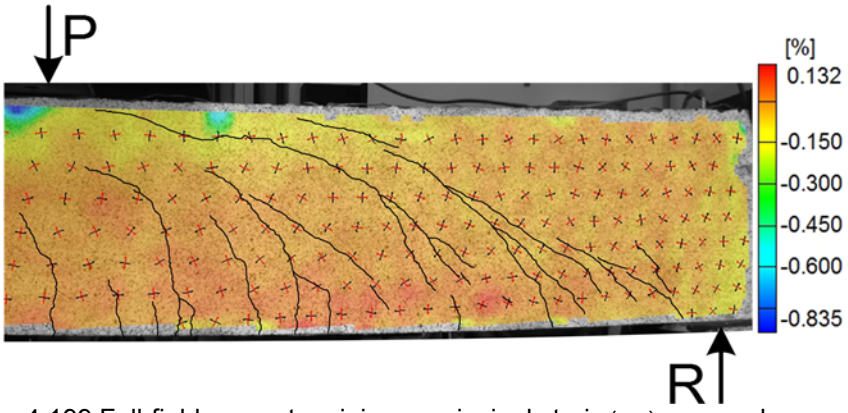

Figure 4.199 Full-field concrete minimum principal strain (σ_2) across shear span for specimen SFRC18b at normalized shear stress of $5.0\sqrt{f'_c}$

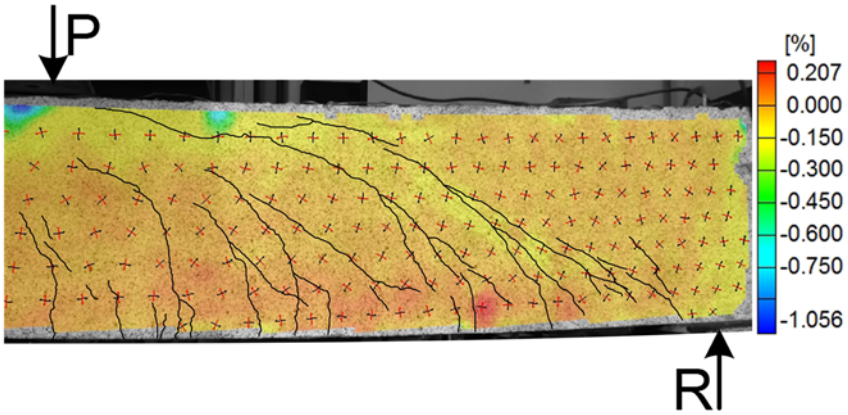

Figure 4.200 Full-field concrete minimum principal strain (σ_2) across shear span for specimen SFRC18b at normalized shear stress of $6.0\sqrt{f'_c}$

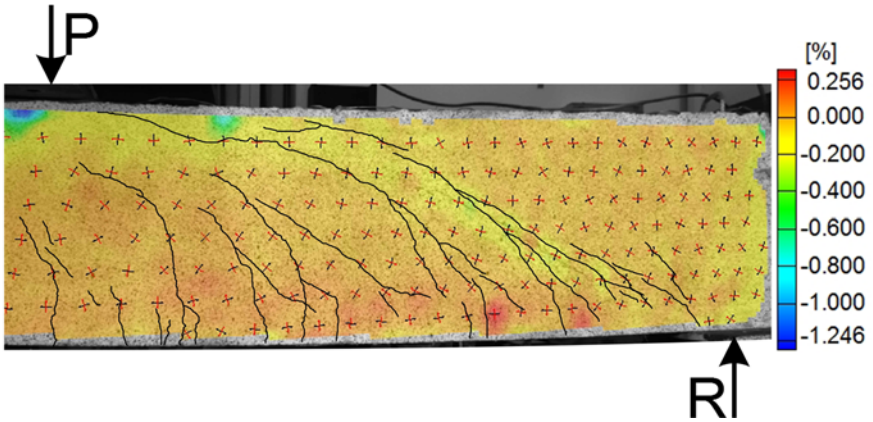

Figure 4.201 Full-field concrete minimum principal strain (σ_2) across shear span for specimen SFRC18b at normalized shear stress of $6.2\sqrt{f'_c}$

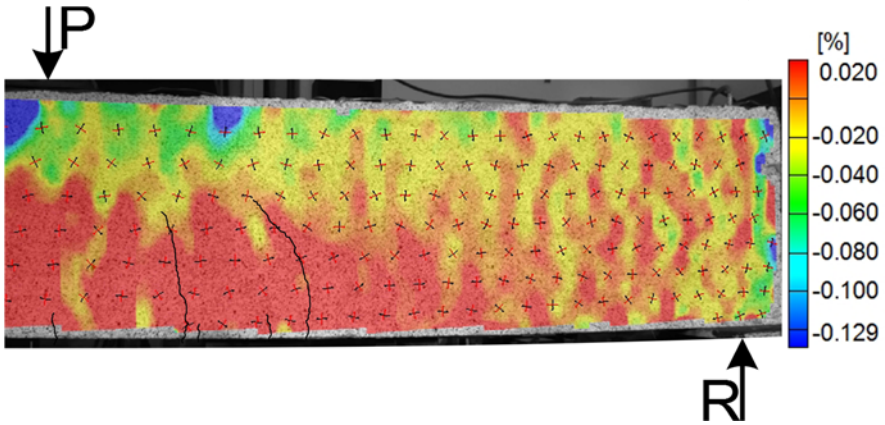

Figure 4.202 Scaled full-field concrete longitudinal strain (ε_x) across shear span for specimen SFRC18b at normalized shear stress of $2.5\sqrt{f'_c}$

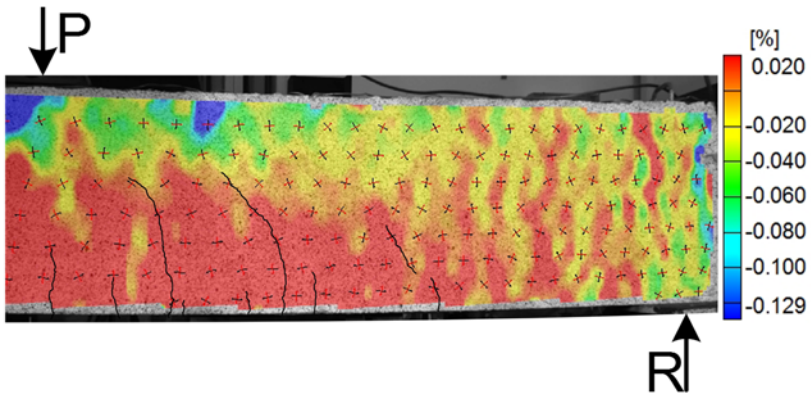

Figure 4.203 Scaled full-field concrete longitudinal strain (ε_x) across shear span for specimen SFRC18b at normalized shear stress of $3.0\sqrt{f'_c}$

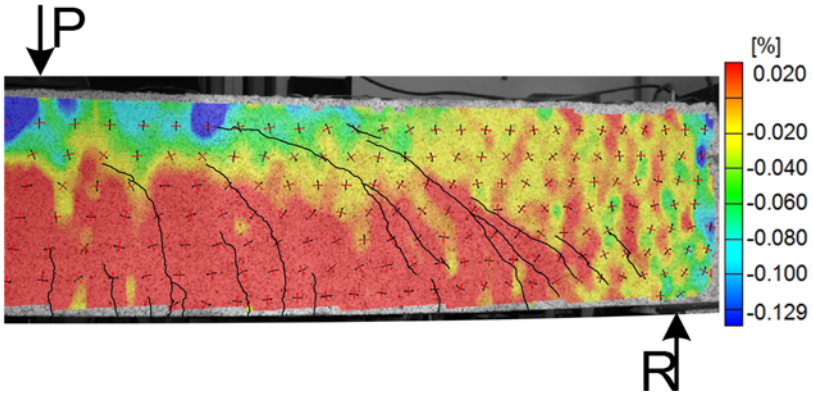

Figure 4.204 Scaled full-field concrete longitudinal strain (ε_x) across shear span for specimen SFRC18b at normalized shear stress of $4.0\sqrt{f'_c}$

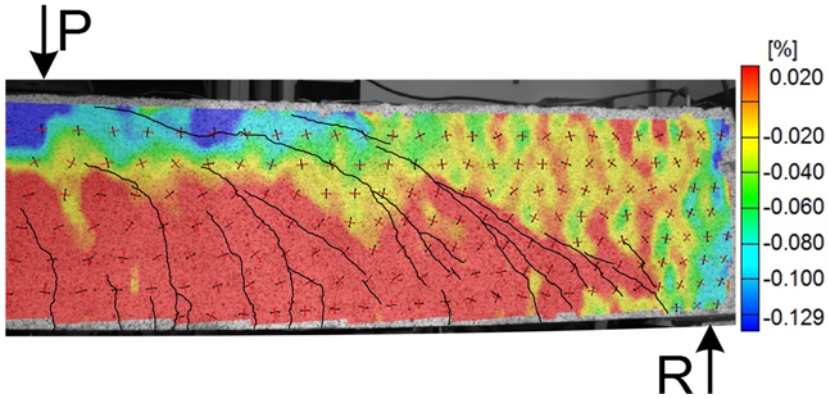

Figure 4.205 Scaled full-field concrete longitudinal strain (ε_x) across shear span for specimen SFRC18b at normalized shear stress of $5.0\sqrt{f'_c}$

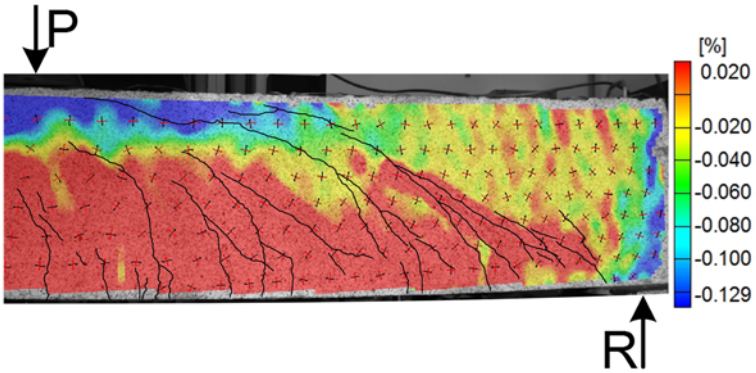

Figure 4.206 Scaled full-field concrete longitudinal strain (ε_x) across shear span for specimen SFRC18b at normalized shear stress of $6.0\sqrt{f'_c}$

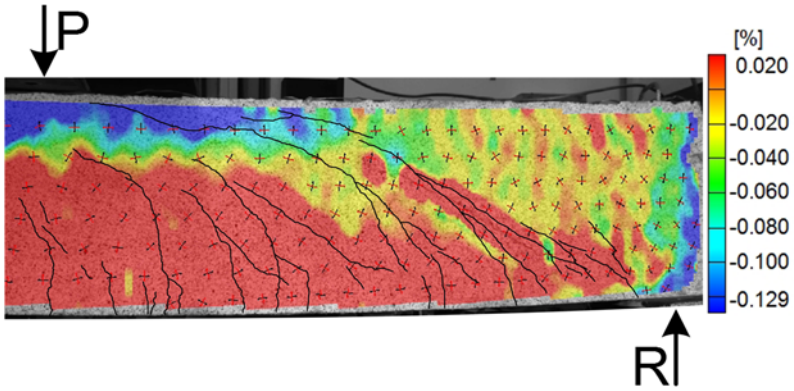

Figure 4.207 Scaled full-field concrete longitudinal strain (ε_x) across shear span for specimen SFRC18b at normalized shear stress of $6.2\sqrt{f'_c}$

4.2.5 Beam SFRC24a

4.2.5.1 Load-deflection relationship, crack pattern, and failure mode

The Load-deflection response of beam SFRC24a is plotted in Figure 4.208. The beam initially cracked in flexure at load 26 kips (corresponding shear stress of $0.90\sqrt{f'_c}$). As frequently observed for the test SFRC beams, the first flexural crack development did not signify in the load-deflection curve. While the load increased, the constant slope of the curve was maintained up to almost 70 kips, where the first shear crack must have been developed in the beam. After that, a nonlinear behavior with a gradually decreasing slope was observed. Because the load was continuously applied at each 20 kips intervals, the visibility of the developed cracks was not checked during of the loading process at each stage. Therefore, based on the earliest time notice, the first shear crack was recognized at 80 kips (corresponding shear stress of $2.76\sqrt{f'_c}$). Eventually, failure in the beam was achieved shortly after load 120 kips (corresponding shear stress of $4.15\sqrt{f'_c}$). The crack pattern for beam SFRC24a is presented in Figure 4.209. Flexural cracking began with the appearance of two vertical cracks adjacent to the loading point: unlike the one initiated from the bottom edge of the beam, the other emerged at the middle one third of the beam

height. Despite the unusual origin observed for the latter, its vertical orientation characteristic prompted us to regard it as a flexural crack. By an increase in the applied load, new flexural cracks spread along the target shear span toward the support. Meanwhile, the existing ones progressed larger in the concrete web. At load 80 kips, a pair of web shear cracks initiated roughly at the middle of the shear span. In spite of a very slow progression of shear cracks observed in the few past test SFRC beams, the swifter rate of the propagation toward the loading point was explicit by visually comparing the length of the shear cracks at loads 80, 100, and 110 kips. From load 100 kips, a series of short inclined cracks gradually came into notice from the lower end of the large propagated shear cracks along the top layer of the longitudinal bars. At upper loads, they seemed to progressively increase in number. Although almost all of the cracks in the entire span ceased propagating at a certain level of height (from load 100 kips), one of the inclined cracks greatly penetrated into the compression zone and caused the failure. The beam failure was triggered by the tension failure of compression zone, where the critical crack intersected the edge of beam at the face of the bearing plate. At the same time, the large number of dowel cracks merged and formed a splitting crack along the bars. Based on the evidences presented and discussed in the next chapter, the tension failure of the compression zone preceded the development of splitting crack and trigger the failure. A view of failure on the both sides of the beam is shown in Figure 4.210.

4.2.5.2 Strain in reinforcing bars

The load versus the average longitudinal strain responses of the bottom layer of the reinforcing bars at two different locations (under the loading point and the middle of the shear span) were plotted in Figure 4.211. As illustrated, before the first drastic change in the initial slope of the curves, as reflecting the local flexural cracking, load had a linear relationship with the variation of strains at the selected locations. With an increase in the

external load, the reinforcing bars under the loading point underwent higher strains as well as higher rate of strain increment. However, as the number of cracks grew adjacent to the mid-shear span gauge, the difference in the strain values between the two positions was becoming lesser. Especially, by initiation of the first shear crack around 80 kips near the mid-shear span gauge, the strain difference was about to totally disappear due to the additional strain induced by shear deformation. Roughly at 100 kips, when the dowel cracks began to develop, the strains under the loading point start reducing. This indicated a gradual change in the load carrying mechanism and the impending beam action termination. Figure 4.211 clearly shows that the maximum longitudinal strain experienced along the reinforcing bars did not exceed even the nominal yielding strain for grade 60 bars ($e_y = 0.00214$). Therefore, no yielding occurred at any point along the longitudinal bars.

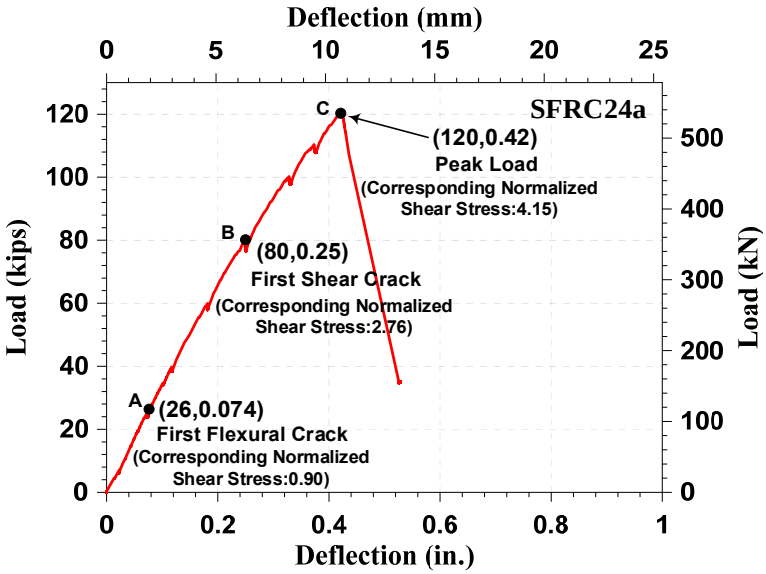

Figure 4.208 load-deflection response for beam SFRC24a

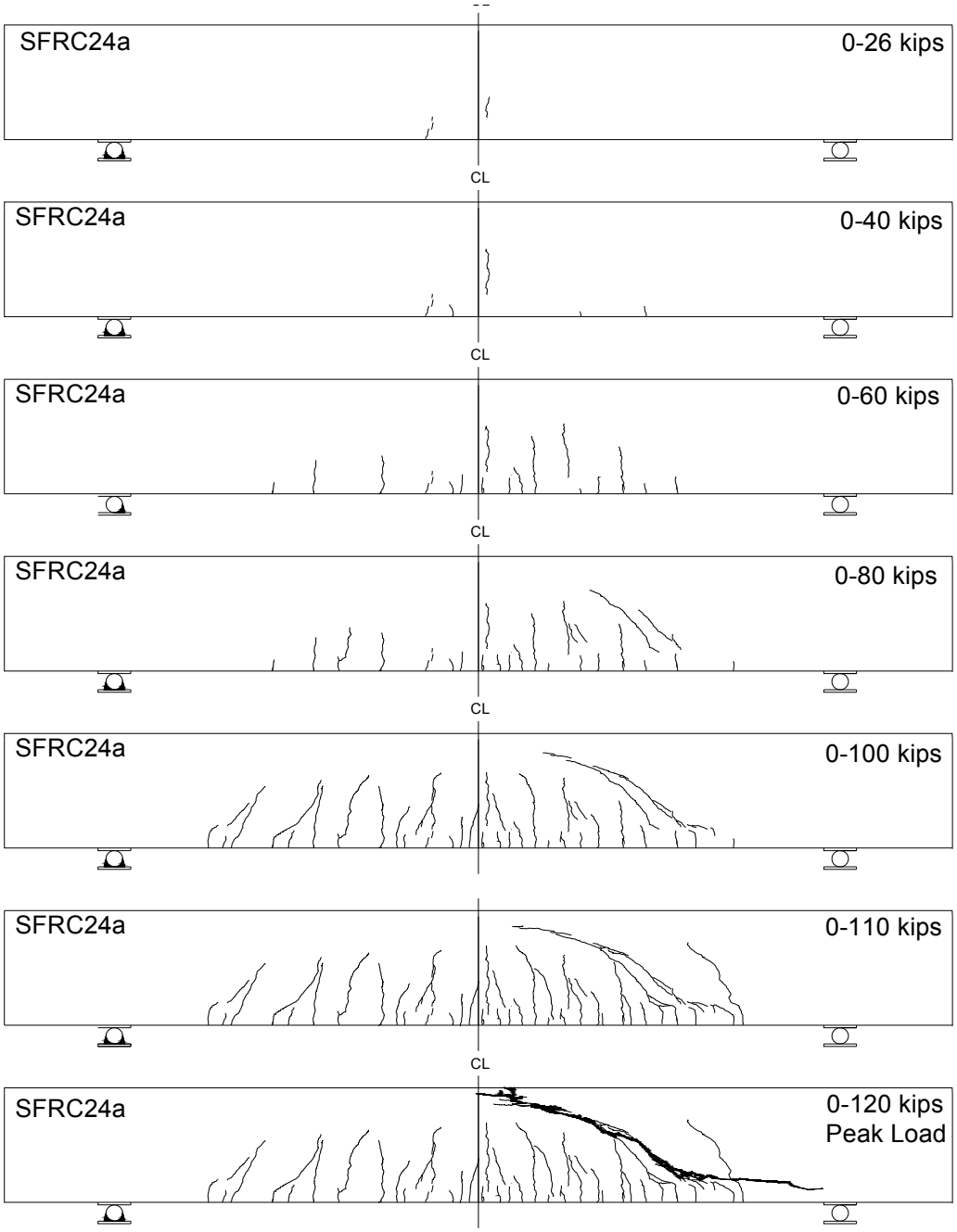

Figure 4.209 Cracking pattern for SFRC24a at different load stages

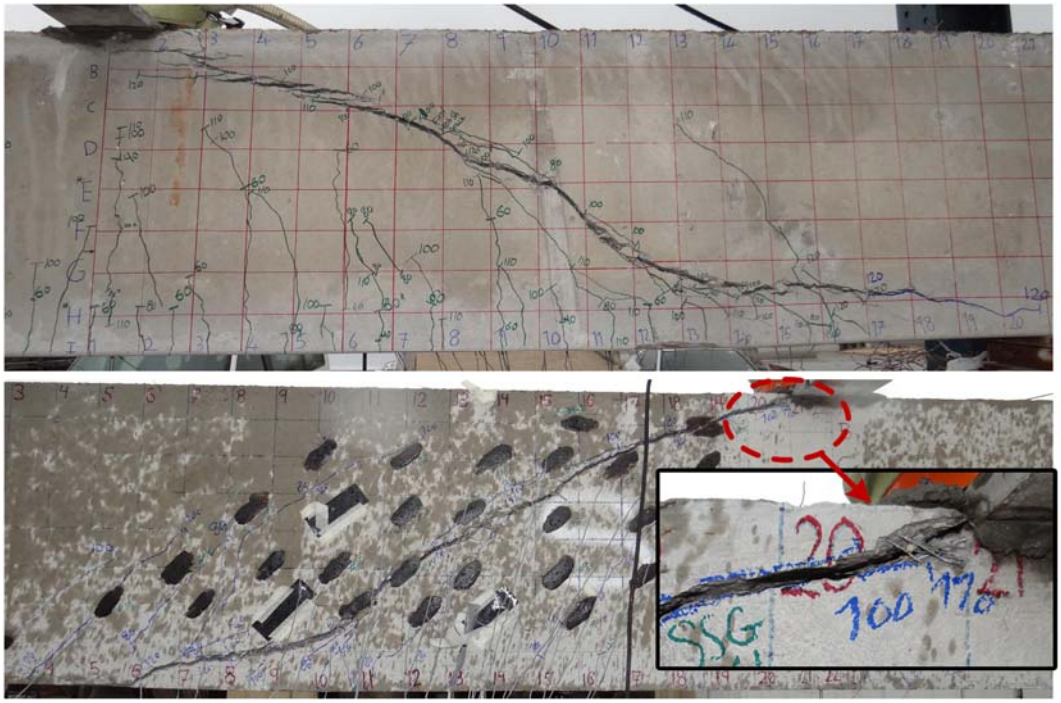

Figure 4.210 A view of failure on both sides of beam SFRC24a

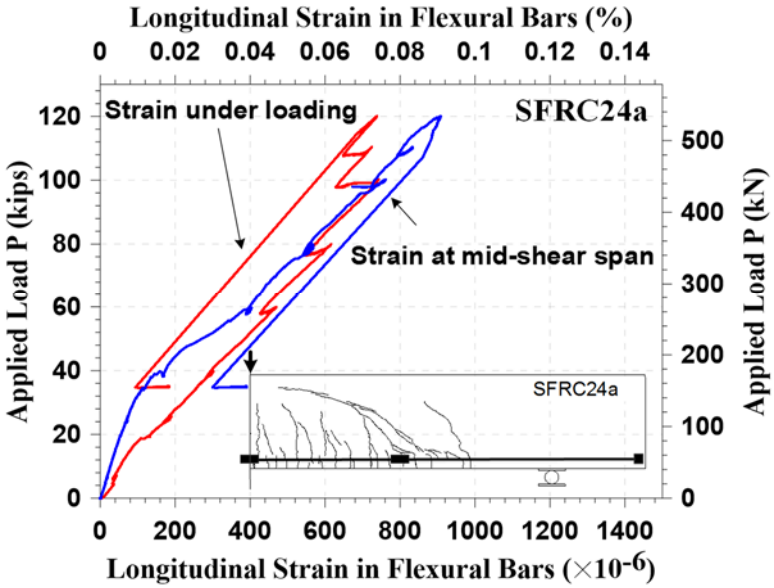

Figure 4.211 Load versus reinforcement strain relationships for beam SFRC24a

4.2.6 Beam SFRC24b

4.2.6.1 Load-deflection relationship, crack pattern, and failure mode

The variation of the applied load with respect to the mid-span deflection for beam SFRC24b is depicted in Figure 4.212. At load 26 kips (corresponding shear stress of $0.90\sqrt{f'_c}$), the beam initially cracked in flexure at a region under the loading point. The development of the first flexural crack slightly reduced the beam stiffness. The applied load at first diagonal cracking was 60 kips. The beam immediately after reaching a maximum load of 171 kips (corresponding shear stress of $5.91\sqrt{f'_c}$) failed in shear. Figure 4.213 shows the cracking patterns of the beam at different load steps. As noticed, the flexural cracking started roughly from mid-span and as the loading progressed, extended to the other parts along the shear span. Unlike beam SFRC24a, the progression of the flexural cracks within the beam web was insignificant by the time of first shear cracking. The first shear cracking appeared in a form of two simultaneous web-shear and flexural-shear cracks that developed in closer distance to the loading point compared to the duplicated beam. By an increase in the applied load, a large number of shear cracks continuously occurred across the shear span. The greater number of inclined cracks for beam SFRC24b in comparison with the one for beam SFRC24a well represents the distinction between these two beams in terms of the internal stress redistribution. The stress redistribution characteristic of an SFRC beam is deeply rooted in direct and indirect effectiveness of steel fibers to enhance the performance of each shear resisting component, what in turn depends on SFRC mix quality. This matter will be extensively discussed in the next chapter. During the loading process up to the failure, all the cracks were observed to be active and propagate in a stable manner. The cracking patterns of the beam associated with the higher loads clearly indicates that all the cracks stopped at a certain level of the

beam height. Finally, at load 171kips, the closest crack to the support became unstable and suddenly advanced within the compression zone toward the loading point and caused the failure. The mode of failure was identified as a diagonal tension failure. The significant relative rotation of the two parts of concrete at the both sides of the critical crack toward each other led the compression zone to crush under the loading point, as clearly illustrated by Figure 4.214. It is worth mentioning that the sudden opening of the critical crack was formed from the point where the crack had the largest curvature.

4.2.6.2 Strain in reinforcing bars

Similar to the duplicated beam (SFRC24a), two pairs of strain gauges were employed to measure the reinforcement strains under the loading point and the middle of the shear span. The strain gauges were mounted on the side reinforcing bars lying in the first bottom layer of reinforcements. The applied load versus the average of strains at each selected location is plotted in Figure 4.215. At the beginning of the test, the load-reinforcing strain relationship was linear for the both curves up to the moment, when a flexural crack initially occurred in the vicinity of the respective gauges. The first-time flexural crack under the loading point altered the curve slope to a great extent, but as for the middle of the shear span, that rendered the curve a big jump in the strain value. In general, the strains measured under the loading point was larger than the ones at the mid-shear span. The maximum strain the reinforcing bars experienced at the middle of the shear span was about 2352 με which was almost identical with the yielding strain value of 2360 με reported by Dinh (2009) for #8 bar. The maximum strain under the loading point was 3347 με. For this reason, the bars seemed yielded at the both locations.

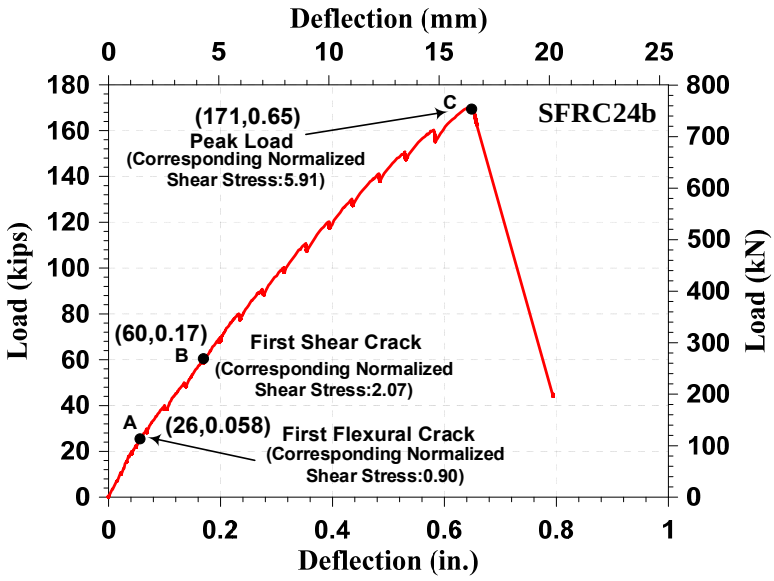

Figure 4.212 load-deflection response for beam SFRC24b

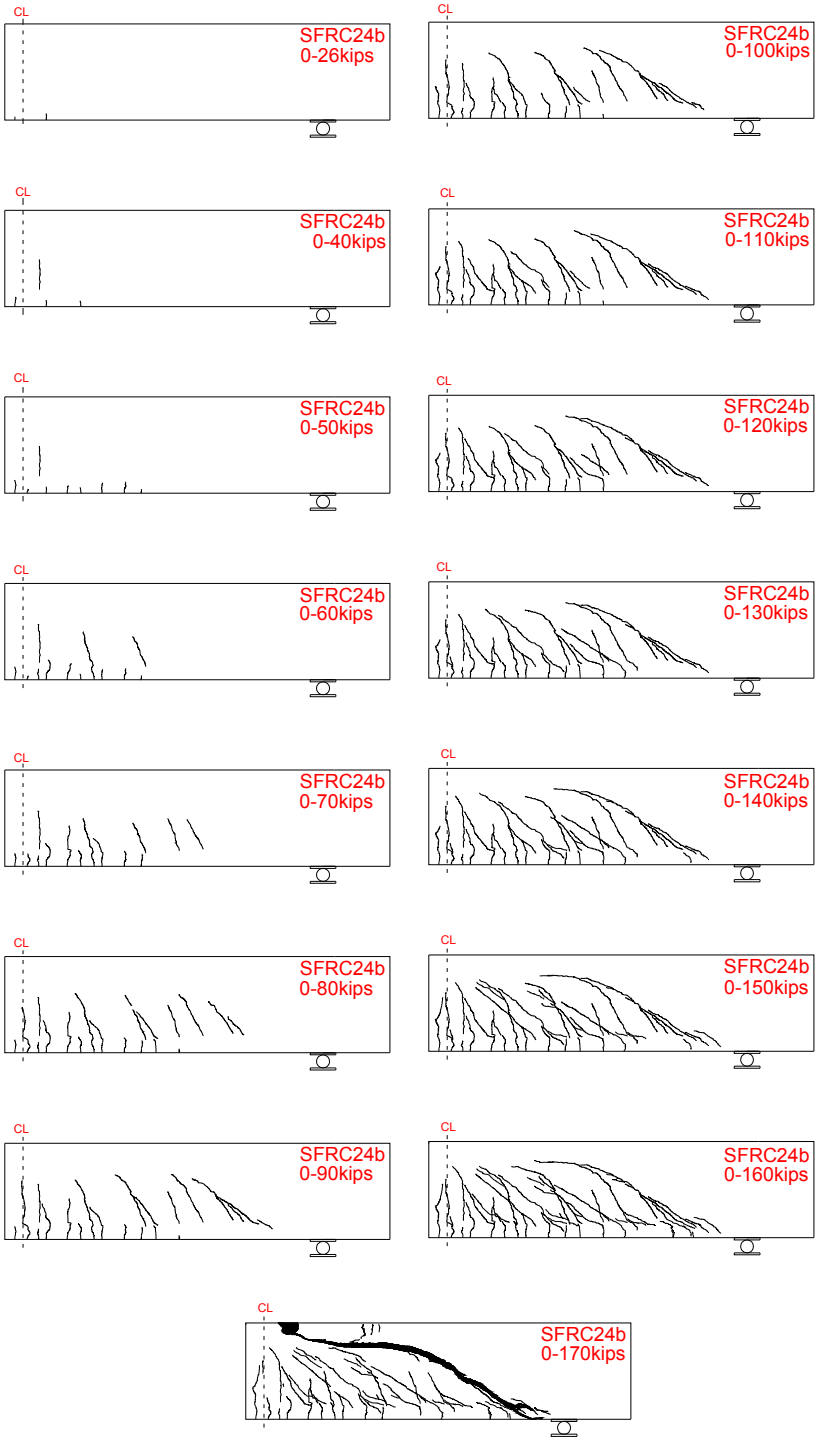

Figure 4.213 Cracking pattern for SFRC24b at different load stages

Figure 4.214 A view of failure for SFRC24b

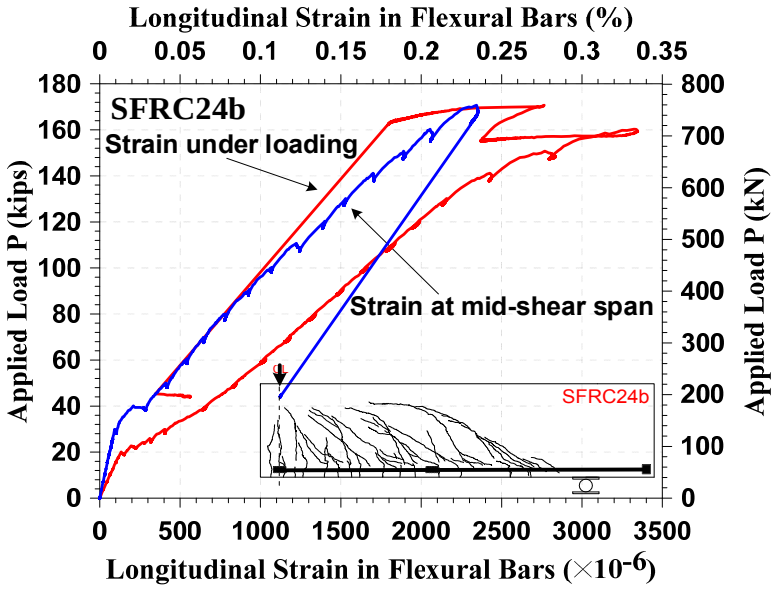

Figure 4.215 Load versus reinforcement strain relationships for beam SFRC24b

4.2.7 Beam SFRC36a

4.2.7.1 Load-deflection relationship, crack pattern, and failure mode

Figure 4.216 presents the load-versus mid-span deflection for beam SFRC36a. The first flexural crack occurred at 60 kips (corresponding to shear stress of $1.10\sqrt{f'_c}$). Shortly after a marginal increase in the applied load, the first shear crack was developed at 80 kips (corresponding shear stress of $1.47\sqrt{f'_c}$). The beam eventually failed in shear

under a maximum load of 307 kips (corresponding shear stress of $5.65\sqrt{f'_c}$). The deflection magnitudes corresponding to the aforementioned applied loads are shown in Figure 4.216.

The cracking patters of beam SFRC36a at various load stages are illustrated in Figure 4.217. As noticed, the cracking of the beam began with a very tiny flexural crack under the loading point. A 20 kips increase in the applied load after the first flexural crack caused a web shear crack to develop very close to the middle of the beam span. At the same time, another flexural crack whose initiation was not from the outermost tension fiber of the section appeared on the side surfaces. Gradually, as the load was going up, numerous shear cracks initiated one after the other and spread along the shear span to the support. On the contrary, the beam experienced a very limited number of flexural cracks. Besides, their penetration within the beam was insignificant. When the load attained 180 kips (corresponding to shear stress of $3.31\sqrt{f'_c}$), a diagonal crack appeared over the shear span that compared to the previous diagonal cracks not only had slighter inclination, but also extended longer by intersecting other developed shear cracks. Raising the applied load, in addition to the development of further shear cracks, led the described crack to become continuously larger in the width to such an extent that it was easily thought of as the critical shear crack. Meanwhile, an abundant number of small inclined cracks formed in dowel zone that they gradually started merging at the lower end of the predicted critical crack. Eventually, the beam failure was observed to be in following to the opening of the critical crack at the beam mid-height, as clearly illustrated by Figure 4.218a. Therefore, the failure was classified as a diagonal tension failure. The beam cracking patterns before and after the failure are shown in Figure 4.218.

For beam SFRC36a, no strain gauge data existed since all the wires were damaged during of the beam transportation to CELB.

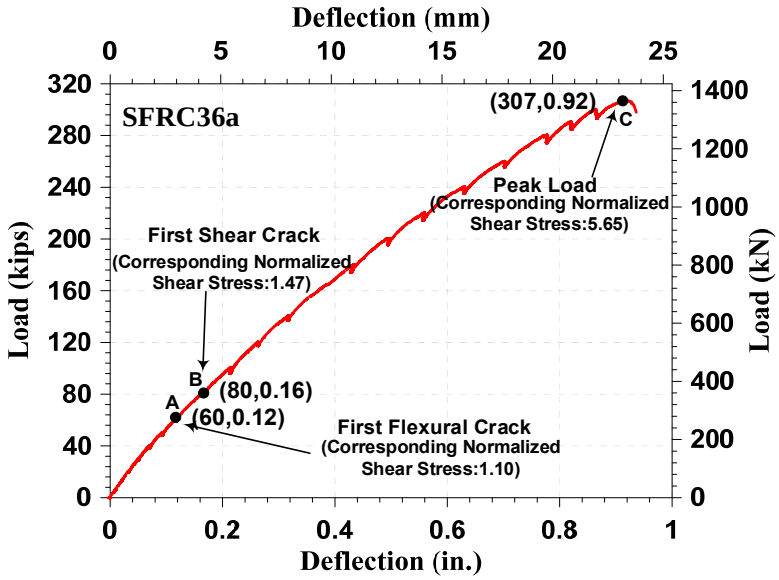

Figure 4.216 load-deflection response for beam SFRC36a

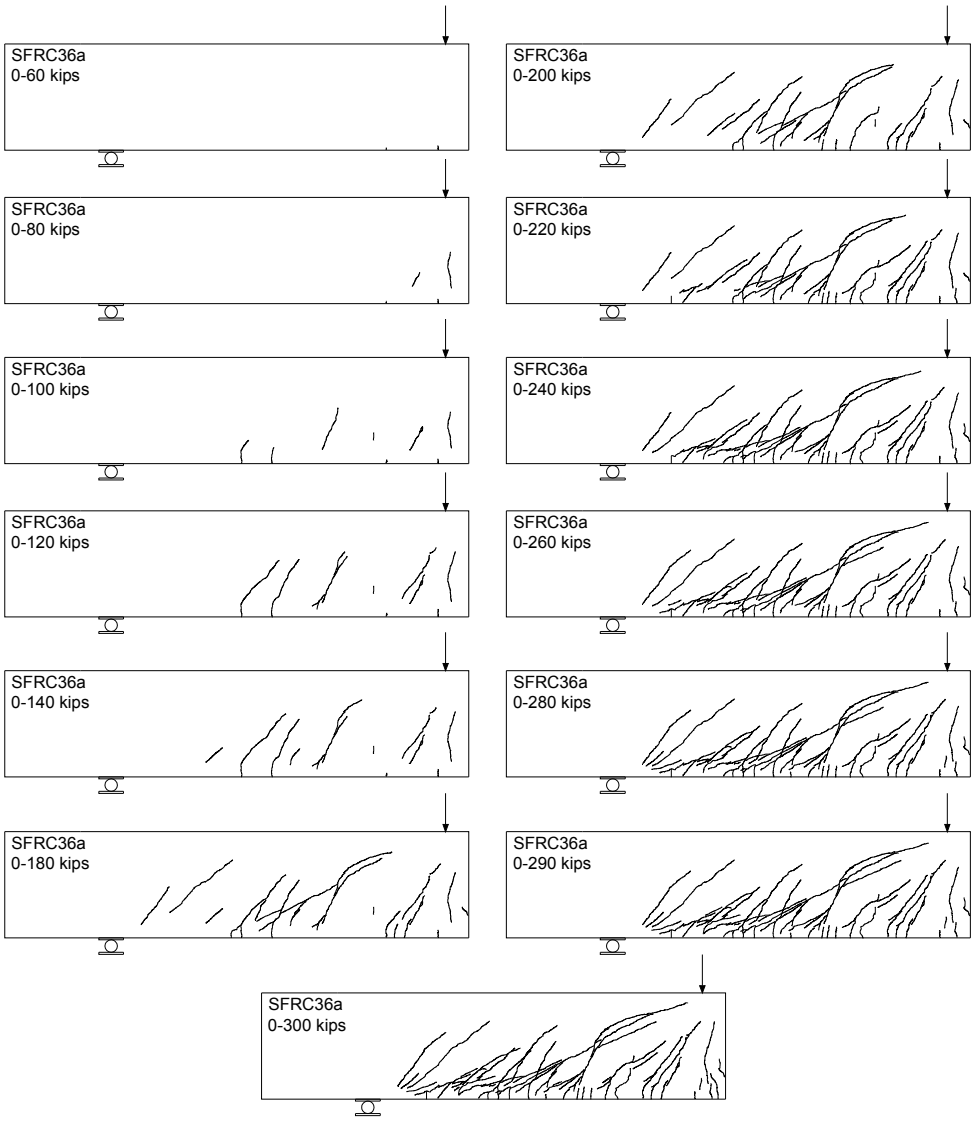

Figure 4.217 Cracking pattern for SFRC36a at different load stages

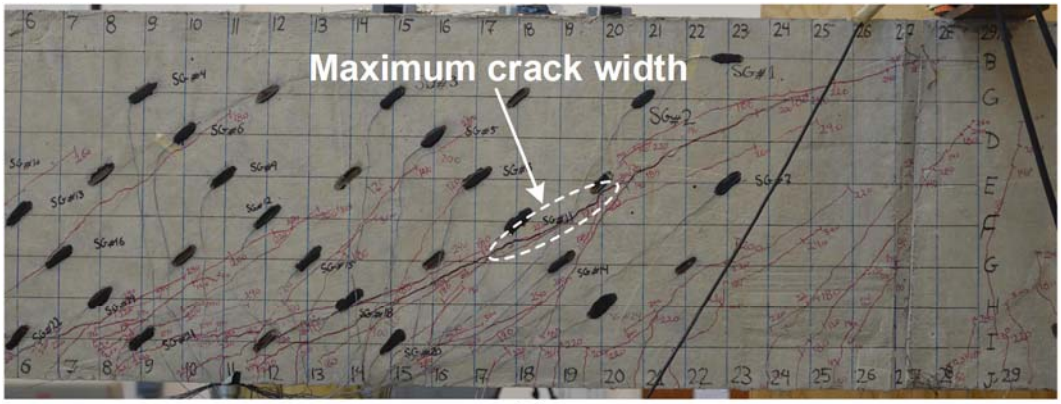

(a)

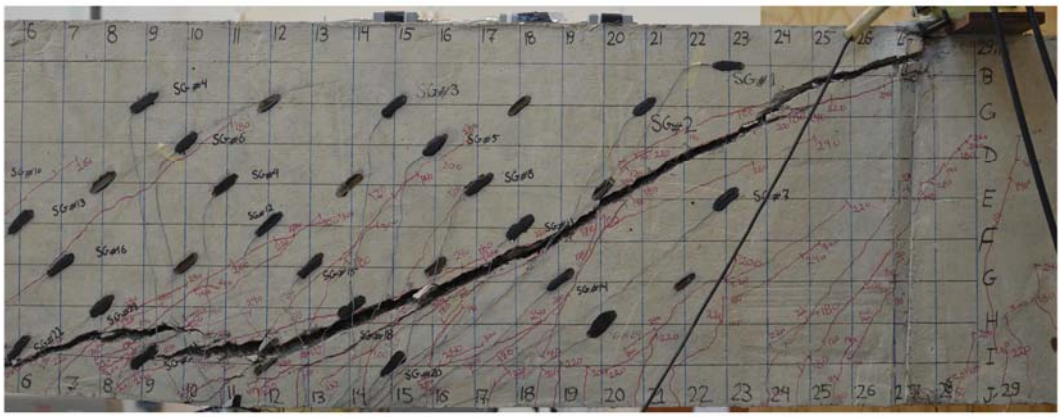

(b)

Figure 4.218 The cracking patterns of beam SFRC36a: (a) before failure; (b) after failure

4.2.8 Beam SFRC36b

4.2.8.1 Load-deflection relationship, crack pattern, and failure mode

The graph shown in Figure 4.219 represents load-mid span deflection relationship for beam SFRC36b. The first visible flexural crack occurred at 50 kips (corresponding to shear stress of $0.92\sqrt{f'_c}$). Up to this point, the curve exhibited almost a linear response like that observed for the duplicated beam (SFRC36a). At load 75 kips (corresponding to shear stress of $1.38\sqrt{f'_c}$), the first shear crack was noticed at a quite close distance to the loading point in a form of web-shear crack. Beyond this point, a marginal nonlinearity was displayed by the curve. The beam reached its ultimate strength at 316 kips (corresponding to shear

stress of $5.81\sqrt{f'_c}$). The carking patterns of the test beam for different applied loads are depicted in Figure 4.220. The presence of steel fiber turned out to not only limit the number of flexural cracks, but also their large penetration into the beam. Similar to beam SFRC36a, the flexural cracks mostly seemed to develop up to the level of longitudinal bars. As opposed to flexural cracks, beam SFRC36b experienced a widely distributed shear cracking, where the cracks highly penetrated into the beam prior to the failure. While increasing the applied load, the dowel zone developed a large amount of small inclined cracks along the top layer of longitudinal bars. Nevertheless, they did not merge and result in the development of a splitting crack which could have deteriorated into the early dowel action failure. The enhanced dowel action behavior can be attributed to the excellent performance of steel fibers to improve bond characteristics and pull-out behavior. Similar to all preceding specimens, a very stable and slow propagation rate was observed for all cracks throughout the shear span. Eventually, the failure was triggered by a sudden opening of the closest shear crack to the support (critical shear crack) from a point being 13 in. apart from the beam compression edge. The failure was recognized to be as a result of tension failure of the compression zone. The failure was brittle and caused the concrete fracture adjacent to the support. The cracking patterns prior to the failure and after that for beam SFRC36b are shown in Figure 4.221.

4.2.8.2 Strain in reinforcing bars

Figure 4.222 illustrates load-reinforcement strain responses for beam SFRC36b at the middle of the shear span and under the loading point. The presence of steel fibers in the concrete considerably enhanced the beam stiffness, what in turn, rendered the strain in the instrumented bars almost negligible up to load 20 kips. After this load, the bars started straining at the two locations. Due to the minor flexural cracking in the region under the loading point, the associated curve did not reflect any drastic change in the measured

strains and its variation rate. Therefore, the curve ascended with a constant slope up to the failure. With regard to the strains measured at the middle of the shear span, strain increased in accordance with the applied load, though with the smaller magnitude and rate than that under the loading point. Around point 170 kips, when a few shear cracks developed near the gauges at the mid-shear span, a minor change in the strain variation can attract the attentions. Based on the maximum strain measured at 2650 μe under the loading point, the bars yielded at the mid-span. However, no yielding was measured at the mid-shear span.

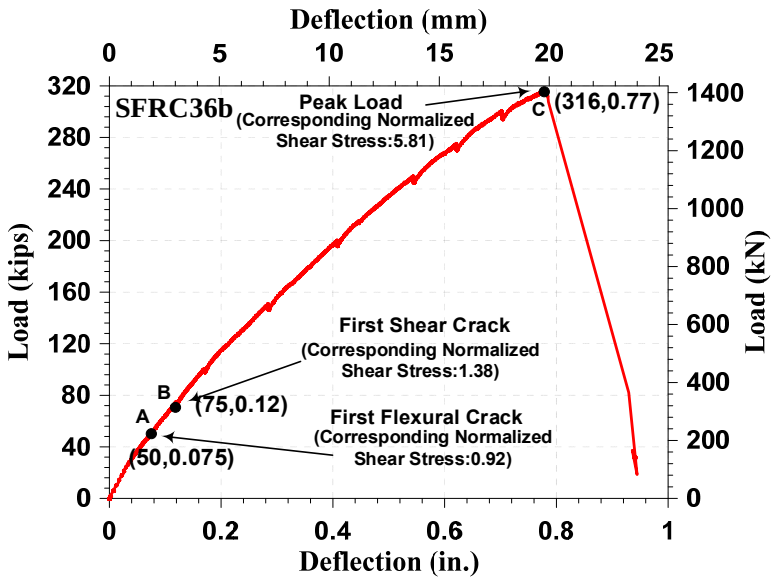

Figure 4.219 load-deflection response for beam SFRC36b

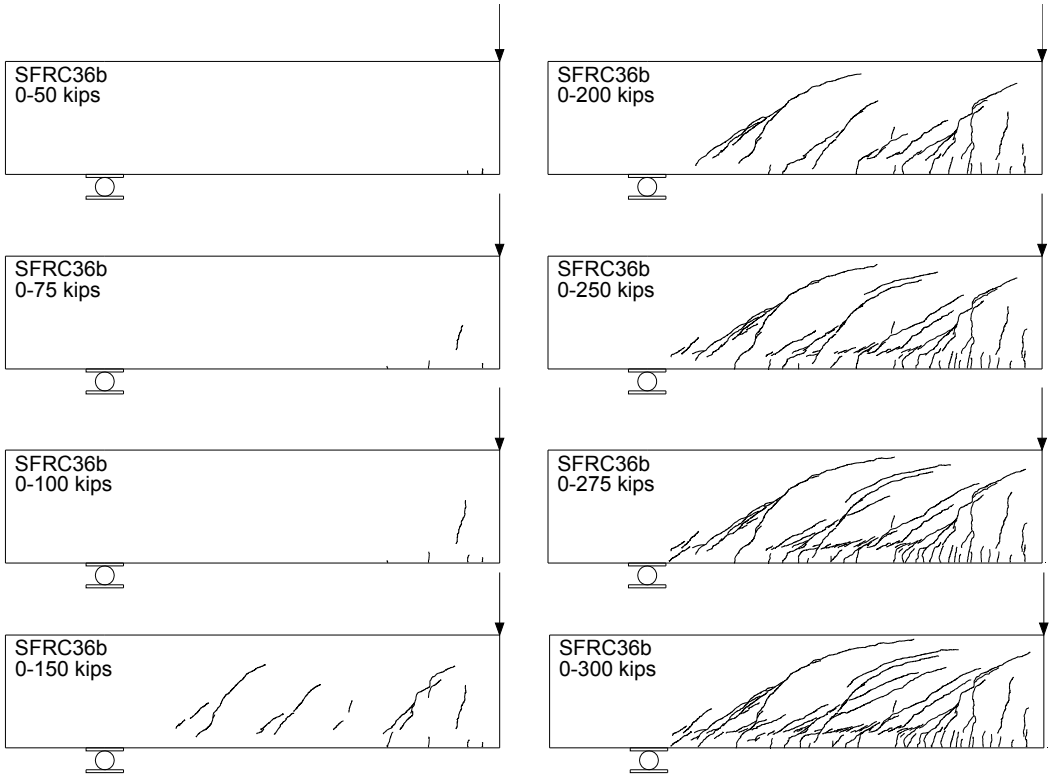

Figure 4.220 Cracking pattern for SFRC36b at different load stages

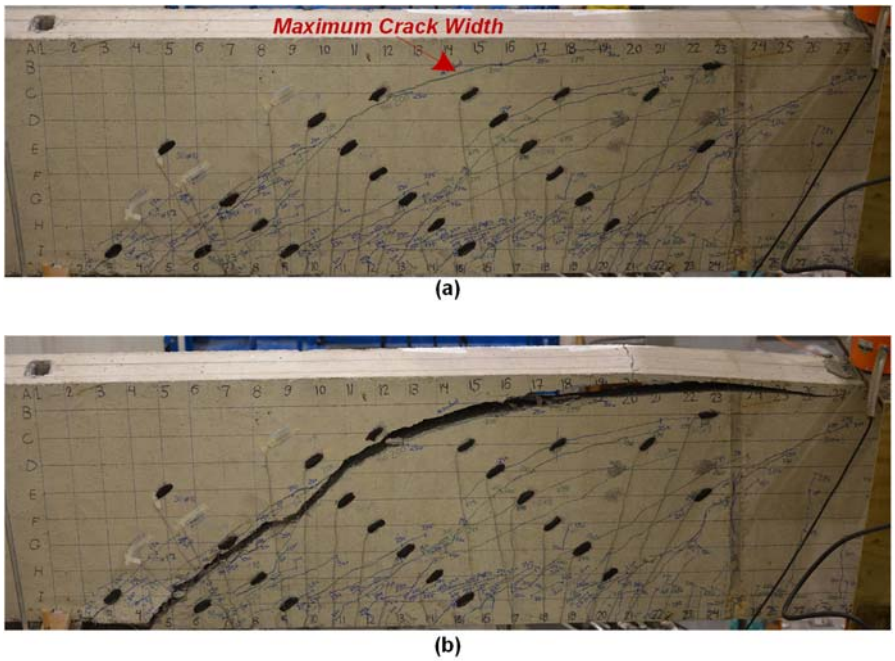

Figure 4.221 The cracking patterns of beam SFRC36b: (a) before failure; (b) after failure

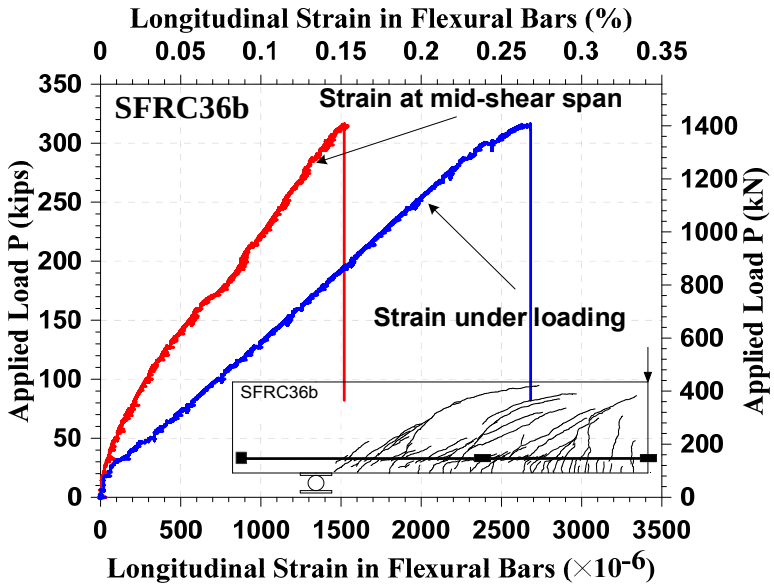

Figure 4.222 Load versus reinforcement strain relationships for beam SFRC36b

4.2.9 Beam SFRC48a

4.2.9.1 Load-deflection relationship, crack pattern, and failure mode

The graph presented in Figure 4.223 is the load-mid span deflection relationship obtained for beam SFRC48a. The first flexural crack was detected at load 50 kips (corresponding to shear stress of $0.56\sqrt{f'_c}$). Prior to the development of first shear crack, the load was linearly increased with respect to the deflection. The first shear crack became visible in a form of web-shear crack near the loading section at load 140 kips (corresponding to shear stress of $1.56\sqrt{f'_c}$). A marginal nonlinearity was observed in the curve up to the failure. The failure occurred at a maximum load of 470 kips (corresponding to shear stress of $5.24\sqrt{f'_c}$). The cracking patterns associated with beam SFRC48a at some of the loading stages are sketched in Figure 4.224. A tiny flexural crack was first observed at the first one third of the shear span from the loading point. By an increase in the applied load, while a few more flexural cracks gradually appeared in a closer distance

to the loading section, their penetrations into the beam were too low. After the first shear cracking, the beam developed in a large number of shear cracks widely distributed across the shear span. During of the loading process, the entire cracks were active and progressively propagated toward the loading point. Nevertheless, their progressions were substantially slow. As frequently observed for the test SFRC beams, the cracks ceased after reaching to a certain level. At final stages of loading, dowel cracks gradually developed along the top layer of longitudinal bars. However, the presence of steel fibers and their grate jobs in holding the crack width and slowing down the crack propagation significantly enhanced the bonding strength between the bars and SFRC, thus improving dowel action performance. Eventually, failure was triggered by sudden extending of the critical crack in the compression zone. Therefore, the mode failure was detected to be tension failure of the compression zone, as indicated by Figure 4.225.

4.2.9.2 Strain in reinforcing bars

The average of the reinforcement longitudinal strains measured at the beam mid span is shown in Figure 4.226. As indicated, the strains in the instrumented bars at the mid span varied linearly by increasing the applied load. This is due to the fact that no significant flexural crack initiated adjacent to the gauges during the entire test period. Note, the wires for the strain gauges mounted on the bars at the mid-shear span were broken during of the beam transportation to CELB.

4.2.9.3 Full-field visualization of strain components developed on the shear span concrete surface

Full-filed strain components developed on concrete surface throughout shear span for specimen SFRC48a were obtained with the aid of DIC technology at different load values and illustrated in Figure 4.227 through Figure 4.250. For the better evaluation of the

relationship between cracking pattern and the state of developed stresses acquired by DIC system, the cracks on the other side of the beam at each desired load were integrated into the corresponding DIC processed images.

The scaled full-field concrete longitudinal strain (ε_x) distributions across shear span at different loads for specimen SFRC48a were visualized from Figure 4.251 to Figure 4.256. Tensile strains are denoted in red, while other colors (yellow to dark blue) represent various magnitudes of compressive strain in the compression zone.

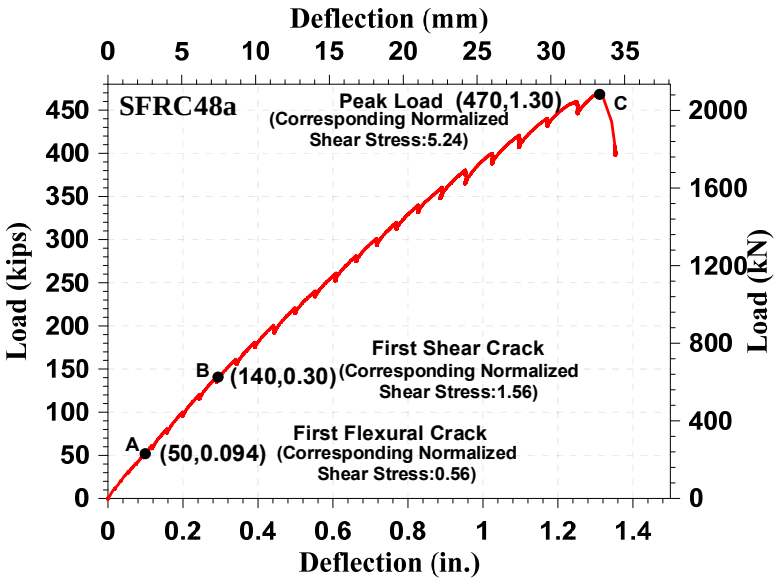

Figure 4.223 load-deflection response for beam SFRC48a

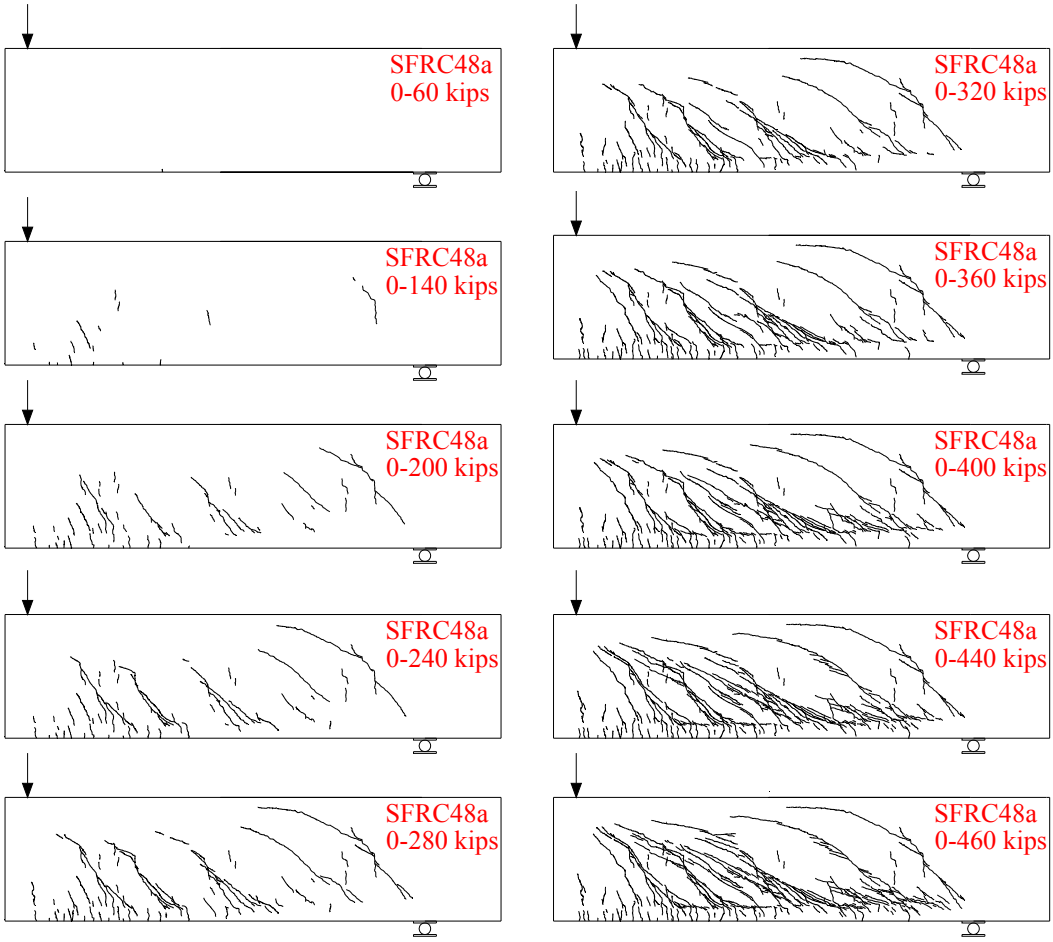

Figure 4.224 Cracking pattern for SFRC48a at different load stages

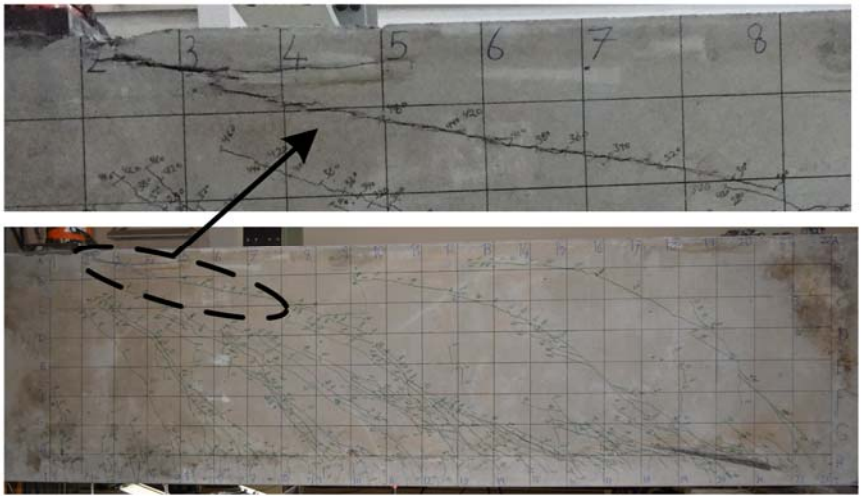

Figure 4.225 Failure of beam SFRC48a and widening of the critical crack in the compression zone

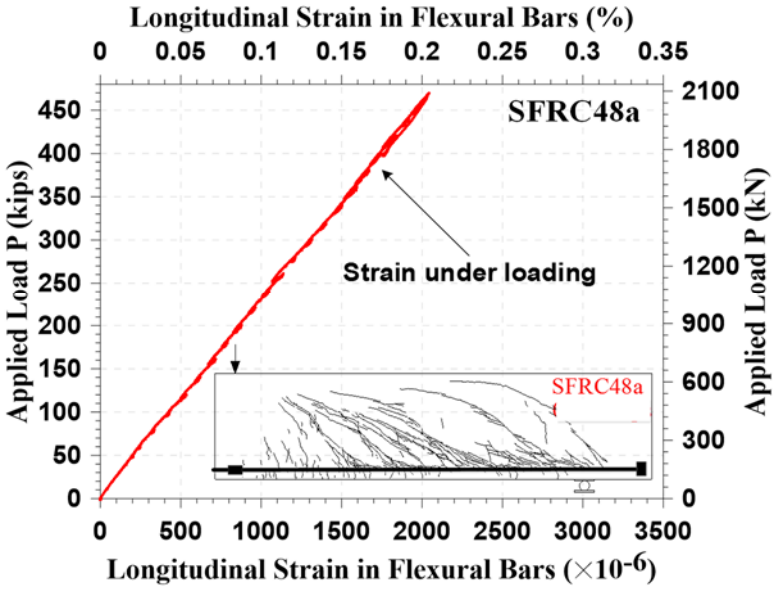

Figure 4.226 Load versus reinforcement strain relationship for beam SFRC48a

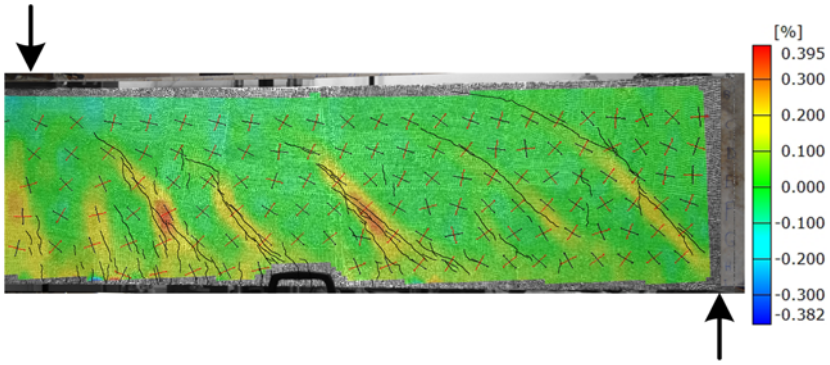

Figure 4.227 Full-field concrete longitudinal strain (ε_x) across shear span for specimen SFRC48a at normalized shear stress of $3.0\sqrt{f'_c}$

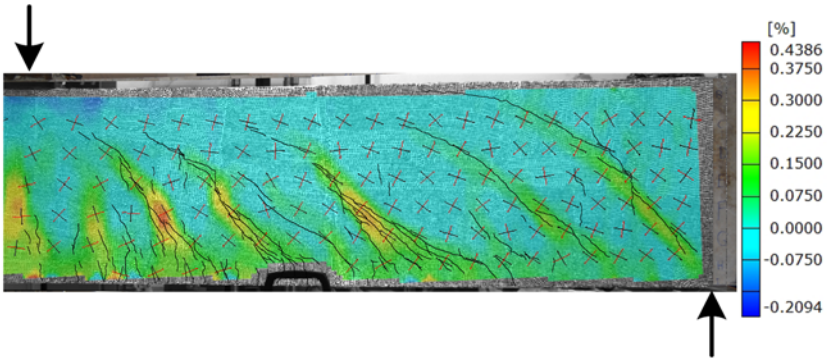

Figure 4.228 Full-field concrete longitudinal strain (ε_x) across shear span for specimen SFRC48a at normalized shear stress of $3.5\sqrt{f'_c}$

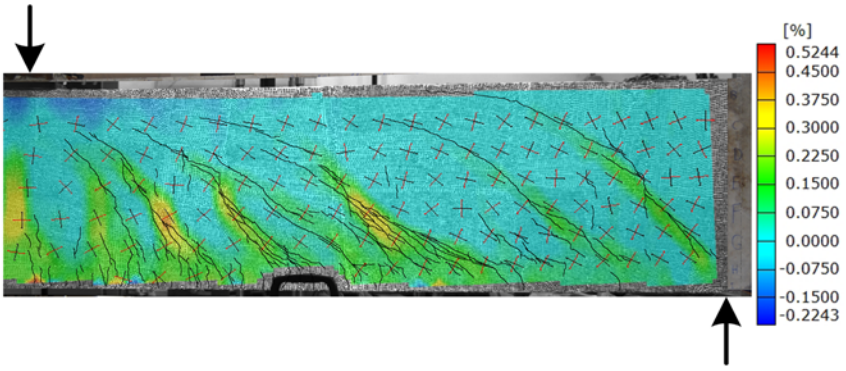

Figure 4.229 Full-field concrete longitudinal strain (ε_x) across shear span for specimen SFRC48a at normalized shear stress of $4.0\sqrt{f'_c}$

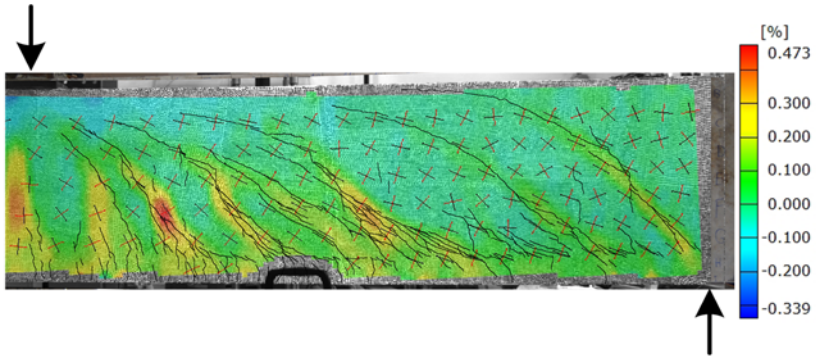

Figure 4.230 Full-field concrete longitudinal strain (ε_x) across shear span for specimen SFRC48a at normalized shear stress of $4.5\sqrt{f'_c}$

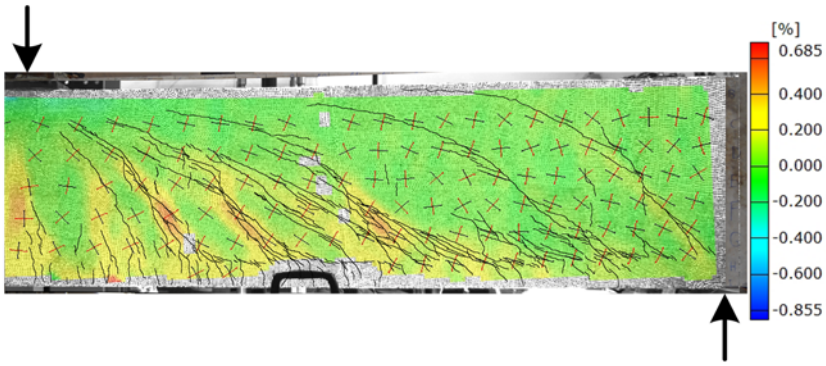

Figure 4.231 Full-field concrete longitudinal strain (ε_x) across shear span for specimen SFRC48a at normalized shear stress of $5.0\sqrt{f'_c}$

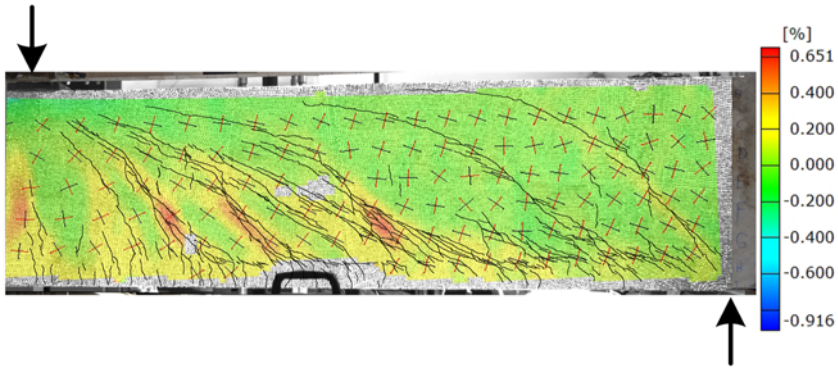

Figure 4.232 Full-field concrete longitudinal strain (ε_x) across shear span for specimen SFRC48a at normalized shear stress of $5.2\sqrt{f'_c}$

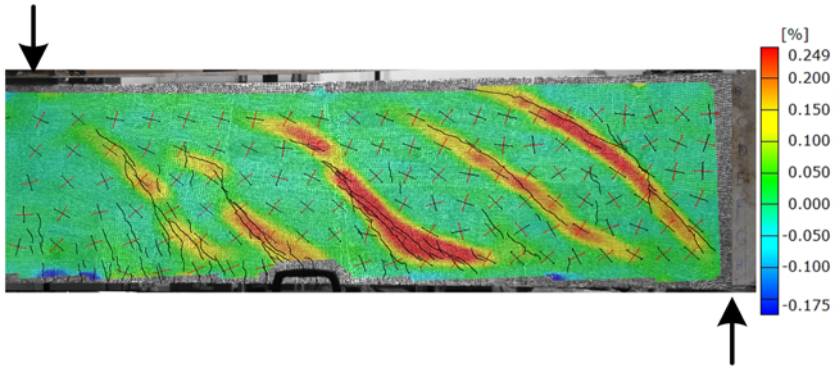

Figure 4.233 Full-field concrete transvers strain (ε_y) across shear span for specimen SFRC48a at normalized shear stress of $3.0\sqrt{f'_c}$

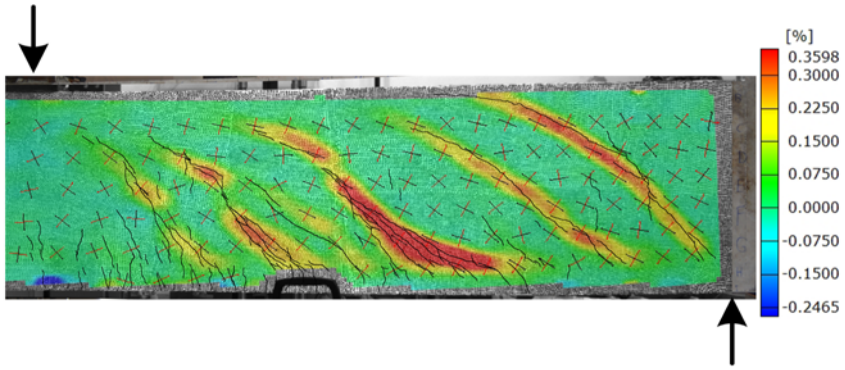

Figure 4.234 Full-field concrete transvers strain (ε_y) across shear span for specimen SFRC48a at normalized shear stress of $3.5\sqrt{f'_c}$

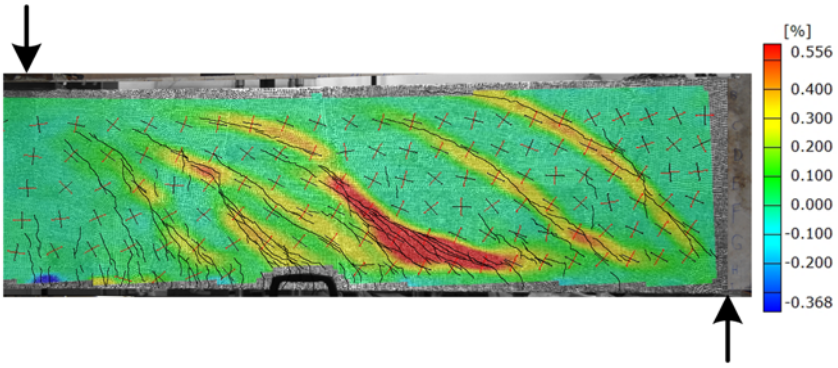

Figure 4.235 Full-field concrete transvers strain (ε_y) across shear span for specimen SFRC48a at normalized shear stress of $4.0\sqrt{f'_c}$

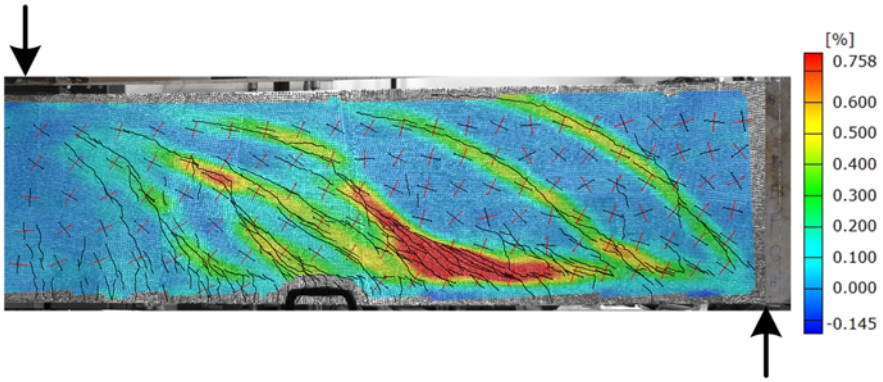

Figure 4.236 Full-field concrete transvers strain (ε_y) across shear span for specimen SFRC48a at normalized shear stress of $4.5\sqrt{f'_c}$

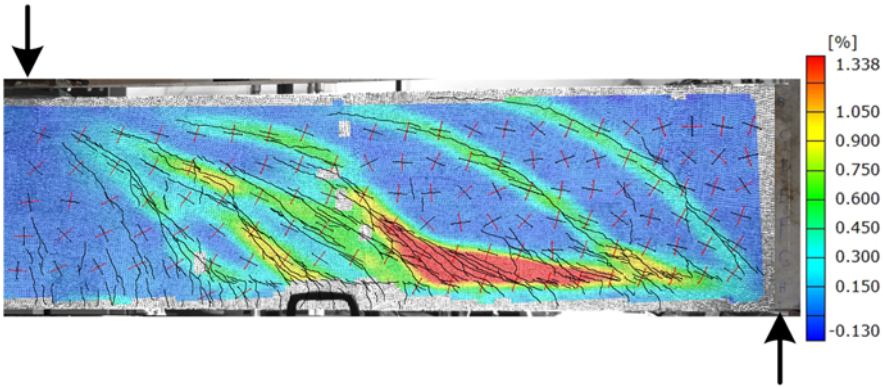

Figure 4.237 Full-field concrete transvers strain (ε_y) across shear span for specimen SFRC48a at normalized shear stress of $5.0\sqrt{f'_c}$

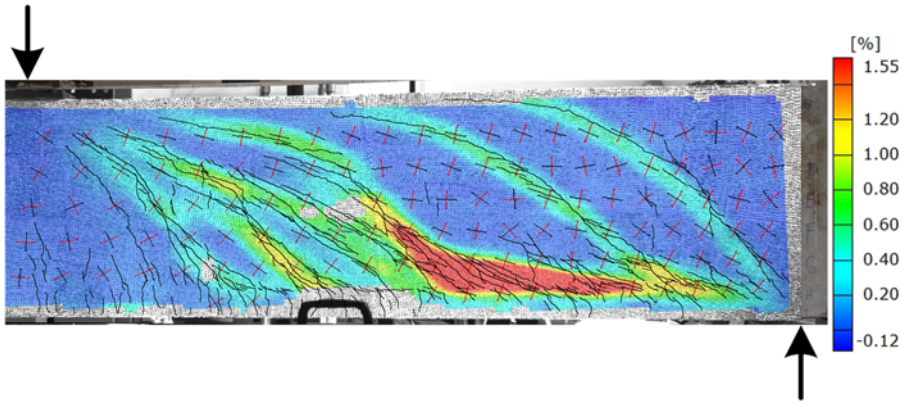

Figure 4.238 Full-field concrete transvers strain (ε_y) across shear span for specimen SFRC48a at normalized shear stress of $5.2\sqrt{f'_c}$

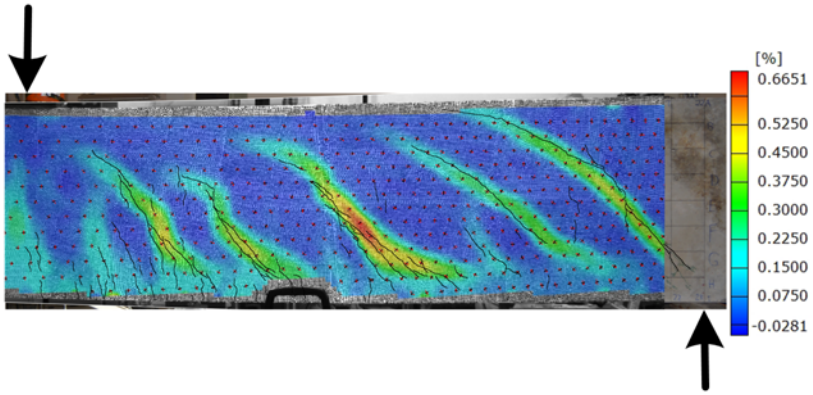

Figure 4.239 Full-field concrete maximum principal strain (σ_1) across shear span for specimen SFRC48a at normalized shear stress of $3.0\sqrt{f'_c}$

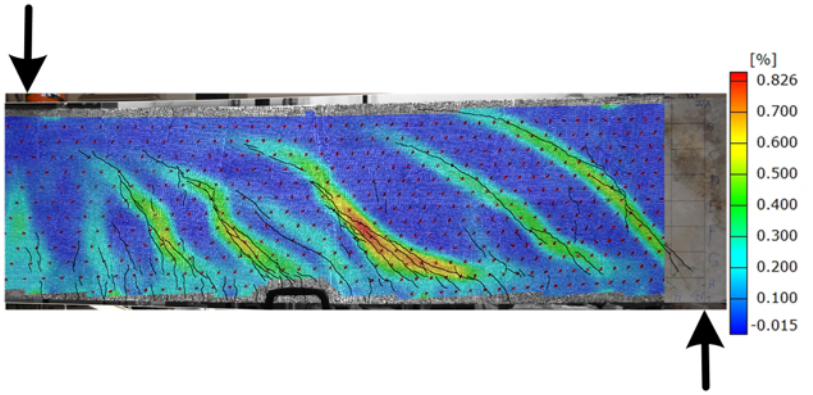

Figure 4.240 Full-field concrete maximum principal strain (σ_1) across shear span for specimen SFRC48a at normalized shear stress of $3.5\sqrt{f'_c}$

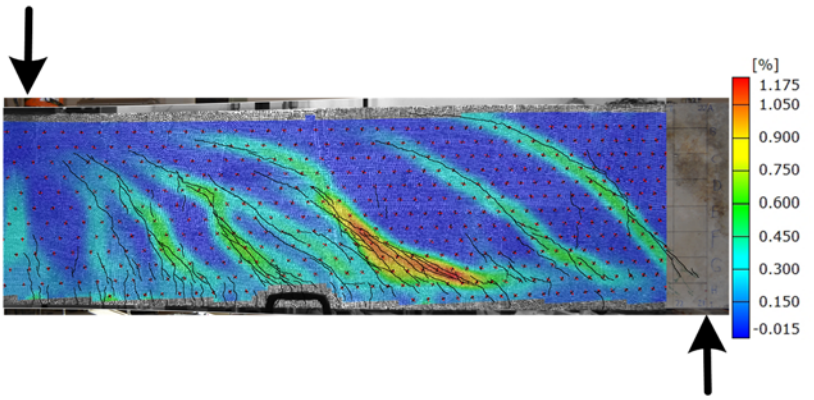

Figure 4.241 Full-field concrete maximum principal strain (σ_1) across shear span for specimen SFRC48a at normalized shear stress of $4.0\sqrt{f'_c}$

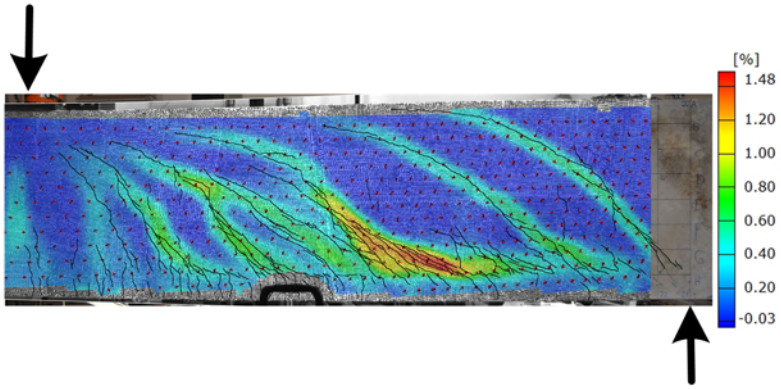

Figure 4.242 Full-field concrete maximum principal strain (σ_1) across shear span for specimen SFRC48a at normalized shear stress of $4.5\sqrt{f'_c}$

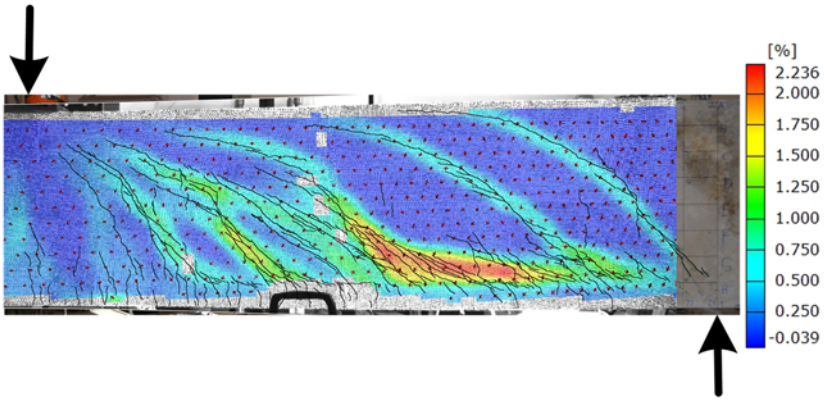

Figure 4.243 Full-field concrete maximum principal strain (σ_1) across shear span for specimen SFRC48a at normalized shear stress of $5.0\sqrt{f'_c}$

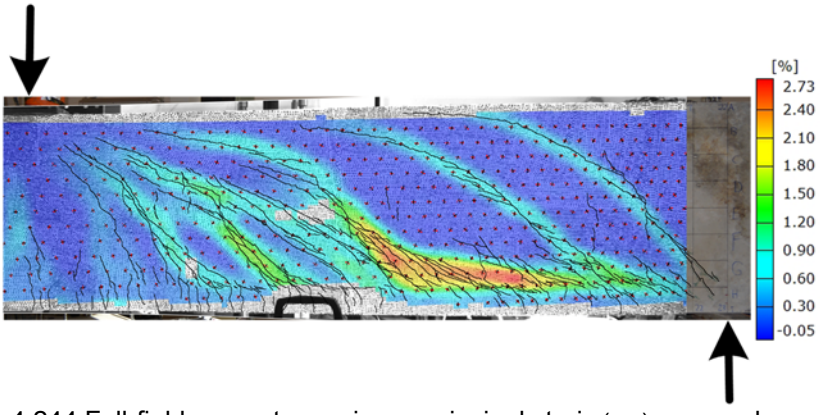

Figure 4.244 Full-field concrete maximum principal strain (σ_1) across shear span for specimen SFRC48a at normalized shear stress of $5.2\sqrt{f'_c}$

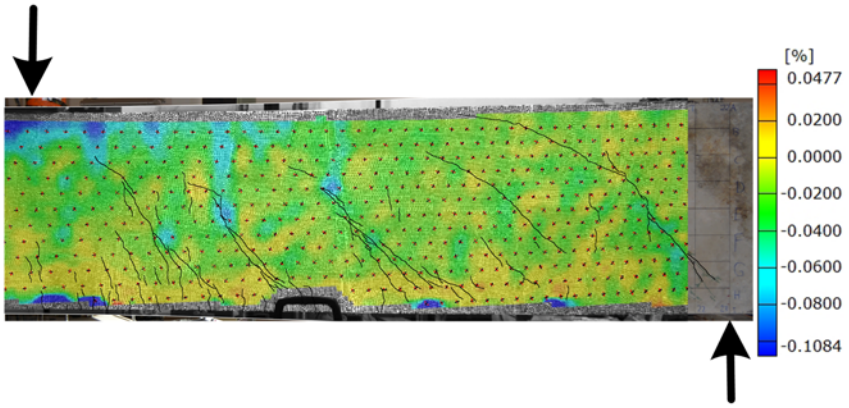

Figure 4.245 Full-field concrete minimum principal strain (σ_2) across shear span for specimen SFRC48a at normalized shear stress of $3.0\sqrt{f'_c}$

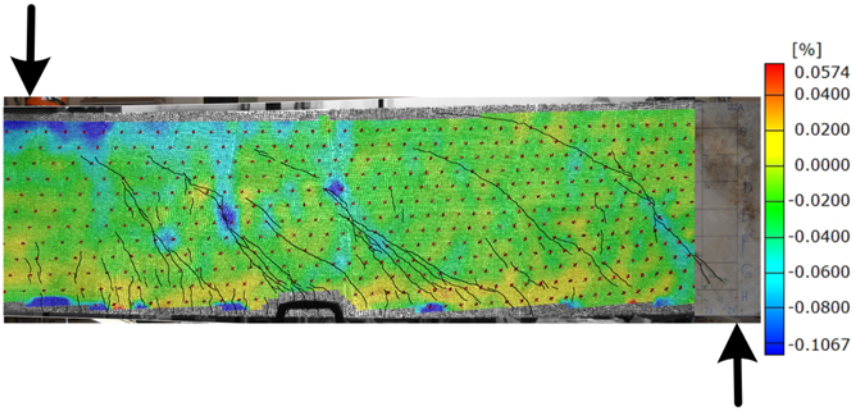

Figure 4.246 Full-field concrete minimum principal strain (σ_2) across shear span for specimen SFRC48a at normalized shear stress of $3.5\sqrt{f'_c}$

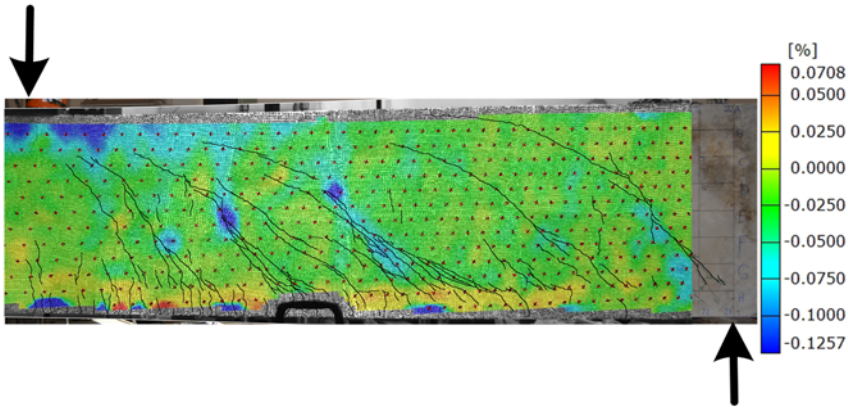

Figure 4.247 Full-field concrete minimum principal strain (σ_2) across shear span for specimen SFRC48a at normalized shear stress of $4.0\sqrt{f'_c}$

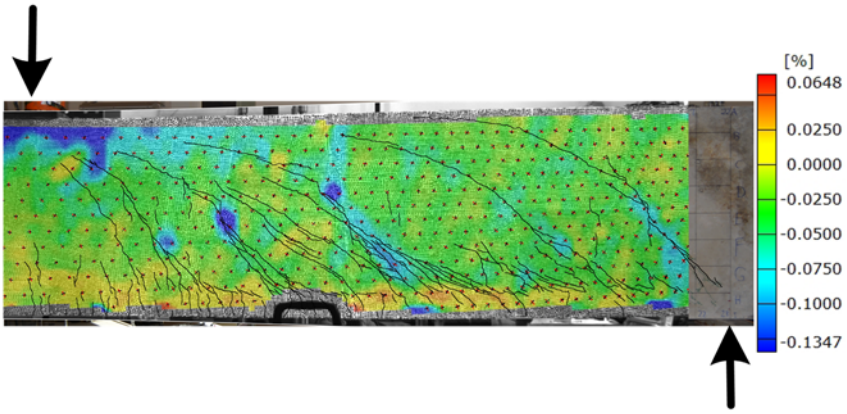

Figure 4.248 Full-field concrete minimum principal strain (σ_2) across shear span for specimen SFRC48a at normalized shear stress of $4.5\sqrt{f'_c}$

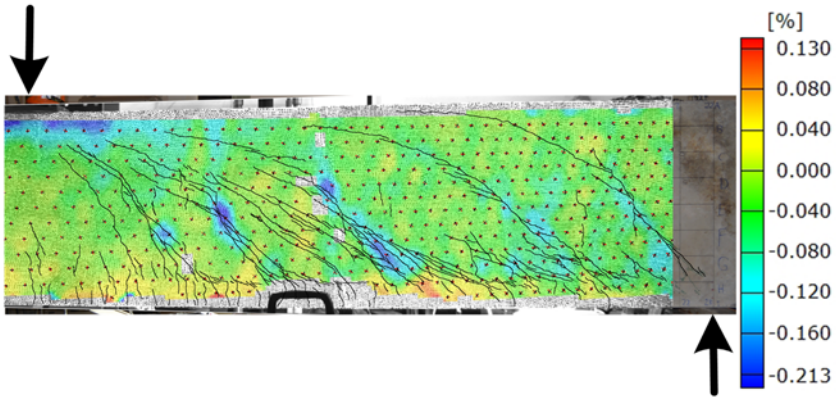

Figure 4.249 Full-field concrete minimum principal strain (σ_2) across shear span for specimen SFRC48a at normalized shear stress of $5.0\sqrt{f'_c}$

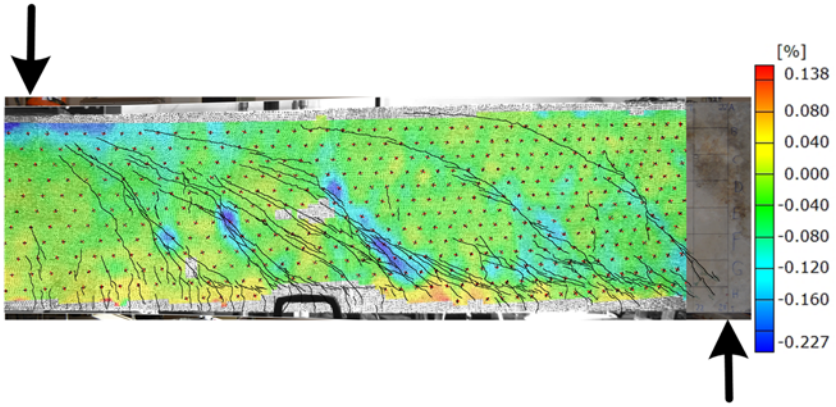

Figure 4.250 Full-field concrete minimum principal strain (σ_2) across shear span for specimen SFRC48a at normalized shear stress of $5.2\sqrt{f'_c}$

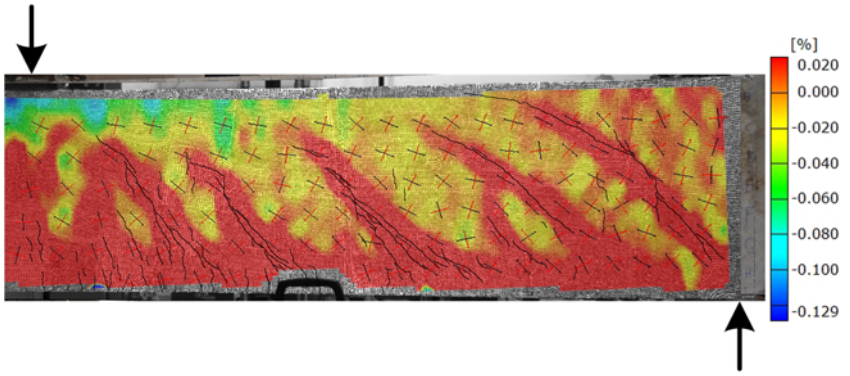

Figure 4.251 Scaled full-field concrete longitudinal strain (ε_x) across shear span for specimen SFRC48a at normalized shear stress of $3.0\sqrt{f'_c}$

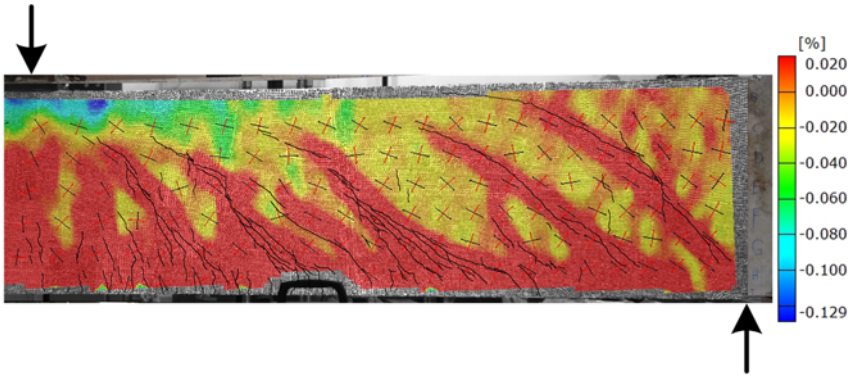

Figure 4.252 Scaled full-field concrete longitudinal strain (ε_x) across shear span for specimen SFRC48a at normalized shear stress of $3.5\sqrt{f'_c}$

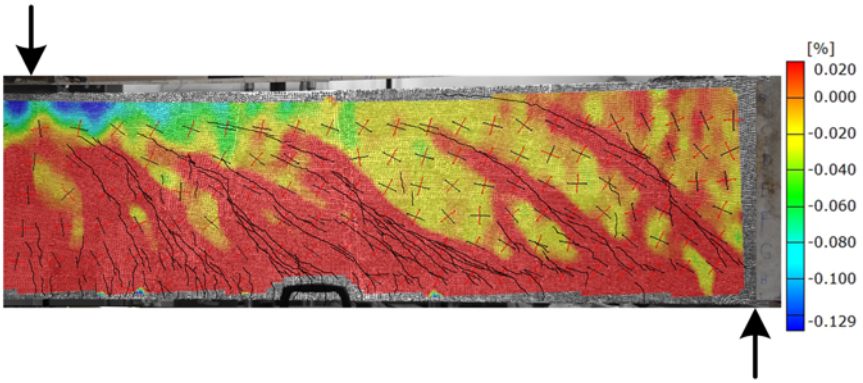

Figure 4.253 Scaled full-field concrete longitudinal strain (ε_x) across shear span for specimen SFRC48a at normalized shear stress of $4.0\sqrt{f'_c}$

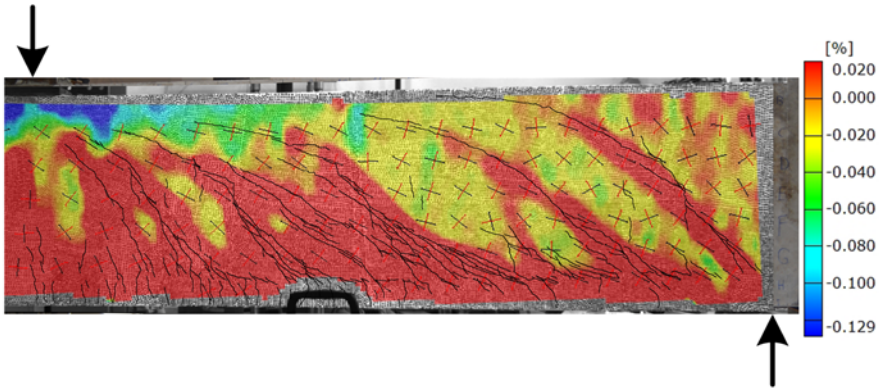

Figure 4.254 Scaled full-field concrete longitudinal strain (ε_x) across shear span for specimen SFRC48a at normalized shear stress of $4.5\sqrt{f'_c}$

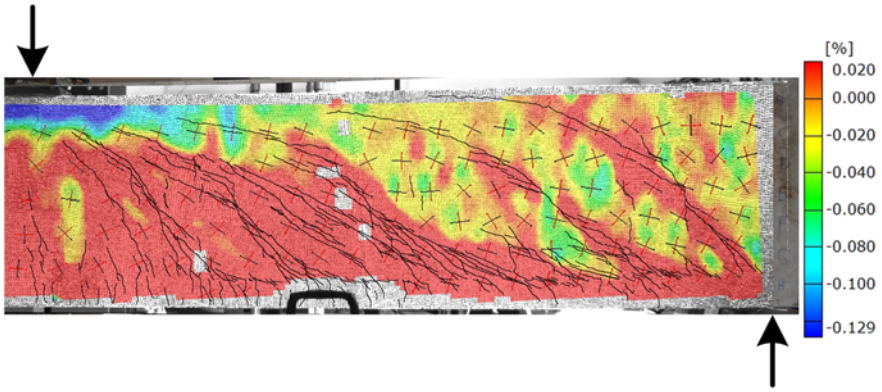

Figure 4.255 Scaled full-field concrete longitudinal strain (ε_x) across shear span for specimen SFRC48a at normalized shear stress of $5.0\sqrt{f'_c}$

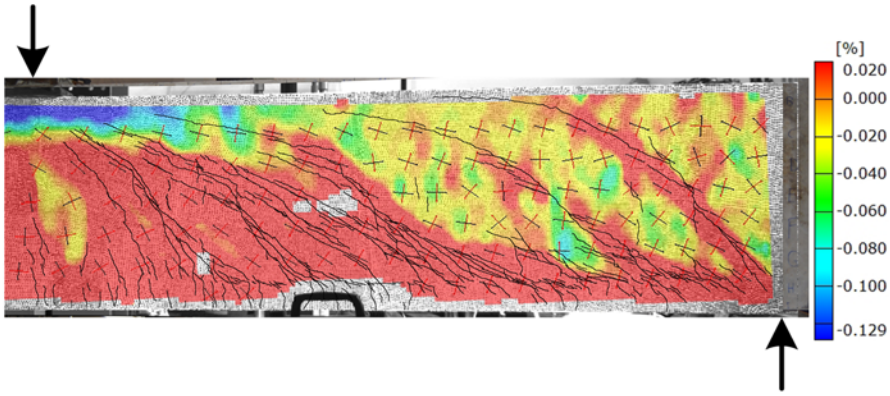

Figure 4.256 Scaled full-field concrete longitudinal strain (ε_x) across shear span for specimen SFRC48a at normalized shear stress of $5.2\sqrt{f'_c}$

4.2.10 Beam SFRC48b

4.2.10.1 Load-deflection relationship, crack pattern, and failure mode

The behavior of beam SFRC48b in terms of the applied load versus mid-span deflection is plotted in Figure 4.257. The first flexural crack occurred at load 80 kips (corresponding to shear stress of $0.89\sqrt{f'_c}$). Subsequently, the beam began to crack in shear at load 140 kips (corresponding to shear stress of $1.56\sqrt{f'_c}$). Eventually, after carrying a maximum load of 454 kips (corresponding to shear stress of $5.06\sqrt{f'_c}$), it failed in an brittle manner. The cracking pattern corresponding to each loading stage is displayed in Figure 4.258. At load 80 kips, a number of small flexural cracks developed all along the shear span, yet their length was too short such that they could be barely detected. Increasing the applied load by 40 kips did not noticeably make any change in the cracking pattern except the formation of a series of small flexural cracks whose initiations were not from the tension edge of the beam, as referred to as web-flexural cracks. After having a little progression in the existing web-flexural cracks, the first shear crack was formed rather close to the loading section. As the load increased, new shear cracks widely distributed over the shear span. The existence of steel fibers effectively stabilized the progression of the cracks and reduced their extension rate. like other tested beams, the large area around the loading point was observed free of cracking even up the higher loads. In the mid time, the typical small inclined dowel cracking was also garbed our attention. The beam eventually failed by a sudden fully extension of a shear crack (critical crack) within the compression zone, as demonstrated by Figure 4.259.

4.2.10.2 Strain in reinforcing bars

The average of the longitudinal strains in a pair of reinforcing bars at two locations of the loading sections and mid shear span is plotted in conjunction with the applied load

in Figure 4.260. The under loading average strain of the instrumented bars linearly varied by an increase in the external load; however, by initiation of the first flexural cracking and a minor jump in the magnitude, it resumed the progress with the initial steady rate up to the failure. The strain induced at each load at the mid shear span location was entirely lower than the corresponding strain under the loading point at the same load. Nevertheless, the applied load maintained its linear relationship with the measured strain up to the load carrying capacity of the beam.

4.2.10.3 Full-field visualization of strain components developed on the shear span concrete surface

Full-filed strain components developed on concrete surface throughout shear span for specimen SFRC48b were obtained with the aid of DIC technology at different load values and illustrated in Figure 4.261 through Figure 4.284. For the better evaluation of the relationship between cracking pattern and the state of developed stresses acquired by DIC system, the cracks on the other side of the beam at each desired load were integrated into the corresponding DIC processed images.

The scaled full-field concrete longitudinal strain (ε_x) distributions across shear span at different loads for specimen SFRC48b were visualized from Figure 4.285 to Figure 4.290. Tensile strains are denoted in red, while other colors (yellow to dark blue) represent various magnitudes of compressive strain in the compression zone.

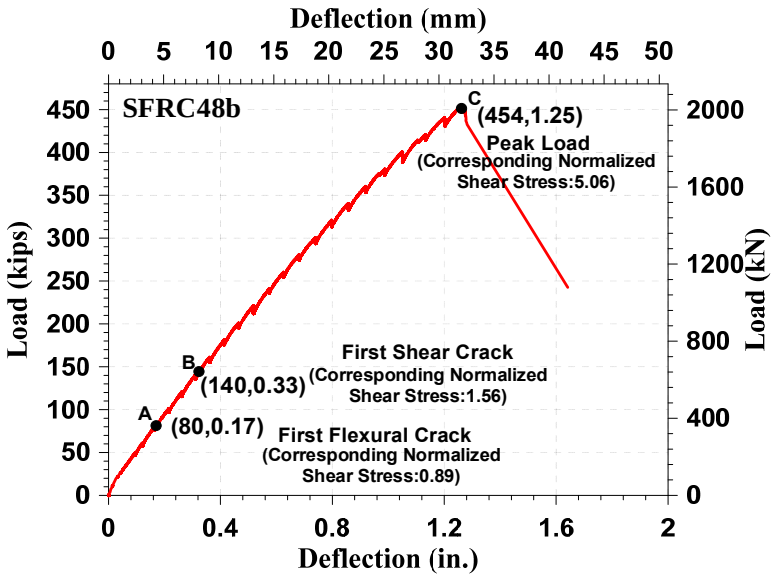

Figure 4.257 load-deflection response for beam SFRC48b

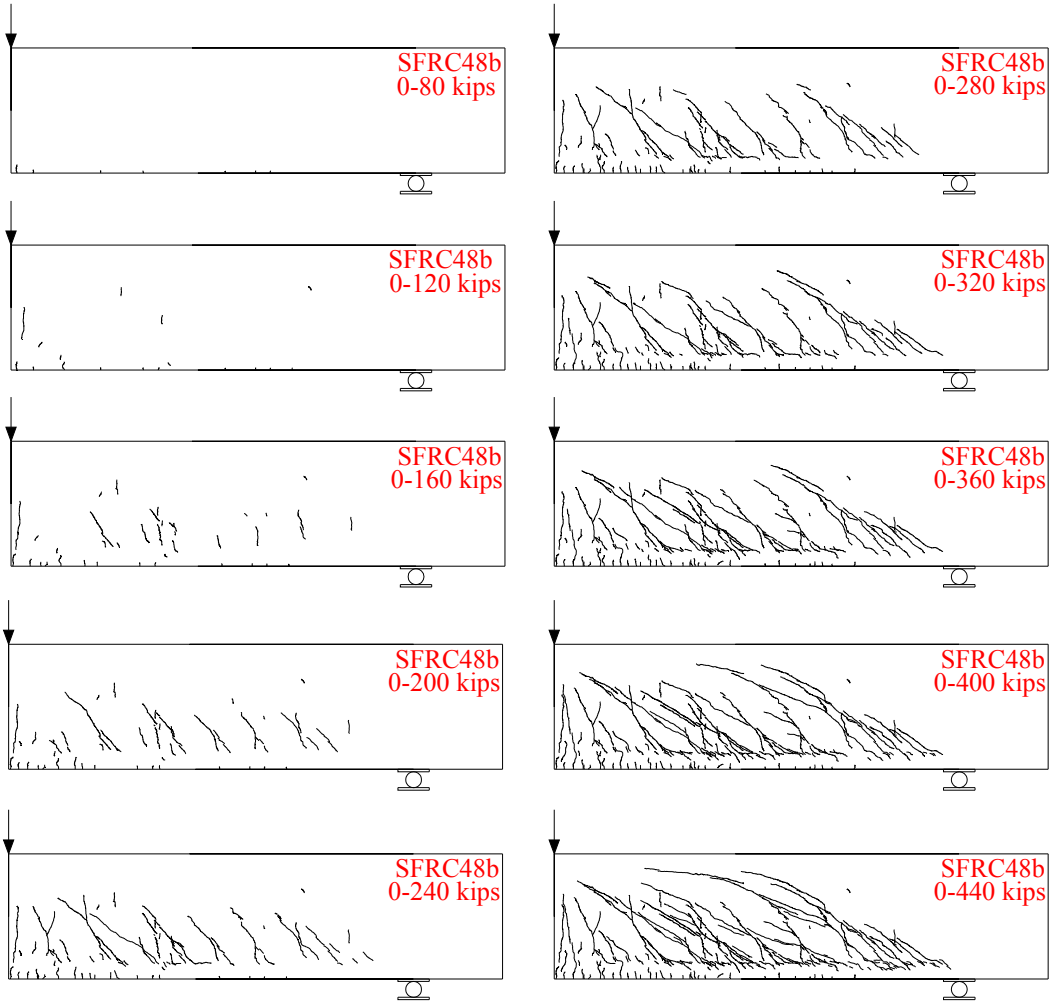

Figure 4.258 Cracking pattern for SFRC48b at different load stages

(a)

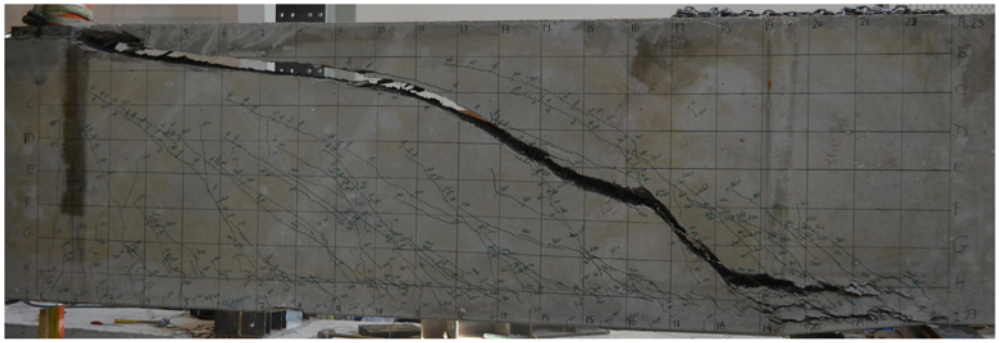

(b)

Figure 4.259 A view of cracking for beam SFRC48b: (a) just before the failure; (b) at failure

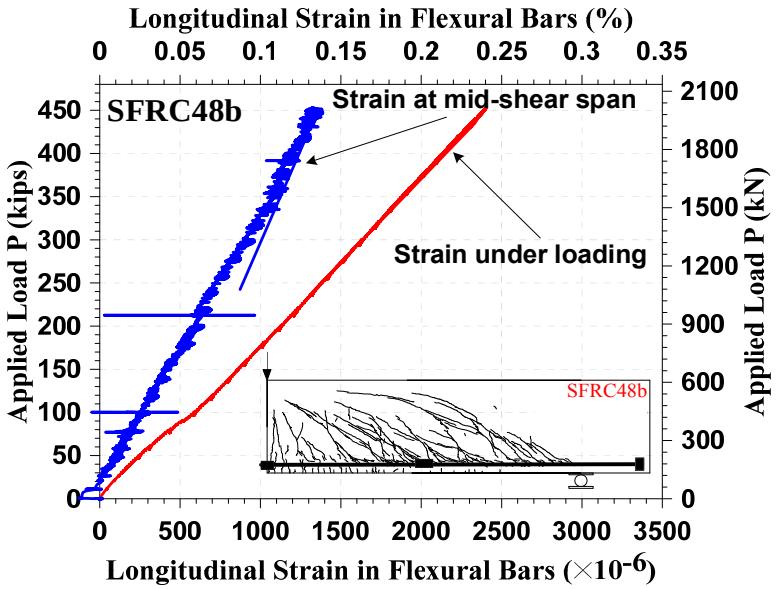

Figure 4.260 Load versus reinforcement strain relationships for beam SFRC48b

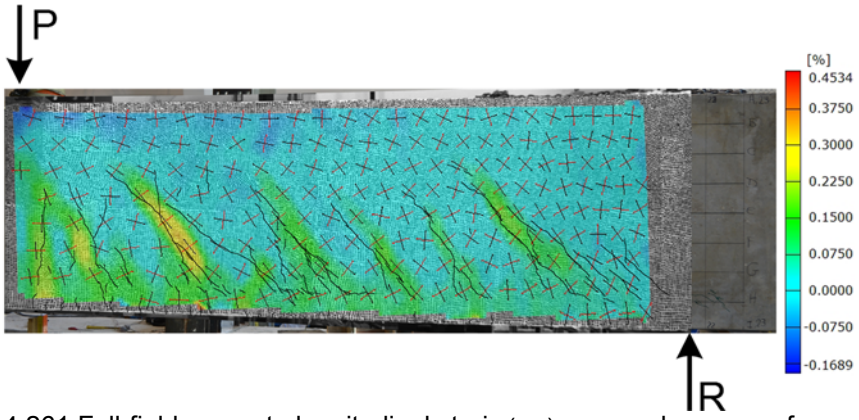

Figure 4.261 Full-field concrete longitudinal strain (ε_x) across shear span for specimen SFRC48b at normalized shear stress of $3.0\sqrt{f'_c}$

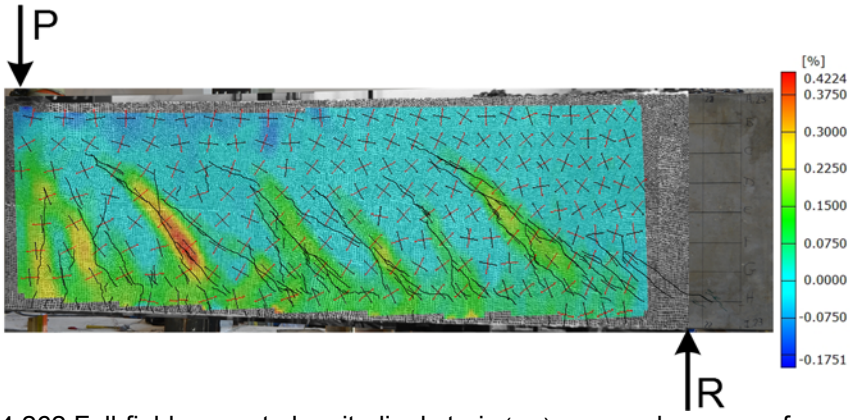

Figure 4.262 Full-field concrete longitudinal strain (ε_x) across shear span for specimen SFRC48b at normalized shear stress of $3.5\sqrt{f'_c}$

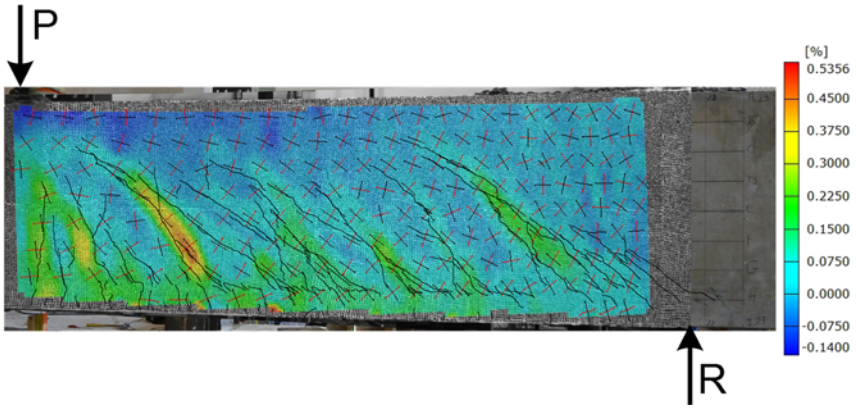

Figure 4.263 Full-field concrete longitudinal strain (ε_x) across shear span for specimen SFRC48b at normalized shear stress of $4.0\sqrt{f'_c}$

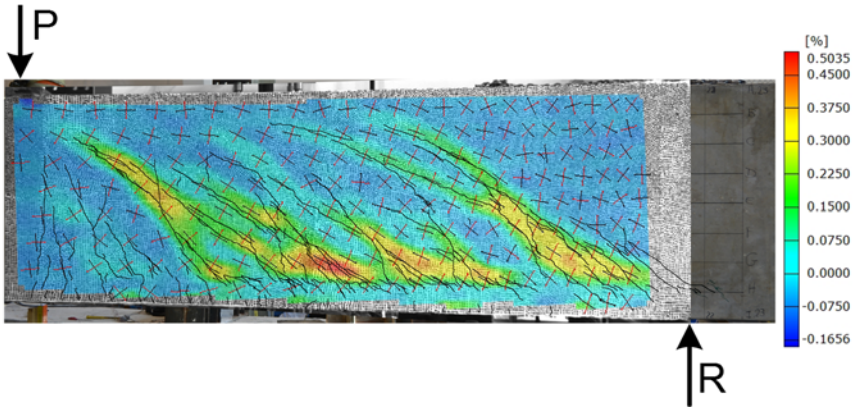

Figure 4.264 Full-field concrete longitudinal strain (ε_x) across shear span for specimen SFRC48b at normalized shear stress of $4.5\sqrt{f'_c}$

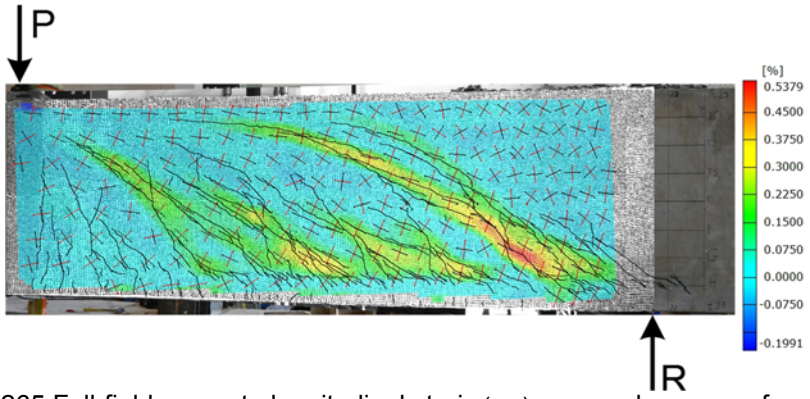

Figure 4.265 Full-field concrete longitudinal strain (ε_x) across shear span for specimen SFRC48b at normalized shear stress of $5.0\sqrt{f'_c}$

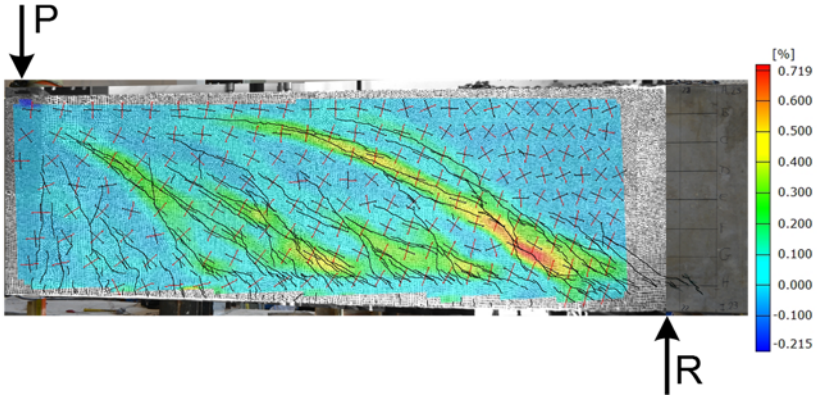

Figure 4.266 Full-field concrete longitudinal strain (ε_x) across shear span for specimen SFRC48b at normalized shear stress of $5.1\sqrt{f'_c}$

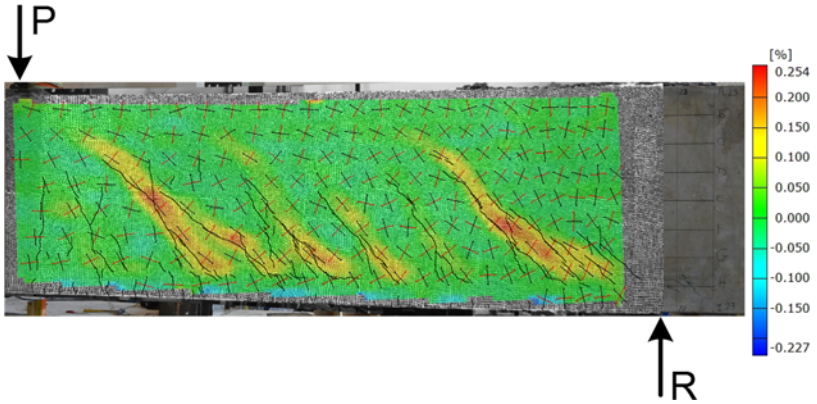

Figure 4.267 Full-field concrete transvers strain (ε_y) across shear span for specimen SFRC48b at normalized shear stress of $3.0\sqrt{f'_c}$

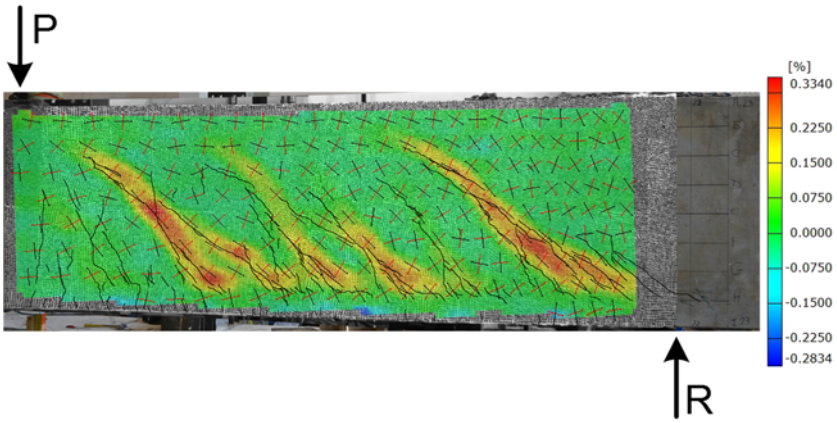

Figure 4.268 Full-field concrete transvers strain (ε_y) across shear span for specimen SFRC48b at normalized shear stress of $3.5\sqrt{f'_c}$

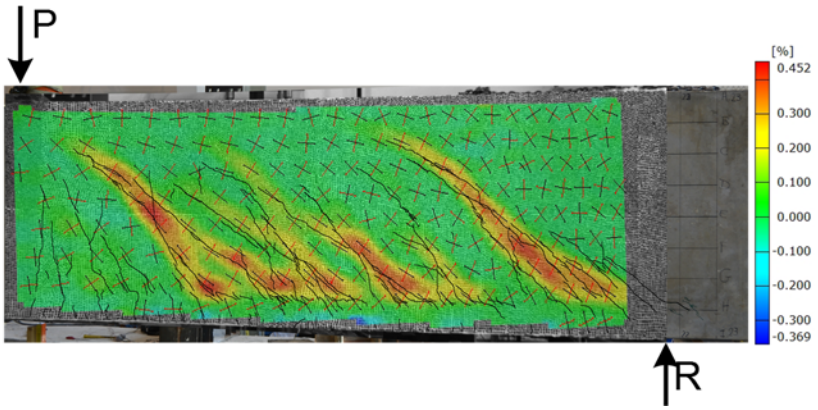

Figure 4.269 Full-field concrete transvers strain (ε_y) across shear span for specimen SFRC48b at normalized shear stress of $4.0\sqrt{f'_c}$

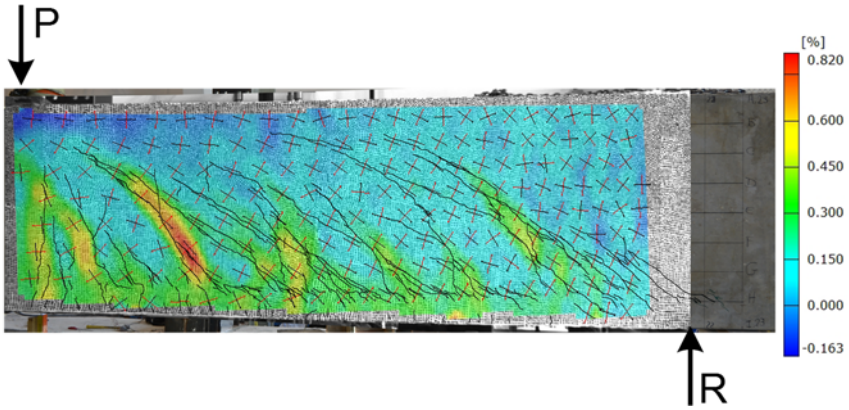

Figure 4.270 Full-field concrete transvers strain (ε_y) across shear span for specimen SFRC48b at normalized shear stress of $4.5\sqrt{f'_c}$

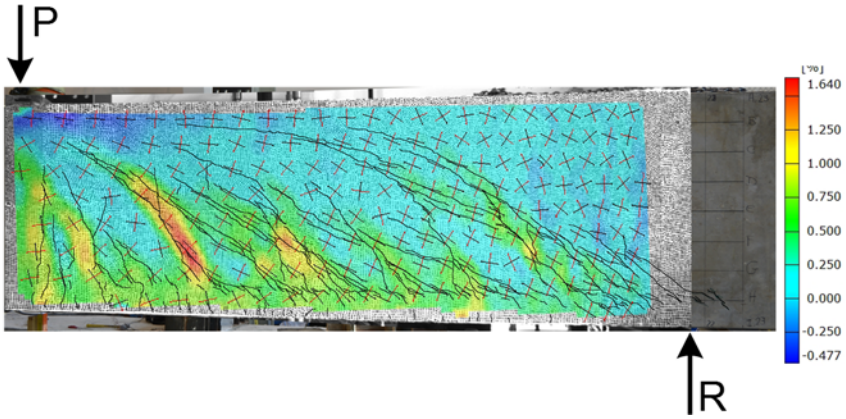

Figure 4.271 Full-field concrete transvers strain (ε_y) across shear span for specimen SFRC48b at normalized shear stress of $5.0\sqrt{f'_c}$

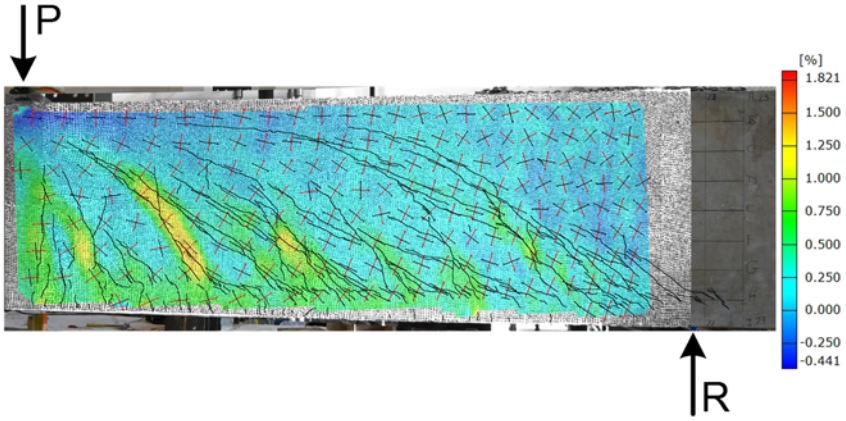

Figure 4.272 Full-field concrete transvers strain (ε_y) across shear span for specimen SFRC48b at normalized shear stress of $5.1\sqrt{f'_c}$

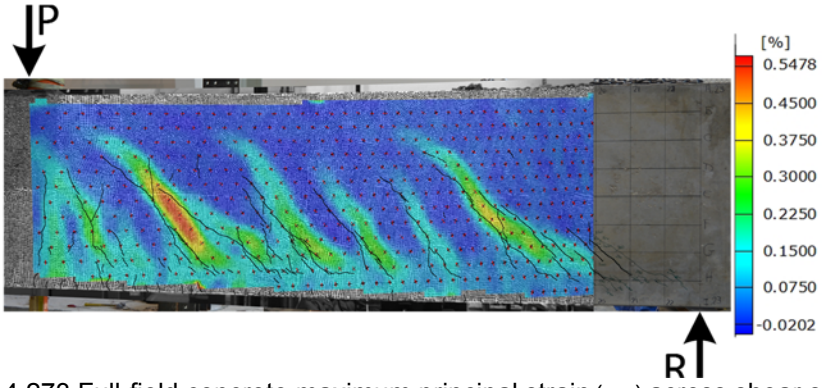

Figure 4.273 Full-field concrete maximum principal strain (σ_1) across shear span for specimen SFRC48b at normalized shear stress of $3.0\sqrt{f'_c}$

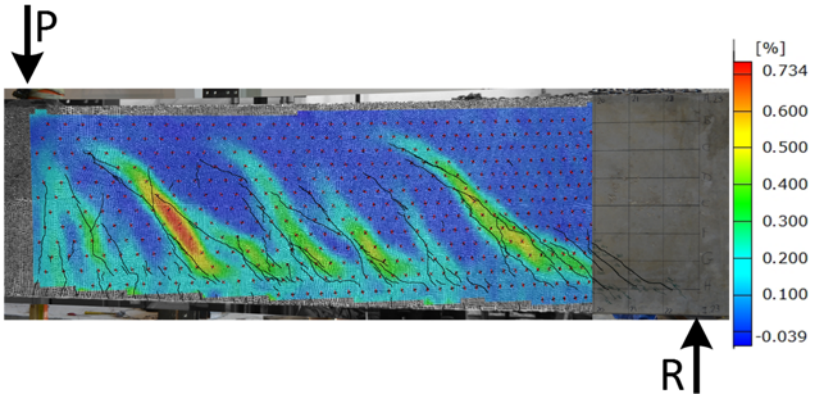

Figure 4.274 Full-field concrete maximum principal strain (σ_1) across shear span for specimen SFRC48b at normalized shear stress of $3.5\sqrt{f'_c}$

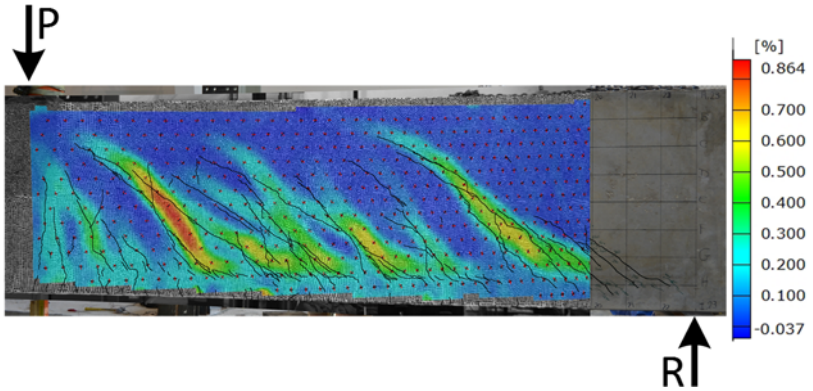

Figure 4.275 Full-field concrete maximum principal strain (σ_1) across shear span for specimen SFRC48b at normalized shear stress of $4.0\sqrt{f'_c}$

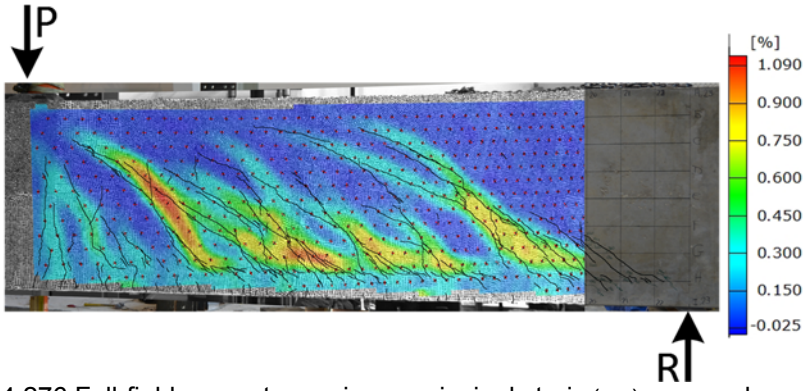

Figure 4.276 Full-field concrete maximum principal strain (σ_1) across shear span for specimen SFRC48b at normalized shear stress of $4.5\sqrt{f'_c}$

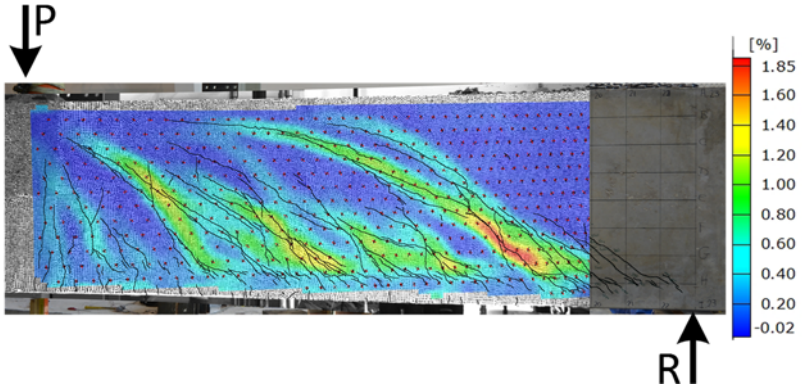

Figure 4.277 Full-field concrete maximum principal strain (σ_1) across shear span for specimen SFRC48b at normalized shear stress of $5.0\sqrt{f'_c}$

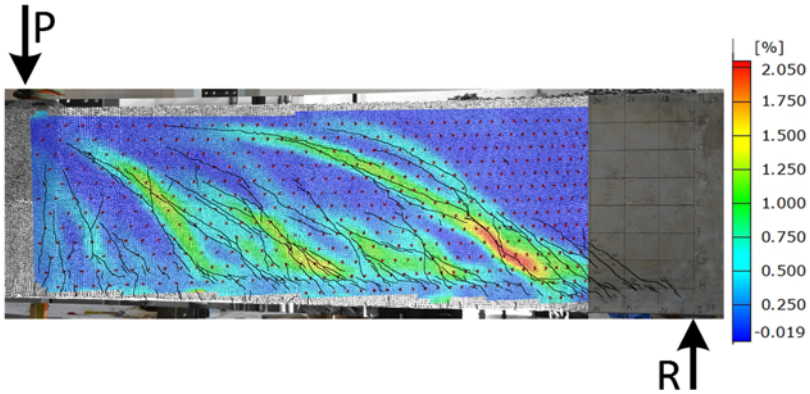

Figure 4.278 Full-field concrete maximum principal strain (σ_1) across shear span for specimen SFRC48b at normalized shear stress of $5.1\sqrt{f'_c}$

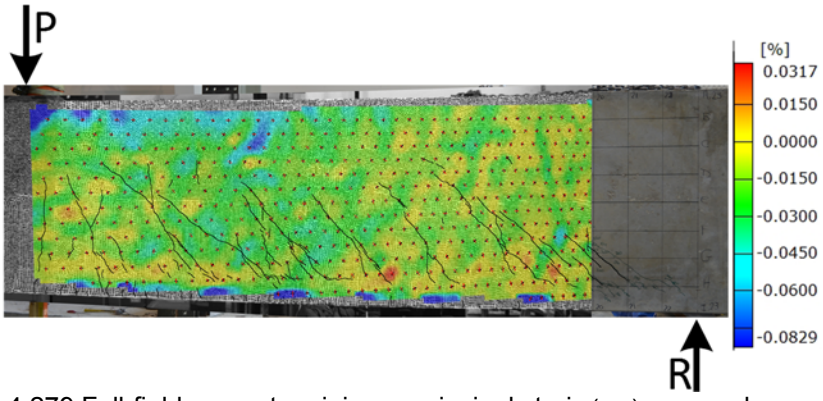

Figure 4.279 Full-field concrete minimum principal strain (σ_2) across shear span for specimen SFRC48b at normalized shear stress of $3.0\sqrt{f'_c}$

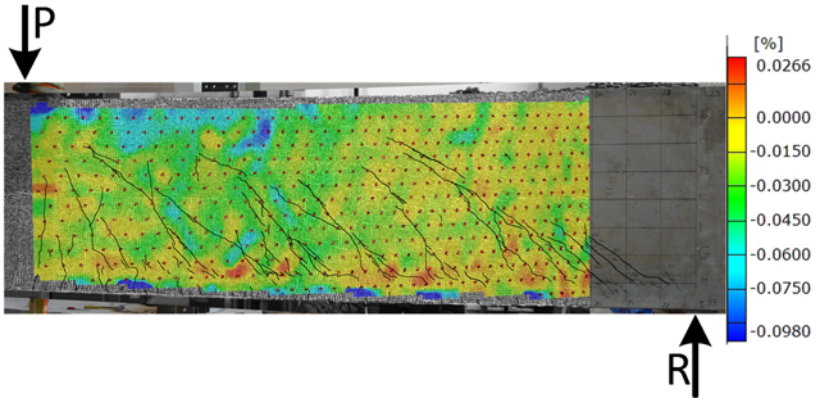

Figure 4.280 Full-field concrete minimum principal strain (σ_2) across shear span for specimen SFRC48b at normalized shear stress of $3.5\sqrt{f'_c}$

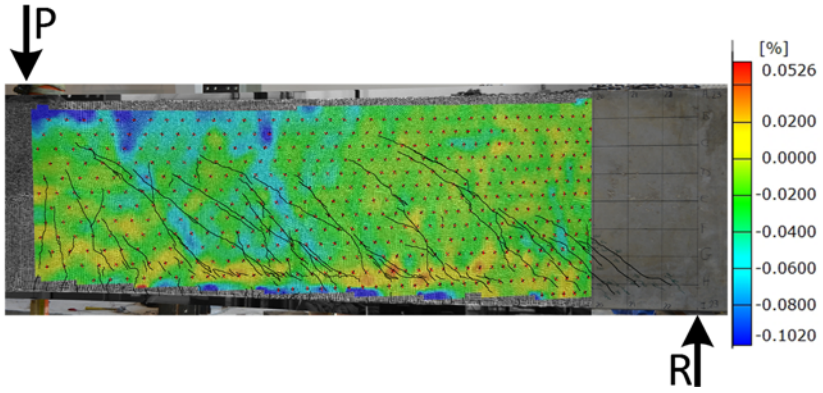

Figure 4.281 Full-field concrete minimum principal strain (σ_2) across shear span for specimen SFRC48b at normalized shear stress of $4.0\sqrt{f'_c}$

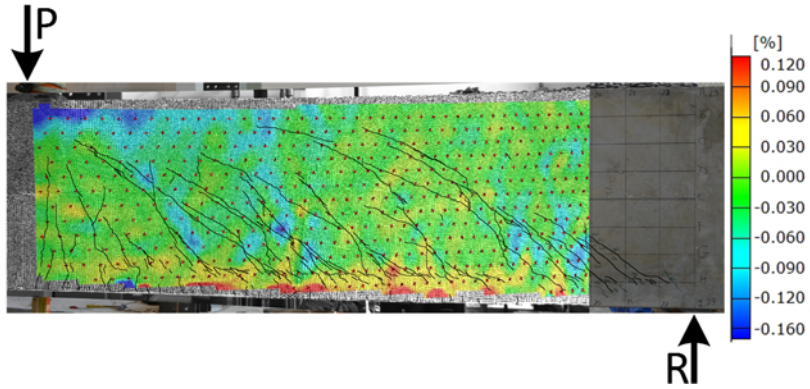

Figure 4.282 Full-field concrete minimum principal strain (σ_2) across shear span for specimen SFRC48b at normalized shear stress of $4.5\sqrt{f'_c}$

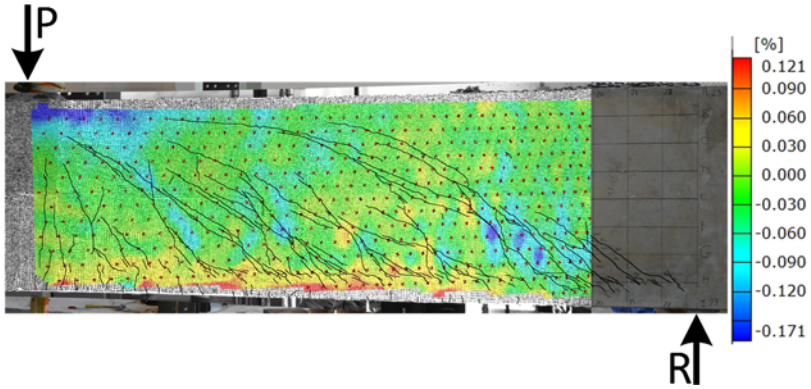

Figure 4.283 Full-field concrete minimum principal strain (σ_2) across shear span for specimen SFRC48b at normalized shear stress of $5.0\sqrt{f'_c}$

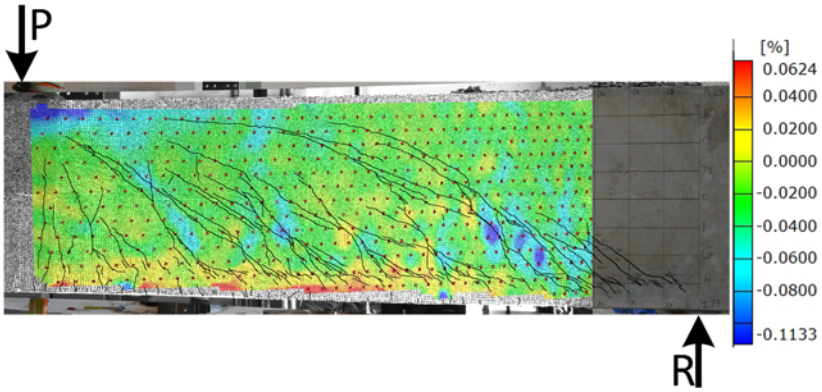

Figure 4.284 Full-field concrete minimum principal strain (σ_2) across shear span for specimen SFRC48b at normalized shear stress of $5.1\sqrt{f'_c}$

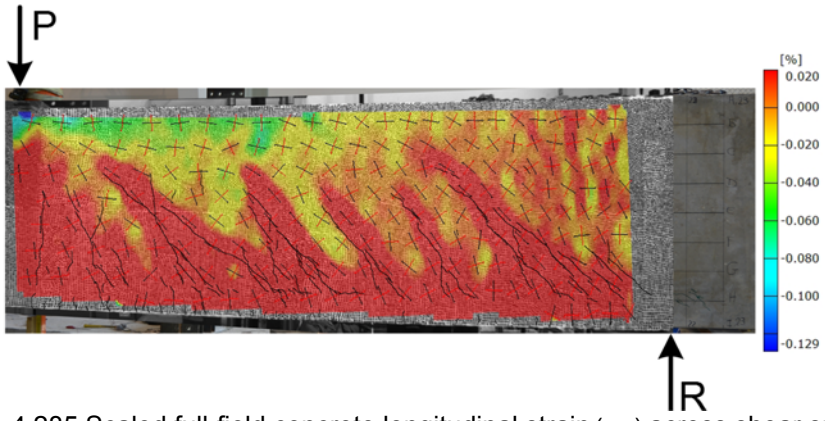

Figure 4.285 Scaled full-field concrete longitudinal strain (ε_x) across shear span for specimen SFRC48b at normalized shear stress of $3.0\sqrt{f'_c}$

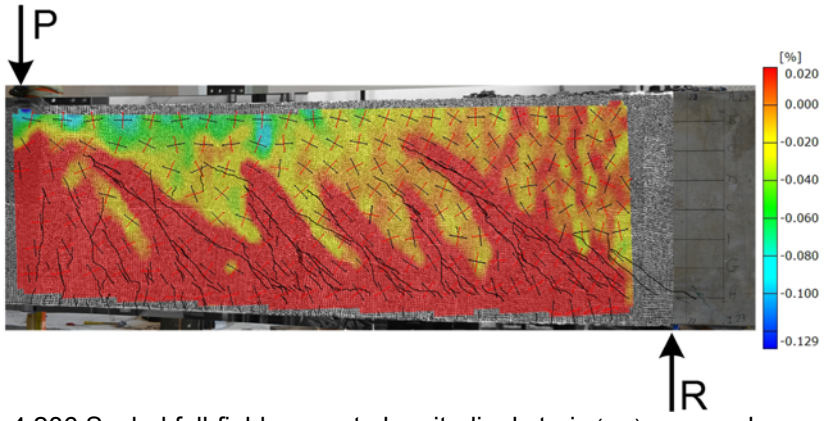

Figure 4.286 Scaled full-field concrete longitudinal strain (ε_x) across shear span for specimen SFRC48b at normalized shear stress of $3.5\sqrt{f'_c}$

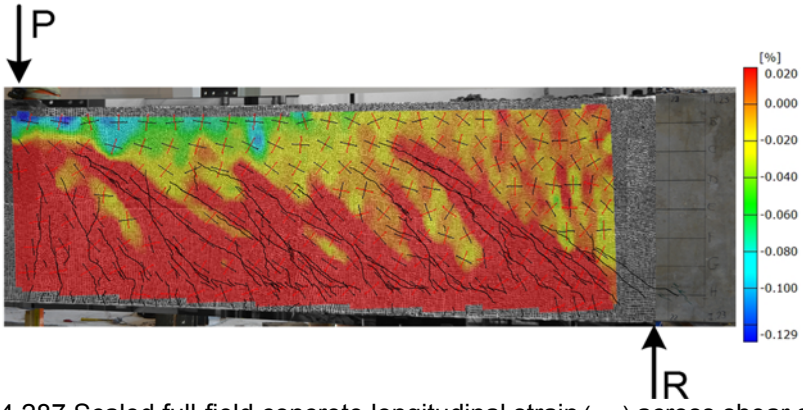

Figure 4.287 Scaled full-field concrete longitudinal strain (ε_x) across shear span for specimen SFRC48b at normalized shear stress of $4.0\sqrt{f'_c}$

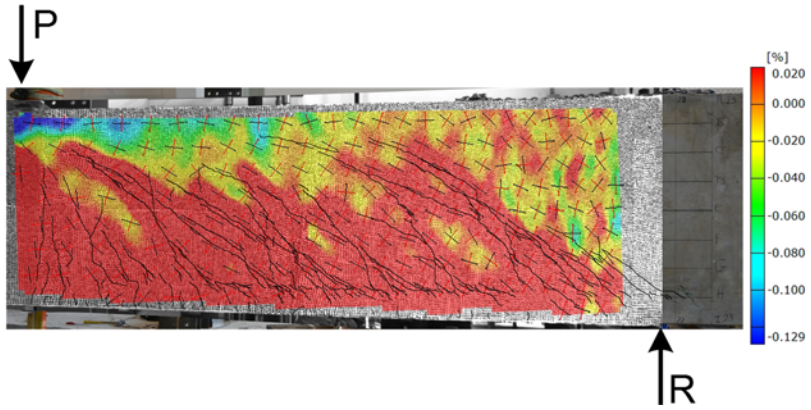

Figure 4.288 Scaled full-field concrete longitudinal strain (ε_x) across shear span for specimen SFRC48b at normalized shear stress of $4.5\sqrt{f'_c}$

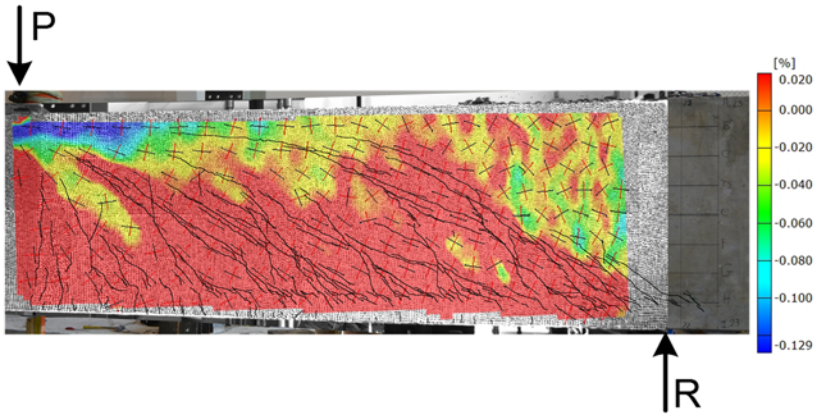

Figure 4.289 Scaled full-field concrete longitudinal strain (ε_x) across shear span for specimen SFRC48b at normalized shear stress of $5.0\sqrt{f'_c}$

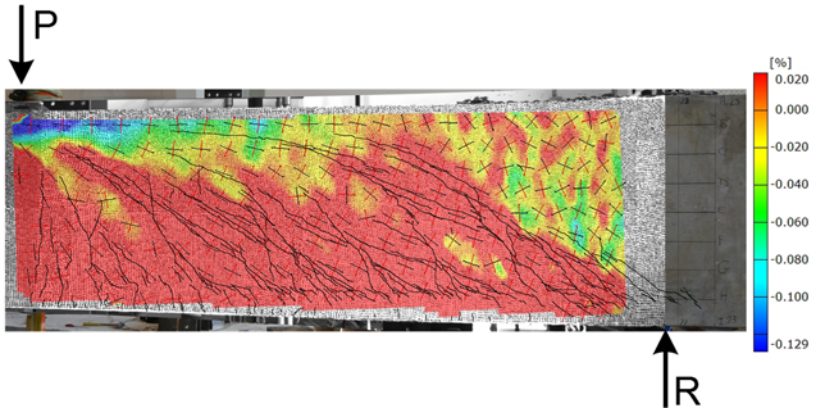

Figure 4.290 Scaled full-field concrete longitudinal strain (ε_x) across shear span for specimen SFRC48b at normalized shear stress of $5.1\sqrt{f'_c}$

Chapter 5

ANALYSIS OF EXPRIMENTAL RESULTS

5.1 General

The ultimate applied load (P_u), average shear stress at failure (v_u), shear strength normalized by $\sqrt{f'_c}$, and the maximum critical crack width at peak load (C_w) for each SFRC and RC specimens are listed in Table 5.1. The following sections discuss the strength-enhancement and resistance mechanisms of SFRC slender beams. The mechanisms were deduced based on the observation of cracking patterns and visualization of the DIC-measured full field deformations occurring on the surface of each test specimen.

Table 5.1 Test Results

Specimen	(P_u) *kips (kN)*	(V_u) *kips (kN)*	(v_u) *psi (MPa)*	($v_u/\sqrt{f'_c}$) $\frac{}{\sqrt{psi}\ (\sqrt{MPa})}$	(V_{cr}) *kips (kN)*	(v_{cr}) *psi (MPa)*	(C_w)[3] *in. (mm)*
SFRC12W6	54 (240)	27 (120)	449.4 (3.1)	6.9 (0.57)	21 (93)	350.0 (2.41)	0.052 (1.32)
SFRC12W24	215 (956)	108 (478)	448.1 (3.1)	6.9 (0.57)	73 (324)	304.0 (2.09)	0.129 (3.28)
SFRC18a	73 (323)	36 (161)	389.7 (2.7)	5.2 (0.43)	23 (102)	241.9 (1.7)	0.054 (1.37)
SFRC18b	88 (389)	44 (194)	470.2 (3.2)	6.2 (0.52)	16 (71)	166.7 (1.1)	0.066 (1.66)
SFRC24a	120 (534)	60 (267)	352.3 (2.4)	4.2 (0.34)	40 (178)	234.7 (1.6)	0.060 (1.52)
SFRC24b	171(759)	85 (380)	500.9 (3.5)	5.9 (0.49)	30 (133)	176.1 (1.2)	0.080 (2.03)
SFRC36a	307 (1365)	154 (683)	479.6 (3.3)	5.7 (0.47)	40 (178)	125.0 (0.9)	0.080 (2.03)
SFRC36b	317 (1408)	158 (704)	494.5 (3.4)	5.8 (0.48)	60 (267)	187.5 (1.3)	0.041 (1.04)
SFRC48a	470 (2091)	235 (1045)	445.1 (3.1)	5.2 (0.44)	80 (356)	151.5 (1.0)	0.077 (1.96)
SFRC48b	454 (2017)	227 (1008)	429.4 (3.0)	5.1 (0.42)	70 (311)	132.6 (0.9)	0.101(2.56)
RC18a	51 (226)	19 (82)	198.5 (1.4)	2.7 (0.22)	13 (57)	139.8 (1.0)	0.001(0.04)
RC18b	45 (202)	17 (73)	177.3 (1.2)	2.4 (0.20)	11 (48)	118.3 (0.8)	0.014 (0.35)

[3]: Maximum crack width at peak load

5.2The Role of the Compression Zone in Shear Strength-Enhancement

The presence of steel fibers appeared to delay the development of flexural cracks as well as reduce their rate of propagation. For this reason, the first diagonal crack in the test SFRC beams with the exception of SFRC12W24 and SFRC18b was observed to predominantly initiate in the form of a web-shear crack with a nearly 45º slope rather than the flexural-shear cracks commonly seen in RC beams. Table 5.1 shows the first shear

cracking strength (v_{cr}). Comparing v_{cr} values for SFRC 18-in-deep specimens with RC beams of identical height indicated a 58% increase in the first shear cracking strength on average. In other words, SFRC beams were subjected to a higher load at the development of the first shear crack. This higher load also induced greater horizontal compressive stresses in the uncracked compression zone. These high horizontal compressive stresses in turn slowed down the crack propagation by reducing the principal tensile stresses. Near the loading point, the vertical compressive stresses under the load further reduced the principle tensile stress due to a biaxial compressive stress state and was able to totally stop the crack propagation. Meanwhile, the vertical compressive stresses over the support likewise limited the bond splitting along the longitudinal rebars (Ferguson et al., 1988; Untrauer and Henry, 1965). Hence, an even higher load is generally required for cracks to further advance in the SFRC beams as clearly indicated by Figure 5.1. That is, the compression zone in SFRC specimens undergoes more gradual changes in the depth as the load increases.

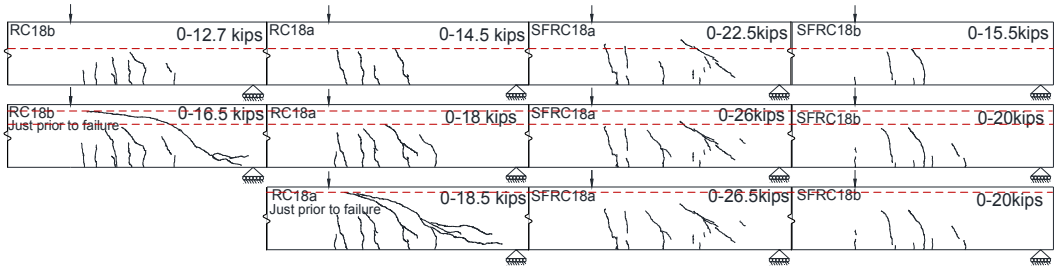

Figure 5.1 Crack propagation rate comparison at the same shear force increment, left to right: RC18b, RC18a, SFRC18a, SFRC18b

In Figure 5.1, the crack propagation rates of the RC and the SFRC 18-in-deep specimens are compared at similar shear force increments. As can been seen, a small increment (0.5 kip in shear) led to a rapid propagation of the critical crack in the RC18a beam; on the other hand, there was nearly no advance of cracks in the SFRC beams at the same load increment. The slow progression of the cracks in the SFRC specimens kept the

compression zone depth large, thereby enabling the compression zone to consistently contribute to shear resistance in an efficient manner. The deeper compression zone will not only contribute to a higher shear resistance but will also help to keep the crack width small. This allows the steel fibers to do a better job of transmitting the interface tensile stresses as well as improve aggregate interlocking. As a result, the external load gradually increases to a value much beyond any load that an identical PC beam can carry. For this reason, the horizontal compressive stresses induced by the bending moment alone (Figure 5.2b) or in combination with the vertical normal stresses resulting from the large applied load (Figure 5.2c) significantly enhance the shear performance of the compression zone.

Figure 5.2b shows how the existing large horizontal normal stress generated by bending moment leads the Mohr's circle to become larger in diameter and shift more to the right along the compression axes in comparison with its size and situation in plain concrete beams (Figure 5.2). The stress element shown in Figure 5.2a represents the state of stress in the compression zone for a PC beam. Therefore, the consequently reduced principal tensile stresses at higher stages of loading in SFRC beams would delay the potential penetration of the existing inclined cracks into the compression zone. As demonstrated later in this paper, the penetration of a critical shear crack would lower the shear capacity of the compression zone. With moving closer to the loading point, this potentiality could become substantially lower or even be completely eliminated due to the development of a large biaxial compressive stress state as demonstrated in Figure 5.2c. For this reason, a large area adjacent to the loading point was observed to be free of cracks even up to failure in all the tested specimens with the exception of SFRC18b.

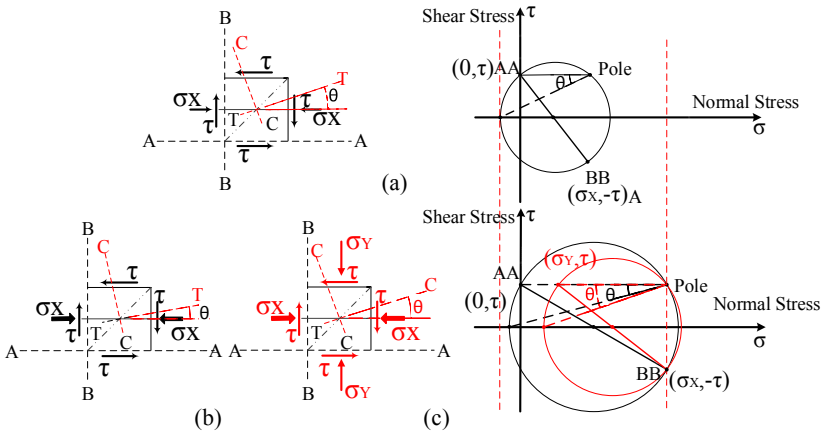

Figure 5.2 Comparison of the stress state and the induced principal stresses in compression zone between PC and SFRC beams: (a) uniaxial stress state in PC beams, (b) uniaxial stress state in SFRC beams, and (c) biaxial stress state in SFRC beams

Figure 5.3 displays the full field horizontal strain obtained from DIC for SFRC48a in which the tensile strains are denoted by red, while other colors (yellow to dark blue) represent various magnitudes of compressive strain in the compression zone. For the purposes of comparison at different loads, the total range of strain was fixed.

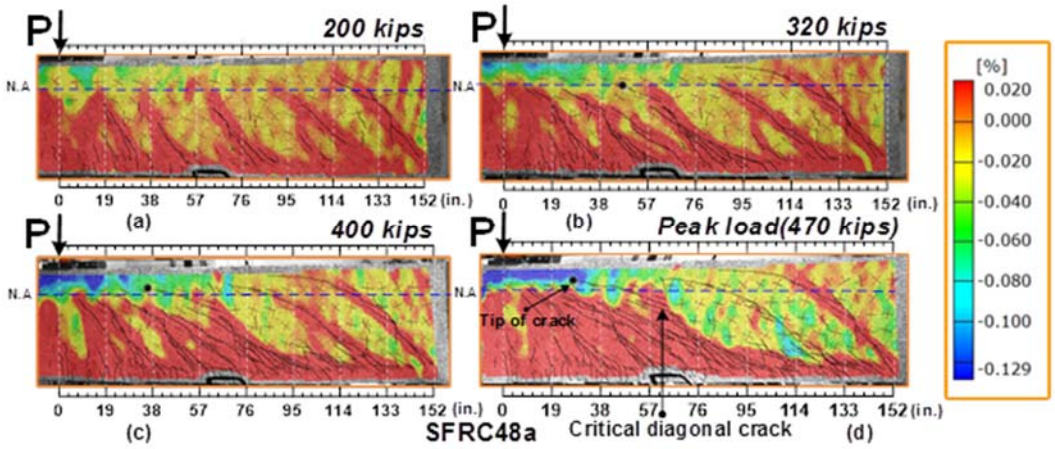

Figure 5.3 Variation of the depth and length of the compression zone in SFRC48a during the development and progression of cracks as a result of the incremental load increase

Figure 5.3 indicates a slow change in both the compression zone depth and length during the loading process up to failure. Figure 5.3 also compares the progression status of each

shear crack at different loads throughout the shear span. It can be clearly seen that as the distance from the loading point is increased, the shear cracks had a higher probability of penetrating into the compression zone. Nevertheless, after the penetration, the high horizontal compressive stresses in the cracked compression zone impeded the immediate advance of the penetrated cracks with the consequent abrupt failure of the beam as noted in the PC beams.

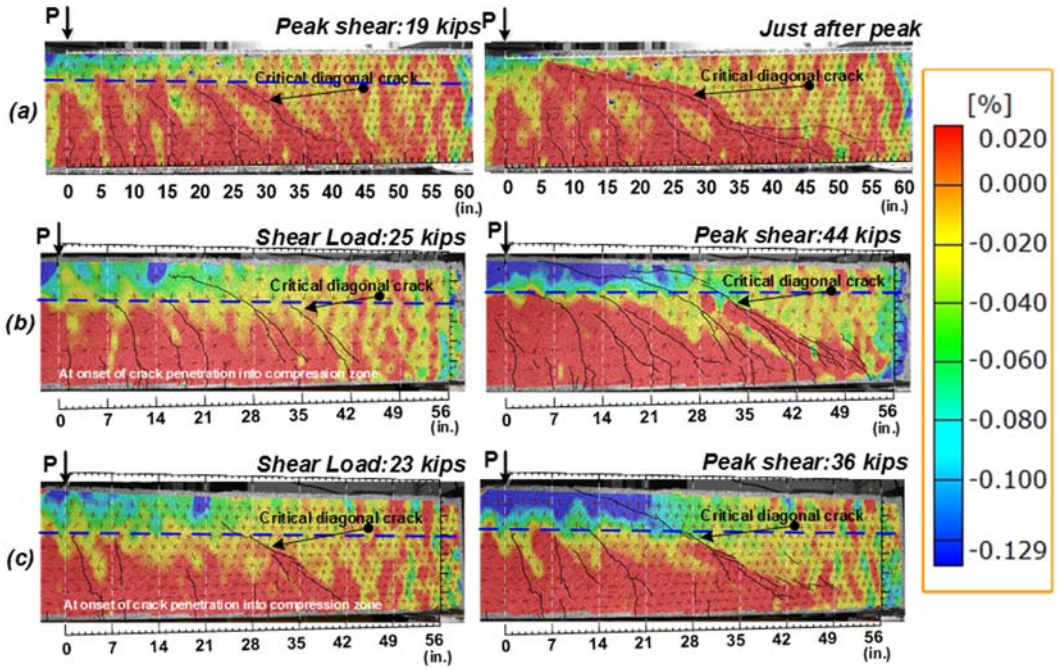

Figure 5.4 Comparison of the effect of the critical crack propagation on the depth and length of compression zone between RC and SFRC beams:(a) RC18a, (b) SFRC18b, and (c) SFRC18a

Figure 5.4 further illustrates the effect of the compression zone on shear strength between geometrically identical SFRC and PC beams. In Figure 5.4a, upon penetration of a shear crack into the PC beam compression zone, the crack suddenly extended completely through the compression zone toward the loading point and resulted in the beam's failure. The left images of Figure 5.4b and Figure 5.4c show the cracking pattern for the SFRC

beams at the onset of the critical shear crack penetration, whereas the right ones indicate the shear crack trajectories at the peak loads. As indicated by the figures, after crack penetration, SFRC specimens maintained their shear resistance well enough such that SFRC18b and SFRC18a could sustain 76% and 56% additional loads before failure.

5.3Dowel Action and its Effect on Shear Strength-Enhancement

The dowel strength of a PC beam is mainly a function of concrete tensile strength (Baumann, 1968). Therefore, the enhanced tensile characteristic of SFRC and the effectiveness of fibers to restrict the width of dowel cracks could improve the dowel resistance. Figure 5.5 displays the full field vertical strains (Y-direction) across the shear span for SFRC48b and SFRC12W6 at loads of 200 kips and 41 kips, respectively. At these load values, the existing shear cracks started reaching the level of the flexural rebars. At this point, dowel action started taking effect. This can be observed in Figure 5.5, while there were no dowel cracks along the longitudinal rebars, the maximum vertical strains due to dowel action were 3890 με and 1150 με for SFRC12W6 and SFRC48b, respectively. These strains sustained by the SFRC beams were significantly greater than the dowel cracking tensile strain of PC beams (500 με reported by Houde and Mirza, 1974). The greater strain capability of SFRC at the dowel zone delayed the development of dowel cracks.

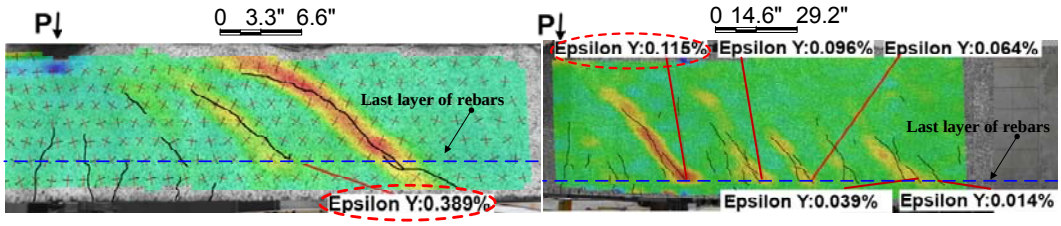

SFRC12W6, Load:41 kips **SFRC48b, Load200 kips**

(b) **(a)**

Figure 5.5 Measured vertical normal strains at the intersections of diagonal cracks and flexural bars: (a) SFRC48b at load 200 kips and (b) SFRC12W6 at load 41kips

After the initiation of dowel crack, steel fibers can still hold the longitudinal bars up in their original place by bridging and restricting the widening of the crack, thereby allowing them to consistently contribute to shear resistance in the form of dowel action. Therefore, the function of steel fibers could be analogous with that of stirrups in a dowel zone. On the other hand, the presence of steel fibers also slows down the propagation of dowel cracks as observed in the test SFRC beams. Figure 5.6 visualizes the strains in the vertical direction (Y direction) at peak load for the different beams. As will be demonstrated later, the dowel action contributes less to shear resistance for shallower SFRC beams. This observation can be recognized in Figure 5.6, which depicts the full field strain in Y-direction. Figure 5.6c and Figure 5.6d show a highly strained region along the longitudinal rebars for the specimens with depths of 36 in. and 48 in. On the other hand, as shown in Figure 5.6a and Figure 5.6b, SFRC12W6 and SFRC18a relied less on dowel action for the shear resistance due to the greater shear resistance provided by the compression zone (discussed later).

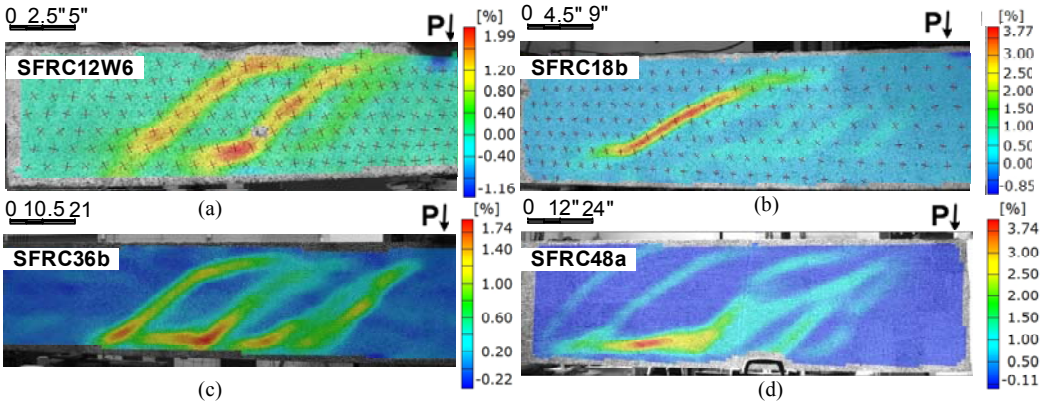

Figure 5.6 Highly strained region developed in dowel zone in vertical direction (Y direction) at peak load: (a) SFRC12W6, (b) SFRC18b, (c) SFRC36b, and (d) SFRC48a

The dowel action provided by SFRC can be seen in Figure 5.7, where multiple oblique small cracks are observed as opposed to horizontal splitting cracks extending along the

longitudinal rebars. The orientation of the cracks became flatter as they moved away from the intersections of the shear cracks and longitudinal rebars.

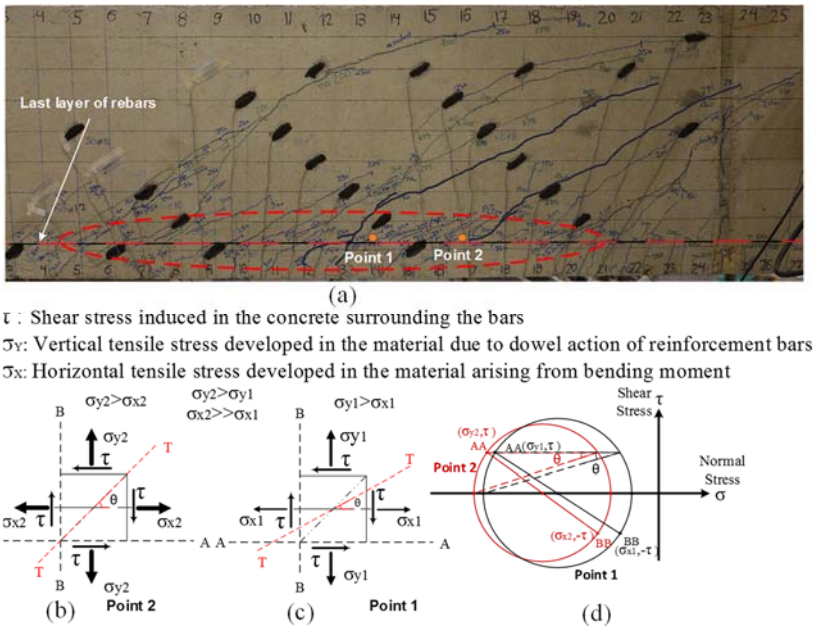

Figure 5.7 (a) A view of the inclined dowel cracks, (b) state of stress induced in dowel zone adjacent to the diagonal crack, Point 2,(c) state of stress in dowel zone away from the diagonal crack, Point 1, and (d)Mohr's circles representing the states of stress in Points 1 and 2

The flatter inclination of the cracks was a result of the reduced tensile stresses developed in the surrounding SFRC along the bars due to the dowel force. This observation can be explained by using the stress state of two given points as shown in Figure 5.7a. Unlike plain concrete, SFRC surrounding the flexural rebars is able to carry part of the tensile stress induced by the bending moment as well as part of the shear stress carried by the dowel zone. The resulting stresses are shown by σ_x and τ, respectively. Furthermore, the vertical tensile stress denoted by σ_y is the tensile stress formed along the longitudinal bars in SFRC due to the dowel action of longitudinal rebars. The mechanical analysis given in Figure 5.7b through Figure 5.7d proves that these stresses, hence the

dowel action, must be present in order to form such cracks oriented along the longitudinal rebars. Figure 5.7a clearly shows that despite the development of a large number of dowel cracks, the presence of steel fibers preserved the contribution of dowel action to shear resistance.

5.4 Aggregate Interlocking

Aggregate interlocking has been considered the primary factor contributing to the shear resistance of plain concrete beams. In other words, in PC beams, when the current shear stress exceeds aggregate interlock capacity, the beam fails in shear (Fenwick and Paulay, 1968; Vecchio and Collins, 1986).

Laboratory test results from different studies have shown shear failure occurring in plain concrete beams when the width of the critical crack reaches a value approximately 0.02 in. (0.5 mm). For instance, Sherwood (2008) observed that the width of critical crack at failure for the deeper specimens (h = 59.4 in. (1510 mm)) was in the range of 0.016 in. (0.4 mm) to 0.02 in. (0.5 mm), whereas the critical crack width became narrower when the height of specimens, h, decreased to 13 in. (330 mm), ranging between 0.002 to 0.004 in. (0.05 to 0.1mm). Minelli et al. (2014) reported the maximum width of the critical crack at failure between 0.01–0.02 in. (0.25–0.50 mm) for their plain concrete beams, where the beam height varied from 20 to 59 in. (500 to 1500 mm). For our study, the maximum crack width at peak load for the specimens is listed in the last column of Table 5.1. The associated values for the pair of PC beams are 0.001 in. (0.04 mm) and 0.014 in. (0.35 mm) and are consistent with the values from past research.

The wide critical crack between 0.041 in. (1.04 mm) and 0.129 in. (3.28 mm) measured before failure of the SFRC beams implies the diminished effect of aggregate interlocking to shear contribution. As such, aggregate interlocking cannot be relied on to resist shear at ultimate.

5.5 The Shear Resistance Mechanism

5.5.1 The critical factor leading to the drop of peak shear strength

The major contributors to the shear resistance of SFRC beams are provided by the compression zone, steel fiber bridging along the critical crack, and dowel action. However, it is imperative to first identify the cause leading to the ultimate drop in shear strength of SFRC beams in order to apply the correct failure criterion.

Our test results indicated two types of failure modes: In Type 1 failure, a major diagonal crack occurred in the compression zone followed by an immediate drop in shear strength. Dowel action was able to carry the residual strength after the compression zone failure (Figure 5.8).

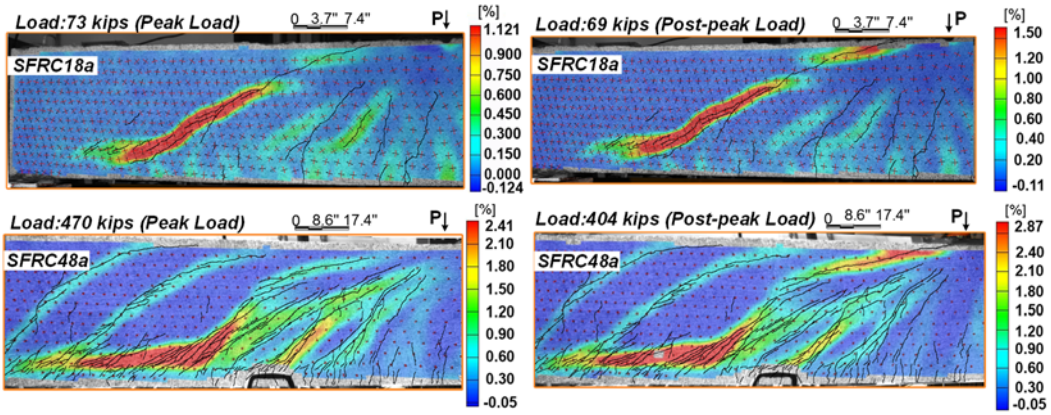

Figure 5.8 A visualization of full field maximum principal strain across shear span for SFRC18a and SFRC48a (Type 1 failure mode)

In Type 2 failure, the compression zone and dowel action failure occurred nearly at the same time and could not be easily distinguished by the naked eye or video. Nevertheless, the DIC images shown in Figure 5.9 clearly show that at the time the specimens reached their peak strength, the strains at the dowel zone remain the same, while the principal tensile strains at the upper part of the critical diagonal cracks (circled by dashed lines) become much larger, which triggers the failure of the compression zone. Therefore, in

either Type 1 or Type 2 failure, the drop in shear strength was initiated by the tension failure of the compression zone.

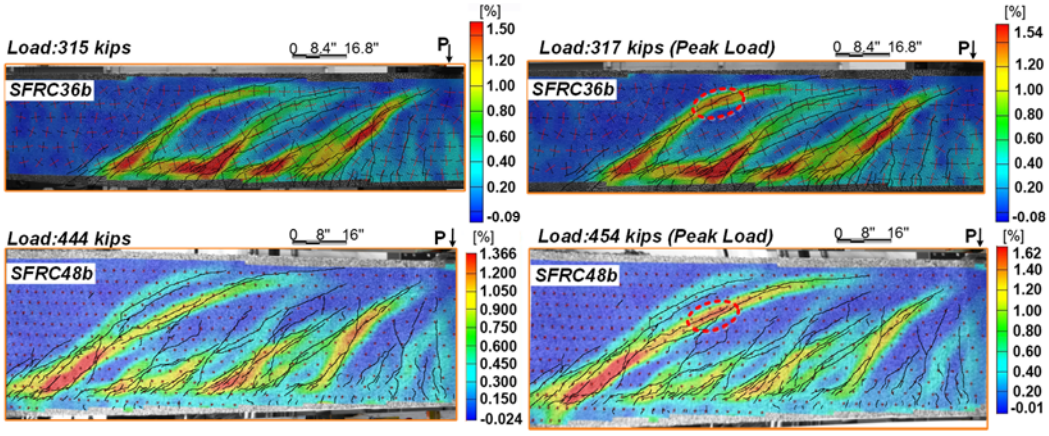

Figure 5.9 A visualization of the full field maximum principal strain across shear span for SFRC36b and SFRC48b (Type 2 failure mode)

5.5.2 Contribution of each component to the ultimate shear strength

Data acquired from the DIC image analysis were used to conduct an assessment to quantify the proportions of ultimate shear force carried by the compression zone, steel fiber bridging, and dowel action of an SFRC beam.

5.5.2.1 Steel fiber bridging

Steel fibers crossing a diagonal crack resist shear forces by means of the vertical component of the tensile stress developed across the crack. The magnitude of the tensile stresses in SFRC depends on the crack width as shown in Figure 5.10a in which the average of the variation of tensile stress for six SFRC tensile specimens under direct tensile test is plotted with respect to crack width. On the other hand, the crack width distribution along the critical crack at the peak load for the large-scale beam specimens was measured by the DIC system. To determine the stress value at each point along the critical crack, the stress for a particular point was picked from the stress-crack width curve as given in Figure 5.10a. Next, the curved crack path was divided into a series of straight

lines with corresponding angles; then, the stress distribution and corresponding resultant force were computed along each line and projected in the vertical direction based on the angle. Finally, all calculated forces were added together to represent the contribution of steel fiber bridging in resisting the total shear at peak load.

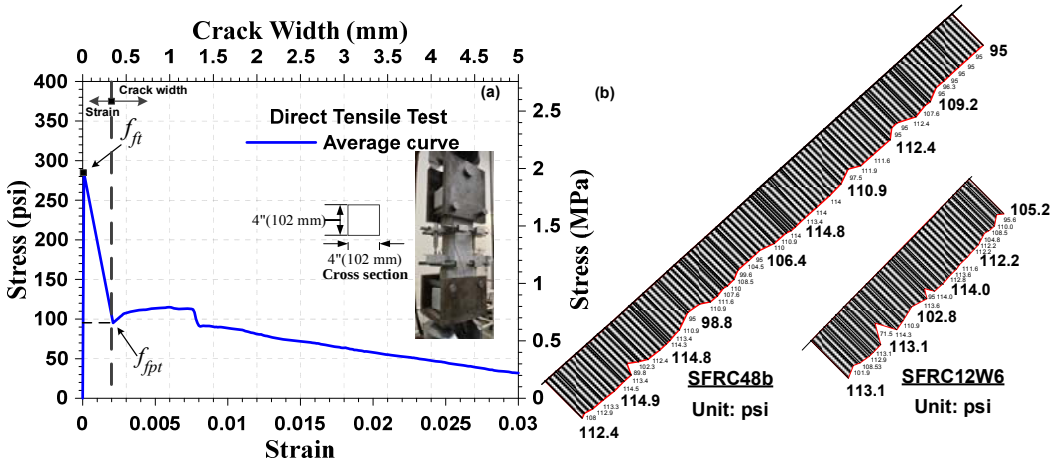

Figure 5.10 (a) Average SFRC responses to direct tensile test and (b) distribution of the steel fiber tensile stress along the critical crack for two specimens, SFRC48b and SFRC12W6

Figure 5.10b displays the magnitude and distribution of the tensile stresses along the critical crack for SFRC12W6 and SFRC48b. Figure 5.10b gives a better sense of the stress distribution along the total length of the critical crack in the tension zone by plotting the stress distributions on a straight line rather than along the curved crack. The shear force carried by steel fibers crossing the critical crack in the tension zone (i.e. below the N.A.) and the percentage of its contribution to the total shear at peak load for the test specimens are listed in Columns 2 and 5 of Table 5.2, respectively.

Table 5.2 Contribution of the main shear components and their percentage in shear capacity

1	2	3	4	5	6	7
Specimen	V_{SF} [1] (kips)	V_{cc} [2] (kips)	V_u [3] (kips)	V_{SF}/V_u (%)	V_{cc}/V_u (%)	V_d/V_u (%)
SFRC12W6	5.5	18.7	27.0	20.4	69.2	10.4
SFRC12W24	36.9	60.2	108.0	34.2	55.8	10.0
SFRC18a	8.7	23.1	36.0	24.2	64.3	11.5
SFRC18b	10.5	23.1	44.0	23.9	52.6	23.5
SFRC36b	35.5	71.1	158.0	22.5	45.0	32.5
SFRC48a	34.6	118.6	235.0	14.7	50.5	34.8
SFRC48b	67.7	81.8	227.0	29.8	36.0	34.2

1: Shear resisted by steel fiber in tension zone at peak; 2: Shear resisted by compression zone at peak; 3: Measured ultimate shear resistance

5.5.2.2 The proportion of the shear force carried by compression zone at peak load

The shear capacity of the compression zone in an SFRC beam can be controlled by either the compression or tension mode of failure (Choi et al., 2007; Kotsovos and Pavlović, 1998). Because concrete's compressive strength is much larger than its tensile strength, the shear failure of the compression zone is typically initiated by tensile cracking (Choi et al., 2007; Kotsovos and Pavlović, 1998). The tension induced failure typically results in the propagation of the critical crack all the way through the compression zone depth. Based on a mechanical based analysis, Choi et al. (2007) demonstrated that the shear failure of the compression zone of an SFRC beam is dominated by tension. Their conclusion was also confirmed by the test observation in our study as shown in Figure 5.8 and Figure 5.9. For this reason, to estimate the shear capacity of the compression zone for the SFRC specimens, Rankin's failure criteria was adopted in the same approach as employed by Choi et al. (2007) which takes into account the interaction between the shear and compressive stresses. As observed in our SFRC beam tests (Figure 5.3): prior to failure, the critical crack had already extended into the compression zone; hence, the shear failure of the compression zone was assumed to occur when the principal tensile stress at

each point along the penetrated critical crack reached the post-cracking tensile strength of SFRC (Equation (5.1)). At the same time, the principal tensile stress along the intact failure path attains the peak tensile strength of the SFRC material. The peak and post-cracking tensile strengths of the SFRC were acquired from direct tensile tests at 285 and 95 psi (Figure 5.10a), respectively. These results are close to the corresponding values of 242 and 91 psi computed from the equations proposed by Naaman (2002, 2003) for the properties of steel fibers (steel fiber type, volume fraction, and fiber aspect ratio) and concrete (tensile strength) used in this study. Rankin's failure criterion predicting tensile failure in the compression zone along the cracked and uncracked failure paths is mathematically expressed as shown in Figure 5.11a and in Equation (5.1):

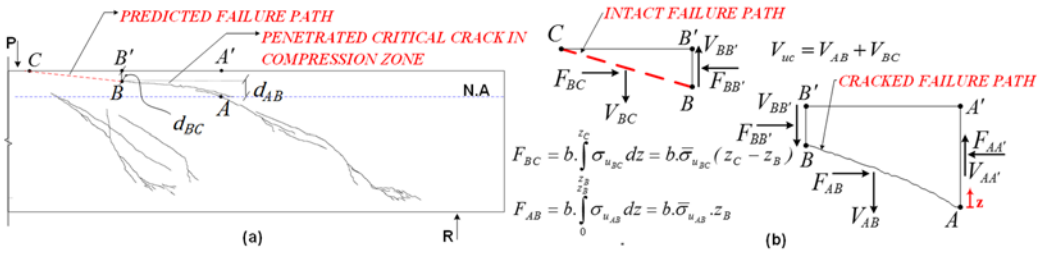

Figure 5.11 Schematic view of: (a) cracked and intact failure path in compression zone; (b) Resultant forces acting along the cracked and intact failure path

$$-\frac{\sigma_{u_{AB}}}{2} + \sqrt{\left(\frac{\sigma_{u_{AB}}}{2}\right)^2 + v_{u_{AB}}{}^2} = f_{fpt} \qquad \text{(Along the penetrated critical crack in compression zone)} \qquad (5.1a)$$

$$-\frac{\sigma_{u_{BC}}}{2} + \sqrt{\left(\frac{\sigma_{u_{BC}}}{2}\right)^2 + v_{u_{BC}}{}^2} = f_{ft} \qquad \text{(Along the failure path)} \qquad (5.1b)$$

where f_{ft} and f_{fpt} = peak and post-cracking tensile strengths of SFRC obtained from direct tensile tests (Figure 5.10a); $\sigma_{u_{AB}}$ and $v_{u_{AB}}$ = the normal compressive and shear stresses at each given point along the critical crack in the compression zone (Figure 5.11a, Path

AB); $\sigma_{u_{BC}}$ and $v_{u_{BC}}$ = the normal compressive and shear stresses at any point along the uncracked failure path in the compression zone (as shown in Figure 5.11a, Path BC).

Rearranging the shear stress in Equation (5.1a) and Equation (5.1b) gives the allowable shear stresses along the failure paths (a function of compressive stress at each given point), which is expressed as:

$$v_{u_{AB}} = \sqrt{f_{fpt}(f_{fpt} + \sigma_{u_{AB}})} \qquad \text{(Along the penetrated critical crack in compression zone)} \qquad (5.2a)$$

$$v_{u_{BC}} = \sqrt{f_{ft}(f_{ft} + \sigma_{u_{BC}})} \qquad \text{(Along the failure path)} \qquad (5.2b)$$

By integrating Equation (5.2a) and Equation (5.2b) over an infinitesimal vertical surface (dA=b×dz where b is the width of cross section and z is the vertical distance measured from neutral axis) along paths AB and BC, we can find the resultant vertical force acting along the failure path in the compression zone (AB and BC in Figure 5.11b). The numerical expression is found as Equation (5.3a) and Equation (5.3b):

$$V_{AB} = b.\int_{0}^{z_B} \sqrt{f_{fpt}(f_{fpt} + \sigma_{u_{AB}})}\,dz \qquad \text{(Along the penetrated critical crack in compression zone)} \qquad (5.3a)$$

$$V_{BC} = b.\int_{z_B}^{z_C} \sqrt{f_{ft}(f_{ft} + \sigma_{u_{BC}})}\,dz \qquad \text{(Along the failure path)} \qquad (5.3b)$$

To simplify the computations, the current compressive stress functions in Equation (5.3a) and Equation (5.3b) along the cracked and intact failure paths were replaced with the average compressive stress (discussed later) denoted by $\overline{\sigma}_{u_{AB}}$ and $\overline{\sigma}_{u_{BC}}$ in Equation (5.4a) and Equation (5.4b), respectively:

$$V_{AB} = b.\int_{z_A}^{z_B} \sqrt{f_{fpt}(f_{fpt} + \overline{\sigma}_{u_{AB}})}\,dz = \sqrt{f_{fpt}(f_{fpt} + \overline{\sigma}_{u_{AB}})}\,b.d_{AB} \qquad (5.4a)$$

$$V_{BC} = b.\int_{z_B}^{z_C} \sqrt{f_{ft}(f_{ft} + \overline{\sigma}_{u_{BC}})}dz = \sqrt{f_{ft}(f_{ft} + \overline{\sigma}_{u_{BC}})}b.d_{BC} \quad (5.4b)$$

d_{AB}, d_{BC} = the vertical distance between points A and B as can be seen in Figure 5.11a; the vertical distance between points B and C are in Figure 5.11a.

The maximum shear force, V_{uc}, resisted by the compression zone is considered as the sum of V_{AB} and V_{BC}, which are expressed as

$$V_{uc} = V_{AB} + V_{BC} \quad (5.5)$$

In Equation (5.4a) and Equation (5.4b), to determine the average of compressive stresses, $\overline{\sigma}_{u_{AB}}$ and $\overline{\sigma}_{u_{BC}}$, generated by the bending moment, the distribution of the compressive strains along paths AB and BC were first obtained by using the DIC system for each test beam at the peak load. Then the corresponding compressive stress of each strain along paths AB and BC was found from the stress-strain relationship obtained from the SFRC cylinder tests (Figure 5.12). To be consistent, the strains of the cylinders were also measured by the DIC system. Lastly, the average compressive stresses, $\overline{\sigma}_{u_{AB}}$ and $\overline{\sigma}_{u_{BC}}$, were calculated based on the compressive stress distributions along paths AB and BC. The maximum shear force carried by the compression zone at peak load and the percentage of its contribution to the total shear resistance are presented in Columns 3 and 6 of Table 5.2. The remaining percentage of shear resistance was attributed to the contribution of dowel action as noted in the last column of Table 5.2. As can be seen, the shear resistance proportion of the compression zone decreases from 69% to 36% when the beam depth increased from 12 in. (305 mm) to 48 in. (1220 mm). However, for the same range of changes in the beam depth, the dowel action contribution was found to vary from 10% to 35% depending on the increase in beam depth. On the other hand, the percentage of steel fiber contribution is nearly constant for all the SFRC beams regardless

of their depths. These analysis gives consistent results as observed from DIC image as shown in Figure 5.6.

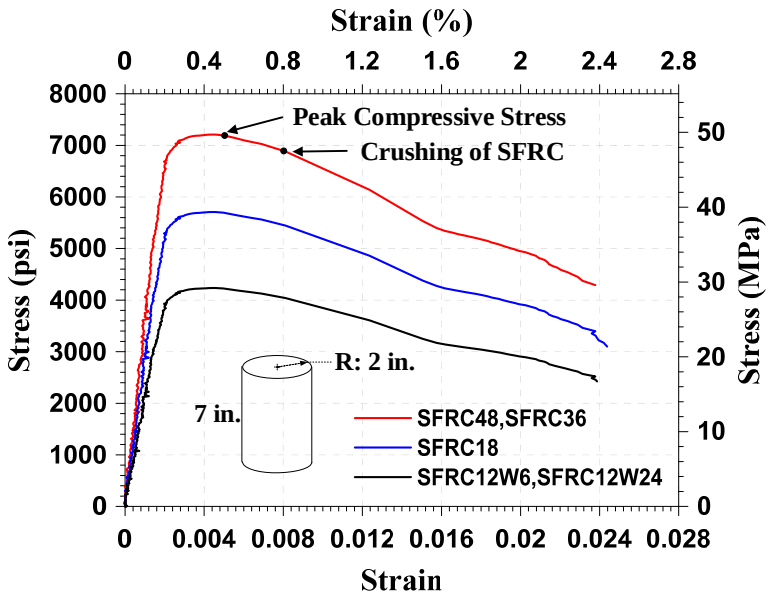

Figure 5.12 The average stress-strain relationships for the sampled SFRC cylinders

5.6 The Effect of Width on the Shear Strength of SFRC Beams (in Terms of Stress)

As discussed in the previous section, the width of each specimen in this study was adjusted in recognition of the negligible effect of width on the ultimate shear strength of RC beams (Kani et al., 1979; Lubell et al., 2004). This study investigated the validity of this observation on SFRC beams. For this purpose, two SFRC specimens (SFRC12W6 and SFRC12W24) with a total height of 12 in. were constructed. Their widths were 6 and 24 in., respectively. Our test results (Table 5.1) indicate that similar to the observation for PC beams, the width of SFRC beams has no effect on ultimate shear strength. The ultimate shear stresses at failure for SFRC12W6 and SFRC12W24 were identical at $6.9\sqrt{f'_c}$ psi.

5.7Arch Action Involvement in the Strength-Enhancement Mechanism

Arch action is an alternative shear-strength enhancement mechanism that might

develop in a PC beam after beam action is destroyed due to the complete loss of bond between the longitudinal rebars and concrete (Park and Paulay, 1975). In other word, the longitudinal rebars sustain nearly the same strain throughout the length. Prior research carried out by Sneed and Ramirez (2010) on the shear strength of geometrically equivalent PC beams with different heights indicated a higher chance of arch action development for the beams with the smallest height (12 in. (305 mm)). Therefore, in this study, the smallest SFRC specimens were selected for arch action investigation. A series of additional strain gauges were mounted on one of the bottom layer reinforcing bars in the shallowest specimens (SFRC12W6 and SFRC12W24). The first 12 gauges were spaced 3 inches apart starting from mid-span up to the center of support, while the remaining two were spaced evenly at 1.5 inches passing the center of support toward the anchorage (Figure 5.13). Figure 5.13 shows the variation of measured strains along the reinforcing bars in SFRC12W6 and SFRC12W24 at the peak loads. Apart from the length being in the vicinity of the mid-span and accounting for one third of the shear span length, non-uniform distribution of strains observed along the longitudinal rebars indicating a lack of either debonding or possibly yielding of the rebars which is necessary for the development of arch action. Therefore, no evidence was produced to indicate that any arch action contributed to the shear-enhancement mechanism.

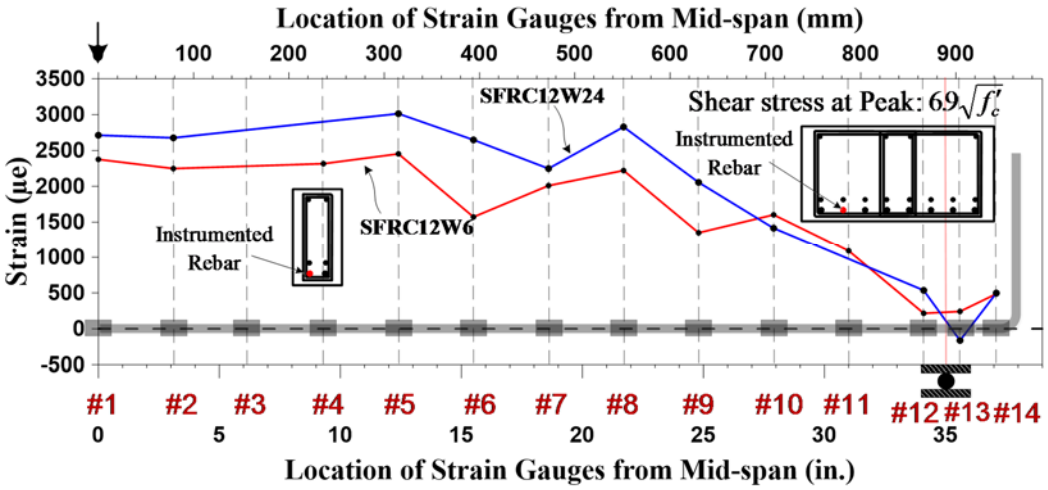

Figure 5.13 Variation of longitudinal strain along a reinforcing bar in SFRC12W6 and SFRCW24 at peak shear stress (f'_c in psi, 1 psi=0.0069 MPa)

5.8 Size Effect and the Intensity in SFRC Beams

The average of shear stresses at failure for each pair of duplicated specimens was normalized by $\sqrt{f'_c}$ and plotted relative to beam effective depth in Figure 5.14.

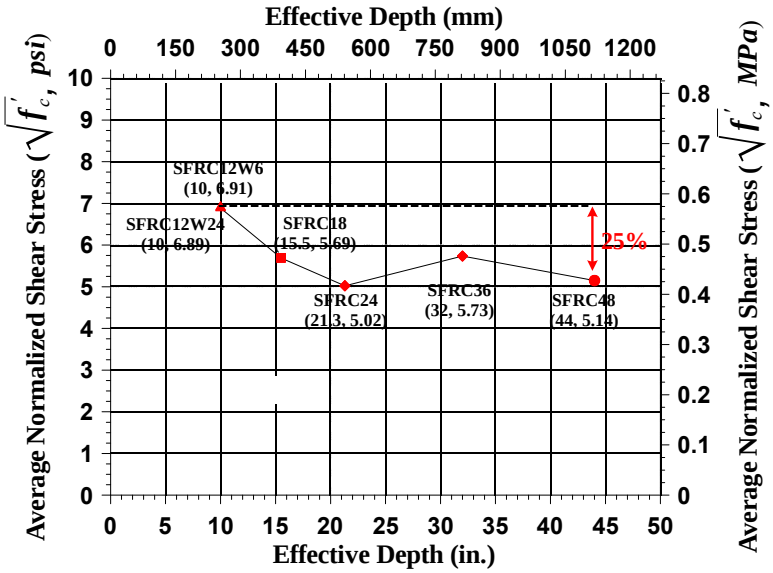

Figure 5.14 Average shear stress at failure in terms of $\sqrt{f'_c}$ versus effective depth for each pair of duplicated specimens

The strength of the largest beams SFRC48 is approximately 25% lower than the smallest beams, SFRC12WX. This variation is less than the SFRC beams with either 0.64% or 1% V_f as reported by Minelli et al. (2014). The average shear strength for all the SFRC specimens was 5.9 $\sqrt{f'_c}$ psi (0.49 $\sqrt{f'_c}$ MPa) with a moderate size effect. Results on laboratory tests from the research studies conducted by Shoaib et al. (2014) and Minelli et al. (2014) were presented in Figure 5.15 along with the shear strength versus beam height curve shown in Figure 5.14. The red dash line on Figure 5.15 represents the average shear strength curve for all depth-identical SFRC beams tested in the two previous studies. As noted, size effect was clearly more severe for SFRC beams tested in the past research programs especially for the beams with a depth exceeding the ACI height limitation of 24 inches irrespective of fiber contents.

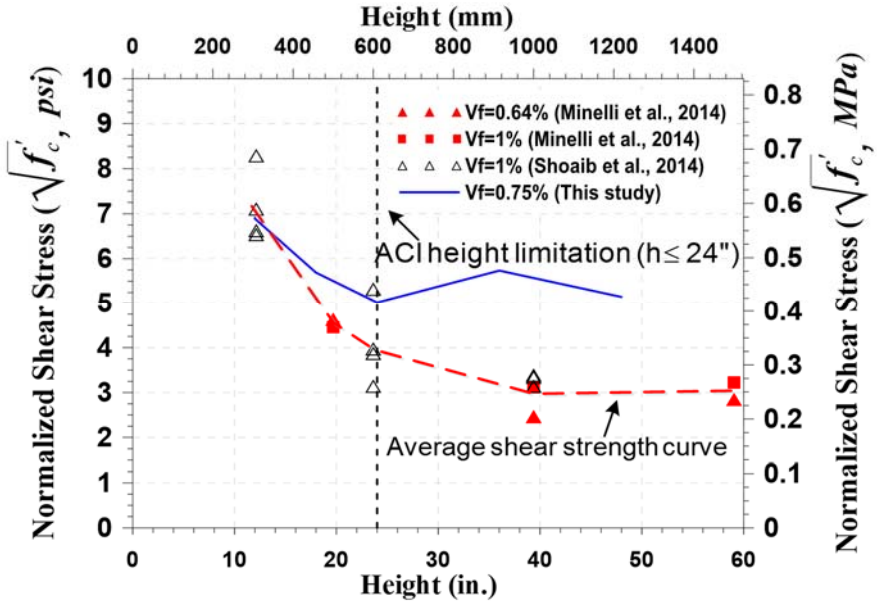

Figure 5.15 Results on laboratory test from the research studies conducted by Shoaib et al. (2014) and Minelli et al. (2014) along with the shear strength-effective depth curve obtained from the current study

As discussed earlier, the size effect in plain concrete beams is conventionally explained by the lower capacity of aggregate interlocking in deeper slender beams due to the wider critical crack. However, as demonstrated earlier, in SFRC beams, aggregate interlock cannot be counted on to resist shear at ultimate. The reduced aggregate interlock due to the lower ability of wider cracks to transmit shear stress in deeper beams cannot be justified to explain the size effect in SFRC beams.

5.9 Fiber Bridging Contribution from our testing

Shoaib et al. (2014) suggested that size effect in SFRC beams is due to a reduction in equivalent interface of fiber tensile stresses along the critical crack as a result to the development of wider cracks in larger size beams. In this study, their hypothesis was examined through an analysis using the crack widths measured by DIC as well as the stress versus crack width relationship obtained from direct tensile test (DTT) of dog bone-shaped SFRC tensile specimens. Our analysis indicates that the shear contribution arising from steel fiber bridging has a complicated nature and cannot be simply explained by the sole factor of equivalent interface tensile stresses along critical crack. In general, the extent of steel fiber bridging contribution will be a function of three primary parameters including: (1) tensile stresses induced in the steel fibers in tension zone across critical crack; (2) critical crack orientation; and (3) the length of the critical crack lying in the tension zone. To elaborate, Figure 5.16 compares the cracking pattern and distribution of equivalent tensile stresses along critical cracks for specimens SFRC12W6 and SFRC12W24.

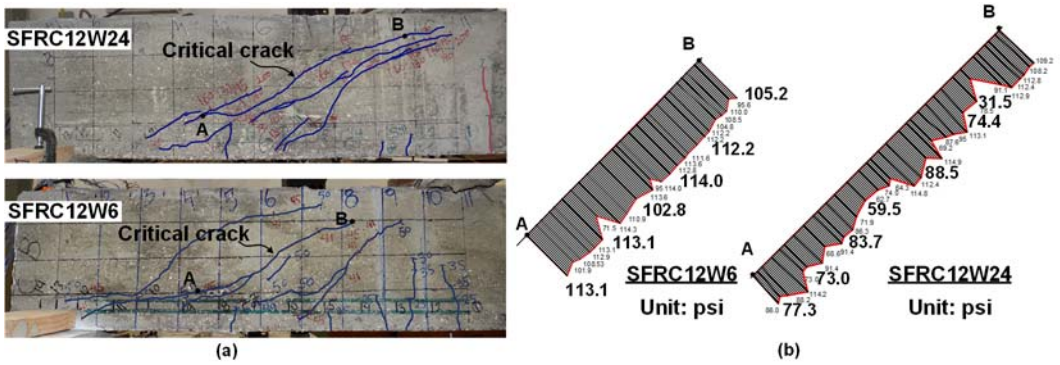

Figure 5.16 (a) a view of the cracking pattern before failure for SFRC12W6 and SFRC12W24; (b) equivalent steel fiber tensile stress distribution corresponding to SFRC12W6 and SFRC12W24

For the ease of visualization of the stress distribution along the total length of the critical crack in tension zone, the stress distribution was plotted on a straight line rather than along the curved crack path. The details of the method, measurements, and calculations were explained earlier in this chapter. It is noteworthy that these two specimens were identical in every aspect except for their width (Table 3.1). As listed in Table 3.2, SFRC12W24 experienced much wider critical crack before failure (C_w = 0.129 in. (3.28 mm)) than SFRC12W6 did (Cw = 0.052 in. (1.23 mm)), and that in turn, led to the lower equivalent tensile stresses along the critical crack. Nevertheless, both specimens had the same ultimate shear strength at $6.9\sqrt{f'_c}$ psi ($0.57\sqrt{f'_c}$ MPa). Our investigation shows that by having a wider critical crack with the consequently larger fiber pull-out, and thus lower equivalent tensile stresses, the steel fiber bridging would not be necessarily subjected to a significant change in its contribution to shear resistance. This is due to the fact that although the crack width was wider, the length was also longer; hence, the decrease due to the wider crack was compensated for by the longer crack length. This is the steel fiber bridging proportion to total shear resistance (column 7 in Table 5.2) that lay nearly invariable for the test specimens with different depths. On the other hand, Table 5.3 shows the portion of

average ultimate shear stress in terms of $\sqrt{f'_c}$ at failure developed in the specimens due to each shear contributor. Checking the quantities presented in column 4 of Table 5.3 clearly indicates that steel fiber bridging contributed an average of 1.44 $\sqrt{f'_c}$ psi (0.12 $\sqrt{f'_c}$ MPa) of the total shear resistance (in terms of stress), irrespective of the beam depths, even though our larger size specimens experienced a wider critical crack compared to the smaller size beams (Table 5.1).

Table 5.3 The portion of average ultimate shear stress at failure due to each shear contributor at failure

1	2	3	4	5
Specimen	$V_u^{\,1}/(b.d\sqrt{f'_c})$ $\sqrt{psi}(\sqrt{MPa})$	$V_{uc}^{\,2}/(b.d\sqrt{f'_c})$ $\sqrt{psi}(\sqrt{MPa})$	$V_{sf}^{\,3}/(b.d\sqrt{f'_c})$ $\sqrt{psi}(\sqrt{MPa})$	$V_d^{\,4}/(b.d\sqrt{f'_c})$ $\sqrt{psi}(\sqrt{MPa})$
SFRC12W6	6.91 (0.57)	4.79 (0.40)	1.41 (0.12)	0.72 (0.06)
SFRC12W24	6.91 (0.57)	3.85 (0.32)	2.36 (0.20)	0.70 (0.06)
SFRC18a	5.12 (0.43)	3.29 (0.27)	1.24 (0.10)	0.60 (0.05)
SFRC18b	6.26 (0.52)	3.29 (0.27)	1.49 (0.12)	1.48 (0.12)
SFRC36b	5.81 (0.48)	2.62 (0.22)	1.31 (0.11)	1.89 (0.16)
SFRC48a	5.24 (0.44)	2.65 (0.22)	0.77 (0.06)	1.82 (0.15)
SFRC48b	5.06 (0.42)	1.82 (0.15)	1.51 (0.13)	1.73 (0.14)

1: Measured ultimate shear resistance; 2: Shear resisted by compression zone at peak; 3: Shear resisted by steel fiber in tension zone at peak; 4: Shear resisted by dowel action at peak.

To assess the effect of crack width (equivalent tensile stress) on steel fiber bridging, and thus size effect, the crack width parameter was isolated from the rest of possible influencing factors (crack length and orientation). As it was, the critical crack length and orientation were generally constant at the peak load for a given specimen, assuming different arbitrary crack widths and computing the corresponding crack interface tensions for that specimen could make general sense over the extent of steel fiber bridging variation for the range of assumed crack widths. To do so, the tensions induced across the critical crack were determined for each test specimen per the minimum and maximum crack widths reported by Shoaib et al. (2014), respectively (e.i. C_{wmin}=0.02 in (0.58 mm) and C_{wmax}=0.17 in (4.39 mm)). The equivalent tensile stress associated with the crack

widths of 0.02 in (0.58 mm) and 0.17 in (4.39 mm) were 109.3 and 39.7 psi (0.75 and 0.27 MPa), as picked from the average stress-crack width curve acquired from direct tensile test on the SFRC mix used in the current study. The difference between the resultant forces across critical crack for each beam due to the two different assumed crack widths reflects the additional amount of shear force and strength that the beam would develop if the narrower crack width governed. A sample of calculations performed for SFRC36b is demonstrated by **Error! Reference source not found.** .The average of the strength differences for all the specimens was found to be 1.27 $\sqrt{f'_c}$ which accounts for 33% of the average shear strength drop (3.88 $\sqrt{f'_c}$) observed by Shoaib et al. (2014) due to size effect. Therefore, the reduced tensile bridging stress alone due to the wider crack in larger members should not mainly represent size effect in ultimate shear.

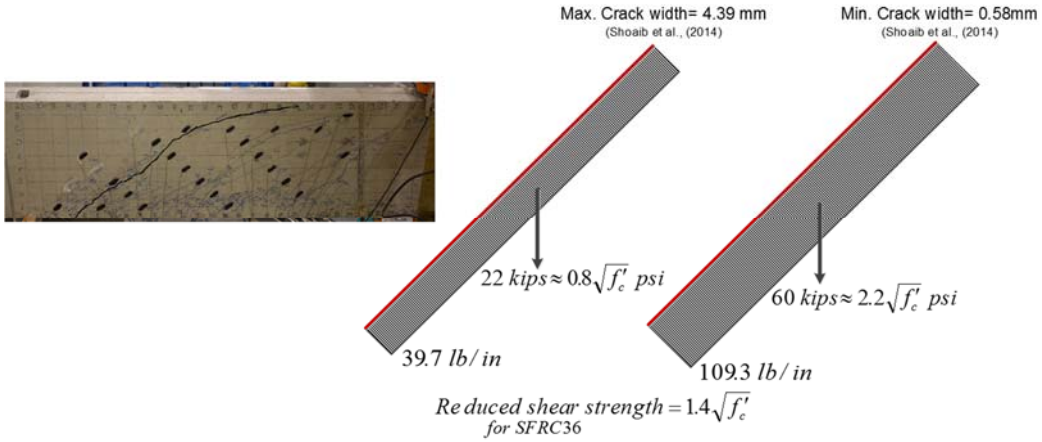

Figure 5.17 Variation of steel fiber bridging forces assuming different critical crack widths for SFRC36b

5.10 Factors Influencing size effect in SFRC beams

Conventionally, the size effect on the ultimate shear strength of plain concrete beams has been related to beam effective depth. Figure 5.18 shows the variation of the ultimate shear strength (in terms of $\sqrt{f'_c}$) versus effective depth, d; shear span length, a;

and shear span effective area, A_{eff} = d×a, respectively, for some series of plain concrete beams with various effective depths reported by Kani (1967) and Shioya et al. (1989). Each series of the beams had similar design parameters such as reinforcement ratio, shear span to effective depth ratio, maximum aggregate size, and concrete compressive strength. As illustrated by Figure 5.18, all the plots indicate exactly the same trend. In other words, while it has been conventionally claimed that size affect is a relationship between ultimate shear strength and the beam depth, it can also be said that the shear strength decreased with the increase of shear span length or the combination of effective depth and shear span length. In a general sense, the shear strength decreases when the distance from the loading point to the support increases.

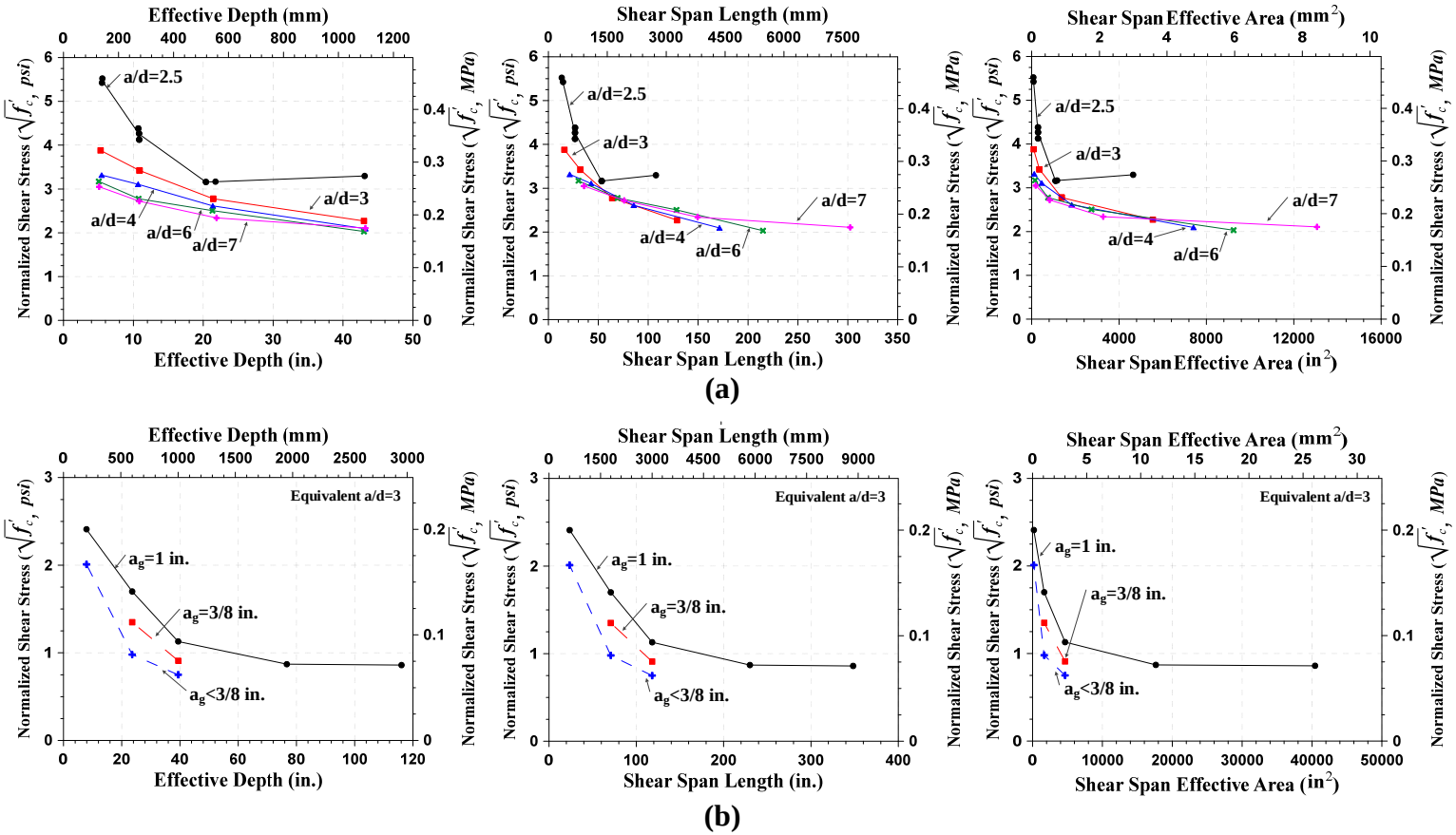

Figure 5.18 From left to right: Normalized shear stress at failure vs. effective depth, shear Span length, shear span effective area; (a) test results adopted from Kani (1967); (b) test results adopted from Shioya et al. (1989) (a_g = Maximum aggregate size)

In order to understand the shear-enhancement mechanism in SFRC beams and the factors influencing the size effect in SFRC beams, two important elements that enhance the shear strength of plain concrete beams are briefly reviewed:

Compression: It is well-known that applying uniaxial compression on concrete members is able to reduce the principal tensile stresses thus increasing the shear strength or delaying the propagation of shear cracks, and a biaxial compression (in order words, the concrete is confined) can completely eliminate the principal tensile stresses (Naaman, 2012). Therefore, any means used to generate uniaxial and biaxial compressive stresses (or confinement) in a concrete member can delay the shear crack propagation and thus increase the shear strength. Observations from the experimental testing of plain concrete beams with concentrated loads indicated that the diagonal cracks which developed were stopped at the location near the loading since the vertical compressive stresses under the load reduced the possibility of further tensile cracking. Likewise, the vertical compressive stresses near the supports limited the bond splitting and diagonal cracking (Ferguson et al., 1988). Leonhardt and Walter (1962) reported a series of plain concrete beam testing in which they compared beams loaded with a concentrated load versus uniform loading. They observed that the lowest shear stress of all beams at failure for uniformly distributed loading was about 40% higher than those for concentrated loads. They concluded that the vertical compressive stresses under the distributed load (in additional to the horizontal compressive stresses due to flexural bending) lead to a favorable effect on the strength of the concrete at the compression face of the beams. Muttoni and Ruiz (2008) reported their testing on a plain concrete beam having cracking control spiral reinforcement in the compression zone. The beam was able to reach its full flexural strength without premature shear failure because the cracks that propagated into the compression zone had much smaller width due to the spiral reinforcement.

Bond (Dowel) Strength: The bond (or dowel) strength of plain concrete is typically minor. As a consequence, once the aggregate interlock or compression zone loses its shear carrying capacity, dowel failure and splitting cracks along the longitudinal rebars often occurs immediately. This bond (dowel) strength can be enhanced when stirrups are used since these support the longitudinal rebars and thus retard the breakdown of bond when splitting cracks develop along the rebars (Park and Paulay, 1975; Bažant and Sun, 1988; Yoon et al., 1996; Stratford and Burgoyne, 2003). In other words, the improved contribution of the dowel action can increase the shear capacity of plain concrete beams. It has been shown that if a structural member is provided at least the minimum required area of stirrups, the reduction in shear failure stress with increasing member size becomes insignificant (Collins and Kuchma, 1999).

5.10.1 Compression zone capacity as a primary reason for size effect

Size effect in SFRC beams is explained by a lower shear strength capacity of the compression zone in larger size beams. Figure 5.19 compares the cracking pattern and compression zone between one of our small (SFRC18b) and large size (SFRC48b) specimens at the peak load. For comparison purposes, the range of viewable strains was fixed between (-0.129%) and (0.02%). Thereby, red color represented tensile strains irrespective of their intensity, while other colors (yellow to dark blue) represent various magnitudes of compressive strain in the compression zone. As clearly illustrated, cracks in the smaller beam were closer to the compression (or confined) zone as shown in the dark blue region of the figure. The higher compressive stresses along the path of the critical crack led to the increased shear strength of the compression zone as justified by the Rankine's model. By contrast, in the larger beam, the compression zone region was further away from many cracks, and the critical crack developed and propagated into the region which had much less confining stresses. For this reason, the shear strength of the

compression zone in a larger beam was smaller. Since an SFRC beam fails by following the failure of its compression zone, the lower capacity of compression zone in a larger beam results in lower ultimate shear strength, thus the size effect.

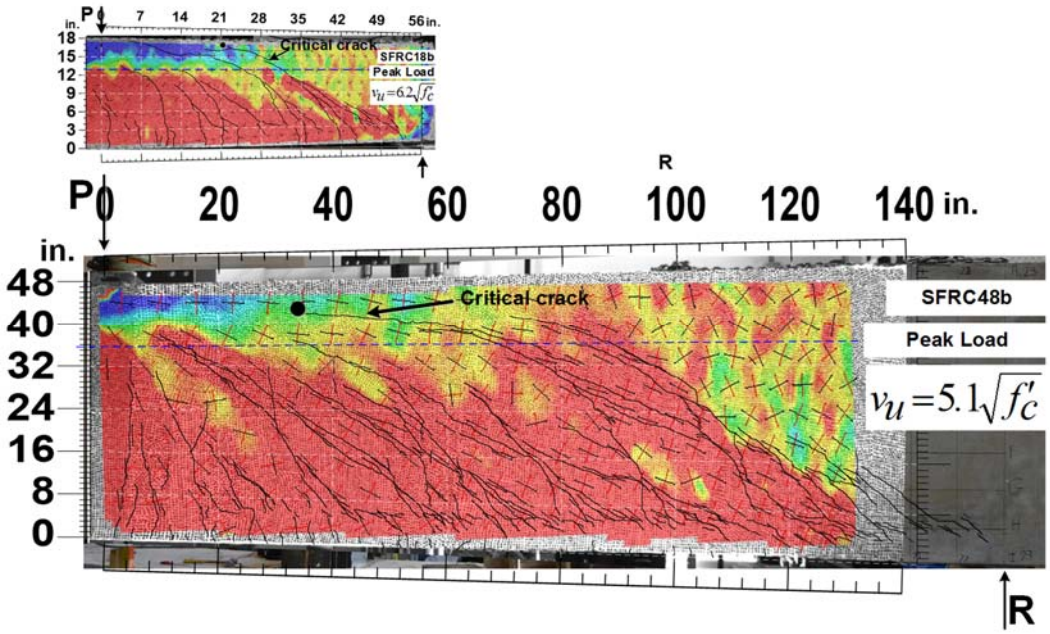

Figure 5.19 Comparison of compression zone and cracking pattern between smaller (SFRC18b) and larger (SFRC48b) size beams

To compare the extent of compressive stresses acting along failure paths (cracked and intact paths) between small and large size SFRC beams and subsequently demonstrate their effectiveness on the shear capacity of the compression zone, all the parameters adopted in Equations (5.4a) and (5.4b) were quantified and listed in Table 5.4. As expected, for those beams whose the critical crack positioned in the more confined region, the averages of the horizontal compressive stresses ($\overline{\sigma}_{u_{AB}}$ and $\overline{\sigma}_{u_{BC}}$) along the failure paths AB and BC in Figure 5.11 were substantially higher (second and third columns in Table 5.4). Therefore, that resulted in the higher compression zone shear capacity (column 8 in Table 5.4).

Table 5.4 Quantified parameters to determine shear capacity of compression zone for test specimens

1	2	3	4	5	6	7	8
Specimen	$\bar{\sigma}_{AB}$ psi	$\bar{\sigma}_{BC}$ psi	d_{AB} in.	d_{BC} in.	b in.	V_{uc} kips	$V_{uc}/b.d\sqrt{f'_c}$ (%)
SFRC12W6	2154	3480	1.4	2.4	6	18.7	4.79
SFRC12W24	3495	3992	2.4	1.0	24	60.2	3.85
SFRC18a	3296	4750	6.0	0.4	6	23.1	3.29
SFRC18b	2407	4619	3.8	1.7	6	23.1	3.29
SFRC36b	1941	3400	12.4	1.63	10	71.1	2.62
SFRC48a	2213	4009	5.0	7.0	12	118.6	2.65
SFRC48b	1159	1339	8.0	6.0	12	81.8	1.82

f_{ft}=95 psi (0.66 MPa); f_{fpt}=285 psi (1.97 MPa)

5.10.2 Dowel Strength on Size Effect

Dowel or bond strength is a secondary factor influencing size effect. As mentioned earlier, the dowel action contribution in shear resistance cannot be ignored. Therefore, if the strength of dowel action is low, the dowel zone cracks and causes additional forces to be transferred to compression zone, thereby leading to an early failure of the compression zone with the consequent prominence of the size effect.

The failure pattern of the SFRC beams tested by Minelli et al. (2014) is depicted in Figure 5.20. As noticed, the significant bond failure along the longitudinal bars due to the inadequate anchoring of the flexural bars resulted in the low strength of dowel action with the consequent early failure of their compression zone. For this reason, the SFRC beams had shown larger intensity of size effect than our beams.

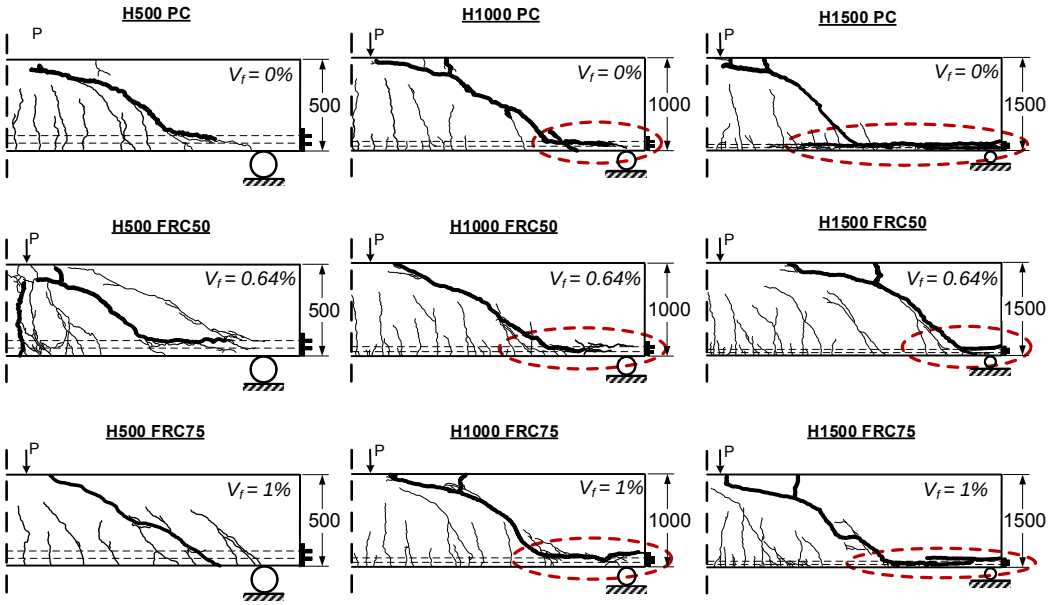

Figure 5.20 Intensified size effect following the anchorage failure in the deeper specimens due to the inadequate anchoring of the flexural rebars (Re-plotted from Minelli et al., 2014; 1 in. = 25.4 mm).

5.10.3 SFRC Mix Quality on Size Effect

Another secondary factor probably affecting size effect is SFRC mix quality. A high quality mix in an SFRC beam improves the redistribution of the internal stresses after the development of the first diagonal crack. As a matter of fact, ample redistribution of internal stresses causes the beam to develop multiple shear cracks. That makes the external load increase. Therefore, the higher compressive stresses induced in the compression zone enhances the shear capacity of the compression zone and subsequently, the ultimate shear strength of the beam. To illustrate, the failure pattern for one of the deepest beams tested by Shoaib et al. (2014) is compared with that of one of our largest SFRC beams, as indicated in Figure 5.21. In spite of the fact that our beam was larger in depth (48 in. versus 39 in.) and reinforced with a lower fiber volume fraction (0.75% versus 1%), our beam exhibited a greater number of multiple shear cracks on the surface, reflecting the improved

redistribution of internal stresses and thus, the quality of the mixture. For this reason, size effect turned out to have a larger effect on their beams.

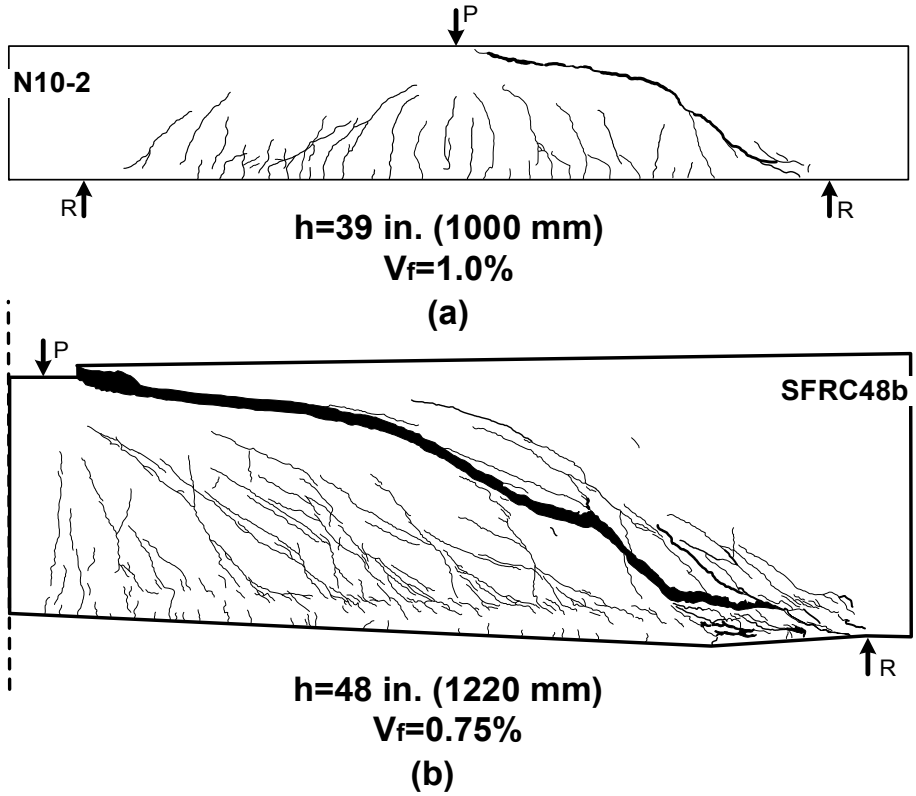

Figure 5.21 Comparison of the quality of mixes used in: (a) our test beam (depth=48 in. (1220 mm)); (b) the specimen (depth=39 in. (1000 mm)) tested by Shoaib et al. (2014) as illustrated by the number of shear cracks.

Chapter 6

SUMMARY AND CONCLUSIONS

6.1 Summary of the experimental program

An extensive experimental study was undertaken to examine strength-enhancement and failure mechanisms as well as size effect in steel fiber-reinforced concrete slender (SFRC) beams. To this end, a total of 10 SFRC beams and a controlling pair of 18-in.-high RC beams were designed, constructed, and finally tested to failure under point load and monotonic test conditions. All the tested beams were identical in terms of reinforcement ratio ($\rho = 2.67\%$), shear span to effective depth (a/d=3.5), and maximum aggregate size (ag=3/8"). Steel fibers were hook-end fibers in compliance with ASTM A820, where their mechanical properties (l/d =67, l = 2.0 in., d = 0.03 in., ft = 159 ksi) were held constant for all the SFRC specimens. The minimum steel fiber content of 0.75% allowed by ACI-318 (2014) was the only amount used to reinforce the instrumented span for shear in all the SFRC beams. Compressive strength of the concrete was targeted at 6000 psi which is the maximum strength of concrete allowed for the use of steel fibers as alternative shear reinforcement in the current code. The series of SFRC beams were cast in a form of 5 pairs of duplicate beams; the two beams in the last pair however differed in their width, as they were designated to investigate the effect of element width on ultimate shear strength. Beam height was the only key parameter varying from one pair of beams to the other in a wide range of 12 to 48 inches.

6.2 Conclusions

Based on the results of this investigation, the following conclusions were drawn:

(1) The first and primary factor contributing to shear strength enhancement of SFRC slender beams lies in delaying the initiation and then slowing the propagation of diagonal shear cracks, which then leads to higher confining stresses in the

compression zone. Therefore, the compression zone is enabled to remain stable even when shear cracks propagate into it.

(2) From the full field deformations measured by the DIC and the Cauchy based mechanical analysis, dowel action was recognized as one of the major contributors to the shear resistance of SFRC beams.

(3) For SFRC beams with 0.75% fiber volume fraction, dowel action accounts for 10 to 35% of the total shear capacity as the height varies from 12 in. (305 mm) to 48 in. (1220 mm). Meanwhile, for this range of beam height, the compression zone contribution decreases from 69 to 36% of the total shear resistance. Additionally, the steel fiber bridging effect was observed to remain constant at approximately 25%.

(4) The conventional hypothesis of size effect on shear strength for plain concrete beams does not apply to SFRC beams. In SFRC beams, the widths of the critical shear cracks before ultimate shear strength are much larger than the maximum crack widths for engaging the aggregate interlock.

(5) Test results obtained from this study indicate a moderate size effect in ultimate shear strength of SFRC beams with 0.75% V_f steel fibers and an overall depth up to 1220 mm (48 in.).

(6) Size effect not only is a function of beam height, but also a function of shear span; that is, how far an inclined shear crack can propagate before it encounters the compression zone.

(7) The most important factor influencing the intensity of the size effect in SFRC beams is the shear strength of the compression zone. The dowel strength and quality of SFRC mixture can also further intensify the size effect on ultimate shear strength.

(8) ACI 318 provision can be safely modified to increase the allowable factor for shear stress to $\phi 4.0\sqrt{f'_c}$ for SFRC slender beams with an overall depth up to 50 inches.

REFERENCES

1. ACI Committee 318, "Building Code Requirements for Structural Concrete (ACI 318-14) and Commentary (ACI 318R-14)," American Concrete Institute, Farmington Hills, MI, 2014, 519 pp.
2. ACI Committee 544, "Design Consideration for Steel Fiber Reinforced Concrete," Report ACI 544R-88, American Concrete Institute, Farmington Hill, MI, 1999.
3. ACI-ASCE Committee 326 (1962), "Shear and Diagonal Tension," *ACI Journal Proceedings, 59* (3).
4. ACI-ASCE Committee 544 (1988). "Design Considerations for Steel Fiber Reinforced Concrete." *ACI Journal Proceedings*, *85*(5), 563-579.
5. Allen, H. G. (1972). "The Strength of Thin Composites of Finite Width, with Brittle Matrices and Random Discontinuous Reinforcing Fibres (Tensile Strength Estimation for Two Dimensional Composite with Brittle Matrix and Randomly Orientated Discontinuous Elastic Fibrous Reinforcement)." *Journal of Physics D (Applied Physics)*, *5*, 331-343.
6. ASCE-ACI Committee 426 (1973). "The Shear Strength of Reinforced Concrete Members," *Journal of Structural Division, ASCE*, *99*(6), 1091-1187.
7. Ashour, S. A., Hasanain, G. S., and Wafa, F. F. (1992). "Shear Behavior of High-Strength Fiber Reinforced Concrete Beams." *ACI Structural Journal, 89*(2), 176- 184.
8. ASTM C1609 / C 1609M, "Standard Test method for Flexural Performance of Fiber-Reinforced Concrete (Using Beam with Third-Point Loading)," ASTM International, West Conshohocken, PA, 2012, pp 9.
9. ASTM C39 / C39M, "Standard Test Method for Compressive Strength of Cylindrical Concrete Specimens," ASTM International, West Conshohocken, PA, 2012.

10. Aveston, J., Mercer, R. A., and Sillwood, J. M. "Fibre Reinforced Cements – Scientific Foundation for Specifications." *Proceedings of National Physical Laboratory Conference*, UK, 93-103.
11. Balaguru, P. N. and Shah, P., *Fiber-reinforced cement composites*, 1st Ed., McGraw-Hill Inc., 1992.
12. Banthia, N. and Trottier, J. F. (1994). "Concrete Reinforced with Deformed Steel Fibers, Part I: Bond-Slip Mechanisms." *ACI Materials Journal*, *91*(5), 435-446.
13. Barragán, B., Gettu, R., Agulló, L., and Zerbino, R. (2006). "Shear Failure of Steel Fiber-Reinforced Concrete Based on Push-Off Tests." *ACI Materials Journal*, *103*(4), 251-257.
14. Baston, G., Jenkins, E., and Spatney, R. (1972). "Steel Fibers as Shear Reinforcement in Beams." *ACI Journal Proceedings*, *69*(10), 640-644.
15. Baumann, H., (1968). "Tests to Study the Dowel Action of the Bending Tension Reinforcement of Reinforced Concrete Beams," *Bericht Nr. 77*, Munich Technischen Hochschule, (English Translation by PCA).
16. Bažant, Z. P. and Sun, H.-H. (1988). "Size Effect in Diagonal Shear Failure: Influence of Aggregate Size and Stirrups." *ACI Materials Journal, July-August*, 259-272.
17. Bentur, A., and Mindess, S., *Fiber Reinforced Cementitious Composites*. 2nd Ed., Taylor & Francis, 2007.
18. Bentz, E.C., Vecchio, F.J. and Collins, M.P. (2006). "Simplified Modified Compression Field Theory for Calculating Shear Strength of Reinforced Concrete Elements." *ACI Structural Journal*, *103*(4), 614-624.
19. Bernard, E. S. (2002). "Correlations in the Behaviour of Fibre Reinforced Shotcrete Beam and Panel Specimens." *Materials and Structures*, *35*, 156-164.

20. Bresler, B. and Pister, K. S. (1958). "Strength of Concrete Under Combined Stresses." *ACI Journal, 55*(9), 321–345.
21. CEB-FIP, "Model Code for Concrete Structures: CEB-FIP International Recommendations, 3rd ed," Comite Euro-International du Beton, Paris, 1978, 348pp.
22. Chao, S. H., Cho, J. S., Karki, N. B., Sahoo, D. R., and Yazdani, N. (2011). "FRC Performance Comparison: Uniaxial Direct Tensile Test, Third-Point Bending Test, and Round Panel Test." *ACI Special Publication*, *276*.
23. Cho, J. S. (2011). "*Shear behavior of steel fiber reinforced prestressed concrete beams without shear reinforcement.*" Doctoral Dissertation, Dept. of Civil and Environmental Engineering, Univ. of Texas at Arlington.
24. Choi, K. K., Park, H. G., and Wight, J. K. (2007). "Shear Strength of Steel Fiber-Reinforced Concrete Beams Without Web Reinforcement." *ACI Structural Journal, 104* (1), 12-21.
25. Collins, M. P., and Kuchma, D. (1999). "How Safe Are Our Large, Lightly-Reinforced Concrete Beams, Slabs and Footings?" *ACI Structural Journal, 96*(4), 482-490.
26. Collins, M.P., Bentz, E.C and Sherwood, E.G. (2008). "Where is Shear Reinforcement required? A Review of Research Results and Design Procedures." *ACI Structural Journal Proceedings*, *59*(9), 1334-1339.
27. Collins, M.P., Mitchell, D., Adebar, P., and Vecchio, F. J. (1996). "A General Shear Design Method." A*CI Structural Journal*, *93*(1), 36–45.
28. Cox, H. L. (1952). "The Elasticity and Strength of Paper and other Fibrous Materials." *British Journal of Applied Physics*, *3*, 72-79.
29. CSA Committee A23.3, "Design of Concrete Structures," Canadian Standards Association, Mississauga, Ontario, 2004, 214pp.

30. Dinh, H. H. (2009). "*Shear behavior of steel fiber reinforced concrete beams without stirrup reinforcement.*" Doctoral Dissertation, Dept. of Civil and Environmental Engineering, Univ. of Michigan, Ann Arbor, MI, 285.
31. Dinh, H. H., Parra-Montesinos, G. J., and Wight, J. K. (2010). "Shear behavior of steel fiber reinforced concrete beams without stirrup reinforcement." *ACI Structural Journal*, *107*(5), 597-606.
32. Dinh, H. H., Parra-Montesinos, G. J., and Wight, J. K. (2011). "Shear strength model for steel fiber reinforced concrete beams without stirrup reinforcement." *Journal of Structural Engineering, 137*(10), 1039-1051.
33. Drucker, D. C. (1961). "On Structural Concrete and the Theorems of Limit Analysis." *IABSE proceedings*, *21*, 49-59.
34. Fanella, D. and Naaman, A. E. (1985). "Stress-Strain Properties of Fiber Reinforced Mortar in Compression." *ACI Journal*, *82*(4), 475-483.
35. Fenwick, R. C. and Paulay, T. (1968). "Mechanisms of Shear Resistance of Concrete Beams." *Journal of Structural Division proceedings, 94*(10), 2325-2350.
36. Ferguson, P. M., Breen, J. E., and Jirsa, J. O., *Reinforced Concrete Fundamentals*. 5th Ed., John Wiley & Sons, Inc., 1988, 768 pp.
37. Gao, J., Sun, W., and Morino, K. (1997). "Mechanical Properties of Steel Fiber-reinforced, High strength, Lightweight Concrete." *Cement and Concrete Composite*, *19*, 307-313.
38. Gustafsson, P.J. and Hillerborg, A. (1988). "Sensitivity in Shear Strength of Longitudinally Reinforced Concrete Beams to Fracture Energy of Concrete." *ACI Structural Journal*, *85*(3), 286-294.
39. Hannant, D. J., *Fibre Cements and Fibre Concrete*, Wiley, Chicester, U.K., 1978.

40. Hanson, J.A. (1958). "Shear Strength of Lightweight Reinforced Concrete Beams." *ACI Journal*, *30*(3), *Proceedings, 55*, 387-403.

41. Hofbeck, J. A., Ibrahim, I. O., and Mattock, A. H. (1969). "Shear Transfer in Reinforced Concrete." *ACI Journal*, *66*(2), 119-128.

42. Houde, J. and Mirza, M. S., "A Finite Element Analysis of Shear Strength of Reinforced Concrete Beams." *ACI-Special Publication*, SP-42, 103-128.

43. Iosipescu, N. (1967). "New Accurate Procedure for Single Shear Testing of Metals." *Journal of Materials*, *2*(3), 537-566.

44. Iosipescu, N. and Negoita, A. (1969). "A New Method for Determining the Pure Shearing Strength of Concrete." *Journal of Concrete Society*, *3*(1), 63.

45. JSCE-SF6, "Method of Test for Shear Strength of Steel Fiber Reinforced Concrete (SFRC)," Japan Society of Civil Engineers, Tokyo, 1990, 67-69.

46. Kani, G.N.J. (1964). "The Riddle of Shear Failure and its Solution." *ACI Journal Proceedings, 61*(4), 441-466.

47. Kani, G.N.J. (1967). "How Safe Are Our Large Reinforced Concrete Beams?" *ACI Structural Journal*, *Proceedings, 64*(3), 128-141.

48. Kani, M. W., Huggins, M. W., and Wittkopp, R. R., *Kani on shear in reinforced concrete*. Toronto, Canada: University of Toronto Press, 1979, 225 pp.

49. Khaja, M. N., and Sherwood, E. G. (2013). "Does the shear strength of reinforced concrete beams and slabs depend upon the flexural reinforcement ratio or the reinforcement strain?" *Canadian journal of civil engineering, 40*(11), 1068-1081.

50. Khaloo, A. R., and Kim, N. (1996). "Mechanical Properties of Normal to High-Strength Steel Fiber-Reinforced Concrete." *Cement, Concrete and Aggregates*, *18*(2), 92-97.

51. Kotsovos, M. D. (1988). "Compressive Force Path Concept: Basis for Reinforced Concrete Ultimate Limit State Design." *ACI Structural Journal, 85*(1), 68-85.

52. Kotsovos, M. D. and Pavlović, M. N., *Ultimate Limit-State Design of Concrete Structures: A New Approach*, Thomas Telford, London, 1998, 208 pp.

53. Kwak, Y.-K., Eberhard, M. O., Kim, W.-S., and Kim, J. (2002). "Shear Strength of Steel Fiber-reinforced Concrete Beams without Stirrups." *ACI Structural Journal, 99*(4), 530-538.

54. Leonhardt, F., and Walther, R. (1962). "Contribution to the Treatment of Shear Problems in Reinforced Concrete." *Beton und Stahlbetonbau*, *56*(12) and *57*(2,3,6,7,8).

55. Leonhardt, F., and Walther, R. (1962). "The Stuttgart Shear Tests, " Translation of articles from *Beton und Stahlbetonbau*, *56*(12), 1961 and *57*(2,3,6,7,8), 1962, Cement and Concrete Association Library Translation No. 111, Wexham Springs, United Kingdom, Dec 1964, 134 pp.

56. Li, V. C., Wang, Y., and Backer, S. (1990). "Effect of Inclining Angle, Bundling and Surface Treatment on Synthetic Fiber Pull-Out from a Cement Matrix." *Composites, 21*(2), 132-140.

57. Lim, T. Y., Paramasivam, P., and Lee, S. L. (1987). "Analytical Model for Tensile behavior of Steel-Fiber Concrete." *ACI Materials Journal*, *84*(4), 286-298.

58. Lubell, A., Sherwood, T., Bentz, E. C., and Collins, M. P. (2004). "Safe Shear Design of Large, Wide Beams." *Concrete International, 26*(1), 66-78 .

59. MacGregor, J. G. and Hanson, J. M. (1969). "Proposed Changes in Shear Provisions for Reinforced and Prestressed Concrete Beams." *ACI Journal proceedings*, *66*(4), 276-288.

60. Mansur, M. A.; Ong, K. C. G.; and Paramasivam, P. (1986). "Shear Strength of Fibrous Concrete Beams without Stirrups." *Journal of Structural Engineering, ASCE, 112*(9), 2066-2079.

61. Minelli, F., Conforti, A., Cuenca, E., and Plizzari, G. (2014). "Are steel fibres able to mitigate or eliminate size effect in shear?" *Materials and structures*, *47*(3), 459-473.

62. Mirsayah, A.A., and Banthia, N. (2002). "Shear Strength of Steel Fiber-Reinforced Concrete." *ACI Material Journal,99*(5), 473-479.

63. Mobasher, B., *Mechanics of Fiber and Textile Reinforced Cement Composites.* Boca Raton, Florida, US: CRC Press Taylor & Francis Group, 2012, 473 pp.

64. Moe, J. (1962) Discussion of ACI-ASCE Committee 326 (1962), *Journal of the American.*

65. Moody, K.G., Viest, I.M., Elstner, R.C. and Hognestad, E. (1954). "Shear Strength of Reinforced Concrete Beams Part 1 –Tests of Simple Beams." *ACI Journal*, 26(4). *Proceedings 51*, 317-332.

66. Moretto, O. (1955) Discussion of Zwoyer and Siess (1954), *ACI Journal*, *27*(4), *Part 2 Proceedings 51*, 200/2-200/5.

67. Morton, J., and Groves, G. W. (1974). "Cracking of Composites Consisting of Discontinuous Ductile Fibers in a Brittle Matrix-Effect of Fiber Orientation." *Journal of Materials Science, 9,* 1436-1445.

68. Muhidin, N. A., and Regan, P. E. (1977). "Chopped Steel Fibers as Shear Reinforcement in Concrete Beams." *Proceedings, Conference on Fiber Reinforced Materials; Design and Engineering Applications,* Institution of Civil Engineers, London, 140-163.

69. Muttoni, A. and Fernández Ruiz, M. (2008). "Shear strength of members without transverse reinforcement as a function of the critical shear crack width." *ACI Structural Journal, 105*(2), 163-172.

70. Naaman, A. E. (1985). "Fiber Reinforcement for Concrete." *Concrete International*, *7*(3), 5.

71. Naaman, A. E. (2002). "Toughness, Ductility, Surface Energy and Deflection-Hardening FRC Composites," *Proceedings of the JCI International Workshop on Ductile Fiber Reinforced Cementitious Composites (DRFCC)—Application and Evaluation* (DFRCC-2002), Japan Concrete Institute. 33-57.

72. Naaman, A. E. and Reinhardt, H. W. (2003). "High Performance Fiber-Reinforced Cement Composites: HPFRCC 4," *RILEM Proceedings* Pro 30, RILEM Publications S.A.R.L., 95-113.

73. Naaman, A. E., and Najm, H. (1991). "Bond-Slip Mechanisms of Steel Fibers in Concrete." *ACI Materials Journal*, *88*(2), 135-145.

74. Naaman, A. E., and Reinhardt, H. W (1995). "Characterization of High Performance Fiber Reinforced Cement Composites." *Proceedings of the Second International Workshop 'High Performance Fiber Reinforced Cement Composites'*, Ann Arbor, USA, 528.

75. Naaman, Antoine E., and Shah, Surendra P. (1976). "Pull-Out Mechanisms in Steel Fiber Reinforced Concrete." *Journal of the Structural Division,* ASCE, 1537-1548.

76. Narayanan, R., and Darwish, I. Y. S. (1987). "Use of Steel Fibers as Shear Reinforcement." *ACI Structural Journal, 84*(3), 216-227.

77. Narayanan, R., and Kareem-Palanjian, A. S. (1984). "Effect of Fiber Addition on Concrete Strengths." *Indian Concrete Journal*, *58*(4), 100-103.

78. Noghabai, K. (2000). "Beams of Fibrous Concrete in Shear and Bending: Experiment and Model." *ASCE Structural Engineering Journal*, *126*(2), 243-251.

79. Park HG, Choi KK, Wight JK. (2006). *"*Strain-based shear strength model for slender beams without web reinforcement.*" ACI Structural Journal, 103*(6), 783–93.

80. *Park, H., Kang, S., and Choi, K. (2013). "Analytical model for shear strength of ordinary and prestressed concrete beams." Engineering Structures, 46, 94-103.*

81. Park, P. and Paulay, T., *Reinforced Concrete Structures*, John Wiley & Sons, Inc., 1975, 769 pp.

82. Parra-Montesinos, G. J. (2006). "Shear Strength of Beams with Deformed Steel Fibers." *Concrete International, 28*(11), 57-66.

83. Pierron, F., and Vautrin, A. (1997). "Measurement of the In-Plane Shear Strength of Unidirectional Composites with the Iosipescu Test." *Composites Science and Technology*, *57*, 1653-1660.

84. Ramakrishnan, V., Brandshaug, T., Coyle, W. V., and Schrader, E. K. (1980). "A Comparative Evaluation of Concrete Reinforced with Straight Steel Fibers and Fibers with Deformed Ends Glued Together into Bundles." *ACI Journal, 77*(3), 135-143.

85. Romualdi J. & Mandel, J. (1964). "Tensile strength of concrete affected by uniformly distributed and closely spaced short lengths of wire reinforcement." *ACI Journal*, *61*(6), 657-671.

86. Rosenbusch, J., and Teutsch, M. (2002). "Trial Beams in Shear: Test Programme 3."

87. Shah, S. P. and Rangan, B. V. (1971). "Fiber Reinforced Concrete Properties." *ACI Journal*, *68*(2), 126-137.

88. Shah, S. P., Stroeven, P., Dalhuisen, D., and Van Stekelenburg, P., *Complete Stress-Strain Curves for Steel Fibre Reinforced Concrete in Uniaxial Tension and Compression*. Testing and Test Methods of Fibre Cement Composites, RILEM Symposium 1978, Construction Press, Lancaster, pp. 399-408.

89. Sherwood, E. G. (2008). "*One-way shear behavior of large, lightly-reinforced concrete beams and slabs*." PhD dissertation, Department of Civil Engineering, University of Toronto, Toronto, ON, Canada, 547 pp.

90. Sherwood, E. G., Bentz, E. C., and Collins, M. P. (2007). "Effect of Aggregate Size on Beam-Shear Strength of Thick Slabs." *ACI Structural Journal*, *104*(2), 180-191.

91. Sherwood, E. G., Lubell, A., Bentz, E. C., and Collins, M. P. (2006). "One-Way Shear Strength of Thick Slabs." *ACI Structural Journal*, *103*(6), 794-802.

92. Shioya, T., Iguro, M., Nojiri, Y., Akiyama, H., and Okada, T., *Shear Strength of Large Reinforced Concrete Beams' Fracture Mechanics: Application to Concrete*. SP 118, American Concrete Institute, Detroit, 1990, 309 pp.

93. Shioya, T., *Shear Properties of Large Reinforced Concrete Member*, Special Report of Institute of Technology, Shimizu Corporation, No. 25, 1989, 198 pp.

94. Shoaib, A., Lubell, A. S., and Bindiganavile, V. S. (2014). "Size Effect in Shear for Steel Fiber-Reinforced Concrete Members without Stirrups." *ACI Structural Journal, 111*(5), 1081-1090.

95. Sneed, L. H., and Ramirez, J. A. (2010). "Influence of effective depth on shear strength of concrete beams experimental study." *ACI Structural Journal*, *107*(05), 554-562.

96. Sneed, L. H., and Ramirez, J. A. (2014). "Influence of Cracking on Behavior and Shear Strength of Reinforced Concrete Beams." *ACI Structural Journal*, *111*(1), 157-166.

97. Song, P. S., and Hwang, S. (2004). "Mechanical properties of high-strength steel fiber reinforced concrete." *Construction and Building Materials*, *18*(9), 669-673.

98. Soroushian, P., and Bayasi, Z. (1991). "Fiber Type Effects on the Performance of Steel Fiber Reinforced Concrete." *ACI Materials Journal*, *88*(2), 129-134.

99. Stratford, T. and Burgoyne, C. (2003). "Shear Analysis of Concrete with Brittle Reinforcement." *Journal of Composites for Construction, ASCE*, 7(4), 323-330.

100. Swamy, R. N. and Andriopoulos, A. D. (1974). "Contribution of Aggregate Interlock and Dowel Forces to the Shear Resistance of RC Beams with Web Reinforcement." *ACI Special Publication SP42-6*, 129-166.

101. Swamy, R. N., Mangat, P. S., and Rao, C. V. S. K. (1974). "The Mechanics of Fiber Reinforcement of Cement Matrices." *Fiber Reinforced Concrete, ACI Special Publication SP-44*, 1-28.

102. Swamy, R.N., and Bahia, H. M. (1979). "Influence of Fiber Reinforcement on the Dowel Resistance to Shear." *ACI Journal Proceedings, 76*(2), 327-355.

103. Swamy, R.N., and Bahia, H. M. (1985). "Effectiveness of Steel Fibers as Shear Reinforcement." *Concrete International: Design* & *Construction, 7*(3), 35-40.

104. Swamy, R.N., Jones, R., and Chiam, A. T. P. (1993). "Influence of Steel Fibers on the Shear Resistance of Lightweight Concrete I-Beams." *ACI Structural Journal, 90*(1), 103-114.

105. Swartz, S. E. and Taha, N. M. (1991). "Crack Propagation and Fracture of Plain Concrete Beams Subjected to Shear and Compression." *ACI Structural Journal*, *88*(2), 169-177.

106. Taylor, H.P.J., *Investigation of Forces Carried across Cracks in Reinforced Concrete Beams by Interlock of Aggregates*. London, TRA 42.447, Cement and Concrete Association, 1970, 22pp.

107. Thomas, J., and Ramaswamy, A. (2007). "Mechanical Properties of Steel Fiberreinforced Concrete." *ASCE Journal of Materials in Civil Engineering*, *19*(5), 385-392.

108. Tureyen, A.K. and Frosch, R.J. (2003). "Concrete Shear Strength: Another Perspective," A*CI Structural Journal*, *100*(5), 609-615.

109. Untrauer, R. E. and Henry, R. L. (1965). "Influence of Normal Pressure on Bond Strength." *ACI Journal Proceedings, 62*(5), 577-586.

110. Valle, M., and Buyukozturk, O. (1993). "Behavior of Fiber Reinforced High-strength Concrete under Direct Shear." *ACI Materials Journal*, *90*(2), 122-133.

111. Van Zijl, G. P. A. G. (2007). "Improved Mechanical Performance: Shear Behavior of Strain-Hardening Cement-Based Composites (SHCC)." *Cement and Concrete Research*, *37,* 1241-1247.

112. Vecchio, F. J. and Collins, M. P. (1986). "The Modified Compression-Field Theory for Reinforced Concrete Elements Subjected to Shear." *ACI Journal, 83*(2), 219-231.

113. Wafa, F. F. and Ashour, S. A. (1992). "Mechanical Properties of High-Strength Fiber Reinforced Concrete." *ACI Material Journal*, *89*(5), 449-455.

114. Walraven, J.C. (1981). "Fundamental Analysis of Aggregate Interlock." *Journal of Structural Engineering, ASCE*, 107(11), 2245-2270.

115. Walther, R. (1962). "Calculation of the Shear Strength of Reinforced and Prestressed Concrete Beams by the Shear Failure Theory." Translation 110, *Cement and Concrete Association*, originally in *Beton-und Stahlbetonbau*, *57*(11), 261-271.

116. Wight, J. K. and MacGregor, J. G., *Reinforced Concrete – Mechanics and Design*. 6th Ed., Upper Saddle River, NH, Prentice Hall, 2012, 1168 pp.

117. Williamson, G. R., and Knab, L., *Full Scale Fiber Concrete Beam Tests*. Proceedings, RILEM Symposium on Fiber Reinforced Cement and Concrete, London, Construction Press Ltd., Hornby, 1975, pp. 209-214.

118. Yoon, Y.-S., Cook, W. D., and Mitchell, D. (1996). "Minimum Shear Reinforcement in Normal, Medium, and High-Strength Concrete Beams." *ACI Structural Journal, 93*(5), 1-9.

119. Zsutty, T. C. (1968). "Beam Shear Strength Prediction by Analysis of Existing Data." *ACI Journal Proceedings*, *65*(11), 943-951.

120. Zwoyer, E.M. and Siess, C.P. (1954). "Ultimate Strength of Simply-Supported Prestressed Concrete Beams without Web Reinforcement." *ACI Journal Proceedings*, *29*(2), 181-200.